OLUSEUN AKINTOLA

Carboxylate-functionalized
triphenylamine-based complexes:
From discrete monomeric complexes
to 2D and 3D extended frameworks

DISSERTATION
(kummulativ)

Chemisch-Geowissenschaftliche Fakultät
Friedrich-Schiller-Universität, Jena

Carboxylate-functionalized triphenylamine-based complexes: From discrete monomeric complexes to 2D and 3D extended frameworks

DISSERTATION

(kumulativ)

zur Erlangung des akademischen Grades doctor rerum naturalium

(Dr. rer. nat.)

vorgelegt dem Rat der Chemisch-Geowissenschaftlichen Fakultät

der Friedrich-Schiller-Universität Jena

von MSc.-Chem. Oluseun Akintola

geboren am 08. Oktober 1981 in Lagos, Nigeria

seit 1558

You cannot teach a man anything; you can only help him discover it in himself.

—————————————————————

Galileo Galilei

An expert is a person who has made all the mistakes that can be made in a very narrow field.

—————————————————————

Niels Bohr

–to my girls–

’tope and ’funke

Contents

Documentation of authorship

This section contains a list of individual author contributions to the publications and manuscripts included in this thesis.

P1: O. Akintola,[1] M. Böhme,[2] M. Rudolph,[3] A. Buchholz,[4] H. Görls,[5] W. Plass,[6] Metal Bonded Triarylamines and their Interactions: Synthesis, Structure, and Redox Properties of Paddle-Wheel Copper Complexes, *Chem. - Eur. J.* **2018**, *Submitted.*

Authors	1	2	3	4	5	6
Conceptual development	✓					
Syntheses	✓					
Physico-chemical characterization	✓				✓	
Theoretical studies		✓				
Electrochemical investigations	✓		✓			
Magnetic studies				✓		
Preparation of the manuscript	✓					
Correction of the manuscript				✓		✓
Supervision of O. Akintola						✓
Proposed publication equivalent	1.0					

P2: O. Akintola,[1] D. Hornig,[2] A. Buchholz,[3] H. Görls,[4] W. Plass,[5] Solvent-dependent selective cation exchange in anionic frameworks based on cobalt(II) and triphenylamine linkers: reactor-dependent synthesis and sorption properties *Dalton Trans.* **2017**, 46, 8037–8050.

Authors	1	2	3	4	5
Conceptual development	✓				
Syntheses	✓				
Physico-chemical characterization	✓			✓	
Theoretical studies		✓			
Magnetic studies	✓		✓		
Preparation of the manuscript	✓				
Correction of the manuscript			✓		✓
Supervision of O. Akintola					✓
Proposed publication equivalent	1.0				

Documentation of authorship

P3: O. Akintola,[1] S. Ziegenbalg,[2] A. Buchholz,[3] H. Görls,[4] W. Plass,[5] Robust anionic pillared-layer framework based on triphenylamine-based linkers: ion exchange and counterion dependent sorption properties *CrystEngComm* **2017**, 19, 2723–2732.

Authors	1	2	3	4	5
Conceptual development	✓				
Syntheses	✓				
Physico-chemical characterization	✓			✓	
Magnetic Studies	✓	✓	✓		
Preparation of the manuscript	✓				
Correction of the manuscript			✓		✓
Supervision of O. Akintola					✓
Proposed publication equivalent	1.0				

P4: O. Akintola,[1] A. Buchholz,[2] H. Görls,[3] W. Plass,[4] Isophthalic acid modulated synthesis of a neutral Co(II) nitrilotribenzoic acid MOF: Magnetic and sorption properties *Eur. J. Inorg. Chem.* **2018** *To be submitted.*

Authors	1	2	3	4
Conceptual development	✓			
Syntheses	✓			
Physico-chemical characterization	✓		✓	
Magnetic studies	✓	✓		
Preparation of the manuscript	✓			
Correction of the manuscript		✓		
Supervision of O. Akintola				✓
Proposed publication equivalent	1.0			

P5: G. Mohammadnezhad,[1] O. Akintola,[2] W. Plass,[3] F. Schacher,[4] F. Steiniger,[5] M . Westermann,[6] Facile synthesis of highly thermally stable nanoporous γ-aluminas from aluminum alkoxide precursors *RSC Adv.* **2015**, *5*, 49493–49500.

Authors	1	2	3	4	5	6
Conceptual development	✓					
Syntheses	✓					
Physico-chemical characterization	✓			✓	✓	✓
Sorption studies		✓				
Preparation of the manuscript	✓	✓				
Correction of the manuscript			✓			
Supervision of O. Akintola			✓			
Proposed publication equivalent		0.5				

P6: G. Mohammadnezhad,[1] O. Akintola,[2] W. Plass,[3] F. Steiniger,[4] M . Westermann,[5] A facile, green and efficient surfactant-free method for synthesis of aluminum nanooxides with an extraordinary high surface area *Dalton Trans.* **2016**, *45*, 6329–6334.					
Authors	1	2	3	4	5
Conceptual development	✓				
Syntheses	✓				
Physico-chemical characterization	✓			✓	✓
Sorption studies		✓			
Preparation of the manuscript	✓	✓			
Correction of the manuscript			✓		
Supervision of O. Akintola			✓		
Proposed publication equivalent		0.5			

Erklärung zu den Eigenteilen des Promovenden sowie der weiteren Doktoranden/Doktorandinnen als Koautoren an den Publikationen und Zweitpublikationsrechten bei einer kumulativen Dissertation

Für alle in dieser kumulativen Dissertation verwendeten Manuskripte liegen die notwendigen Genehmigungen der Verlage ("Reprint permissions") für die Zweitpublikation vor.

Die Ko-Autoren der in dieser kumulativen Dissertation verwendeten Manuskripte sind sowohl über die Nutzung als auch über die oben angegebenen Eigenanteile informiert und stimmen dem zu. Die Anteile der Ko-Autoren an den Publikationen sind in den vorausgehenden Tabellen (Documentation of authorship) aufgeführt.

Ich bin mit der Abfassung der Dissertation als publikationsbasiert, d.h. kumulativ, einverstanden und bestätige die vorstehenden Angaben. Eine entsprechend begründete Befürwortung mit Angabe des wissenschaftlichen Anteils des Doktoranden/der Doktorandin an den verwendeten Publikationen werde ich parallel an den Rat der Fakultät der Chemisch- Geowissenschaftlichen Fakultät richten.

Oluseun Akintola		Jena	——————
Name des Promovenden	Datum	Ort	Unterschrift

Prof. Dr. Winfried Plass		Jena	——————
Name Erstbetreuer	Datum	Ort	Unterschrift

Chapter 1

Introduction

Coordination polymers are a group of compounds characterized by their repetitive array of metal ions and organic ligands linked *via* coordination bonds and the last quarter century has seen so much effort devoted to their study. They typically display variety in their structures—from the 1D chains, to the 2D nets and up to the 3D frameworks.[1] Often, due to the preorganized structure of the comprising ligands, the result is the formation of rigid networks, which in the case of the 2- and 3D systems, can potentially contain voids. In such instances where the cavities are permanent they are referred to as metal−organic frameworks (MOFs).[2]

Coordination polymers (CPs) have come quite a long way and have emerged as a large, extensive and growing group of compounds possessing extraordinarily high porosity and large internal surface areas with some being reported to have over $7000\,\mathrm{m^2\,g^{-1}}$ as accessible surface area.[3] A major advantage of these MOFs is their crystalline nature, which allows their structures to be easily determined by X-ray diffraction. This enables the correlation of their structures with their properties as well as tunability of the design so as to obtain certain desired properties.[4] An example of this has already been seen in CPs with high adsorption capabilities whose architectures sprung out of conscious and rational design.[5]

CPs have shown greater flexibility and tunability especially when compared with their zeolite cousins and in fact offer several advantages over them. The much larger surface area of the former in addition to the milder synthetic conditions, which they require makes them more preferable to zeolites. Furthermore, the ease of ligand modification implies that functionalizing the linkers allows the possibility of exerting greater control over the properties of the ensuing MOF.[6]

Overall, MOFs are a very desirable and much sought after class of compounds. It comes therefore as no surprise that there has been a huge surge in the number of publications on coordination polymers particularly in the last decade. Many of these reported compounds have been applied in different areas, some of which include gas sorption and separation,[7−10] catalysis,[11−13] ion exchange,[14−16] luminescence,[17−20] sensing,[21−25] drug delivery,[26−28] and magnetism.[29−33]

1. Introduction

Growth in the areas of crystal engineering and in particular metallosupramolecular chemistry has led to great strides being made in the advancement of coordination polymer research. The understanding, advocated by crystal engineering, is that molecules have a certain self-organization principle and this could be exploited by way of deliberate *engineering* in order to obtain new materials with certain desired properties. This is made possible by the knowledge that material properties are controlled by the molecules that constitute them. As such, a sum-up of this principle is that the self-organization or assembly of molecules into networks such as coordination polymers are controlled by molecular forces, which are of course brought about by tectons or building units.[34]

It was then proposed that infinite networks such as CPs could be obtained by linking metal centres with either tetrahedral or octahedral array of valences by rod-like connecting units and that the framework would generate a regular array of cavities.[35] These metal centres can be regarded as the tectons or synthons of the CPs and they come in the form of metal complexes but are commonly referred to as secondary building units (SBUs). SBUs provide seemingly unlimited possibilities with respect to the connectivities and direction and this singular fact can be regarded as one of the main attractions of CPs.[36] However, to truly obtain materials by design there is the need to identify the topological possibilities these CPs might assume. This premise has been utilized in several examples, in which the MOFs were created with specific targeted topologies with the aim of gaining greater porosity.[37,38] Combination of this strategy with computational analysis and simulation has led to even more success such as NU-109 and 110, of which the latter currently has the highest surface area reported for any porous solid ($7140 \, \mathrm{m^2 \, g^{-1}}$).[39] This approach has also been applied in obtaining MOFs with an eye on optimizing them for catalytic applications. Such systems sometimes involve the metal or metal cluster connecting points being used to catalyze organic transformations or active catalytic sites being generated from the functional groups within the MOF scaffold.[40–42]

In synthesizing CPs, it is generally the practice to use well-soluble metal salts as the source for the metal component with the organic components being mostly poly-carboxylic acids or amines or even the occasional bifunctional ligand combining both groups. Polytopic carboxylate linkers have the advantage of conferring structural rigidity on the porous frameworks particularly when combined with polynuclear clusters.[43–45] For the reaction media, polar organic solvents such as dimethylformamide or diethylformamide are some of the most commonly used, while other solvents like ethanol and water have been occasionally employed. In the case of dimethylformamide (DMF), it can undergo decarbonylation under solvothermal conditions, the consequent products of which can in turn template the formation of anionic frameworks.[46]

Judicious metal ion selection happens to be one of the ways in which control is exerted over the structure. In this regard, the easily predictable coordination chemistry of most transition metal ions has made them a frequent target for use.[47] Furthermore, their tendency to have preferred SBUs, with the

most popular being the *iconic* Zn-tetranuclear and the Cu(II) paddle wheel SBUs, which can both act as octahedral or square joints within the frameworks (see Fig. 1.1), makes them even more attractive. [48]
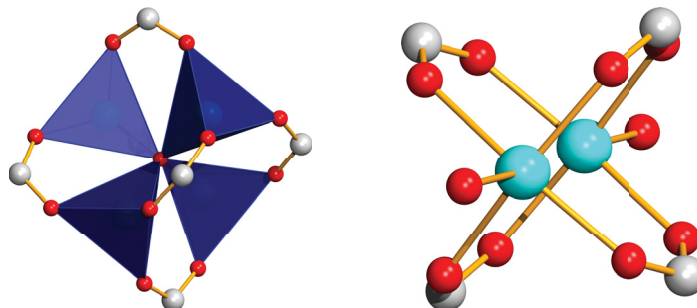

Figure 1.1: Common $Zn_4(\mu_4\text{-}O)$ and $Cu_2(RCOO)_4(L)_2$ SBUs, respectively.

Being a typically metal-based property, magnetism is one of the well-known attributes of coordination polymers and it has been implemented by incorporating magnetic moment carriers such as paramagnetic metals within the framework along with organic ligands. The fact that the linkage is most often *via* the diamagnetic linkers, which are in turn able to effectively mediate magnetic interactions, has aroused considerable interest in them. The possibility of varying the mode of linkage along with the size, geometry, chemical functionality, and various coordination modes of the linkers offers the tantalizing prospect of controlling or even modulating the magnetic properties in these compounds. [49]

Generally, porous magnetic materials fall into two broad classes—the porous organic frameworks consisting of open-shelled ligands and the porous inorganic-organic hybrids. In the case of the former, the spin bearing moieties are commonly organic radicals and their interactions occur *via* non-covalent bonds. Furthermore, inclusion of suitable functional groups may allow formation of interactions, which may in turn influence the solid state behaviour. However, supramolecular organic magnets suffer from the disadvantage of their interactions being weak and generally hard to control. [50] MOFs belonging to the second group are more common due to the greater flexibility they tend to offer. They can also be further divided into two groups—those incorporating radical ligands and those with regular diamagnetic ligands. In the case of the former, the radicals also act as additional paramagnetic centres within the MOF in a strategy called the metal-radical approach with the basic idea being to combine the magnetic characters of both the radical and the metal centre. [51] The result is the formation of an alternating network comprising both the metal ions and the radicals, in which there exists some form of magnetic exchange between the centres with each possessing a distinct moment. A well-known case is the triphenylmethyl radical that has been incorporated into frameworks containing Co(II) and Cu(II) ions. [52–54]

The second class, which is the more widely spread group, consists of diamagnetic ligands and metal centres. In this approach, the ligands act as linkers and often, additionally, as transmitters of magnetic exchange along the framework. The actual paramagnetic centres, usually the SBUs, are more important

in this regard. Therefore a very essential step during magnetic MOF design is the consideration of the metal to be used as well as the common SBUs that should result from it. Quite a few examples are also well known, among which is the HKUST-1 that had a paddle wheel Cu(II) SBU. It was claimed to demonstrate both intra- and inter-dimer interactions with antiferro- and ferromagnetic interactions respectively.[55] In regards to magnetic CPs, a common metal ion often used is the Co(II) ion due to its large anisotropy, which has been known to give rise to single-molecular magnetism (SMM) and of which several complexes are already quite well known. However, only relatively fewer CPs with Co(II) have ever been reported to exhibit SMM behaviour. Furthermore, the cobalt(II) ion typcially has no particular preferential SBU and has been seen to adopt various arrangements, which can range from the dinuclear paddle wheel to centres with even higher nuclearity.[56]

As previously stated, the formation of polynuclear clusters is quite common, especially in the case of carboxylate functionalized ligands. As the indvidual metal centres within these clusters are bridged by the carboxylate groups, it is axiomatic that the nature of the bridging mode would influence any magnetic properties, which may result.[57] According to the Goodenough and Kanamori rules, ideal ferromagnetic exchange generally occurs when the M−O−M bridging angle is closer to 90° and while for antiferromagnetic exchange, it is 180°.[58] In addition, the bridging mode of the carboxylate oxygen with the transition metal within the polymer plays an important role in determining the type of magnetic exchange. The most commonly observed bridging modes of the carboxylate oxygen in these structures are *syn-syn*, *syn-anti*, and *anti-anti* arrangements (Fig. 1.2). Both the *syn-syn* and *anti-anti* conformations exhibit relatively stronger interactions when compared to the *syn-anti* mode and often result in antiferromagnetic exchange. The *syn-anti* on the other hand has been commonly seen giving rise to ferromagnetic behaviour.[59]
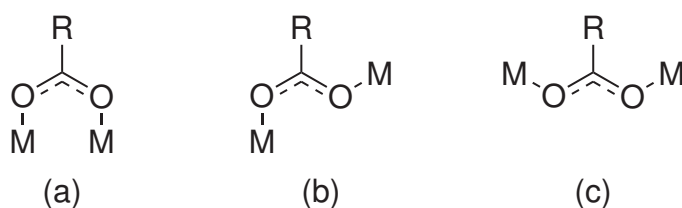

Figure 1.2: Selected binding modes commonly found for metal(II) carboxylates (a) *syn-syn* mode (b) *syn-anti* mode (c) *anti-anti* mode.

In this context, Chapter 2 provides a look at the properties of one of the common basic building blocks found in magnetic MOFs possessing the well-known paddle wheel motif. These are monomeric complexes based on redox-active 4,4'-disubstituted monocarboxyltriphenylamine ligands and copper(II) ions. The purpose is to utilise the SBU premise but without the continuous connection in order to obtain isolated magnetic behaviour of these SBUs. By utilizing various substituents on the *para* positions, the electronic effect on the magnetic behaviour of the complexes can be studied. This also presents

the opportunity of investigating the electronic effect of the substituents on the ease of oxidizing the central amine nitrogen. The oxidizability of the central nitrogen in the redox-active monocarboxyltriphenylamine offers the tantalizing prospect of creating radical cations in the complexes with interesting magnetic consequences.

As already mentioned earlier, coordination polymers are mostly known for their porosity and of all their properties, it has been the most studied and most exploited with an overwhelming number of studies each year on porous coordination polymers (PCPs). The early 90s saw the resurgence of study into porous coordination polymers but their lack of permanent porosity and tendency to undergo structural collapse upon solvent removal was a challenge.[60] However, the discovery of MOF-5, which incorporated Zn^{2+} ions and terephthalic acid linkers, which even at that time showed remarkably high surface area of between 2500 to 3000 m^2/g changed such perception.[61] It was later shown to have better gas storage capacity than materials available in that period along with its isoreticular cousin IRMOF-6, which had high methane adsorption capacities.[44] A major development, which considerably upped the stakes in this area was the report of the hydrogen adsorption capability of the previously mentioned MOF-5, the first of many to come.[62] This was important in itself because it came at a time when attention was beginning to shift from fossil fuels due to the escalating pollution problems arising from their exploration and consumption. Usage of hydrogen has been advocated as a viable alternative due to the fact that the by-product of its combustion is water and also its energy output in terms of gravimetric energy density far outstrips that of gasoline.[63] Additionally, hydrogen fuel cells have been shown to have higher efficiency when compared with internal combustion engines. However, the major obstacle to its use remains the lack of a safe, efficient, and economical storage system.[64,65]

Because of their high adsorption capacities, it is only natural that MOFs would be touted as one of the possible solutions to the problem of hydrogen storage. And while they have indeed shown potential in this respect, it is still a challenge to obtain a material, which would be able to meet the US Department of Energy requirements (7.5% H_2 or 70 g/L at 298 K).[66] To attain such would require a material with adsorption enthalpies between 15–20 kJ/mol and that is able to bind multiple H_2 molecules per metal cation. Till now this remains a goal to be attained.

Tunability of porosity in CPs is mainly achieved by the selection of ligands, which can then help to adjust the size of the ensuing pores. An example is seen in the isoreticular series where elongating the ligands made it possible to obtain polymers with increased porosity (Fig. 1.3).[44,67,68]

While this strategy has enjoyed substantial success it can sometimes backfire with additional networks being formed within the original network due to the resulting low densities. This is commonly known as entanglement and often significantly diminishes the accessible pore surface in any framework.[69] It has however been seen on occasion to reinforce the structure without the attendant loss in porosity.[70,71]
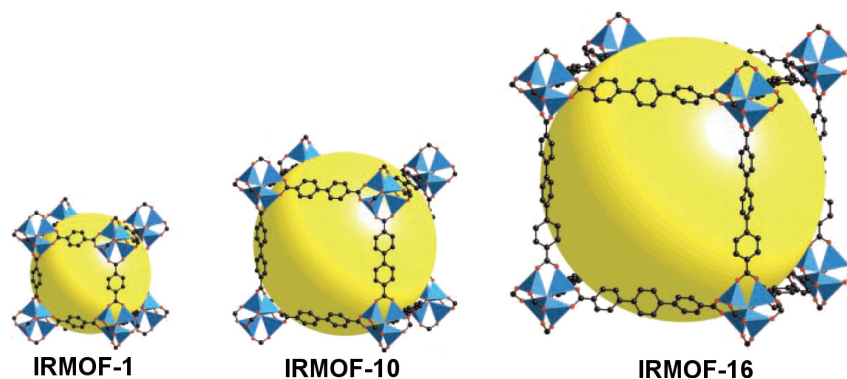
Figure 1.3: Isoreticular MOF series IRMOF-1, 10, and 16 with increasing percentage free volumes 79.8, 87.0, and 91.1 % resulting from addition of spacer groups.

Another means to enable tunability of the porosity is through the use of charged frameworks. The vast majority although have been anionic frameworks as these seem relatively easier to prepare than their positively charged counterparts. The syntheses of these interesting compounds have been largely achieved through templating methods using charged organic species such as dimethylammonium as templating ion, which is a by-product of the hydrolysis of DMF.[72,73]
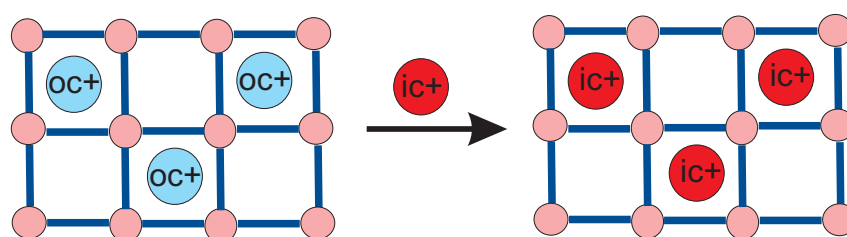
Figure 1.4: Representation of guest cation exchange in MOFs. Pink balls: metal nodes, blue lines: linkers, ic^+: inorganic cations, oc^+: organic cations.

The resulting cations are naturally encapsulated within the pores of the CPs and can be regarded as extra-framework species. But their charged nature makes them impossible to remove by simple evacuation and due to the large size of the organic cations, they often become hinderances to obtaining materials with sufficient porosity. However, these cations have been successfully exchanged with smaller inorganic cations such as Li^+, which could offer a way to tune their porosity by exploiting the size exclusion and pore partition effects.[74–78] Other uses of anionic CPs include as supports in catalysis,[79,80] sensitizing lanthanide cations[81] and sensing.[82]

Tuning of MOF structure can also be achieved by varying solvents or reactor vessels or even the inclusion of structural templates or directors.[83–85] In the case of the templates, some of these have been found to include metalloporphyrins, surfactants or organic acids.[86,87] Their mechanism of action has not been completely understood and tends to vary depending on the properties of the modulators and could range from pH modulation to size control.[83,88]

A major issue for most MOFs or CPs, is the occasional challenge to completely rid them of guests without irreparably damaging the framework in order to gain complete access to the pores. While in most cases conventional heating in vacuum has worked, there are many others, which result in complete breakdown of the pore structure due to the surface tension generated as the solvent molecules leave, leading to the structure being torn apart. The last few years has seen supercritical processing gain ground as a mild alternative method for evacuating MOFs without causing any damage to the framework. Usually, a solvent such as ethanol, which is miscible with liquid CO_2 is used to replace the guests. The new occluded solvents are then exchanged with liquid CO_2, after which the gas is brought to supercritical conditions before being released.[89] This has led to a greater retention of the pore structure and greater access to the internal pores has become possible.[90,91]

In light of this, Chapter 3 is focused on two anionic polymers, which are based on 4,4',4"-tricarboxytriphenylamine with Co(II) ions. These two polymers have been obtained using the same ligand with the only difference being the size of the reactor vessels. By exchanging the organic cation with different inorganic cations it has been possible to tune the adsorption behaviour as well as the pore width. Chapter 4 presents a similarly anionic MOF with mixed ligands, synthesized using 4,4',4"-tricarboxytriphenylamine (H_3ntb) in addition to terephthalic acid by applying the coordination copolymerization technique leading to a pillar-layered MOF. It also exhibits the ability to undergo cation exchange resulting in tunable sorption properties.

In Chapter 5 the use of templates in influencing MOFs is dealt with. In this, a neutral MOF realized *via* isophthalic acid modulated synthesis is presented. The influence of the type of activation process used on the sorption properties is likewise examined. The use of aluminum alkoxides as templates in synthesizing high surface area aluminas have been explored as well and these are discussed in Chapter 6.

Chapter 2

Discrete dicopper(II) carboxylate complexes

Part of this chapter has been submitted for publication in P1: <u>Oluseun Akintola</u>, Michael Böhme, Manfred Rudolph, Axel Buchholz, Helmar Görls, Winfried Plass, *Chem-Eur. J.* **2018** *Submitted.*

    This chapter takes a look at the well-known paddle wheel SBU incorporated into monocarboxylate substituted triphenylamine. For this purpose, 4,4'-disubstituted-monocarboxyltriphenylamines were used to generate copper(II) complexes, which possess this dinuclear unit. The effect of the different substituents on the coupling as well as the electronic nature of the central amine nitrogen has been explored and is here discussed.

Copper(II) complexes of monocarboxyltriphenylamines

Triphenylamines are noted mainly for the ease in their oxidation, a fact which has been behind their extensive applications in electroluminescent and associated devices.[92,93] When oxidized their radical cations are known for their stability particularly when the *para*-positions are occupied.[94] In instances where any of the *para*-positions are vacant, triphenylamines will naturally undergo dimerization. This occurs *via* oxidative coupling and has been exploited as a route to obtain tetraphenylbenzidines by exploiting this behaviour.[95] However, it is their electrochemistry, which makes them most interesting as there is a clear dependence on the nature of the substituents on these positions. Therefore, incorporating carboxylate groups into these redox active compounds offers the chance to obtain metal(II) complexes whose behaviour may be possibly tuned or influenced by using various groups on the *para*-positions.

    The dinuclear copper(II) core has been combined with the triphenylamine system in order to study

the ultimate effect of the electronic character of the substituents on the magnetic properties. For this purpose, four different substituents were selected where R = H, methyl (Me), *tert*-butyl (*t*Bu), and methoxy (OMe). The ligands are denoted as 4-(diphenylamino)benzoic acid (Hdaba), R = H, 4-(bis(4-tolylphenyl)amino)benzoic acid (Htaba), R = Me, 4-(bis(4-tert-butylphenyl)amino)benzoic acid (Hteaba), R = *t*Bu, and 4-(bis(4-methoxyphenyl)amino)benzoic acid (Hmaba), R = OMe. The complexes had the formulae [Cu$_2$(daba)$_4$(DMF)$_2$] (**1**), [Cu$_2$(taba)$_4$(DMF)$_2$] (**2**), [Cu$_2$(teaba)$_4$(DMF)$_2$] (**3**), and [Cu$_2$(maba)$_4$(DMF)$_2$] (**4**), respectively.
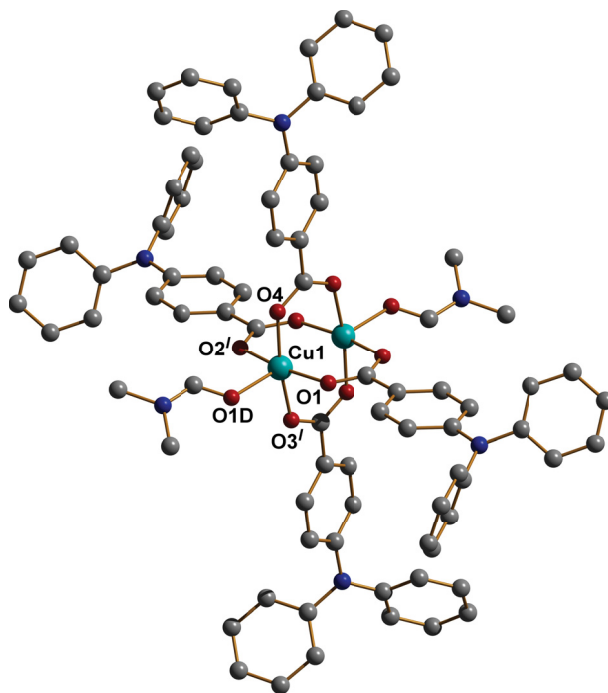
Figure 2.1: Molecular structure of **1** with solvent and hydrogen molecules hidden.

All four complexes **1**–**4**, adopt the same paddle wheel structure (Fig. 2.1), in which the core is the dinuclear Cu$_2$O$_{10}$. A comparison of the main structural parameters within the dinuclear core shows no significant differences between all four complexes. They also do not deviate much from reported values found in literature.

However, due to the varying substituents at the *para*-positions of the free triphenylamine ligands, slight variations in the overall structure and packing can be observed. This is reflected in two particular ways—the twisting of the plane around the central nitrogen of the amine as well as the torsion between the plane of the phenyl group directly attached to the carboxylate and the plane of the carboxylate itself. These are depicted in Fig. 2.2 and summarized in Table 2.1.

It is clear that the methyl analogue **2** shows the smallest variation in its θ when compared with the other three complexes while the largest is seen in the methoxy **4** case with a variation between 9.3-29.2°. Furthermore, all the four central nitrogen atoms are in the same plane and can be considered
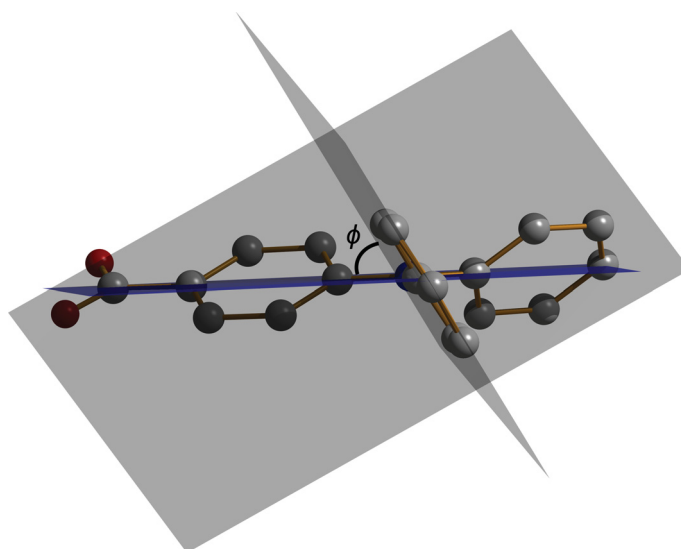
(a) Depiction of angle (ϕ) between amine and phenyl planes in the complexes represented by violet and grey planes, respectively.
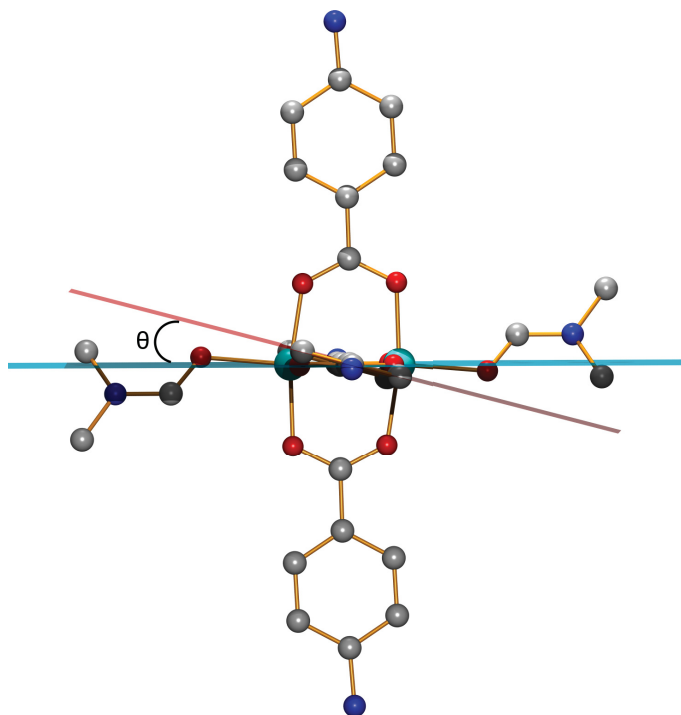
(b) Depiction of angle (θ) between carboxylate and phenyl planes in the complexes represented by light blue and red planes, respectively.

Figure 2.2: Portrayal of structural variations for **1**–**4**.

as the vertices of a rectangle with dimensions also presented in Table 2.1.

The voltammetric studies on both the ligands and complexes show the same behaviour. For the unsubstituted ligand Hdaba and its complex, its voltammogram can only be described in terms of an irreversible process due to the absence of any substituent on its free *para*-positions.[96,97] As such it is appar-

Table 2.1: Comparison of structural variations for **1**–**4**

Compound	ϕ (°)	θ (°)		N$\cdots$N separation	Diagonal separation
1	28.2−60.2	7.4	15.0	$11.4 \times 11.8 \, \text{Å}$	$16.4 \, \text{Å}$
2	31.8−46.5	6.3	8.6	$11.0 \times 12.3 \, \text{Å}$	$16.4 \, \text{Å}$
3	32.1−54.1	7.9	22.3	$11.5 \times 11.8 \, \text{Å}$	$16.4 \, \text{Å}$
4	21.7−65.4	9.3	29.2	$10.9 \times 12.4 \, \text{Å}$	$16.4 \, \text{Å}$

ent that the ensuing radical cation underwent quick dimerization to generate the tetraphenylbenzidine (TBP) (Scheme 2.1).
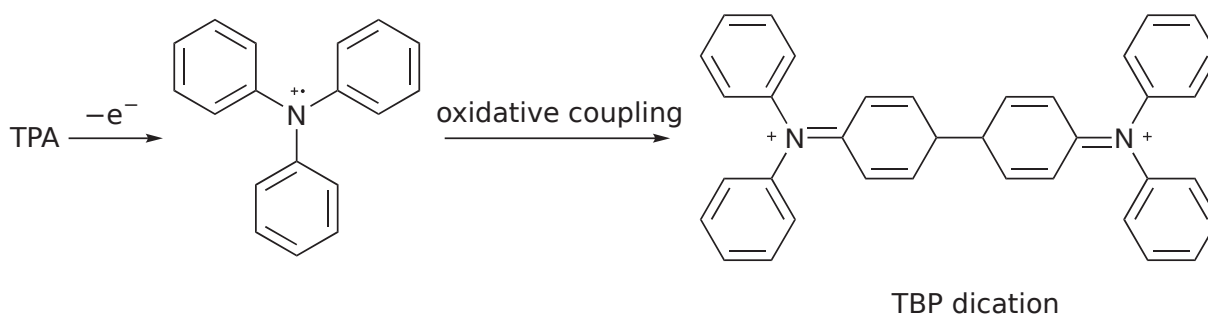
Scheme 2.1: Dimerization mechanism of triphenylamine (TPA) to TPB dication.

The other three analogues, Htaba, Hteaba, and Hmaba all show reversible behaviour in their voltamogramms and from this it can be deduced that the presence of the substituents on the *para*-positions of the free phenyl rings in both ligand and complexes enhanced the stability of the resultant radical cations. The complexes show the same stability with the reversible voltamogramm. Infact, the oxidation process can be described as a single electron process in spite of the presence of four oxidizable centres in the case of the complexes. This should only occur theoretically if there are no interactions between the four electrochemically active species, in addition to the process of charge transfer being virtually reversible.[98,99] Furthermore, there is a clear trend in the diffusion coefficients obtained for the compounds. The $tert$-butyl compound shows the slowest diffusion coefficient, which is the expected trend followed by the methoxy and the methyl analogues. Additionally, the complexes exhibit slower diffusion than the ligands along the same pattern, with the tBu also being the slowest. Furthermore, the values of the standard potentials match the expected electronic trend with the methoxy showing the lowest while the tBu had the highest.

The spectroelectrochemical measurements of both complexes and ligands of the p-substituted compounds display a four-fold increase in the extinction coefficient of the former, which is evidence that the oxidation is a ligand centred process and does not involve the metal centres. Additionally the maxima for the complexes only show slight shifts in as compared to the ligands. This behaviour was also seen in the complexes generated by chemical oxidation with AgBF$_4$. Sequential oxidation of the

Table 2.2: Comparison of voltammetric parameters for **1**–**4** and their ligands

Compound	Htaba	Hteaba	Hmaba	**2**	**3**	**4**
D (cm^2 s^{-1})	8.5×10^{-6}	6.9×10^{-6}	7.8×10^{-6}	4.75×10^{-6}	3.2×10^{-6}	4.0×10^{-6}
$E°$ (V)	0.550	0.556	0.388	-	-	-
$E_4°$ (V)[a]	-	-	-	0.555	0.562	0.389

[a] Values obtained from fourth oxidation step in the case of the complexes.

methoxy complex was possible using increasing amounts of the oxidizing agent. This supports the low accessible potential of the methoxy complex. However, the other two—*tert*-butyl and methyl—were unable to undergo serial oxidation and required an excess of the same oxidant to generate their radical cations. This was consistent with the comparatively higher potentials obtained from their voltammetric measurements.

The presence of the radical cations was also confirmed by ESR spectroscopy. Both ligands and complexes had expected isotropic signals with the methoxy and *tert*-butyl showing additional hyperfine coupling as well. The g-factors in all six compounds were in the range expected for organic radicals (about 2.0). The derived fitted parameters are given in Table 2.3.

Table 2.3: Fitted parameters obtained from fitting ESR-spectroscopic data for ligands and complexes **1**–**4**

	Htaba	**2**	Hteaba	**3**	Hmaba	**4**
g	2.0016	2.0026	2.0025	2.0026	2.0031	2.0032
A (MHz)	21.2	21.6	24.7	25.5	21.8	22.0
Line-width (mT)	0.192	0.169	0.069	0.046	0.038	0.043

Magnetic studies into all four complexes showed expected behaviour for copper(II) complexes. In fitting the obtained magnetic data, their experimental data were best reproduced with values of J between -290–-330 cm^{-1}. This confirmed that all four complexes exhibited the typically strong antiferromagnetic exchange expected in dinuclear complexes with coupling constants in this range.

Table 2.4: Values of parameters obtained from fit of magnetic data of **1**–**4**

Complex	J / cm^{-1} (g)
1	-321 (2.14)
2	-295 (2.12)
3	-330 (2.18)
4	-321 (2.23)

From the structures of all four complexes, no significant variation was expected in the magnetic behaviour as there are no major differences in the dinuclear core. Consequently, there is no correlation of the strength of the exchange with the electronic character of the substituents. This lack of correlation is thought to stem from the distance of the groups to the dinuclear core as greater proximity might be

required in order to adequately influence the coupling between the two copper ions.

In summary, this study discusses four copper(II) complexes of 4,4'-disubstitututed monocarboxylt-riphenylamine and its derivatives, in which all had the paddle wheel core. The effect of the substituents was quite clear on the electrochemical behaviour with the unsubstituted compounds displaying oxidative coupling as a result of the free *para*-positions on the triphenylamine ligands. The magnetic behaviour was not so straight forward as all four complexes showed coupling within the usual range expected for these types of compounds but with no correlation with the nature of the groups at the *para*-positions.

2D and 3D anionic cobalt(II) coordination polymers

Part of this chapter has been submitted for publication in P2: <u>Oluseun Akintola</u>, David Hornig, Axel Buchholz, Helmar Görls, Winfried Plass, *Dalton Trans.* **2017**, 46, 8037–8050.

This chapter deals with two anionic coordination polymers, which were synthesized from the same 4,4',4"-nitrilotribenzoic acid ligand but using differently sized vessels. This was used to highlight the influence of synthetic conditions on the final structure adopted by coordination polymers. The anionic nature of both polymers was also exploited by exchanging the organic cation with small inorganic cations thus tuning their sorption properties.

Co(II) anionic frameworks constructed from nitrilotribenzoic acid

Alterations in any of the synthetic conditions can have such strong effect on the eventual outcome of MOF formation. Pressure, temperature, or solvent all play important roles in MOF synthesis. By altering the size of the reaction vessel while maintaining the same amount of reactants, the two anionic MOFs **5** and **6** were obtained (3.1). Both polymers had the formulae $\{(Me_2NH_2)_2[Co(ntb)Cl]_n \cdot nH_2O \cdot nDMF\}$ and $\{(Me_2NH_2)_2[Co_5(ntb)_4(H_2O)_3(Me_2NH)]_n \cdot 13\,nDMF \cdot 2\,nH_2O\}$, respectively. The negative charge on both MOFs is counter balanced by the presence of dimethylammonium cations. The latter is an outcome of the *in situ* decarbonylation of DMF under the solvothermal conditions during synthesis, which then templates the formation of the anionic networks.[46]

Both networks differ vastly in both structure and topology. Where **5** is a two-dimensional net made up of pseudo-tetrahedral mononuclear Co(II) units, **6** consists of a mixture of dinuclear and trinuclear
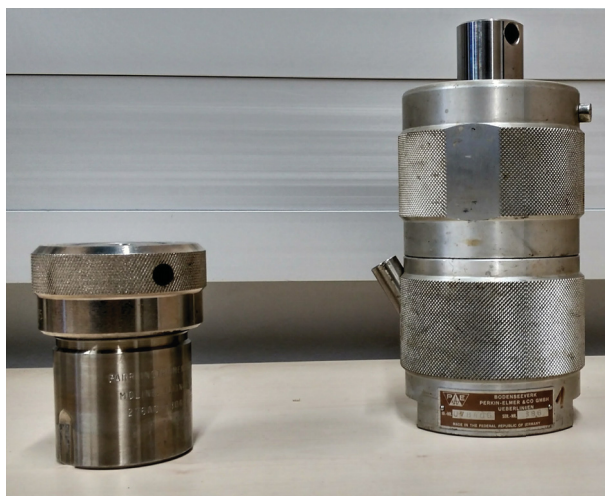
Figure 3.1: Reactor vessels utilized in MOF syntheses: (left) 23 mL Parr acid digestion bomb for **5**. (right) 110 mL Perkin Elmer acid digestion bomb for **6**.

Co(II) clusters all linked by the ligand within a three-dimensional network. The dinuclear cluster in **6** has the same paddle-wheel arrangement typically occurring in copper(II) carboxylate complexes. Both **5** and **6** assume the **hcb** and 3,6T80 topologies, respectively (3.2). The network of **6** is quite fascinating due to its adoption of a Kagome lattice with the alternating triangular and hexagonal channels.

The magnetic studies into both compounds do not reveal very significant properties. In **5**, the isolated nature of the mononuclear Co(II) units implies that the magnetic behaviour should be simple enough. It however displays minimal anisotropy with a zero-field splitting factor, D, estimated around $-16.4\,\mathrm{cm^{-1}}$ as obtained from its magnetization data. It also shows a slight peak in its in-phase and out-of-phase AC susceptibility data, an evidence of single molecule magnetism. But this is only minimal as the peak occurs below 2.5 K. In contrast, **6** shows complicated magnetic behaviour due to the mixture of polynuclear clusters (di- and trinuclear) in addition to the occurrence of mixed geometries within the clusters. These factors make it difficult to extract significant information from the magnetic data as any attempt to do so only led to failure. This was thought to be a result of the coexistence of strong spin-orbit coupling as well as the intracluster exchange interactions. However, theoretical calculations of its magnetic properties showed existence of antiferromagnetic exchange within the clusters. This was confirmed by the fit of the χ_M^{-1} above 100 K, which gave a Weiss constant of -47.3 K.

The possibility of exchanging the organic cations in both frameworks was investigated by using Eu(III) and Li cations. The former was selected due to its distinct fluorescence bands, which meant the uptake of the Eu ions by the framework could be monitored *via* depletion of the intensities in the fluorescence spectra. This was done using two different solvents—DMF and ethanol—to gain insight into probable dependence of the exchange process on solvent used, which would imply some measure of selectivity exists. DMF was selected due to it being the solvent used in the synthesis while ethanol was
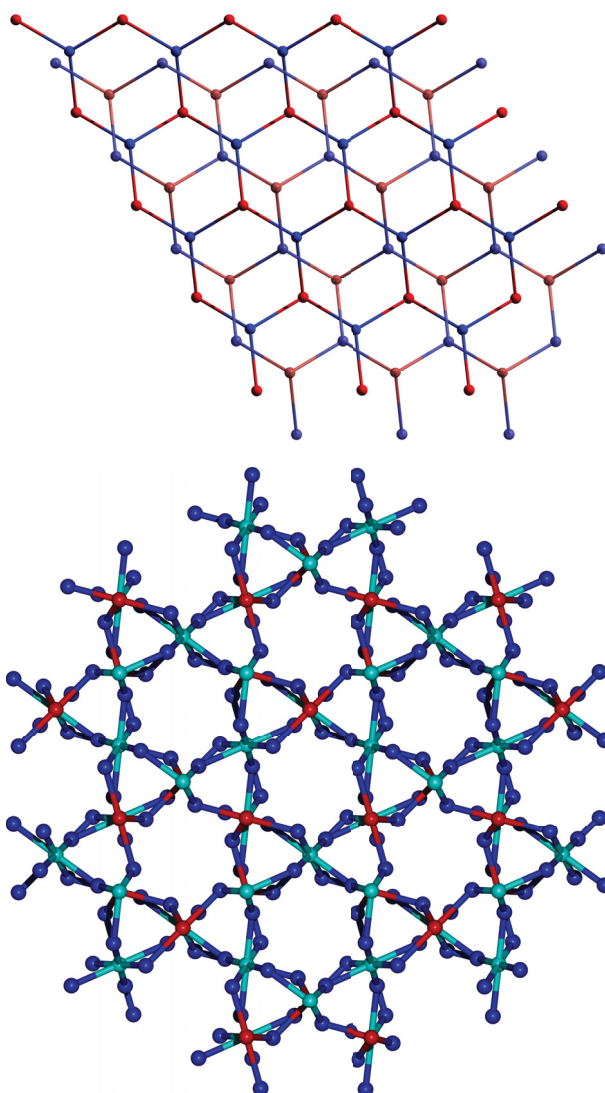
Figure 3.2: Underlying topological nets in both MOFs **5** (above) and **6** (below). Left: Red balls and blue balls represent Co(II) units and central triphenylamine nitrogen, respectively. Right: Red and torqoiuse balls represent Co(II) units, blue balls represent central triphenylamine nitrogen.

chosen due to its intended use in supercritical CO_2 exchange to obtain the dried samples for sorption measurements. From the fluorescence measurements, it is apparent that both MOFs show differing levels of selectivity for the Eu(III) cation depending on the solvent used. **5** exhibits a strong preference for DMF as solvent and shows complete exchange of its two counter-cations whereas in ethanol, it only shows partial uptake. **6** on the other hand does not demonstrate any selectivity in neither ethanol nor in DMF and shows only partial uptake in both solvents. The cation exchange was then extended to Li, and from this it was found that **5** undergoes only partial exchange with the removal of just one of the organic cations, irrespective of solvent used. For **6**, ethanol is the preferred solvent for the exchange process with only partial exchange being observed in DMF (see 3.1).

For the sorption investigations, the samples were selected based on the solvent, in which the best

Table 3.1: Solvent-selectivity of cation exchange process in **5** and **6**

Sample	Exchange	Solvent
5(Li)E	Partial	Ethanol
5(Li)D	Partial	DMF
5(Eu)E	Partial	Ethanol
5(Eu)D	Complete	DMF
6(Li)E	Complete	Ethanol
6(Li)D	Partial	DMF
6(Eu)E	Partial	Ethanol
6(Eu)D	Partial	DMF

cation exchange was observed. Sorption properties were then studied by meauring the N_2 isotherms on supercritical CO_2 dried samples of both the as-synthesized and the selected cation-exchanged samples of the two MOFs. It is expected that the smaller size of the Li ion should ease entry of guests into the pores. Eu(III) while not being a small cation in that sense, has a higher charge, which should give an added advantage of decongesting the pores. It is expected that the higher charge, which would result in a stoichiometry of three equivalents of the framework to one of the Eu(III) ion should have the attendant effect of reducing the number of cation guests thus making the pores more accessible. Also, since the MOFs had already been shown to demonstrate selectivity in their cation exchange behaviour, the sorption measurements were expected to provide additional evidence of this. A correlation of the obtained BET surface area for the ion-exchanged samples is given in **??**.

Table 3.2: Sorption data from N_2 isotherms of samples based on **5** measured at 77 K

Sample	aBET ($m^2\,g^{-1}$)	Total pore volume ($cm^3\,g^{-1}$)
5	13	0.02
5(Li)D	24	0.05
5(Eu)D	216	0.27

For **5**, the as-synthesized sample showed negligible BET surface area ($13\,m^2\,g^{-1}$), which is an indication of reduced access to the internal pores. This can be inferred to be a result of steric demand being imposed by the organoammonium cations hence the low surface area. With the cation-exchanged samples, there was a two-fold increase in the measured surface area when the organic cations were replaced with lithium ions (**5**(Li)D; $25\,m^2\,g^{-1}$). The lack of significant increase despite cation exchange can be attributed to the inability to completely exchange all the organoammonium cations. With the europium-exchanged sample **5**(Eu)D, there was a large increase in the sorption, which was reflected in its aBET (16-fold) as well as a corresponding increase in its total pore volume (3.3). This conclusively showed that access can be increased when the steric issue resulting from occupation by the dimethylammonium cations is resolved by partial and complete replacement by the smaller inorganic cations.
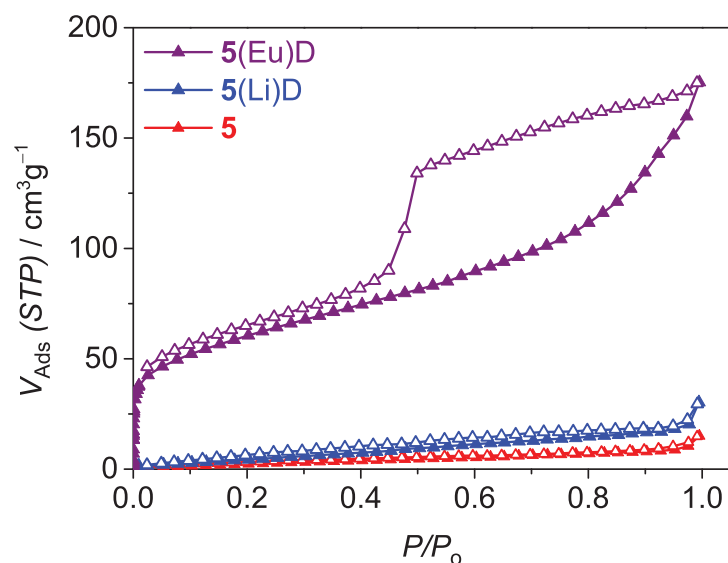
Figure 3.3: Comparison of N_2 isotherms for as-synthesized, lithium-, and europium-exchanged samples of **5** measured at 77 K.

The isotherm for **5**(Eu)D can be described as a Type II with an H2 hysteresis resulting from the presence of cylindrical pores.[100,101]
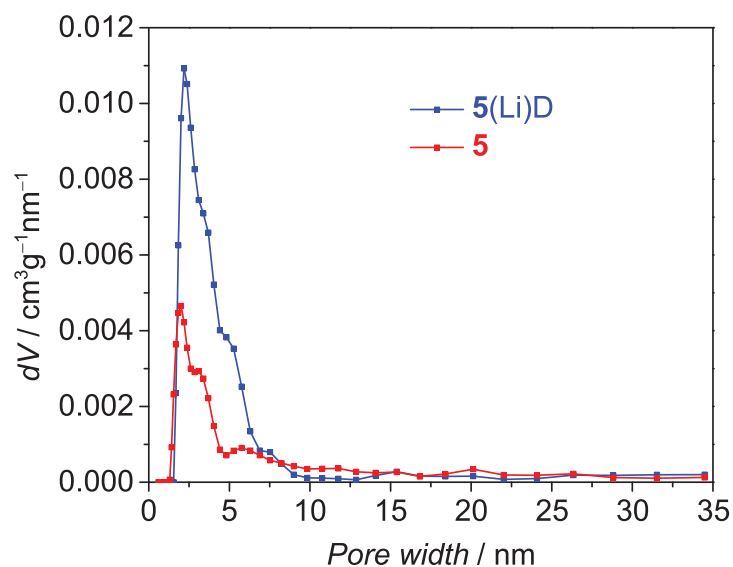

Figure 3.4: Pore distribution data for **5** and **5**(Li)D fitted using N_2 at 77 K on carbon (slit pores, QSDFT equilibrium model).

The pore distribution data obtained from fitting the isotherms using the Quenched solid density functional theory (QSDFT) method implemented in kernels provided by Quantachrome Instruments.[102] are shown in **??**. Accordingly, these show agreement with the observed increase in sorption with both partial and total cation exchange. There is a clear increase in the population of accessible pores as soon as the organoammonium cations are replaced. This is most prominent in **5**(Eu)D, which shows the
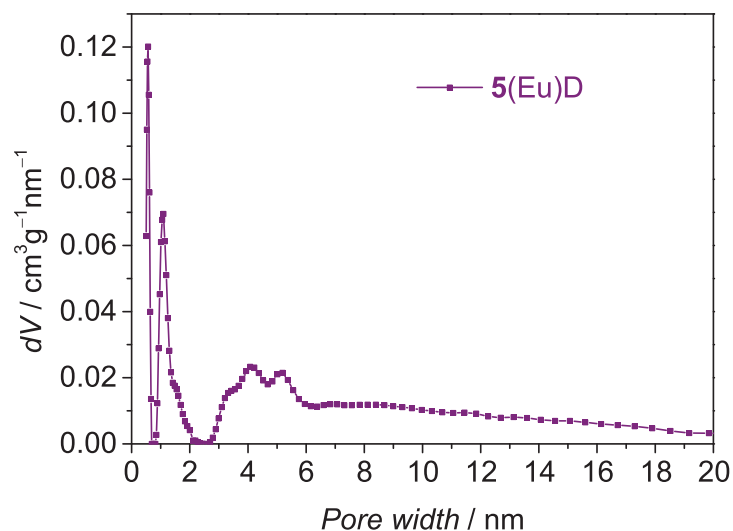
Figure 3.5: Pore distribution data for **5**(Eu)D fitted using N_2 at 77 K on carbon (slit/cylindrical pores, QSDFT adsorption branch model).

largest increase in its sorption as well as a greater population of its micropores (< 2 nm).

Table 3.3: Sorption data from N_2 isotherms of samples based on **6** measured at 77 K

Sample	aBET ($m^2\,g^{-1}$)	Total pore volume ($cm^3\,g^{-1}$)
6	21	0.03
6(Li)E	380	0.29
6(Eu)E	194	0.14

The sorption behaviour for **6** showed the same trend seen in **5**. Its as-synthesized sample also shows poor BET surface area as well as low pore volume ($21\,m^2\,g^{-1}$ and $0.03\,cm^3\,g^{-1}$), an observation, which was attributed to the guest dimethylammonium cations reducing access to the pores. This was confirmed in **6**(Eu)E, which demonstrated partial cation exchange and showed a slight improvement in amount of gas adsorbed. The most drastic change was found in **6**(Li)E where complete exchange of the organoammonium ions occurred, where it displayed a corresponding 20-fold increase in the BET surface area.

As with **5**, the presence of the dimethylammonium cations in the the as-synthesized sample resulted in the low surface area observed due to how they restricted access to the pores. This was corroborated by the increased sorption seen in the partially-exchanged samples with an even more remarkable increase in the surface area upon total exchange. This gradual increment in the surface areas following progressive replacement of the organic cation can be easily attributed to the decreased steric demand from the organic cations subsequently allowing better micropore access.

The pore distribution data obtained by fitting the isotherms using the QSDFT kernels show agreement with the observed sorption behaviour. In all cases, there is the unmistakable increase in accessible
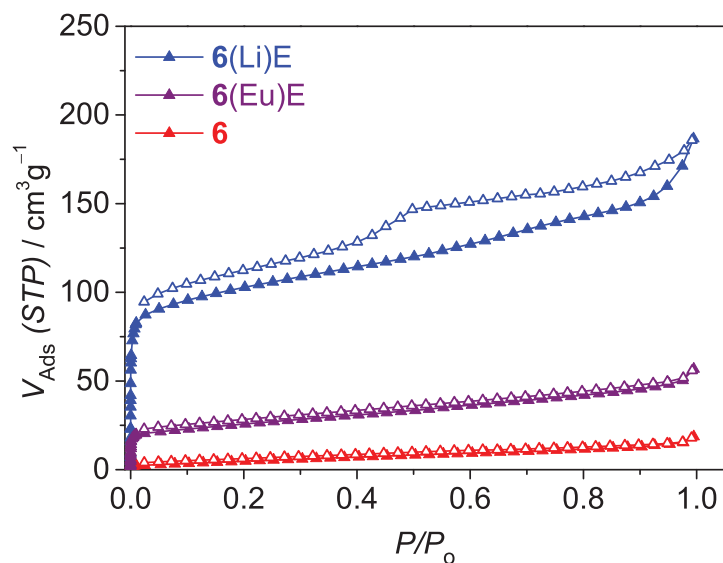
Figure 3.6: Comparison of N_2 isotherms for as-synthesized, lithium-, and europium-exchanged samples of **6** measured at 77 K.
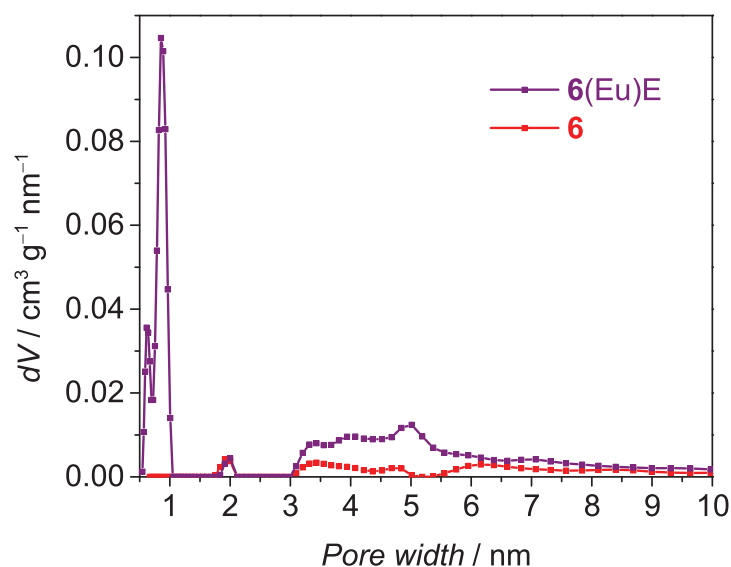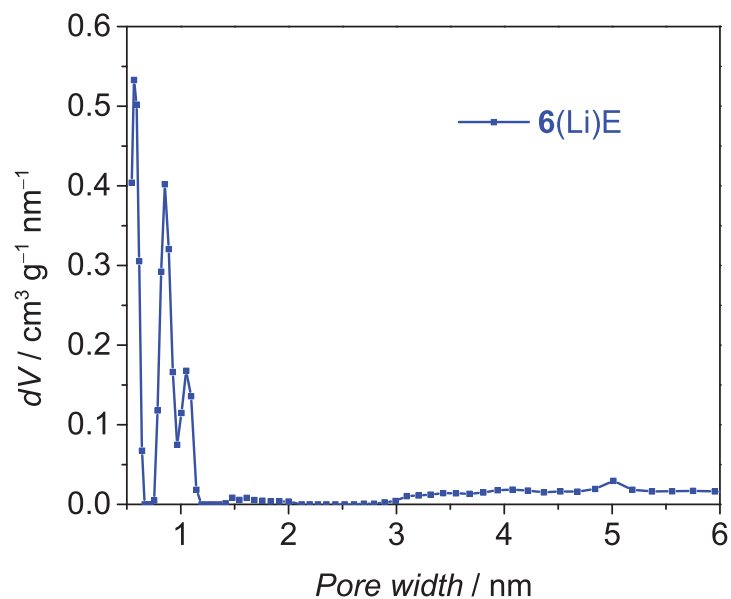

Figure 3.7: Pore distribution data for **6**, and **6**(Eu)E fitted using N_2 at 77 K on carbon (slit pores, QSDFT equilibrium model).

pores upon replacement of the organic cations with the effect being most noticeable in **6**(Li)E. It also has the highest population of the micropores.

In conclusion, by altering the reactor size it became possible to influence the structure adopted by the two anionic metal-organic frameworks. The charged nature of both compounds ensued from the decomposition of the DMF solvent utilized for their reactions. The organoammonium cations in the resulting anionic MOFs could be post-synthetically replaced with europium and lithium, which also showed solvent dependent selectivity. The cation exchange leads to improved sorption properties for

Figure 3.8: Pore distribution data for **6**(Li)E fitted using N_2 at 77 K on carbon (slit/cylindrical pores, QSDFT adsorption branch model).

both compounds, which stems from the better access to the micropores ensuing from the removal of the organic cations. This clearly demonstrates the possibility of tuning sorption behaviour *via* the size of the cation and as such suitable choice of cation is necessary.

Chapter **4**

Robust pillared-layer cobalt(II) framework

Part of this chapter has been published in P3: <u>Oluseun Akintola</u>, Sven Ziegenbalg, Axel Buchholz, Helmar Görls, Winfried Plass, *CrystEngComm* **2017**, 19, 2723–2732.

This chapter describes the combination of two well-known linkers into a single anionic framework using the coordination copolymerization process. In this regard, terephthalic acid has been selected as the second linker in combination with the redox-active 4,4',4"-tricarboxytriphenylamine already used in the previous chapter.

Mixed Ligand Co(II) MOFs

The MOFs already described in the preceeding chapter could be considered as 'binary' networks with regards to their being composed of just the ligand (with emphasis on aromatic-based ligands) and metal ion. This category is where the majority of MOFs fall into, requiring merely a combination of the ligand and the metal salt. With the goal of obtaining porous polymers, tuning has been frequently achieved by extending the ligands by the use of spacer groups. This approach is called the isoreticular method and with this, frameworks with even larger pores have been achieved (see 1.3). A drawback is that upon reaching a certain limit, the frameworks can either become unstable and fragile followed by collapse. In some other cases, the frameworks will undergo entanglement with the formation of extra networks, which are then interlinked with each other. This is far from desired as the result is lack of access to the pores of the MOF.

A further limiting factor is the design of the ligands themselves. Generally, for the purpose of structure tunability, new ligand development is always an essential step. However, this can often be

a cumbersome process from conception to execution and sometimes results in failure. Therefore, the act of combining two already known ligands into one framework leading to a 'ternary' network with three components offers a new level of functionality besides avoiding the stress of synthesizing new linkers and at the same time maximize the use of already known linkers. Furthermore, functionalizing the pillar linkers can present routes to new functionalities in the resulting complexes.[103]

The major challenge of this approach would be competition between the two ligands, which could result in the formation of two discrete frameworks rather than a single multicomponent network. The key to overcoming this would be to experiment with the ligand ratios in order to obtain an optimal proportion thereby optimizing the synthetic route. An example is the combination of a tritopic ligand (with three possible binding pockets) and a ditopic linker. Kinetics would dictate that the tritopic ligand would be consumed faster, as such a slight excess of the ditopic linker might be necessary to maintain equilibrium in order to obtain the desired mixed ligand framework.

To this end, the 4,4',4"-nitrilotribenzoic acid from the previous chapter has been employed as ligand in addition to terephthalic acid. The two ligands were used in the ratio of 6:4 and in combination with cobalt(II) chloride resulted in a three-dimensional framework, **7**, for which the formula $\{((CH_3)_2NH_2)_2\,[Co_3(ntb)_2(bdc)]_n \cdot 4\,n\mathrm{DMF} \cdot 2\,n\mathrm{H}_2\mathrm{O}\}$ could be determined.
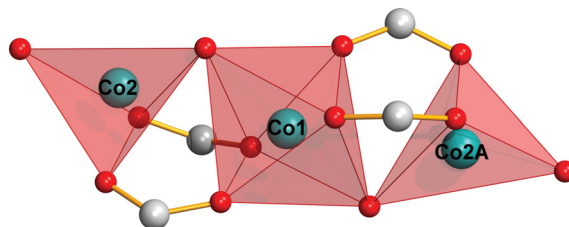

Figure 4.1: Linear trinuclear clusters in **7** with mixed T_d-O_h-T_d geometries.

7 is an anionic framework consisting of linear trinuclear clusters of cobalt atoms in a mixture of octahedral and tetrahedral coordination geometries 4.1. It is relatively rare to encounter mixed geometries with the more common occurrence being when all three atoms exist solely in octahedral geometries. The cluster is symmetric due to the central cobalt atom being on a centre of inversion. The anionic charge of the framework is balanced by the presence of two dimethylammonium cations, which are a by-product of the decarbonylation of DMF under the synthetic conditions.[46]

The architecture of the MOF is one, by which the triphenylamines generate layered networks with the cobalt ions. These layered nets are then connected to each other *via* the terephthalic acid ligands, which then act as pillars (4.2). The resultant network **7** is called a pillar-layered framework due to its unique architecture. Its underlying net was analysed and the topology was broken down to its trinuclear clusters and amine nitrogen centre, that serve as nodes. The trinuclear clusters were found to be eight-connected (six through the ntb^{3-} ligands and two through the bdc^{2-} ligands) while the
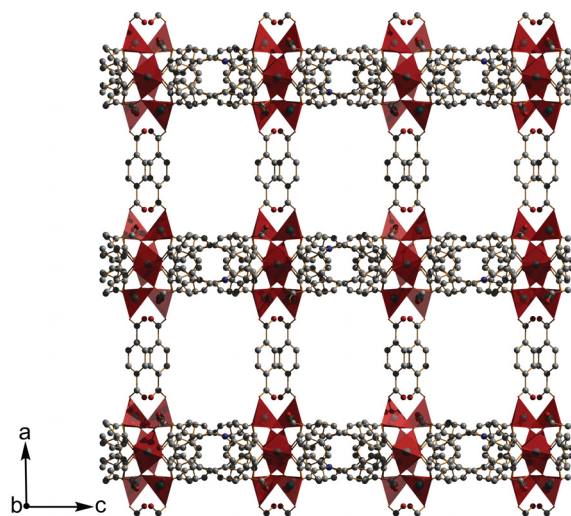
Figure 4.2: Network of **7** viewed along [010] direction showing 2D nets connected *via* terephthalic acid pillars leading to overall 3D framework. Cobalt centres denoted by red polyhedra.

nitrogen amine offered a three-connected node. Analysis with TOPOS[104] gave a 3,8-connected **tfz-d** topology with point symbols $(4^3)_2(4^6.6^{18}.8^4)$.

The magnetic behaviour of **7** was assumed to be based on the individual trinuclear clusters, with consideration of possible intercluster exchange through the terephthalate linkers. Unfortunately, due to the mixture of octahedral and tetrahedral geometries within the clusters a simple approach was required so as to avoid overparametrization. Therefore no successful fit of the susceptibility data was obtained. Nonetheless due to the assumption of a spin effective $S' = 1/2$ for octahedral Co(II) ions at low temperatures, it was possible to create a simple interaction model (see 4.3) to fit the magnetization data, which was obtained at sufficiently low temperatures (2–5 K). Since the effective spin $S' = 1/2$ was considered for the octahedral cobalt ion therefore the ZFS parameter D was only assumed for the tetrahedral ion. Fitting the magnetization data then led to the values below being obtained

Table 4.1: Fitted parameters obtained from magnetization data for **7**

Parameter	Value
g	2.75
J (cm^{-1})	-6.5
zJ'^c (cm^{-1})	0.06
D^d (cm^{-1})	-2.9

^{c}connotes intercluster exchange.
^{d}represents zero field splitting parameter.

The fit of the data was consistent with antiferromagnetic interactions between the adjacent cobalt(II) ions with the value being comparable with values for similar reported complexes.[105] The small value of the intercluster interactions zJ' was also consistent with the idea of the clusters being isolated enough

to allow little exchange through the ligands. The antiferromagnetic exchange was attributed to the nature of the coordination modes in **7**, which had the *syn-syn-$\mu_{1,3}$* and the $\mu_{1,1}$ type bridges with the former being well-known to result in antiferromagnetic coupling. The latter case leads to a Co−O−Co bridge, of which the angle is a good indicator of what kind of coupling should result. Angles greater than 100° are known to result in antiferromagnetic interactions.[31,106]
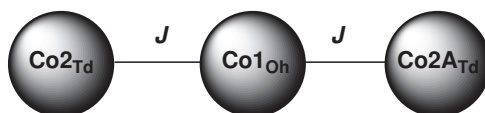

Figure 4.3: Model of exchange coupling in **7**.

The possibility of exchanging the countercations in the framework of **7** was then attempted. Replacement of the organic cation with lithium ions by simply immersing the sample in saturated LiNO$_3$ ethanolic solution was attempted and also found to be successful showing that the dimethylammonium ions could be easily replaced. This was corroborated by elemental analysis indicating two Li ions to one mole of the compound while powder diffraction confirmed the retention of the framework. Repeating the exchange in DMF showed the same behaviour, which indicates no selectivity in its exchange with lithium ions (see 4.2).

Table 4.2: Summary of solvent-selectivity of cation exchange process in **7**

Sample	Exchange	Solvent
7(Li)E	Complete	Ethanol
7(Li)D	Complete	DMF

Sorption studies into **7** before and after cation exchange show marked improvement in the porosity with an increase in quantity adsorbed (4.4). Correspondingly, there is a three-fold increase in the measured BET surface area while the pore volume can be seen to undergo an almost two-fold increase (4.3). From this it was deduced that the steric demands posed by the dimethylammonium cations were sufficient to hinder access to the internal pores of the MOF. By performing post-synthetic cation exchange, it becomes possible to overcome these hinderances and enable greater access as seen in the increment in adsorption upon exchange. However, the isotherms show that the general nature of the pores were consistent from the shape of the hysteresis observed in both materials.

Table 4.3: Sorption data from N$_2$ isotherms of samples based on **7** measured at 77 K

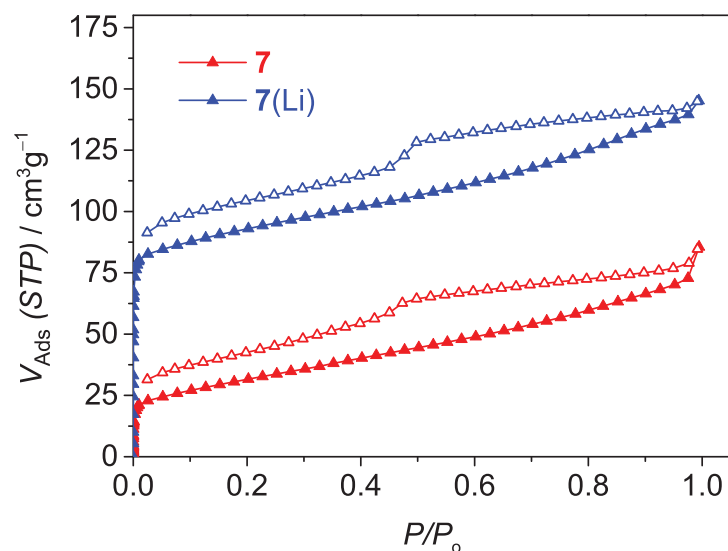| Sample	aBET (m^2 g^{-1})	Total pore volume (cm^3 g^{-1})
7	113	0.13
7(Li)E	335	0.22

Figure 4.4: Comparison of N_2 isotherms for as-synthesized and lithium-exchanged samples of **7** measured at 77 K.
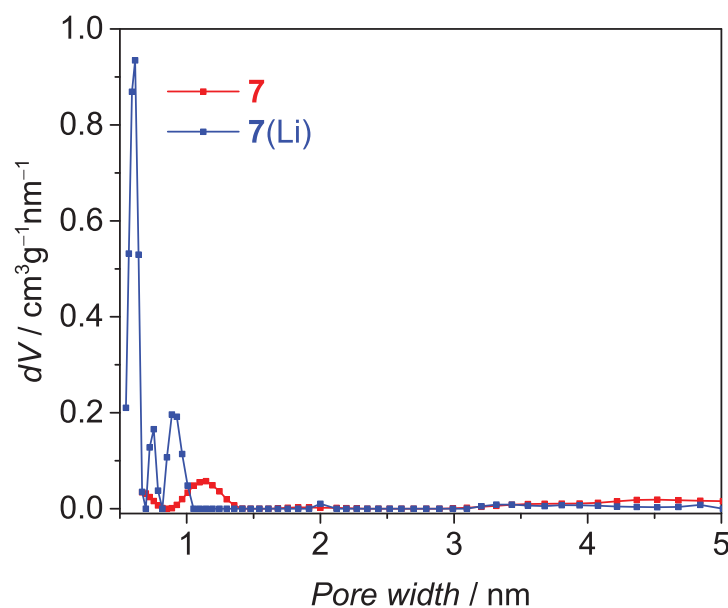

Figure 4.5: Pore distribution data for **7** and **7**(Li) fitted using N_2 at 77 K on carbon (slit/cylindrical pores, QSDFT adsorption branch model).

The pore distribution data for both materials show an increase in the micropore content upon cation exchange thus confirming the availability of previously inaccessible pores resulting from the guest cation substitution. An additional point is how the porosity of anionic frameworks can be tuned by careful selection of the replacement cation leading to increased access to these pores. This can be seen in how the lithium-exchanged sample became more microporous as evidenced by the increased quantity of micropores present when compared with its unexchanged counterpart (see 4.5).

In conclusion, by combining two different ligands *via* the coordination copolymerization route it

was possible to obtain a pillared-layer framework, which as a result of DMF decomposition was anionic. Its anionic nature was however exploited by exchanging the organic cation with inorganic cations *via* post-synthetic treatment of the materials. The successful replacement was found to reflect in the increased sorption capabilities of the MOF. Overall, the use of two well-known ligand systems offers the possibility of creating new materials without having to go through the whole cumbersome process of designing new ligands. Additionally, tunability of its sorption properties *via* cation size is possible and only depends on judicious cation selection.

Isophthalic acid-modulated synthesis of a neutral Co(II) nitrilotribenzoic acid framework

Part of this chapter is earmarked for publication in P4: <u>Oluseun Akintola</u>, Axel Buchholz, Helmar Görls, Winfried Plass, *Eur. J. Inorg. Chem.* **2018**.

This chapter details the use of a coordination modulator to influence the structure of a MOF. The role of isophthalic acid as a structure director in the synthesis of a neutral framework containing the redox-active 4,4',4"-tricarboxytriphenylamine already used in the previous chapters.

3D neutral isophthalate templated framework

In the last two chapters, the effect of the dimethylammonium cations on the outcome of MOF synthesis, especially their role in obtaining anionic polymers has been demonstrated. However, these are merely side-products of the breakdown of the DMF solvent molecule. Beyond this, solvents occupy a very powerful position during MOF preparation and can strongly influence the eventual structure of the MOF.[107–109] In addition to solvents, other compounds exist that can template the formation of different polymers and quite a few of them are known. Here, isophthalic acid has been employed as structure modulator/template with the result being a neutral MOF, which had the formula $\{[Co_9(ntb)_6(H_2O)_{12}]_n \cdot 6\,n(H_2O) \cdot 3\,n(DMF) \cdot nH_2ip\}$ as well as the same structural topology as already seen in **6** (Chapter 3). The inclusion of the isophthalic acid is thought to have a two-fold effect. In the first, it suppressed the formation of dimethylammonium ation, which could have led to the formation of the anionic framework. As DMF decarbonylation generally depends on a basic pH, the presence of the acid is suspected to have prevented this, thus hindering formation of the dimethylammonium cation.

In its second role, it is believed to have templated the formation of the neutral framework. This was seen from the evidence for the continued presence of isophthalic acid in the pores as obtained from the elemental CHN and thermogravimetric analyses.

The importance of the isophthalic acid was further demonstrated by performing the synthesis at the same temperature (130 °C) but excluding isophthalic acid and also at 150 °C but this time with its inclusion (see Table 5.1). In both cases, no product could be seen, which confirmed the alternate outcome to be a result of isophthalic acid. Also, the use of phthalic acid led to no crystalline product being obtained.

Table 5.1: Influence of isophthalic acid and temperature on synthesis of **8**

Temperature	Template	Result
130°C	Isophthalic acid	**8**
130°C	Phthalic acid	Noncrystalline product
130°C	Absent	No product
150°C	Present	No product

While the structure of **8** is quite similar to that of **6**, there are a few key differences. One of these was the occurrence of trinuclear cobalt clusters throughout the framework, which act as the metal-centred nodes as compared with mixed dinuclear and trinuclear clusters in **6**. Also, due to the neutral nature of **8** there are no dimethylammonium countercations. The clusters are likewise linear and consist of two slightly different types, one of which is regular and symmetric due to its inversion centre and the other, which is slightly irregular. Both clusters contain the same bridging coordination modes (*syn-syn*-$\mu_{1,3}$) and $\mu_{1,1}$.
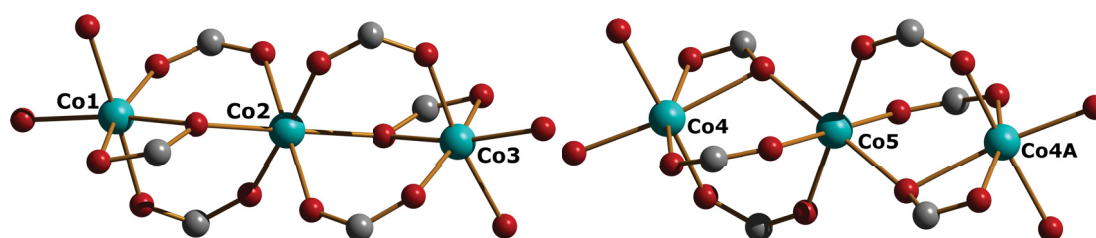

Figure 5.1: Linear trinuclear clusters in **8** with irregular cluster (left) and regular cluster (right).

In terms of the appearance, the pseudo-hexagonal channels in **8** are large and slightly more rounded in comparison with **6**. These large channels, which extend along the (001) plane contain guest solvent molecules as well as isophthalic acid. The existence of the latter could not be confirmed crystallographically but evidence of its presence was supported by elemental CHN and TG analyses. In terms of the topology however, both **6** and **8** share the same topology, which was obtained from analysis using TOPOS.[104] The trinuclear clusters were regarded as six-connected nodes while the central amine nitrogen furnished the three-connected node. As such its net was 3,6-connected with the topological
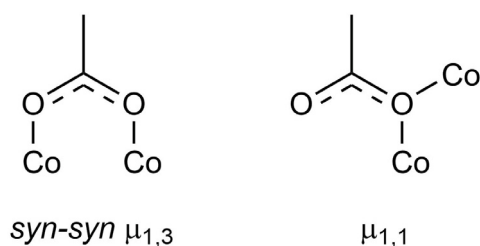
Figure 5.2: Carboxylate bridging coordination modes occurring in **8**.
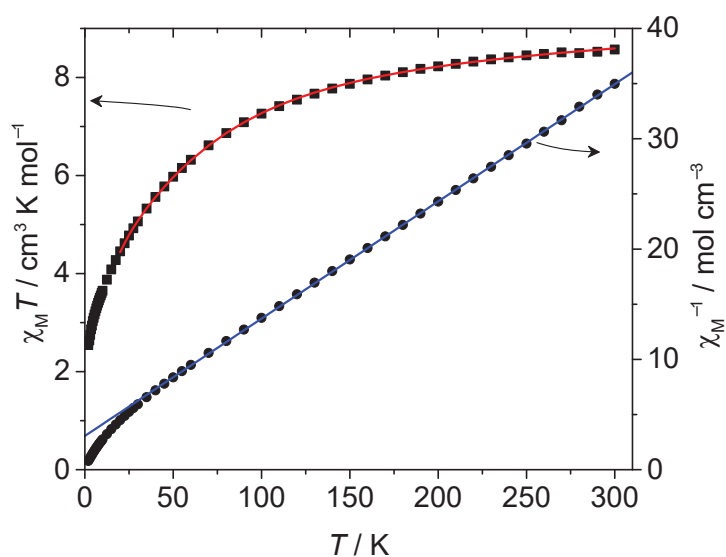
symbol 3,6T80.

Figure 5.3: Temperature dependence of the magnetic susceptibility $\chi_M T$ (black squares) and χ_M^{-1} (black circles) per Co_3 unit in **8** measured at an applied field of 2 kOe. Lines represent best fit.

Its magnetic behaviour could be described on the basis of the trinuclear clusters present. Based on this fact, a simple interaction model was used to fit the susceptibility data utilizing a single set of parameters for all three cobalt(II) ions (see Fig. 5.3). The fit of the data between 20–300 K then resulted in the parameters given in Table 5.2.

Table 5.2: Fitted parameters obtained from susceptibility data for **8**

Parameter	Value
g	2.48
J (cm^{-1})	-2.4
D^d (cm^{-1})	74.4

[d]represents zero field splitting parameter

From the obtained parameters, **8** clearly shows antiferromagnetic interactions within its trinuclear clusters between the adjacent cobalt atoms. This was corroborated by the fit of its χ_M^{-1} vs T data, from

which a Weiss constant of about $-28.8\,\text{K}$ was obtained (see Fig. 5.3). The nature of this exchange can attributed to the nature of the coordination modes existing within the clusters. In carboxylate-bridged clusters, the occurrence of the *syn-syn* type coordination is always an indication of the existence of antiferromagnetic exchange. Also the Co−O−Co bridge arising from the $\mu_{1,1}$ type coordination is about 109°, which is in the range expected for antiferromagnetic coupling. The magnitude of the bridging angle can also be a good clue as to what sort of interactions will predominate in such clusters and angles above 100° are generally known to give rise to antiferromagnetic coupling.[31,106]

Sorption studies on **8** were carried out to show the effect of using two contrasting activation methods on the sorption behaviour. In the first case, activation was performed by exchanging the cocrystallized DMF with dichloromethane followed by air-drying. The replacement of the high-boiling point DMF found in the framework with a low boiling point solvent such as dichloromethane is expected to ease pore evacuation without totally destroying the pore structure. The reasoning behind this is, by applying vacuum or heat or both, the surface tension generated by such high-boiling point solvents when leaving the pores might lead to a degradation of the framework with the consequent collapse of the pores. This could then render a normally porous material non-porous. However, the sample activated by exchange with dichloromethane $\mathbf{8}^{dcm}$, performed fairly with a BET surface area of just $213\,\text{m}^2\,\text{g}^{-1}$ as well as a total pore volume of $0.12\,\text{cm}^3\,\text{g}^{-1}$. Activation using supercritical CO_2 is touted to be an even milder method of treating porous samples. The basis of the method is the use of conditions, which are above critical ($30\,°\text{C}$, $73\,\text{bar}$). Under these conditions there is negligible tension between the surface of the MOFs and the supercritical CO_2, as such removal would lead to a retention of most of the pore structure. This premise was validated by the two-fold increase in the BET surface area seen in the supercritical CO_2 dried sample, $\mathbf{8}^{scd}$. A corresponding increase could be seen in the pore volume as well.Table 5.3

Table 5.3: Sorption data from N_2 isotherms of samples based on **8** measured at $77\,\text{K}$

Sample	aBET ($\text{m}^2\,\text{g}^{-1}$)	Total pore volume ($\text{cm}^3\,\text{g}^{-1}$)
$\mathbf{8}^{dcm}$	213	0.12
$\mathbf{8}^{scd}$	383	0.22

Both isotherms can be classified as irreversible type I isotherms characteristic of the dominant presence of micropores (Fig. 5.4). They also display H3 hysteresis loops, which would likewise imply the presence of some mesopores as well in addition to slit-shaped pores. Pore distribution plots of both samples showed a large concentration of the pores in both materials to be in the micropore area ($<2\text{nm}$). Comparing both however, there was a clear increase in the micropore population resulting from supercritical CO_2 activation, which tallies with the observed increased surface area.Fig. 5.5

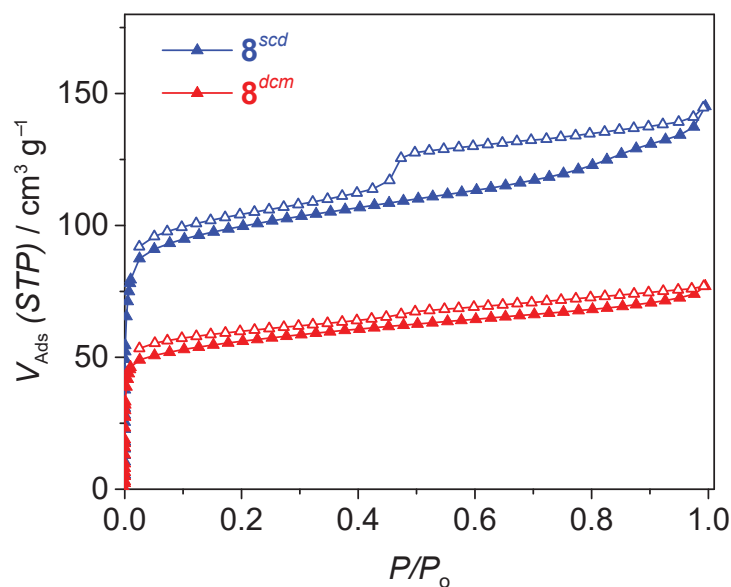In summary, this study demonstrates how inclusion of modulators can be used to alter the pathway

Figure 5.4: Comparison of N_2 isotherms of both dichloromethane-exchanged (8^{dcm}) and supercritical CO_2 dried samples (8^{scd}).
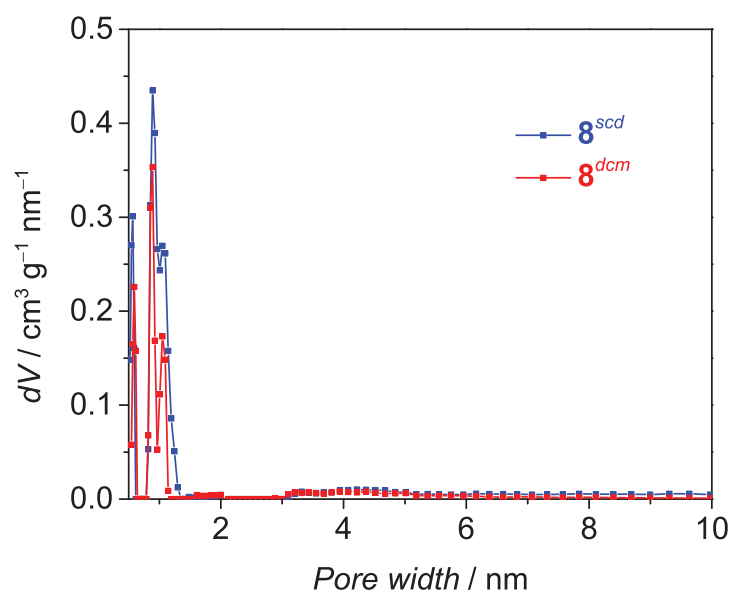

Figure 5.5: QSDFT calculated pore distribution data for samples derived from **8**, fitted using N_2 at 77 K on carbon (slit/cylindrical pores, QSDFT adsorption).

of the synthetic route of a MOF. In this case, the isophthalic acid that had been earmarked as co-ligand instead mediated the synthesis of a neutral MOF. The same reactants without the isophthalic acid could only yield an anionic MOF with a similar topology to **8**. Additionally, the beneficial effect of supercritical CO_2 in the drying process was demonstrated by the higher surface area as well as micropore population displayed by the supercritical-CO_2-exchanged sample. This was in contrast to employing solvent exchange with a low-boiling point solvent like dichloromethane.

Chapter 6

Templated synthesis of high surface area aluminas

Part of this chapter has already been published in P5 and P6: Gholamhossein Mohammadnezhad, <u>Oluseun Akintola</u>, Winfried Plass, Felix H. Schacher, Frank Steiniger and Martin Westermann, *RSC Adv.* **2015**, 5, 49493-49500; Gholamhossein Mohammadnezhad, <u>Oluseun Akintola</u>, Winfried Plass, Frank Steiniger and Martin Westermann, *Dalton Trans.* **2016**, 45, 6329-6334.

The action of structure directors in MOF synthesis has been described in the previous chapter, in which isophthalic acid was shown to direct and template the synthesis of a neutral MOF. In a similar scenario, structural directors in the guise of aluminum alkoxide precursors have been employed to obtain highly stable aluminas with high surface areas. In the first section, aluminium alkoxide precursors were used as templates with the inclusion of triblock copolymers to obtain highly stable aluminas with moderate surface areas. For the second section, high surface area aluminum nanooxides were realized but this time without any copolymers while retaining the use of aluminum alkoxide precursors as templates.

6.1 Templated synthesis of highly thermally stable nanoporous γ-aluminas

The synthesis of mesoporous aluminas has most often been achieved by the use of agents such as surfactants or even block copolymers. In the case of the latter, non-ionic triblock copolymers have served as soft templates in the synthesis of the ordered aluminas.[110] These are generally, easily available while being low priced in addition to having the attractive feature of inducing formation of large and uni-

form pore structures. However, they suffer from the disadvantage of having a complicated hydrolytic behaviour as well as the necessity for strict control of the synthetic conditions. To this end, a combination of these triblock copolymers with aluminum precursors such as $Al(O^iPr)_3$ and $Al(O^sBu)_3$ have been successfully used in synthesizing highly ordered mesoporous aluminas by employing a simple sol-gel process in ethanol.[111] From these, it has been found that the nature of the precursors plays a significant role in defining the physicochemical properties of the resulting alumina. Generally, aluminum oxide precursors have enjoyed frequent use in combination with the triblock copolymers.[112] Furthermore, the rate of hydrolysis as well as condensation of the aluminum alkoxides display a strong dependence on the nature of the alkoxide groups in addition to the coordination environment of the aluminum centres.[113]

Four aluminum alkoxide precursors have been used as molecular precursors to obtain the aluminum oxides. They were prepared by a simple evaporation-induced self-assembly with the inclusion of P123 triblock copolymer in the presence of nitric acid. As such four different functional groups were explored in the precursors namely: isopropoxide, phenoxide, methoxyethoxide, and methoxyethoxyethoxide (for **Al-1**, **Al-2**, **Al-3**, and **Al-4**, respectively). These were expected to present additional donor sites while lowering the hydrolysis rates. The synthesis was followed by calcination at both 400 and 900 °C for 4 h.

SAXS (small angle X-ray scattering) measurements carried out on the samples calcined at 400 °C showed occurrence of a strong reflection (100) around 0.6–0.7° in all of them, which was a clear-cut indication of mesoporous structure (6.1). The intensity of the band was observed to vary in the order of **Al-1**>**Al-4**>**Al-3**>**Al-2** indicating that the alkyl and alkylether groups performed better in comparison to the phenoxyl group in **Al-4**. This is ascribed to the positive effect of the released organic molecules after hydrolysis of the related alkoxide. Calcining the samples at 900 °C did not result in a loss of the mesoporous structure as demonstrated by the retention of the (100) peak in the SAXS pattern. Wide angle X-ray scattering of the samples calcined at 900 °C shows a conversion to γ-alumina with the exception of **Al-2**.

Studies into the porous properties of the samples calcined at 400 °C revealed all four samples exhibited type IV isotherms with the exception of **Al-2**-400, which was a combination of type II and type IV (see **??**). The type IV isotherms are a firm indication of the mesoporous nature of the materials, which was likewise confirmed from the type of hysteresis loops displayed. In the case of **Al-2**-400 its isotherm showed the presence of micropores in addition to the significant population of mesopores demonstrating the impact of the aryloxy precursor used.

For the samples calcined at 900 °C, two clear ranges could be identified as far as the pore distribution is concerned (see 6.1). Both **Al-1** and **Al-2** showed mean pore widths around 9 nm whereas **Al-3** and **Al-4** had their average pore widths in the region of 16–17 nm. This further supports the influential role played by the alkoxy/aryloxy precursor. Upon closer inspection, it was revealed that both **Al-3** and
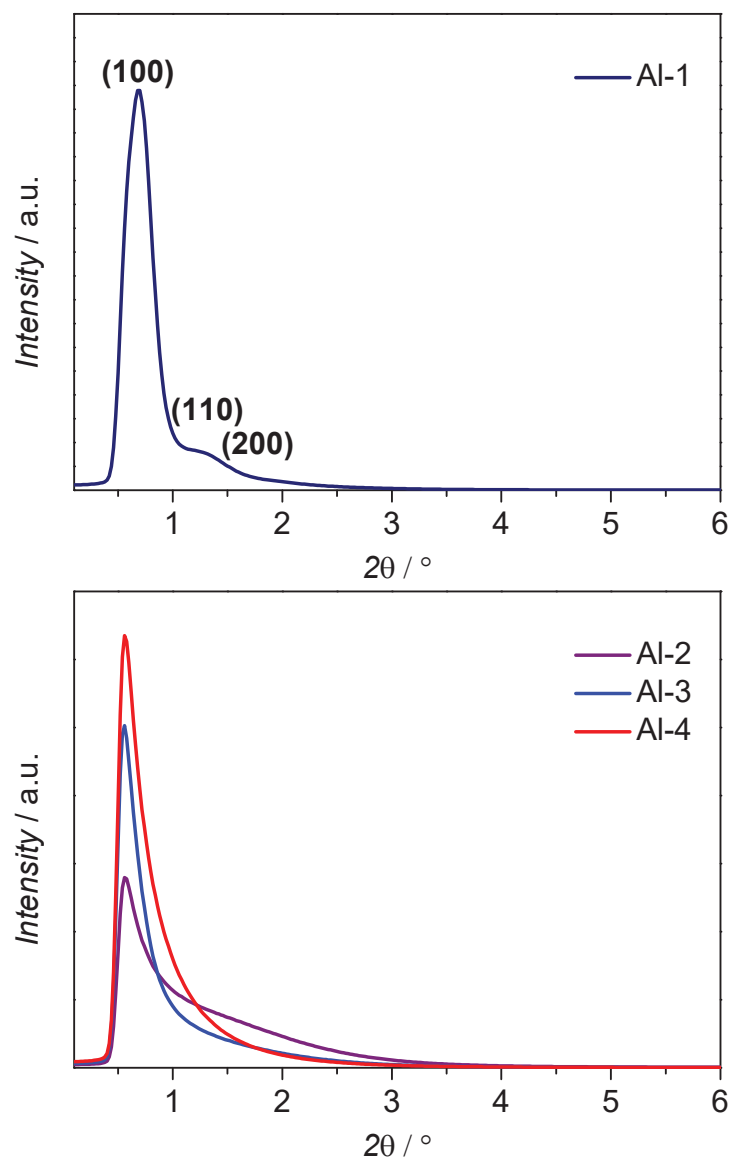
Figure 6.1: SAXS patterns for **Al-1**, above and **Al-2**–**Al-4**, below calcined at 400 °C.

Table 6.1: Sorption data from N_2 isotherms of samples **Al-1**–**Al-4** calcined at 400 and 900 °C measured at 77 K

Sample	aBET ($m^2\,g^{-1}$)	Total pore volume ($cm^3\,g^{-1}$)	Average pore width (nm)
Al-1-400	312	0.57	7.3
Al-1-900	147	0.33	9.0
Al-2-400	480	0.29	2.4
Al-2-900	99	0.22	8.9
Al-3-400	366	0.58	6.4
Al-3-900	97	0.40	16.5
Al-4-400	269	0.63	9.3
Al-4-900	109	0.47	17.0
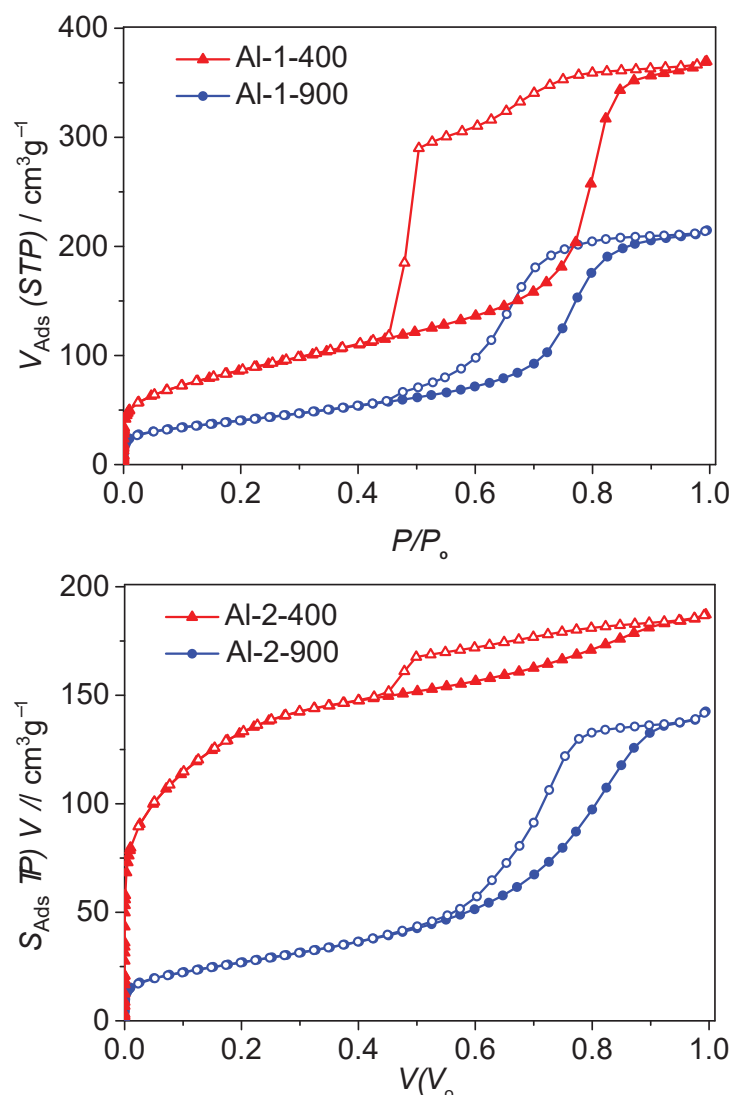
Figure 6.2: Nitrogen adsorption-desorption isotherms of **Al-1** and **Al-2** calcined at 400 and 900 °C represented with red and blue symbols, respectively.

Al-4 had higher surface areas as well as pore volumes. This fact could be linked to the extension of the alkoxy chain with the extra donor groups of the ether moieties, which clearly had impact on the pore structures of both samples.

In conclusion, the influence of the alkoxide precursors in the preparation of mesoporous aluminas has been explored in this section. All synthesized aluminas demonstrated high thermal stability as well as high mesoporosity. The type of the alkoxide used in the precursor clearly played a significant role in the porosity of the ensuing aluminas. This can be seen in the variation of the surface areas/pore volumes with the structure of the alkoxy/aryloxy moeity. Overall, it has been clearly shown that the physico-chemical properties of aluminas can be significantly affected by the nature of the alkoxide templates used in their synthesis.
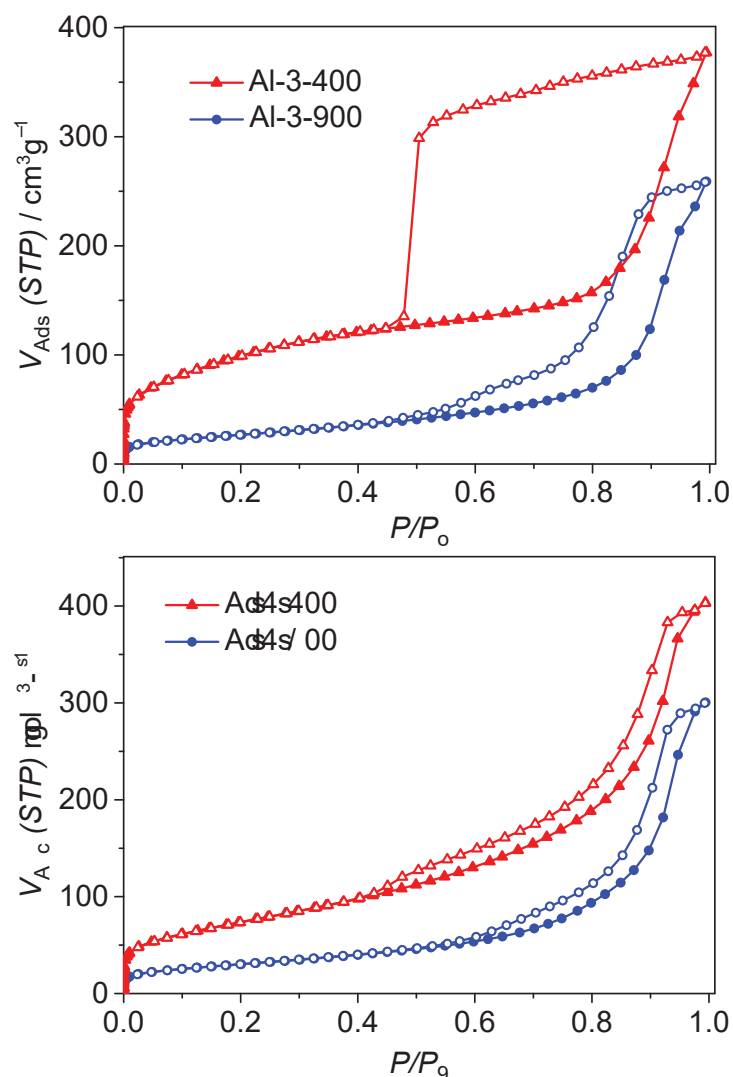
Figure 6.3: Nitrogen adsorption-desorption isotherms of **Al-3** and **Al-4** calcined at 400 and 900 °C represented with red and blue symbols, respectively.

6.2   Surfactant-free synthesis of nano-boehmite with high surface area

The previous section showcased the use of triblock copolymers in the synthesis of aluminas with high thermal stability. However, while the use of surfactants in alumina synthesis is advantageous due to their propensity to influence the properties of the products, they are not without their own problems, some of which include probable biocompatibility. This in addition to irreversible adsorption on the surface of the nanoparticles can lead to unpredictable and undesirable impact on their properties, resulting in the reduction of the accessible surface.[114–116]

Generally, in surfactant-free synthesis of inorganic nanoparticles the commonly used media have been aqueous or nonaqueous while employing hydrolytic or nonhydrolytic conditions. A few stand-out traits of this approach typically include better yields, less impurities, usage of environmental-friendly

solvents, simplicity, and higher surface area. This makes them appealing both from the scientific and economic standpoint.[117,118] This also comes with its own issues as the products tend to dislay certain flaws, which include low or complete lack of crystallinity, need for strict control of synthetic conditions, and complicated hydrolytic behaviour arising from the dual character of water as a solvent and ligand.[119]

To bypass this issue, anhydrous alcohols with the same alkyl groups as the corresponding aluminum alkoxides precursors (aluminum 2-propoxide and aluminum 2-methoxyethoxide) were used in the synthesis of nano-boehmite and γ-alumina. Hydrolysis of solutions of the precursors in their parent alcohols was carried out by adding acetic acid then refuxing the ensuing solutions followed by aging for 24 h. The reaction is such that the only by-products are the alcohols, which are simultaneously the solvent as well as the organic acid. By exploiting the lower surface tension of the alcohols it was possible to remove the alcohols under vacuum using an evaporator. This was followed by drying under vacuum at mild temperatures (70 °C) to remove the acetic acid. The ensuing white powders are denoted **Al-1*** and **Al-2*** (from 2-propoxide and 2-methoxyethoxide, respectively).

Wide-angle X-ray diffraction (WAXRD) studies show the presence of the boehmite phase in the diffractograms of both samples. Due to the reflux temperature of **Al-2*** being higher (a consequence of the boiling point of its corresponding alcohol, 125 °C), it clearly displayed higher crystallinity as compared with its propoxide analogue, **Al-1***. These are displayed in 6.4.
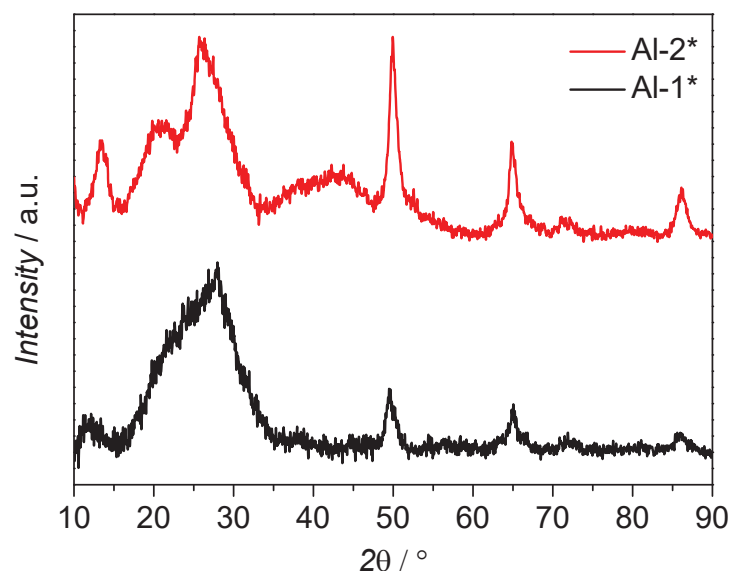

Figure 6.4: WAXRD patterns for **Al-1*** and **Al-2*** dried at 70 °C.

Both **Al-1*** and **Al-2*** were then calcined at 600 and 800 °C, respectively. In the case of **Al-1*** there was already formation of the γ-alumina form at 600 °C that was not observed for **Al-2***. However, both samples clearly showed full conversion to the γ-alumina form at 800 °C. Sorption investigations into both as-synthesized as well as calcined materials are displayed in 6.5.
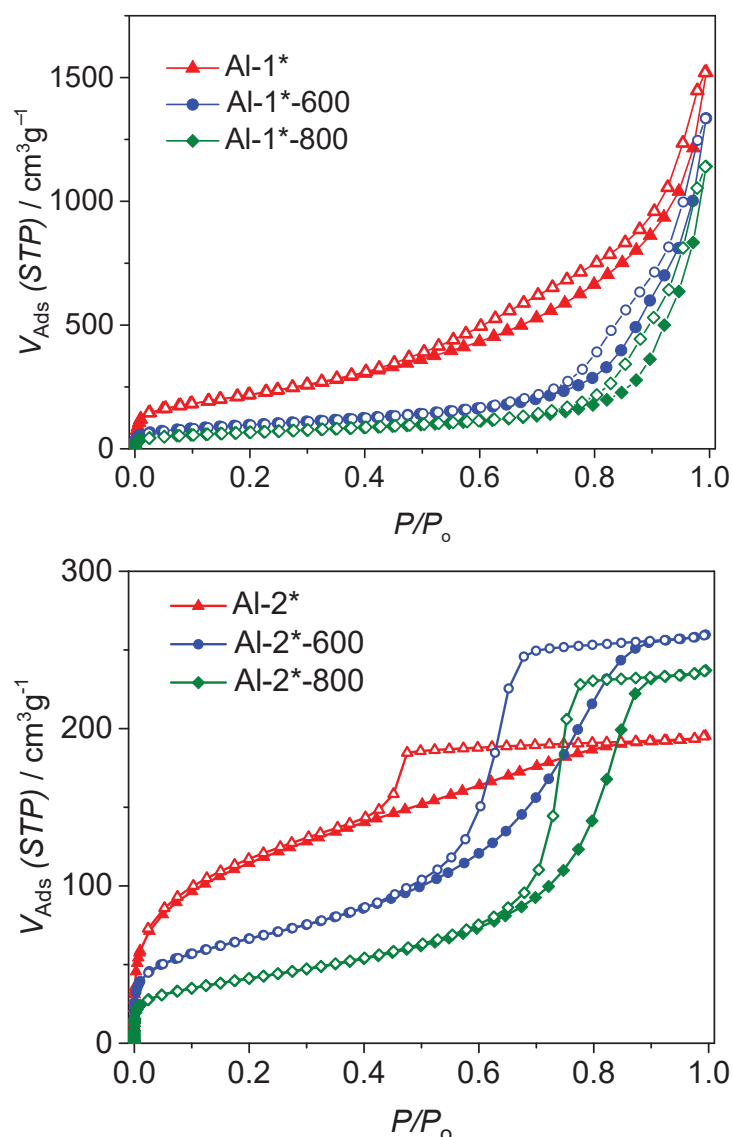
Figure 6.5: Nitrogen adsorption-desorption isotherms of **Al-1*** and **Al-2*** calcined at 600 and 800 °C.

Accordingly, the isotherms of both as-synthesized and calcined samples of **Al-1*** show Type II isotherms with respect to IUPAC classification. This was in addition to them displaying H3 type hysteresis loops. The shape of these loops can be correlated to the presence of non-rigid aggregates within the plate-like framework giving rise to slit-shaped mesopores. For as-prepared **Al-2*** and its calcined samples, these displayed Type IV isotherms as indicated by the plateau seen for all three samples at higher relative pressures. The shape of the isotherm as well as Type H2 hysteresis loops, which they exhibit implies the presence of a mixture of both micropores as well as mesopores. This fact was corroborated by the t-plot analysis, which confirmed the presence of micropores. The differences in the sorption behaviour of both samples demonstrates the role played by the precursors in influencing the physical characteristics of the resultant aluminas.

Table 6.2: Sorption data from N_2 isotherms of **Al-1*** and **Al-2*** calcined at 600 and 800 °C measured at 77 K

Sample	aBET ($m^2 g^{-1}$)	Total pore volume ($cm^3 g^{-1}$)	Average pore width (nm)
Al-1*	802	2.35	11.7
Al-1*-600	343	2.07	24.1
Al-1*-800	242	1.77	29.2
Al-2*	420	0.30	2.9
Al-2*-600	239	0.40	6.7
Al-2*-800	149	0.37	9.9

The sorption parameters are summarized in 6.2. The 2-propoxide templated nano-boehmite (**Al-1***) clearly displayed the highest surface area in addition to the high pore volume as well. This contrasts with examples of alumina typically obtained using aqueous-based preparative methods, in which the surface areas generally tend to vary inversely with the pore volumes. This trend was likewise seen in its calcined samples as well with the total pore volumes decreasing in like manner as the surface areas. The 2-methoxyethoxide analogue (**Al-2***) also showed the same trend with the exception of the as-synthesized sample showing low pore volume.

The morphological changes resulting from calcination was likewise monitored through TEM. Both as-synthesized **Al-1*** and **Al-2*** consisted of folded plates with different thicknesses with these also showing aggregation. The calcined samples demonstrate a clear change in morphology with a resultant conversion to more curved and partially rolled plates, which have nanotube-like consistency.

In conclusion, the surfactant-free synthetic approach is one that is evironmental friendly with the avoidance of any non-green additives. This is in addition to the ease, with which the employed alcohols can be recovered that can then be saved for further reuse. Furthermore, using very low amounts of water as well as organic acid facilitated the removal of the alcohol under mild conditions leading to retention of the structure while allowing isolation of highly pure samples.

Summary

The study of coordination polymers/MOFs has, since the beginning of the 90s, seen so much effort invested into it. Much of these have focused on their use in different ways, which generally range from gas storage, ion exchange to magnetism. The inherent flexibility of MOF design, by which the eventual architecture is influenced by the preorganization priniciple has been often exploited and has led to lots of success in MOF research. This is more fascinating when it is considered that simple selection of both components can result in targeted compounds. Generally, this principle is demonstrated especially in magnetic MOFs where the incorporated metal centres often prefer particular cluster arrangements (Secondary Building Units, SBUs). It thus becomes easy to combine the metal centres with the desired ligand leading to an extended framework incorporating the desired metal. Even more interesting is when a redox-active ligand with the ability to generate radicals by the use of external stimuli for example guest molecules or irradiation or a combination of both, can be incorporated within the framework. This creates the intriguing prospect of combining the created radical with the paramagnetic metal centres, which can lead to propagation of magnetic order through-out the network.

It is nonetheless intriguing to study the isolated behaviour of these SBUs as simple monomeric complexes before incorporating them in these extended networks where additional cooperative effects may come into play. Therefore, 4,4'-disubstituted monocarboxyltriphenylamines were combined with copper(II) ions and this led to the metal ions adopting their well-known paddle-wheel arrangement. The four ligands used were the unsubstituted monocarboxyltriphenylamine, the methyl-, $tert$-butyl- as well as the methoxy monocarboxyltriphenylamines (Hdaba **1**, Htaba **2**, Hteaba **3**, and Hmaba **4**, respectively). All four corresponding complexes possess similar structural arrangements in spite of the different substituents at their p-positions but with slight variations in their packing. This similarity at the level of the dinuclear core meant that the complexes display no correlation between the electronic nature of the substituents at the 4,4'-positions and the strength of the coupling between the Cu(II) ions. This was especially seen in the fitted value for the coupling constants in the range of -290 to $-330\,\mathrm{cm}^{-1}$ indicating strong antiferromagnetic exchange. On the other hand, due to the proximity of the groups to the central amine nitrogen, the electrochemical behaviour of both ligands and complexes demonstrates
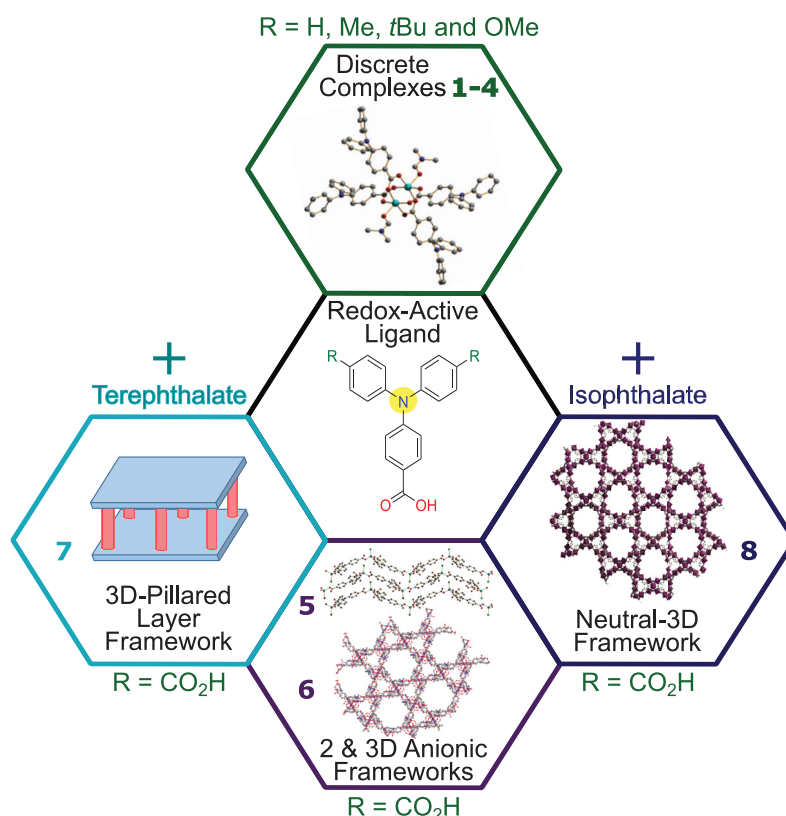
Figure S1: Graphical summary of Chapters 2 to 5.

a direct correlation with the substituents. The ease of oxidation of the central amine nitrogen was found to be independent of coordination of the metal ions. The generation of the radical cations on the complex using a chemical oxidizing agent was shown to be successful.

Functionalizing all three p-positions on the triphenylamine ligand with carboxylate groups and then combining them with cobalt(II) ions led to two different anionic coordination polymers, **5** and **6**. This was achieved by altering the reactor sizes whilst keeping the absolute amount of reactants constant. This clearly demonstrated the influence of altering reaction conditions on the ultimate outcome of MOF synthesis. The counter charge in both anionic networks is provided by dimethylammonium, which was a by-product of the decarbonylation of DMF under solvothermal conditions. The organoammonium cation was also considered to have acted as a template for obtaining both coordination polymers. **5** is a 2D framework made up of mononuclear Co(II) SBUs while **6** is a 3D network with a mixture of dinuclear and trinuclear Co(II) clusters. The difference in the structures had implications for the topologies where **5** had a 2D **hcb** net while **6** was a 3D network with 3,6T80 topology. Magnetic studies showed **5** to have SMM properties but this was insignificant due to the efficient quantum tunneling relaxation. **6** on the other hand was regarded as a simple paramagnet and the existence of the mixed clusters meant little information could be gleaned from its magnetic behaviour. This was attributed to the presence of both strong spin-orbit coupling as well as the intra-cluster exchange interactions. The two compounds

are able to successfully undergo guest cation exchange whereby the organoammonium cations can be easily replaced by inorganic cations. Depending on the solvent used (DMF or ethanol), partial or total exchange of the organic cations could be achieved. This cation exchange ability had consequences for the sorption properties of both compounds in the form of definite increases in the surface areas as well as pore volumes. This was likewise correlated to the extent of the exchange with a gradual increase in sorption from the non-porous as-synthesized compounds to the partly porous partially exchanged materials. The culmination of this trend was seen in the completely exchanged materials, which both showed large increases in their accessible surface areas. This opens up a vista of possibilities in tuning the porosity of anionic networks by careful selection of the guest cation.

Addition of spacer groups to extend the ligands has been one of the ways, by which porosity of porous coordination polymers can be enhanced. However, the large sizes of the pores and the resulting low density of the framework bound by a single ligand can lead to a weak structure with attendant collapse. The structure itself may attempt to resolve this by undergoing entanglement but with the additional consequence of reduced porosity. One rational way to actualize this is the construction of pillared-layer frameworks where the structure is reinforced by the inclusion of ditopic ligands. By combining the tricarboxytriphenylamine with terephthalic acid while using the Co(II) ion, end-result was the anionic pillared-layer network **7**. This was achieved through the coordination copolymeriza-tion route wherein the optimal reaction ratio of the reactants was used thereby avoiding formation of two discrete networks. The anionic network also has its charge balanced by two dimethylammonium cations resulting from in-situ decomposition of DMF. The network is structurally composed of linear trinuclear Co(II) clusters containing mixed T_d-O_h-T_d geometries. Each cluster is linked within the lay-ers to each other *via* the tricarboxytriphenylamine ligand while the interlayer links were through the terephthalates. Toplogical analysis of the network gave a 3,8-connected **tfz-d** topology. By implica-tion, the Co(II) centres display magnetic interactions between them, transmitted over the carboxylate bridges just like in the copper paddle-wheel complexes. There was also propagation of magnetic ex-change over the terephthalate groups but this was relatively low. Its countercation, stemming from its anionic character, was also found to be replaceable with inorganic cations, which then led to the internal pores opening up. This was seen in the improved sorption behaviour of the post-exchange compound with a three-fold increase in its apparent surface area. The pores are also located mostly in the micropore region with the lithium exchanged sample showing a dramatic increase in its ultrami-cropore distribution. Overall, this was in corroboration of the behaviour already seen in the previous anionic MOFs and also illustrates the prospect of tuning porosity by judicious choice of cationic guests.

Inclusion of coordination modulators during MOF synthesis has been shown to influence the fi-nal structure the MOFs adopt without these playing any role in the overall structure assumed. By combining isophthalic acid with the tricarboxytriphenylamine and cobalt salt, the result is a neutral

Summary

coordination polymer **8**, which does not contain the isophthalic acid as part of its structure but rather as a framework guest. It was found to be identical to **6** in terms of its topology where the main difference was the charge of both frameworks. The isophthalic acid is believed to have lowered the pH thus favouring less the decarbonylation of DMF that would have formed the dimethylammonium cation, which is known to template anionic MOFs. Just like **7**, **8** is also composed of trinuclear cobalt clusters albeit with all the three centres having octahedral geometry. Magnetic investigations only revealed the existence of antiferromagnetic interactions between the neighbouring cobalt centres. This was likewise attributed to the nature of the bridging between the Co(II) ions particularly the high Co−O−Co angle (109°) as well as the *syn-syn* bridge. Sorption studies showed that it is a microporous compound with pores in both the ultramicropore and supermicropore ranges respectively (<0.7 nm and 0.7-2 nm). The effect of activation of the material *via* exchange with low boiling point solvents as well as supercritical CO_2 drying on the sorption properties was likewise studied. From this supercritical CO_2 extraction was conclusively demonstrated to be the more efficient method and showed a two-fold higher surface area as well as greater pore volume than the sample activated by simple solvent exchange with dichloromethane.
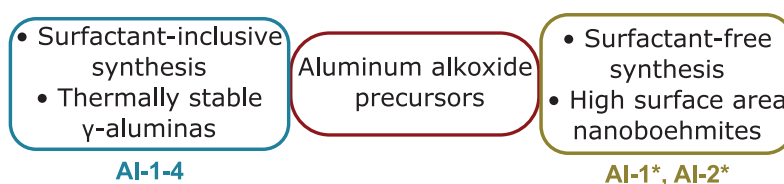

Figure S2: Graphical summary of Chapter 6.

Still following the thread of templated synthesis, aluminum alkoxide precursors were combined with triblock copolymers using a simple sol-gel route to obtain a series of aluminas. These were shown to possess high thermal stability while undergoing conversion to the γ-form at 900 °C. Of all four substituents used (isopropoxide (**Al-1**), phenoxide (**Al-2**), methoxyethoxide (**Al-3**) and methoxyethoxyethoxide (**Al-4**)), the phenoxy linker shows the highest surface area in addition to being both micro- and mesoporous. The ether derivatives likewise had a clear effect on the pore structures of the samples, such as an increase in the average pore widths as well as volumes. This was attributed to the extended alkoxide chains in addition to the extra potential donor groups. Furthermore, due to the occasional negative effect of the surfactants such as potential adsorption onto the nanostructures, surfactant-free synthesis of nano-aluminas was also performed. This was carried out under non-aqueous conditions using the alkoxides (2-propoxide, (**Al-1***) and 2-methoxyethoxide, (**Al-2***)) as templates with the corresponding alcohols as solvent. Through this approach, it was then possible to obtain the high surface area nano-boehmites.

Overall, the use of the redox-active triphenylamine ligand was demonstrated to lead to different

possibilities, which was achieved through the variable functionalization with carboxylate groups. By monofunctionalization of the triphenylamine and combination with copper(II) ions, a series of discrete monomeric complexes were obtained. The redox property of the ensuing complexes were tunable by adjusting the type of substituent on the 4,4'-positions. Trifunctionalization with the same carboxylate group and combining with cobalt(II) ions two different charged frameworks, which showed tunable sorption properties *via* guest countercation selection were obtained. This would mark the first time, in which two utterly different networks were obtained by using the same absolute amount of materials but only changing the size of the reactors. Combining the trifunctionalized triphenylamine with a terephthalic acid co-ligand would then result in a robust anionic 3D pillared-layer network, which would also display countercation-dependent sorption behaviour. In both cases the demonstration of the dependence of the sorption properties on the sort of countercation present offers the possibility of tuning porosity simply by choice of the guest cations. Finally, by introduction of a coordination modulator it was possible to alter the pathway of MOF formation from anionic framework to a neutral network. This was done by the simple inclusion of isophthalic acid during the synthesis of the MOF. This raises the prospect of changing the structural outcome of MOF synthesis through the use of structural directors whilst still retaining the original reactants used.

Also, the use of different aluminum alkoxide precursors as templates have been demonstrated to have strong influence on the physicochemical properties of the ensuing products. Variation of the alkoxy and aryloxy groups in the aluminum alkoxides were clearly shown to affect the porosities of the corresponding aluminas. Additionally, exclusion of surfactants in the synthesis of the aluminas led to materials with high surface area as well as large pore volumes.

Zusammenfassung

Die Forschung auf dem Gebiet der Koordinationspolymere/MOFs wird seit den 1990er Jahren sehr intensiv betrieben. Hierbei lag der Fokus vor allem auf ihren vielseitigen Anwendungen, die von Gasspeicherung über Ionenaustausch bis hin zu Magnetismus reichen. Dafür wurde vor allem die inhärente Flexibilität des MOF-Designs, bei der die Architektur vom Präorganisationsprinzip beeinflusst wird, genutzt, was zu vielen Fortschritten in der MOF-Forschung führte. Dabei ist besonders der Aspekt faszinierend, dass eine einfache Auswahl beider Komponenten gezielt zu Verbindungen führen kann. Im Allgemeinen wird dieses Prinzip primär bei magnetischen MOFs genutzt, bei denen die eingeschlossen Metallzentren oft besondere Clusteranordnungen (Secondary Building Units, SBUs) bevorzugen. Dadurch ist es einfach, die Metallzentren mit den entsprechenden Liganden zu kombinieren, was zu einem erweiterten Molekülgerüst führt, der das gewünschte Metall enthält. Zudem ist besonders die Integration von redoxaktiven Liganden in das Gerüst interessant, da diese zu einer Radikalbildung aufgrund von externer Stimuli führen können. Als Beispiele seien hier die Bestrahlung, der Lösungsmittelaustausch von Gastmolekülen oder die Kombination aus beiden genannt. Dies schafft die Möglichkeit das erzeugte Radikal mit den paramagnetischen Metallzentren zu kombinieren, was zu einer Ausweitung der magnetischen Ordnung durch das Netzwerk führen kann.

Außerdem ist es von Interesse das isolierte Verhalten dieser SBUs als einfache monomere Komplexe zu untersuchen bevor sie in diese erweiterten Netzwerke eingebunden werden, wo zusätzliche kooperative Effekte ins Spiel kommen können. Deshalb wurden 4,4'-disubstituierte Monocarboxyltriphenylamine mit Kupfer(II)-Ionen kombiniert, was dazu führte, dass die Metallionen ihre literaturbekannte 'Schaufelrad'-Anordnung einnahmen. Die verwendeten Liganden sind das unsubstituierte Monocarboxyltriphenylamin sowie Methyl-, *tert*-Butyl- und Methoxy-Monocarboxyltriphenylamin (Hdaba **1**, Htaba **2**, Hteaba **3** und Hmaba **4**). Alle vier synthetisierten Komplexe besitzen trotz der verschiedenen Substituenten an ihren p-Positionen ähnliche strukturelle Anordnungen mit leichten Variationen in ihrer Packung. Die Ähnlichkeit auf der Ebene des dinuklearen Kerns bedeutet, dass die Komplexe keine Korrelation zwischen der elektronischen Natur der Substituenten an den 4,4'-Positionen und der Stärke der Kopplung zwischen den Cu(II)-Ionen zeigen. Dies wurde besonders in den gefitteten
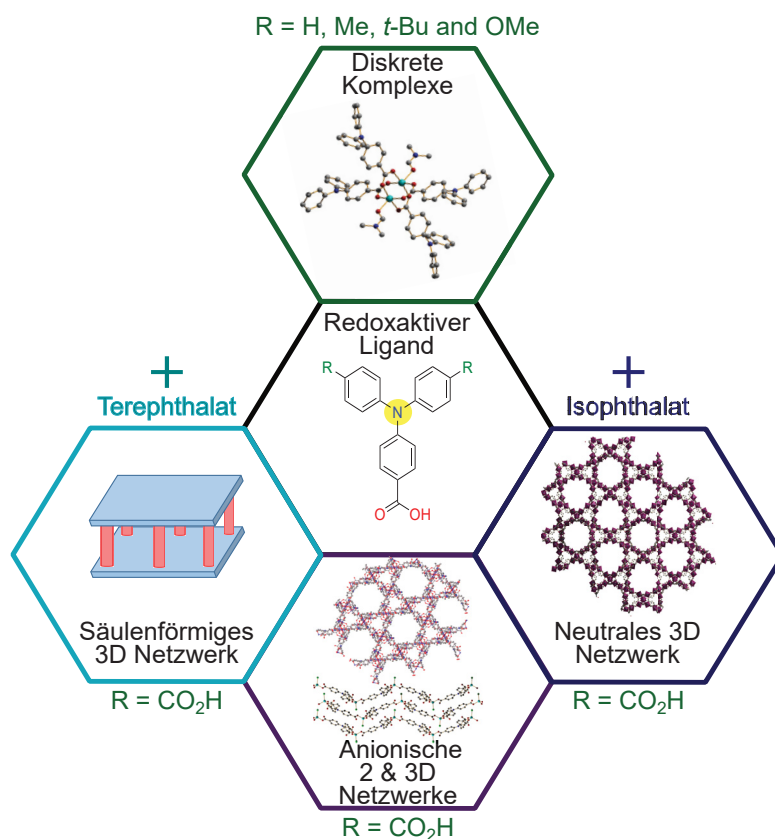
Abbildung Z1: Grafische Zusammenfassung der Kapitel 2 bis 5.

vier Kopplungkonstanten im Bereich von -290 bis $-330\,\text{cm}^{-1}$, welche eine starke antiferromagnetische Wechselwirkung anzeigen. Aufgrund der Nähe der Substituenten zum zentralen Amin-Stickstoff zeigt das elektrochemische Verhalten beider Liganden und Komplexe eine direkte Korrelation mit den entsprechenden Substituenten. Die Möglichkeit der Oxidation am zentralen Amin-Stickstoff wurde unabhängig von der Koordination der Metallionen festgestellt. Die Erzeugung der Radikalkationen mit dem Komplex unter Verwendung eines chemischen Oxidationsmittels war ebenso erfolgreich.

Die Funktionalisierung aller drei p-Positionen am Triphenylaminliganden mit Carboxylatgruppen und anschließender Kombination mit Cobalt(II)-Ionen führte zu den zwei verschiedenen anionischen Koordinationspolymeren **5** und **6**. Diese wurden lediglich durch eine Veränderung der Reaktorgrößen erhalten, während die absolute Menge an Reaktanten konstant gehalten wurde, was eindeutig den Einfluss der Reaktionsbedingungen auf das endgültige Ergebnis der MOF-Synthese zeigt. Zum Ladungsausgleich wurden in beiden anionischen Netzwerken Dimethylammoniumionen bereitgestellt, welche ein Nebenprodukt der Decarbonylierung von DMF unter solvothermen Bedingungen sind. Dabei wurden die Organoammoniumkationen auch als strukturgebender Modulator betrachtet, um beide Koordinationspolymere zu erhalten. **5** zeigt ein 2D-Gerüst aus mononuklearen Co(II) SBUs, **6** ein 3D-Netzwerk mit einer Mischung aus zwei- und dreikernigen Co(II)-Clustern. Die Unterschiede in

den Strukturen wirkten sich auch auf die Topologie aus, was bei **5** zu einem 2D **hcb** Netz und bei **6** zu einem 3D-Netzwerk mit 3,6T80 Topologie führte. Magnetische Studien an **5** zeigen dessen SMM-Eigenschaften, welche jedoch durch signifikante Quantentunnelprozesse geprägt sind. **6** erwies sich dagegen als einfacher Paramagnet. Die Existenz der gemischten Cluster führt zu starken Intracluster-Wechselwirkungen, welche in Kombination mit der starken Spin-Bahn-Kopplung der Co(II)-Ionen dazu führte, dass wenige Informationen aus dem magnetischen Verhalten entnommen werden konnten. Mit beiden Verbindungen konnte erfolgreich Gastkationenaustausch durchgeführt werden, wobei die Organoammoniumkationen leicht durch anorganische Kationen ersetzt werden konnten. Je nach verwendetem Lösungsmittel (DMF oder Ethanol) konnte ein teilweiser oder vollständiger Austausch der organischen Kationen erreicht werden. Diese Kationenaustauschfähigkeit wirkte sich auf die Sorptionseigenschaften beider Verbindungen in Form definierter Zunahmen der Oberflächen und Porenvolumina aus. Dies korreliert ebenfalls mit dem Ausmaß des Austausches mit einer allmählichen Zunahme der Sorption von den nicht porösen frisch-synthetisierten Verbindungen zu den teilweise porösen, teilweise ausgetauschten Materialien. Das Maximum dieses Trends zeigt sich in den vollständig ausgetauschten Materialien, welche bei beiden Verbindungen eine große Zunahme in ihren zugänglichen Oberflächen zeigen. Dies eröffnet die Möglichkeit die Porosität der anionischen Netzwerke durch sorgfältige Wahl des Gastkations zu optimieren.

Eine weitere Möglichkeit die Porosität der Koordinationspolymere zu erhöhen ist die Zugabe von Liganden mit eingebauten Spacergruppen. Allerdings können erhebliche Porengrößen und die daraus resultierende geringe Dichte zu einer schwachen Struktur mit begleitendem Kollaps führen. Anstelle des Kollapses kann auch eine Verflechtung der Struktur in sich selbst erfolgen, was wiederum mit der Abnahme der Porosität verbunden ist. Ein rationaler Weg dies zu verwirklichen ist die Konstruktion von säulenförmigen Schichtgerüsten, in denen die Struktur durch die Einbeziehung von ditopen Liganden verstärkt wird. Die Kombination des Tricarboxyltriphenylamins mit Terephthalsäure unter Verwendung von Co(II)-Ionen führte zum anionische säulenförmige Schichtnetzwerk (**7**). Dieses wurde durch den Koordinationspolymerisationsweg unter Verwendung des optimalen Reaktionsverhältnisses der Reaktanten erreicht, wodurch die Bildung von zwei diskreten Netzwerken vermieden wurde. Das anionische Netzwerk wird durch zwei Dimethylammoniumkationen ausgeglichen, die aus einer in situ-Zersetzung von DMF resultierten. Das Netzwerk setzt sich strukturell aus linearen trinuklearen Co(II)-Clustern zusammen, die gemischte T_d-O_h-T_d Geometrien besitzen. Jeder Cluster ist innerhalb der Schicht über den Tricarboxyltriphenylaminliganden und zwischen den Schichten durch die Terephthalate miteinander verknüpft. Die topologische Analyse des Netwerks ergab eine 3,8-verbundene **tfz-d** Topologie. Die Co(II)-Zentren zeigen dabei magnetische Wechselwirkungen, die wie bei den Cu(II)-Schaufelrad-Komplexen über Carboxylatbrücken vermittelt werden. Des Weiteren konnte eine relativ geringe Vergrößerung der magnetischen Wechselwirkungen über die Terephthalatgruppen beobachtet

werden. Das Gegenion des anionischen Netzwerks wurde ebenfalls mit anorganischen Kationen ersetzt, welches zur Öffnung der inneren Poren und zu einer dreifachen Erhöhung der scheinbaren Oberfläche führte. Die Größe der Poren ist meist in der Mikroporenregion angeordnet. Die Lithiumausgetauschten Probe zeigte sogar eine drastische Zunahme der Ultramikroporenverteilung verbunden. Insgesamt ist dies eine Bestätigung des Verhaltens, das bereits in den bisherigen anionischen MOFs gefunden wurde und zeigt die Möglichkeit die Porosität durch die Wahl der kationischen Gäste zu manipulieren auf.

Die Einbeziehung von Koordinationsmodulatoren während der MOF-Synthese hat gezeigt, dass sie die endgültige MOF-Struktur beeinflussen, ohne jedoch in der Gesamtstruktur eine Rolle spielen. Durch die Kombination von Isophthalsäure mit dem Tricarboxyltriphenylamin und einem Cobaltsalz war das Ergebnis ein neutrales Koordinationspolymer (**8**), welches die Isophthalsäure nicht als Teil ihrer Struktur, sondern als Gastmolekül im Gerüst enthielt. Es wurde festgestellt, dass es mit **6** in Bezug auf seine Topologie identisch ist. Der Hauptunterschied liegt bei der Ladung der beiden Gerüste. Durch die Verwendung der Isophthalsäure wurde der pH-Wert gesenkt, in Folge dessen war die Decarbonylierung von DMF, welche in den anderen anionischen MOFs das Dimethylammoniumkation gebildet hat, weniger bevorzugt. Dies verhinderte die Bildung von Dimethylammoniumionen als Gegenionen eines anionischen Netzwerkes. Genau wie **7** besteht **8** aus dreikernigen Cobaltclustern, jedoch weisen alle drei Zentren eine oktaedrische Geometrie auf. Magnetische Untersuchungen zeigten das Auftreten von antiferromagnetischer Wechselwirkungen zwischen den benachbarten Cobaltzentren. Dies wird ebenfalls der Art der Verbrückung zwischen den Co(II)-Ionen zugeschrieben, insbesondere dem hohen Co—O—Co-Winkel (109°) sowie der *syn-syn* Verbrückung. Sorptionsstudien ergaben, dass es sich um eine mikroporöse Verbindung mit Poren im Ultramikroporen- und Supermikroporenbereich handelt ($< 0{,}7\,nm$ beziehungsweise $0{,}7\text{-}2\,nm$). Ebenfalls untersucht wurde der Einfluss der Art der Materialaktivierung auf die Sorptionseigenschaften, welche beispielsweise durch Austausch mit einem niedrigsiedenden Lösungsmittel oder durch die überkritische CO_2-Abscheidung erreicht wurde. Dabei hat sich gezeigt, dass die Behandlung mit überkritischem CO_2 die effizienter Methode ist, da eine zweifach größere Oberfläche sowie größere Porenvolumina als bei der Probe, die durch einfachen Lösungsmittelaustausch mit Dichlormethan aktiviert wurde, erhalten werden konnte.
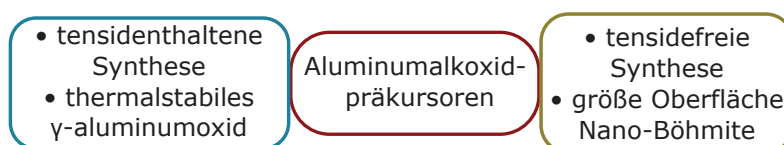

Abbildung Z2: Grafische Zusammensfassung des 6. Kapitels.

Um eine Reihe von Aluminiumoxiden zu erhalten wurden die Aluminiumalkoxidpräkursoren ebenfalls auf dem Weg der Templatsynthese unter Verwendung einer einfachen Sol-Gel-Route mit Triblock-Copolymeren kombiniert. Diese zeigen eine hohe thermische Stabilität, da sie sich erst bei 900 °C in

die γ-Form umwandeln. Von allen vier verwendeten Substituenten (Isopropoxid (**Al-1**), Phenoxid (**Al-2**), Methoxyethoxid (**Al-3**) und Methoxyethoxyethoxid (**Al-4**)) hat der Phenoxy-Linker neben Mikro- und Mesoporosität die größte Oberfläche. Die Etherderivate hatten durch eine Erhöhung der mittleren Porenbreiten sowie -volumina ebenfalls einen deutlichen Einfluss auf die Porenstrukturen der Proben. Dies wird neben den zusätzlichen potentiellen Donorgruppen den erweiterten Alkoxidketten zugeschrieben. Aufgrund der gelegentlichen negativen Wirkung der Tenside, wie der potentiellen Adsorption an die Nanostrukturen, wurde auch eine tensidfreie Synthese von Nanoaluminumoxiden durchgeführt. Diese wurde unter nicht-wässrigen Bedingungen und unter Verwendung der Alkoxide (2-Propoxid (**Al-1***) und 2-Methoxyethoxid (**Al-2***)) als Matrizen mit den entsprechenden Alkoholen als Lösungsmittel durchgeführt. Durch diesen Ansatz war es möglich Nano-Böhmite mit großen Oberflächen zu erhalten.

Zusammenfassend wurde gezeigt, dass der Einsatz des redoxaktiven Triphenylaminliganden zu unterschiedlichen Ergebnissen führt, welche durch die variable Funktionalisierung mit Carboxylatgruppen erreicht wurden. Mittels Monofunktionalisierung des Triphenylamins und der Kombination mit Kupfer(II)-Ionen wurde eine Reihe von diskreten monomeren Komplexen erhalten. Die Redoxeigenschaften der Komplexe ist durch Variation der Substituenten an den 4,4'-Positionen bestimmbar. Außerdem durch Trifunktionalisierung mit der gleichen Carboxylatgruppe und Kombination mit Cobalt(II)-Ionen wurden zwei verschiedene anionische Gerüste erhalten, die durch Gast-Gegenkation-Auswahl abstimmbare Sorptionseigenschaften zeigen. Somit wurden erstmalig zwei völlig unterschiedliche Netzwerke erhalten, obwohl die gleiche Absolutemenge an Materialien verwendet und lediglich die Größe der Reaktoren geändert wurde. Die Kombination des trifunktionalisierten Triphenylamins mit einem Terephthalsäure-Coliganden führte zu einem robusten anionischen 3D-säulenförmiges Schichtnetzwerk, das auch ein kontraktionsabhängiges Sorptionsverhalten aufweist. In beiden Fällen bietet die Abhängigkeit der Sorptionseigenschaften von der Art der Gegenkation die Möglichkeit, die Porosität durch die Wahl der Gegenionen abzustimmen. Schließlich war es durch die Einführung eines Koordinationsmodulators möglich den Weg der MOF-Bildung vom anionischen Rahmen zu einem neutralen Netzwerk zu verändern. Das geschah durch die einfache Einbeziehung von Isophthalsäure während der Synthese des MOF. Dies eröffnet die Möglichkeit das strukturelle Ergebnis der MOF-Synthese durch den Einsatz von Strukturvermittlern zu verändern, während die ursprünglichen Reaktanten weiterhin beibehalten werden.

Auch die Verwendung verschiedener Aluminiumalkoxidpräkursoren als Vorlagen hat gezeigt, dass sie einen starken Einfluss auf die physikochemischen Eigenschaften der nachfolgenden Produkte haben. Eine Variation der Alkoxy- und Aryloxygruppen in den Aluminiumalkoxiden zeigt eine eindeutig Auswirkung auf die Porosität der entsprechenden Aluminiumoxide. Darüber hinaus führt der Ausschluss von Tensiden bei der Synthese der Aluminiumoxide zu Materialien mit hoher Oberfläche sowie

großen Porenvolumina.

Bibliography

[1] Robin, A. Y.; Fromm, K. M. *Coord. Chem. Rev.* **2006**, *250*, 2127–2157.

[2] Batten, S. R.; Champness, N. R.; Chen, X.-M.; Garcia-Martinez, J.; Kitagawa, S.; Öhrström, L.; O'Keeffe, M.; Suh, M. P.; Reedijk, J. *Pure Appl. Chem* **2013**, *85*, 1715–1724.

[3] Zhou, H.-C.; Long, J. R.; Yaghi., O. M. *Chem. Rev.* **2012**, *112*, 673–674.

[4] Li, J.-R.; Sculley, J.; Zhou, H.-C. *Chem. Rev.* **2012**, *112*, 869–932.

[5] Kitagawa, S.; Matsuda, R. *Coord. Chem. Rev.* **2007**, *251*, 2490–2509.

[6] Weller, M.; Overton, T.; Rourke, J.; Armstrong, F. *Inorganic Chemistry*, 6th ed.; Oxford University Press, 2014.

[7] Li, J.-R.; Kuppler, R. J.; Zhou, H.-C. *Chem. Soc. Rev.* **2009**, *38*, 1477–1504.

[8] Chen, B.; Ockwig, N. W.; Millward, A. R.; Contreras, D. S.; Yaghi, O. M. *Angew. Chem. Int. Ed.* **2005**, *44*, 4745–4749.

[9] Lee, J.; Olson, D.; Pan, L.; Emge, T.; Li, J. *Adv. Funct. Mater.* **2007**, *17*, 1255–1262.

[10] Chen, S.-S.; Chen, M.; Takamizawa, S.; Wang, P.; Lv, G.-C.; Sun, W.-Y. *Chem. Commun.* **2011**, *47*, 4902–4904.

[11] Wang, Z.; Chen, G.; Ding, K. *Chem. Rev.* **2009**, *109*, 322–359.

[12] Farrusseng, D.; Aguado, S.; Pinel, C. *Angew. Chem., Int. Ed.* **2009**, *48*, 7502–7513.

[13] Ma, L.; Abneya, C.; Lin, W. *Chem. Soc. Rev.* **2009**, *38*, 1248–1256.

[14] Fei, H.; Rogow, D. L.; Oliver, S. R. J. *J. Am. Chem. Soc.* **2010**, *132*, 7202–7209.

[15] Carlucci, L.; Ciani, G.; Maggini, S.; Proserpio, D. M.; Visconti, M. *Chem. Eur. J.* **2010**, *16*, 12328–12341.

[16] Zhao, X.; Bu, X.; Wu, T.; Zheng, S.-T.; Wang, L.; Feng, P. *Nat. Commun.* **2013**, *4*, 1–9.

[17] Chen, B.; Wang, L.; Zapata, F.; Qian, G.; Lobkovsky, E. B. *J. Am. Chem. Soc.* **2008**, *130*, 6718–6719.

[18] Chen, B.; Wang, L.; Xiao, Y.; Fronczek, F. R.; Xue, M.; Cui, Y.; Qian, G. *Angew. Chem., Int. Ed.* **2009**, *48*, 500–503.

[19] Xu, H.; Liu, F.; Cui, Y.; Chen, B.; Qian, G. *Chem. Commun.* **2011**, *47*, 3153–3155.

[20] Liu, S.-J.; Huang, Y.; Lin, Z.-J.; Li, X.-F.; Cao, R. *RSC Adv.* **2013**, *3*, 9279–9287.

[21] Kreno, L. E.; Leong, K.; Farha, O. K.; Allendorf, M.; Duyne, R. P. V.; Hupp, J. T. *Chem. Rev.* **2012**, *112*, 1105–1125.

[22] Xiao, Y.; Cui, Y.; Zheng, Q.; Xiang, S.; Qian, G.; Chen, B. *Chem. Commun.* **2010**, *46*, 5503–5505.

[23] Xie, Z.; Ma, L.; deKrafft, K. E.; Jin, A.; Lin, W. *J. Am. Chem. Soc.* **2010**, *132*, 922–923.

[24] Zhao, B.; Chen, X.-Y.; Cheng, P.; Liao, D.-Z.; Yan, S.-P.; Jiang, Z.-H. *J. Am. Chem. Soc.* **2004**, *126*, 15394–15395.

[25] Wong, K.; Law, G.-L.; Yang, Y.-Y.; Wong, W.-T. *Adv. Mater.* **2006**, *18*, 1051–1054.

[26] Rojas, S.; Carmona, F. J.; Maldonado, C. R.; Horcajada, P.; Hidalgo, T.; Serre, C.; Navarro, J. A.; Barea, E. *Inorg Chem* **2016**, *55*, 2650–2663.

[27] Della Rocca, J.; Liu, D.; Lin, W. *Acc. Chem. Res.* **2011**, *44*, 957–968.

[28] Horcajada, P. et al. *Nat. Mater.* **2010**, *9*, 172–178.

[29] Zhou, Y.-L.; Wu, M.-C.; Zeng, M.-H.; Liang, H. *Inorg. Chem.* **2009**, *48*, 10146–10150.

[30] Zeng, M.-H.; Zhang, W.-X.; Sun, X.-Z.; Chen, X.-M. *Angew. Chem., Int. Ed.* **2005**, *44*, 3079–3082.

[31] Zeng, M.-H.; Feng, X.-L.; Zhang, W.-X.; Chen, X.-M. *Dalton Trans.* **2006**, 5294–5303.

[32] Liu, C.-M.; Zhang, D.-Q.; Zhu, D.-B. *Inorg. Chem.* **2009**, *48*, 4980–4987.

[33] Mori, F.; Nyui, T.; Ishida, T.; Nogami, T.; Choi, K.-Y.; Nojiri, H. *J. Am. Chem. Soc.* **2006**, *128*, 1440–1441.

[34] Simard, M.; Su, D.; Wuest, J. D. *J. Am. Chem. Soc.* **1991**, *113*, 4696–4698.

[35] Hoskins, B. F.; Robson, R. *J. Am. Chem. Soc.* **1989**, *111*, 5962–5964.

[36] Goesten, M. G.; Kapteijn, F.; Gascon, J. *CrystEngComm* **2013**, *15*, 9249–9257.

[37] Eddaoudi, M.; Kim, J.; O'Keeffe, M.; Yaghi, O. M. *J. Am. Chem. Soc.* **2002**, *124*, 376–377.

[38] Luebke, R.; Belmabkhout, Y.; Weseliński, Ł. J.; Cairns, A. J.; Alkordi, M.; Norton, G.; Wojtas, Ł.; Adil, K.; Eddaoudi, M. *Chem. Sci.* **2015**, *6*, 4095–4102.

[39] Farha, O. K.; Eryazici, I.; Jeong, N. C.; Hauser, B. G.; Wilmer, C. E.; Sarjeant, A. A.; Snurr, R. Q.; Nguyen, S. T.; Özgür Yazaydin,; Hupp, J. T. *J. Am. Chem. Soc.* **2012**, *134*, 15016–15021.

[40] Hasegawa, S.; Horike, S.; Matsuda, R.; Furukawa, S.; Mochizuki, K.; Kinoshita, Y.; Kitagawa, S. *J. Am. Chem. Soc.* **2007**, *129*, 2607–2614.

[41] Evans, O. R.; Ngo, H. L.; Lin, W. *J. Am. Chem. Soc.* **2001**, *123*, 10395–10396.

[42] Wu, P.; He, C.; Wang, J.; Peng, X.; Li, X.; An, Y.; Duan, C. *J. Am. Chem. Soc.* **2012**, *134*, 14991–14999.

[43] Wang, J.; Lin, Z.; Ou, Y.-C.; Yang, N.-L.; Zhang, Y.-H.; Tong, M.-L. *Inorg. Chem.* **2008**, *47*, 190–199.

[44] Eddaoudi, M.; Kim, J.; Rosi, N.; Vodak, D.; Wachter, J.; O'Keeffe, M.; Yaghi, O. M. *Science* **2002**, *295*, 469–472.

[45] Eddaoudi, M.; Moler, D. B.; Li, H.; Chen, B.; Reineke, T. M.; O'Keeffe, M.; Yaghi, O. M. *Acc. Chem. Res.* **2001**, *34*, 319–330.

[46] Burrows, A. D.; Cassar, K.; Friend, R. M. W.; Mahon, M. F.; Rigby, S. P.; Warren, J. E. *CrystEngComm* **2005**, *7*, 548–550.

[47] Dhakshinamoorthy, A.; Garcia, H. *Chem. Soc. Rev.* **2014**, *43*, 5750–5765.

[48] Ockwig, N. W.; Delgado-Friedrichs, O.; O'Keeffe, M.; Yaghi, O. M. *Acc. Chem. Res.* **2005**, *38*, 176–182.

[49] Rao, C. N. R.; Cheetham, A. K.; Thirumurugan, A. *J. Phys.: Condens. Matter* **2008**, *20*, 0823202.

[50] Roques, N.; Mugnaini, V.; Veciana, J. *Top. Curr. Chem.* **2010**, *293*, 207–258.

[51] Caneschi, A.; Gatteschi, D.; Sessoli, R.; Rey, P. *Acc. Chem. Res.* **1989**, *22*, 392–398.

[52] Maspoch, D.; Ruiz-Molina, D.; Wurst, K.; Rovira, C.; Veciana, J. *Chem. Commun.* **2004**, 1164–1165.

[53] Maspoch, D.; Domingo, N.; Ruiz-Molina, D.; Wurst, K.; Hernandez, J.-M.; G. Vaughan, C. R.; Lloret, F.; Tejada, J.; Veciana, J. *Chem. Commun.* **2005**, 5035–5037.

[54] Maspoch, D.; Ruiz-Molina, D.; Wurst, K.; Domingo, N.; Cavallini, M.; Biscarini, F.; Tejada, J.; Rovira, C.; Veciana, J. *Nat. Mater.* **2003**, *2*, 190–195.

[55] Chui, S. S.; Lo, S. M. F.; Charmant, J. P. H.; Orpen, A. G.; William, I. D. *Science* **1999**, *283*, 1148–1150.

[56] Kurmoo, M. *Chem. Soc. Rev.* **2009**, *38*, 1353–1379.

[57] Fabelo, O.; Canadillas-Delgado, L.; Pasán, J.; Delgado, F. S.; Lloret, F.; Cano, J.; Julve, M.; Ruiz-Pérez, C. *Inorg. Chem.* **2009**, *48*, 11342–11351.

[58] Goodenough, J. B. *Magnetism and the chemical bond*; Interscience(Wiley), 1963.

[59] Mahata, P.; Sarma, D.; Natarajan, S. *J. Chem. Sci.* **2010**, *122*, 19–35.

[60] Davis, M. E. *Nature* **2002**, *417*, 813–822.

[61] Li, H.; Eddaoudi, M.; O'Keeffe, M.; Yaghi, O. *Nature* **1999**, *402*, 276–279.

[62] Rosi, N. L.; Eckert, J.; Eddaoudi, M.; Vodak, D. T.; Kim, J.; O'Keeffe, M.; Yaghi, O. M. *Science* **2000**, *300*, 1127–1129.

[63] van der Berg, A.; Arean, C. *Chem. Commun.* **2008**, *6*, 668–681.

[64] Ma, S.-Q.; Collier, C. D.; Zhou, H.-C. In *Design and Construction of Coordination Polymers*; Hong, M.-C., Chen, L., Eds.; John Wiley & Sons, Inc., Hoboken, NJ, USA, 2009; Chapter 12.

[65] Rowsell, J. L. C.; Yaghi, O. M. *Angew. Chem., Int. Ed.* **2005**, *44*.

[66] US Department of Energy, Office of Energy Efficiency. Renewable Energy and Hydrogen Storage; Fuel Cell Technologies Office Multi-Year Research, Development, And Demonstration Plan. 2015; http://energy.gov/sites/prod/files/2015/05/f22/fcto_myrdd_storage.pdf.

[67] Furukawa, H.; Go, Y. B.; Ko, N.; Park, Y. K.; Uribe-Romo, F. J.; Kim, J.; O'Keeffe, M.; Yaghi, O. M. *Inorg Chem* **2011**, *50*, 9147–9152.

[68] Yao, Q.; Bermejo Gomez, A.; Su, J.; Pascanu, V.; Yun, Y.; Zheng, H.; Chen, H.; Liu, L.; Abdelhamid, H. N.; Martin-Matute, B.; Zou, X. *Chem. Mater.* **2015**, *27*, 5332–5339.

BIBLIOGRAPHY

[69] Kesanli, B.; Cui, Y.; Smith, M. R.; Bittner, E. W.; Bockrath, B. C.; Lin, W. *Angew. Chem., Int. Ed.* **2004**, *44*, 72–75.

[70] Chen, B.; Eddaoudi, M.; Hyde, S. T.; O'Keeffe, M.; Yaghi, O. M. *Science* **2001**, *291*, 1021–1023.

[71] Ma, L.; Lin, W. *Angew. Chem.,* **2009**, *48*, 3637–3640.

[72] Zhang, J.; Liu, R.; Feng, P.; Bu, X. *Angew. Chem., Int. Ed.* **2007**, *46*, 8388–8391.

[73] Hao, X.-R.; Wang, X.-L.; Su, Z.-M.; Shao, K.-Z.; Zhao, Y.-H.; Lana, Y.-Q.; Fu, Y.-M. *Dalton Trans.* **2009**, 8962–8966.

[74] Yang, S.; Lin, X.; Blake, A. J.; Walker, G. S.; Hubberstey, P.; Champness, N. R.; Schröder, M. *Nat. Chem.* **2009**, *1*, 487–493.

[75] Li, Z.-J.; Khani, S. K.; Akhbari, K.; Morsali, A.; Retailleau, P. *Microporous Mesoporous Mater.* **2014**, *199*, 93–98.

[76] Quartapelle Procopio, E.; Linares, F.; Montoro, C.; Colombo, V.; Maspero, A.; Barea, E.; Navarro, J. A. R. *Angew. Chem.* **2010**, *122*, 7466–7469.

[77] Tan, Y.-X.; He, Y.-P.; Zhang, J. *Chem. Commun.* **2011**, *47*, 10647.

[78] Chen, S.; Zhang, J.; Wu, T.; Feng, P.; Bu, X. *J. Am. Chem. Soc.* **2009**, *131*, 16027–16029.

[79] Genna, D. T.; Wong-Foy, A. G.; Matzger, A. J.; Sanford, M. S. *J. Am. Chem. Soc.* **2013**, *135*, 10586–10589.

[80] Beheshti, S.; Morsali, A. *RSC Adv.* **2014**, *4*, 41825–41830.

[81] An, J.; Shade, C. M.; Chengelis-Czegan, D. A.; Petoud, S.; Rosi, N. L. *J. Am. Chem. Soc.* **2011**, *133*, 1220–1223.

[82] Qin, J.-S.; Zhang, S.-R.; Du, D.-Y.; Shen, P.; Bao, S.-J.; Lan, Y.-Q.; Su, Z.-M. *Chem. Eur. J.* **2014**, *20*, 5625–5630.

[83] Guo, H.; Zhu, Y.; Wang, S.; Su, S.; Zhou, L.; Zhang, H. *Chem. Mater.* **2012**, *24*, 444–450.

[84] Li, P.-Z.; Wang, X.-J.; Li, Y.; Zhang, Q.; Tan, R. H. D.; Lim, W. Q.; Ganguly, R.; Zhao, Y. *Microporous Mesoporous Mater.* **2013**, *176*, 194–198.

[85] Zhang, Z.; Zaworotko, M. J. *Chem. Soc. Rev.* **2014**, *43*, 5444–5455.

[86] Seoane, B.; Dikhtiarenko, A.; Mayoral, A.; C. Tellez, J. C.; Kapteijn, F.; Gascon, J. *CrystEngComm* **2015**, *17*, 1693–1700.

[87] Bajpe, S. R.; Kirschhock, C. E. A.; Aerts, A.; Breynaert, E.; Absillis, G.; Parac-Vogt, T. N.; Giebeler, L.; Martens, J. A. *Chem. Eur. J.* **2010**, *16*, 3926–3932.

[88] Diring, S.; Furukawa, S.; Takashima, Y.; Tsuruoka, T.; Kitagawa, S. *Chem. Mater.* **2010**, *22*, 4531–4538.

[89] Gedrich, K.; Senkovska, I.; Klein, N.; Stoeck, U.; Henschel, A.; Lohe, M. R.; Baburin, I. A.; Mueller, U.; Kaskel, S. *Angew. Chem. Int. Ed.* **2010**, *49*, 8489–8492.

[90] Nelson, A.; Farha, O.; Mulfort, K.; Hupp., J. *J. Am. Chem. Soc.* **2009**, *131*, 458–460.

[91] Farha, O. K.; Hupp, J. T. *Acc. Chem. Res.* **2010**, *43*, 1166–1175.

[92] Mallegol, T.; Gmouh, S.; Meziane, M.; Blanchard-Desce, M.; Mongin, O. *Synthesis* **2005**, 1771–1774.

[93] Shirota, Y.; Kuwabara, Y.; Inada, H.; Wakimoto, T.; Nakada, H.; Yonemoto, Y.; Kawami, S.; Imai, K. *Appl. Phys. Lett.* **1994**, *65*, 807–809.

[94] Stickley, K. R.; Blackstock, S. *Tetrahedron Lett.* **1995**, *36*, 1585–1588.

[95] Sreenath, K.; Suneesh, C. V.; Kumar, V. K. R.; Gopidas, K. R. *J. Org. Chem.* **2008**, *73*, 3245–3251.

[96] Quinton, C.; Alain-Rizzo, V.; Dumas-Verdes, C.; Miomandr, F.; Audebert, P. *Electrochim. Acta* **2013**, *110*, 693–701.

[97] Yao, C.-J.; Zhong, Y.-W.; Yao, J. *Inorg. Chem.* **2013**, *52*, 10000–10008.

[98] Jin, B.; Liu, P.; Wang, Y.; Zhang, Z.; Tian, Y.; Yang, J.; Zhang, S.; Cheng, F. *J. Phys. Chem. B* **2007**, *111*, 1517–1522.

[99] Morrison, W. H.; Krogsrud, S.; Hendrickson, D. N. *Inorg. Chem.* **1973**, *12*, 1998–2004.

[100] Thommes, M.; Kaneko, K.; Neimark, A. V.; Olivier, J. P.; Rodriguez-Reinoso, F.; Rouquerol, J.; Sing, K. S. W. *Pure Appl. Chem.* **2015**, *87*, 1051–1069.

[101] Sing, K. S. W.; Everett, D. H.; Haul, R. A. W.; Moscou, L.; Pierotti, R. A.; Rouquerol, J.; Siemieniewska, T. *Pure & Appl. Chem. Vol.* **1985**, *57*, 603–619.

[102] QUANTACHROME, Application of QSDFT (Quenched Solid Density Functional Theory) - A novel density functinal theory for an accurate pore size analysis of disordered porous carbons.

[103] Ding, B.-B.; Weng, Y.-Q.; Mao, Z.-W.; Lam, C.-K.; Chen, X.-M.; Ye, B.-H. *Inorg. Chem.* **2005**, *44*, 8836–8845.

[104] Blatov, V. A.; Shevchenko, A. P.; Proserpio, D. M. *Cryst. Growth Des.* **2014**, *14*, 3576–3586.

[105] Yao, M.-X.; Zeng, M.-H.; Zou, H.-H.; Zhou, Y.-L.; Liang, H. *Dalton Trans.* **2008**, 2428–2432.

[106] Liu, Y.; Li, H.; Han, Y.; Lv, X.; Hou, H.; Fan, Y. *Cryst. Growth Des.* **2012**, *12*, 3505–3513.

[107] Chae, H. K.; Kim, J.; Friedrichs, O. D.; O'Keeffe, M.; Yaghi, O. M. *Angew. Chem. Int. Ed.* **2003**, *42*, 3907–3909.

[108] Hao, X.-R.; Wang, X.-L.; Shao, K.-Z.; Yang, G.-S.; Su, Z.-M.; Yuan, G. *CrystEngComm* **2012**, *14*, 5596.

[109] Zhang, B.; Zhang, J.; Liu, C.; Sang, X.; Peng, L.; Ma, X.; Wu, T.; Han, B.; Yang, G. *RSC Adv.* **2015**, *5*, 37691–37696.

[110] Márquez-Alvarez, C.; Žilková, N.; Pérez-Pariente, J.; Čejka, J. *Catal. Rev.: Sci. Eng.* **2008**, *50*, 222–286.

[111] Yuan, Q.; Yin, A.-X.; Luo, C.; Sun, L.-D.; Zhang, Y.-W.; Duan, W.-T.; Liu, H.-C.; Yan, C.-H. *J. Am. Chem. Soc.* **2008**, *130*, 3465–3472.

[112] May, M.; Navarrete, J.; Asomoza, M.; Gomez, R. *J. Porous Mater.* **2007**, *14*, 159–164.

[113] Tadanaga, K.; Ito, S.; Minami, T.; Tohge, N. *J Non-Cryst Solids* **1996**, *201*, 231–236.

[114] wook Jun, Y.; sil Choi, J.; Cheon, J. *Angew. Chem. Int. Ed.* **2006**, *45*, 3414–3439.

[115] Park, J.; Joo, J.; Kwon, S.; Jang, Y.; Hyeon, T. *Angew. Chem. Int. Ed.* **2007**, *46*, 4630–4660.

[116] Pinna, N.; Niederberger, M. *Angew. Chem. Int. Ed.* **2008**, *47*, 5292–5304.

[117] Garnweitner, G.; Niederberger, M. *J. Am. Ceram. Soc.* **2006**, *89*, 1801–1808.

[118] Mohammadnezhad, G.; Amini, M. M.; Khavasi, H. R. *Dalton Trans.* **2010**, *39*, 10830.

[119] Jolivet, J.-P.; Froidefond, C.; Pottier, A.; Chanéac, C.; Cassaignon, S.; Tronc, E.; Euzen, P. *J. Mater. Chem.* **2004**, *14*, 3281–3288.

List of abbreviations

_t_Bu   _tert_-butyl

BET   Brunauer–Emmet–Teller

CPs   Coordination polymers

DMF   dimethylformamide

Hdaba 4-(diphenylamino)benzoic acid

Hmaba 4-(bis(4-methoxyphenyl)amino)benzoic acid

Htaba 4-(bis(4-tolylphenyl)amino)benzoic acid

Hteaba 4-(bis(4-tert-butylphenyl)amino)benzoic acid

MOFs   metal–organic frameworks

PCPs   porous coordination polymers

QSDFT Quenched solid density functional theory

SBUs   secondary building units

SMM   single-molecular magnetism

TBP   tetraphenylbenzidine

List of publications

Publications

These are the articles included within the scope of this thesis including those about to be submitted.

- **Isophthalic acid modulated synthesis of a neutral Co(II) nitrilotribenzoic acid MOF: Magnetic and sorption properties.** Oluseun Akintola, Axel Buchholz, Helmar Görls, and Winfried Plass *Eur. J. Inorg. Chem.* **2017**. *In preparation*

- *p*-**Substituent dependent redox behaviour of four 4,4'-disubstituted monocarboxyl-triphenylamine ligands and their copper(II) complexes.** Oluseun Akintola, Manfried Rudolph, Axel Buchholz, Helmar Görls, and Winfried Plass *Chem. - Eur. J.*, **2018** *Submitted.*

- **Solvent-dependent selective cation exchange in anionic frameworks based on cobalt(II) and triphenylamine linkers: reactor-dependent synthesis and sorption properties.** Oluseun Akintola, David Hornig, Axel Buchholz, Helmar Görls, and Winfried Plass *Dalton Trans.*, **2017**, 46, 8037–8050.

- **Robust anionic pillared-layer framework based on triphenylamine-based linkers: ion exchange and counterion dependent sorption properties.** Oluseun Akintola, Sven Ziegenbalg, Axel Buchholz, Helmar Görls, and Winfried Plass *CrystEngComm*, **2017**, 19, 2723–2732.

- **A facile, green and efficient surfactant-free method for synthesis of aluminum nanooxides with an extraordinary high surface area.** Gholamhossein Mohammadnezhad, Oluseun Akintola, Winfried Plass, Frank Steiniger and Martin Westermann *Dalton Trans.*, **2016**, *45*, 6329–6333.

- **Facile synthesis of highly thermally stable nanoporous γ-aluminas from aluminum alkoxide precursors.** Gholamhossein Mohammadnezhad, Oluseun Akintola, Winfried Plass, Felix H. Schacher, Frank Steiniger and Martin Westermann *RSC Adv.*, **2015**, *5*, 49493–49499.

Other peer-reviewed publications

These are the articles not included within the scope of this thesis

- **Size-dependent self-assembly of Lanthanide-based coordination frameworks with phenanthroline-2,9-dicarboxylic acid as pre-organized ligand in hybrid materials.** Mahboubeh Alipour, <u>Oluseun Akintola</u>, Axel Buchholz, Masoud Mirzaei, Hossein Eshtiagh-Hosseini, Helmar Görls, and Winfried Plass *Eur. J. Inorg. Chem*, **2016** *2016*, 5356–5365.

- **The specific surface versus electrochemically active area of the carbon/polypyrrole capacitor: the correlation of ion dynamics studied by an electrochemical quartz crystal microbalance with BET surface.** Heike L.K.S. Mosch, <u>Oluseun Akintola</u>, Winfried Plass, Stephanie Hoeppener, Ulrich S. Schubert, Anna Ignaszak *Langmuir*, **2016**, *32*, 4440–4449.

Public Talks

- Oct. 17-21, **2015**:
  16th International seminar of Phd students on organometallic and coordination chemistry, Lichtenfels, Germany.

- Mar. 22-24, **2015**:
  Deutsches Koordinationschemie-Treffen, Paderborn, Germany.

- Sep. 11, **2014**:
  12th Mitteldeutches Anorganicker Nachwuchssymposium, Chemnitz, Germany.

Acknowledgements

The completion of this dissertation would not have been possible without the huge support which I have received from so many people over the years. I therefore wish to express my deepest and most heartfelt appreciation to the following people.

First and foremost, my sincere gratitude goes to my supervisor, Prof. Dr. Winfried Plass for his constant support during my program and in particular for his patience and motivation in this period. His guidance was extremely invaluable while carrying out the research and writing of this thesis. I can not imagine having a better supervisor and mentor for my Ph.D study.

Special thanks also goes to Dr Axel Buchholz for his help throughout the project. Your advice during the times when I had to pick your brains on issues when I needed a different pair of eyes were invaluable. I also enjoyed immensely all our educational trips around Germany.

Since money is the lifeblood of scientific research and without it none of what we do would be possible. I would therefore like to express my deep appreciation to the Evangelisches Studienwerk for my scholarship. I wish to thank also the Graduierten Akademie for the Kurzzeit Stipendium.

I would like to also thank all scientific and technical employees of the Chemistry institutes at the University of Jena for the different analyses. I would not have been able to achieve this without you all. In particular, I would mention the NMR team for the timely measurements, Mr. Florian Reinhardt and Dr. Axel Buchholz (again!) for the TGA, ESR and SQUID measurements as well as treatment of the results. Special thanks to Ms. Antje Wermann for being patient with me and my constant requests for more powder XRD measurements as well as the prompt responses. Dr. Helmar Görls deserves special mention too, for his aid in deciphering the complicated crystal structures of my coordination polymers.

As for my colleagues in the work group (Sofia, Michael, Svenchen, Benjamin), I confess that I was fortunate to work alongside you, you were all simply great. Thank you also for the fun memories and I will treasure every single one of them. Specifically, thanks to Svenchen and Micha for your assistance in proof-reading the German translation of the summary of my work. I thank the rest of the group also for the genial atmosphere as well, you really helped me settle down to life in Germany. I also want to

remember all the interns who worked alongside me (Zuhartze, Robert, Ferenc), you guys were great.

I reserve my deep gratitude to my family and friends, for the emotional support and backing. I do not make light of your prayers and good wishes throughout my time here.

Special thanks to my dear little daughter, for taking care of her mom like she promised to.☺ Most importantly, I wish to appreciate my wife, Tope. She was my backbone as well as a listening ear and available shoulder when I needed to vent or cry. It is no exaggeration when I say she was one force that kept me fired at times when I felt like turning back. Thank you for your support and for taking care of our little one when I was not there. None of this would have been possible without you.

Declaration of authorship/Selbstständigkeitserklärung

I certify that the work presented here is, to the best of my knowledge and belief, original and the result of my own investigations, except as acknowledged, and has not been submitted, either in part or whole, for a degree at this or any other university.

Ich erkläre, dass ich die vorliegende Arbeit selbstständig und nur unter Verwendung der angegebenen Hilfsmittel, persönlichen Mitteilungen und Quellen angefertigt habe und dass ich nicht die gleiche, eine in wesentlichen Teilen ähnliche oder eine andere Abhandlung bei einer anderen Hochschule als Dissertation eingereicht habe.

Jena,

———————————————

Oluseun Akintola

Publications

Publication 1

Metal Bonded Triarylamines and their Interactions: Synthesis, Structure, and Redox Properties of Paddle-Wheel Copper Complexes

Oluseun Akintola, Michael Böhme, Manfred Rudolph, Axel Buchholz, Helmar Görls, and Winfried Plass
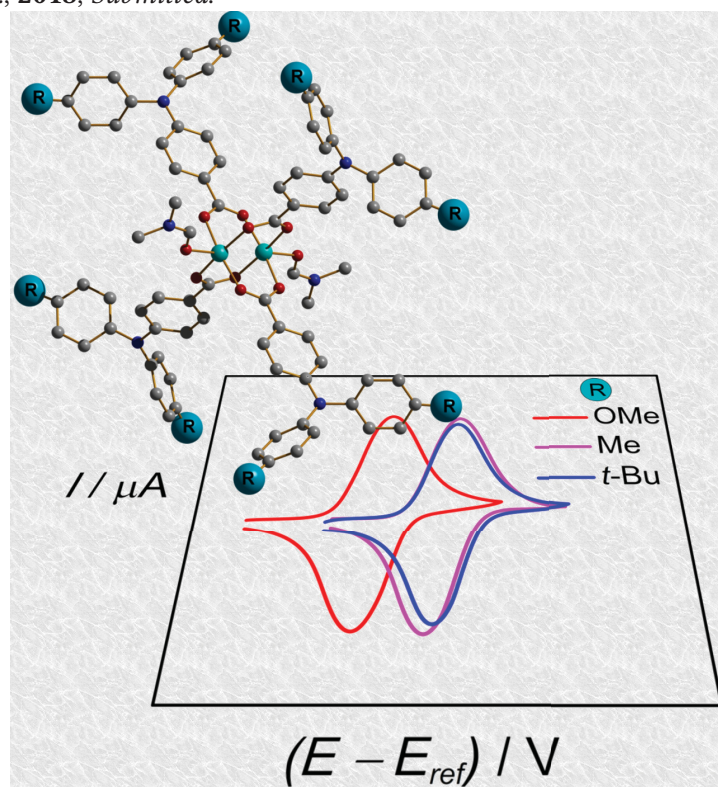
Metal Bonded Redox-Active Triarylamines and their Interactions: Synthesis, Structure, and Redox Properties of Paddle-Wheel Copper Complexes

Oluseun Akintola, Michael Böhme, Manfred Rudolph, Axel Buchholz, Helmar Görls, and Winfried Plass$*$[a]

[a] Dr. O. Akintola, M. Böhme, Dr. M. Rudolph, Dr. A. Buchholz, Dr. H. Görls, Prof. Dr. W. Plass
   Institut für Anorganische und Analytische Chemie
   Friedrich-Schiller-Universität Jena
   Humboldtstr. 8
   07743 Jena, Germany
   E-mail: sekr.plass@uni-jena.de

Abstract: Four new triphenylamine ligands with different substituents in para-position and the corresponding copper(II) complexes are reported. This includes their structural, spectroscopic, magnetic, and electrochemical properties. The complexes posses a dinuclear copper(II) paddle-wheel core, a building unit also common in metal-organic frameworks (MOFs). Electrochemical measurements demonstrate that the triphenylamine ligands and the corresponding complexes are susceptible to oxidation resulting in the formation of stable radical cations. The square-wave voltammograms observed for the complexes are similar to those of the ligands, except for a slight shift in potential. Square-wave voltammetry data shows that in the complexes these oxidations can be described as individual one-electron processes centered on the coordinated ligands. Spectroelectrochemistry reveals that during the oxidation of the complexes no difference can be detected for the spectra of successively oxidized species. For the absorption bands of the oxidized species of the ligands and complexes only a slight shift is observed. ESR spectra for the chemically oxidized complexes indicate ligand centered radicals. The copper ions of the paddle-wheel core are strongly antiferromagnetic coupled. DFT calculations for the fully oxidized complexes indicate a very weak ferromagnetic coupling between the copper ions and the ligand radicals, whereas a very weak antiferromagnetic coupling is found among the ligand radicals.

Introduction

Triphenylamine-based molecules and their derivatives are a class of compounds widely studied due to their importance for the design of electronic materials,[1] which is particularly related to their pronounced hole-transport ability.[2] This fact coupled with the relatively low ionization potentials of triarylamines has led to their extensive application in electroluminescent devices as well as in photovoltaic materials.[3] Triarylamines typically undergo oxidation with ease resulting in the formation of a stable triarylammonium radical cation, the stability of which depends on whether a *para* substitution at the aromatic rings is present or not.[4] For the cases of triphenylamines with an unsubstituted *para* position, these radicals are known to undergo dimerization to give tetraphenylbenzidines in a well-known oxidative coupling process. However, for the substituted derivatives a reversible redox behavior is observed, which can be tuned by varying the substituents attached to the aromatic rings in particularly at the *para* positions.[5] Moreover, the molecular framework of triarylamines is also known to possess structural flexibility, which when coupled together with bulky substituents can lead to distortion or rotation within its structure.[6]

The unique electronic character of the triphenylamine moiety has led to its incorporated into ligand frameworks. This allows for interesting combinations of electronic and photophysical properties leading to new materials with appealing characteristics.[7] In particular, transition metal complexes with triphenylamine based ligands have been used to investigate the charge transfer properties of mixed valance systems.[8] In the latter cases, the well-known dinuclear paddle-wheel motif $M_2(RCOO)_4$ was used in combination with carboxylate functionalized triphenylamine ligands. Moreover, this paddle-wheel motif is a common building unit for microporous coordination polymers the so-called metal-organic frameworks (MOFs).[9] In particular, the dinuclear paddle-wheel fragment found in copper(II) acetate,[10] which can be regarded as an archetype for such building units, has been extensively utilized in MOFs since the seminal report on HKUST-1.[11] Such copper-based MOF systems are attracting significant interest and have been intensively investigated towards their electronic structure and other properties as well as potential applications.[12] On the other hand, 4,4′,4″-nitrilotribenzoic acid (H_3ntb), a carboxylate derivative of triphenylamine, has found extensive use as linker in the construction of MOFs.[13] The molecular properties of the ntb^{3-} linker result in characteristic redox- and photo-active behavior of the corresponding MOFs which has led to specific applications such as sensing, catalysis, and generation of nanoparticles for hydrogen storage.[14−16] In fact, MOFs containing redox-active linkers of different type have been recently addressed toward their electrochemical behavior[17] and it could be shown that this can be used to control the properties of the corresponding frameworks.[18] Moreover, the combination of ntb^{3-} with ditopic linkers has been employed in the coordination copolymerization approach leading to multicomponent MOFs with interesting architectures including pillared-layer frameworks.[19] In this context, it should also be mentioned that extended triphenylamine-based linkers with two nitrogen centers have been utilized in the construction of MOFs with unusual architectures and properties.[20−22] In addition, also the generation of MOFs based on a branched triphenylamine-based linker with even four nitrogen centers has been described.[23]

In this contribution, we present molecular model systems for the interaction of the copper paddle-wheel moiety with triphenylamine-based ligands. For this purpose, the synthesis and characterization of

four complexes of the general formula $[Cu_2(L)_4(dmf)_2]$ with ligands derived from 4-(diphenylamino)benzoic acid is reported. Of particular interest here is the redox behavior of the triphenylamine moiety and its interaction with the dinuclear core. This is investigated in view of the electronic and steric variation of the substituent at the *para* positions of the phenyl groups of the 4-(diphenylamino)benzoic acid ligand (R = H, Me, *t*-Bu, and OMe). To this end, electrochemical, structural, and magnetic properties are reported and complemented by theoretical calculations.

Results and Discussion

Synthesis and characterization

The ligand 4-(diphenylamino)benzoic acid (Haba, **1**) was obtained in a two-step synthetic route. In the first step, the formylation of triphenylamine was performed through the Vilsmeier-Haack reaction using phosphoryl chloride in dimethylformamide.[24] The resulting aldehyde was subsequently oxidized with $KMnO_4$ under alkaline conditions followed by acidification of the resultant potassium salt using concentrated aqueous HCl according to a modified published procedure for the 4,4′-(phenylazanediyl)dibenzoic acid (see Scheme 1).[25]
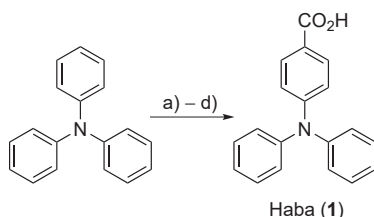
Scheme 1. Synthesis of 4-(diphenylamino)benzoic acid (Haba, **1**): (a) $POCl_3$, dmf, 0 °C; (b) reflux under N_2 for 22 h; (c) K_2CO_3, $KMnO_4$, acetone, reflux, 12 h; (d) HCl.

On the other hand, the ligands with substituents at the *para* position of the two phenyl rings, namely 4-(bis(4-methylphenyl)amino)benzoic acid (Haba-Me, **2**), 4-(bis(4-*tert*-butylphenyl)amino)benzoic acid (Haba-tBu, **3**), and 4-(bis(4-methoxyphenyl)amino)benzoic acid (Haba-OMe, **4**) were obtained via a Buchwald−Hartwig palladium catalyzed coupling reaction. For each ligand its bromophenyl precursor (4-bromotoluene, 4-*tert*-butylbromobenzene, and 4-bromoanisole for **2**, **3**, and **4**, respectively) was combined with methyl 4-aminobenzoate while using Cs_2CO_3 as base. The resultant ester was subsequently subjected to alkaline hydrolysis followed by acidification with concentrated aqueous HCl (see Scheme 2).[26]

The synthesis of the copper complex $[Cu_2(aba)_4(dmf)_2]$ (**5**) was performed by a solvothermal process in dmf using copper(II) nitrate. The use of acetonitrile was avoided due to its reported tendency to aid oxidation of triphenylamines in the presence of copper(II) ions, which in turn leads to the formation of the benzidine derivative.[27] An alternative route to synthesize **5** is given by reacting the ligand and copper(II) nitrate in ethanol. By layering the resultant solution with dmf it was possible to obtain green crystals of **5** within a period of 2−3 weeks. Both routes led to good quality crystals suitable for
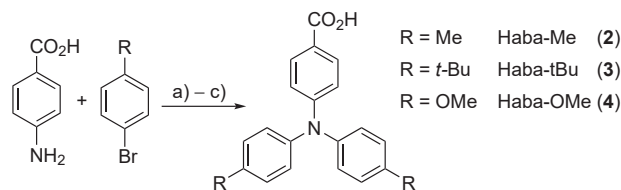
Scheme 2. Preparation scheme for **2-4**; (a) Pd/P(*t*-Bu)$_3$, Cs$_2$CO$_3$, toluene, 110 °C, 5−7 d; (b) KOH, MeOH, reflux; (c) HCl.

X-ray crystallographic studies. Similarly also the complex [Cu$_2$(aba-Me)$_4$(dmf)$_2$] (**6**) was prepared via the solvothermal route, which yielded a light green solution. To reduce the solubility of the product methanol was slowly layered on top of the obtained solution, which was allowed to stand for a few hours, upon which a light green precipitate formed. Additional material as green block crystals was obtained from the filtrate after it was left standing for slow evaporation. An alternative route to **6** was established by heating a solution of both the ligand and copper(II) nitrate in dmf at 110 °C for 30 min. Subsequent cooling of the reaction solution and allowing it to stand for a few days resulted in the formation of micro-crystalline product, which was unfortunately not suitable for X-ray crystallography. This latter route of simply refluxing a mixture of the metal salt and ligand in dmf was successfully used in the synthesis of the complex [Cu$_2$(aba-tBu)$_4$(dmf)$_2$] (**7**), yielding crystalline material also suitable for X-ray structure determination. For the complex [Cu$_2$(aba-OMe)$_4$(dmf)$_2$] (**8**) again the solvothermal route similarly to **5** and **6** was employed for the synthesis. However, this only led to the formation of dark green micro crystals which were not suitable for single crystal X-ray studies. Nevertheless, crystals suitable for X-ray studies were obtained by stirring both ligand and metal salt in dmf for about 20 min followed by slowly layering methanol on top of this solution. Both solvents were then allowed to slowly evaporate over 4 weeks to yield green crystals of **8**.

The composition of the obtained bulk material for compounds **5**−**8** was analyzed by elemental and thermogravimetric analysis, which revealed the presence of varying amounts of different solvent molecules of crystallization. The corresponding data is given in Figure S1 and Table S1.

X-ray crystal structures

The crystallographic characterization reveals that all four complexes **6**−**8** crystallize in the triclinic space group P1̄ (see Table S2 for details). The molecular structure of **5** depicted in Figure 1 is representative of the other isostructural complexes **6**−**8** and shows that a dimeric paddle-wheel arrangement is adopted. As the center of the paddle-wheel dimers, for the crystal structures of all complexes, is situated on a crystallographic inversion center, only half of the complex molecules are within the asymmetric units. A comparison of the selected bond lengths in all four complexes is summarized in Table S3 and additional representations of the molecular structures of **6**−**8** including full labeling are given in Figures S2−S5.

The molecular structure consists of four bridging carboxylate ligands and two axial coordinated dmf ligands at the two copper(II) ions as shown in Figure 1. Each copper ion is coordinated by four oxygen atoms from different carboxylate groups in the equatorial plane with distances at around 196 pm. The

5
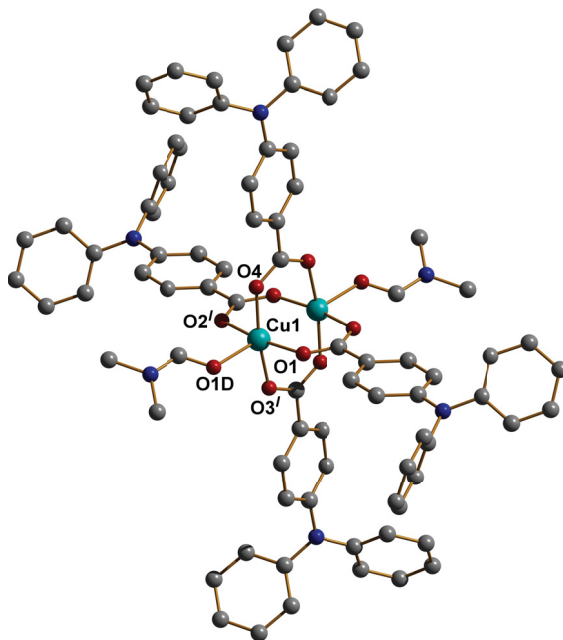
Figure 1. Molecular structure of **5** with hydrogen atoms omitted for clarity.

carboxylate C−O bond lengths are close to 126 pm, while the Cu···Cu distances are at about 260 pm. Together with the oxygen donor of the coordinating dmf molecule in the axial position at a distance of about 216 pm (Cu1−O1D, see Table S3) this leads to a square pyramidal coordination geometry. For all complexes the copper centers are displaced by about 18 pm from the basal [O_4] plane towards the dmf oxygen donor atom.

The phenyl rings of the triphenylamine moieties in the complexes are twisted out of the plane of the central nitrogen atom (cf. Figure S6). This is enforced by repulsion between the phenyl rings and packing effects, leading to corresponding angles ϕ within the range form 21 to 65° (see Table S4). Moreover, also the planarity at the central nitrogen atom varies considerably (average distance of the nitrogen atom from the plane: 3.4, 5.9, 7.1, and 13.9 pm for **5**, **6**, **7**, and **8**, respectively; cf. Table S4), which is most likely also indicative for electronic effects of the substituents at the *para* position. In contrast, the dihedral angle between the carboxylate group coordinating the central paddle-wheel unit and the connected phenyl group (see Figure S7) shows a considerably smaller variation within the range from 5.2 to 27.8°, consistent with an overall reduced influence of the above mentioned effects. As expected the four nitrogen centers of the triphenylamine moieties show an almost rectangular planar arrangement with N···N distances of about 1160 pm along the edges with the largest variation observed for **8** (1088.0 and 1234.6 pm), while the diagonal distances are approximately 1647 pm (see Figure S8 and Table S5).[28]

The powder diffraction measurements carried out on bulk material for all four complexes displayed agreement with the simulated patterns obtained from the single crystal X-ray measurements (see Figure S9).
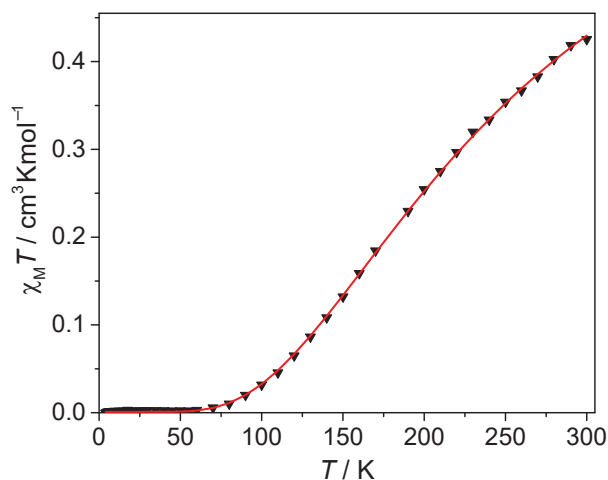
Figure 2. Temperature dependence of the magnetic susceptibility $\chi_M T$ for complex **5** measured at an applied field of 2 kOe. The solid red line represents the best fit.

Table 1. Parameters obtained from fitting the magnetic susceptibility data of **5−8** with corresponding data obtained from theoretical calculations (vide infra).

	g	J_{exp} / cm^{-1}	J_{calcd} / cm^{-1}
5	2.14	−321	−345
6	2.12	−295	−351
7	2.18	−330	−336, −346[a]
8	2.23	−320	−345

[a] The single-crystal structure of **7** contains a disorder for the dmf co-ligands at the copper(II) centers.

Magnetic properties

The magnetic susceptibility data for the complexes **5−8** were obtained in the temperature range from 4 to 300 K. Figure 2 shows the representative data for complex **5** as temperature-dependent plot of $\chi_M T$ (for data of **6−8** see Figure S10). The $\chi_M T$ values at 300 K for the four complexes **5−8** are about 0.46 cm^3 K mol^{-1}, which is only slightly above half the spin-only value of 0.75 cm^3 K mol^{-1} expected for two independent copper(II) ions.[29] Upon lowering the temperature the $\chi_M T$ value decreases to very small values in all cases at a temperature of about 70 K indicating a diamagnetic ground state. Overall, this behavior is consistent with antiferromagnetic exchange coupling between the copper(II) centers of the paddle-wheel moeity.[30] The experimental data were fitted using the program PHI[31] applying the Heisenberg Hamiltonian $\hat{\mathcal{H}} = -J\hat{S}_1\hat{S}_2$. The best fit is obtained for the parameters given in Table 1. The resulting exchange coupling constants of the four complexes are virtually invariant with respect to the type of substituent present at the *para* positions of the phenyl groups of the triphenylamine ligand moieties.

To corroborate the experimental data and to gain further insight with respect to the coupling constants we have performed broken-symmetry DFT (BS-DFT) calculations for the complexes **5−8**. The

corresponding results are included in Table 1 (for detailed data see Table S6). The BS-DFT calculations confirm the strong antiferromagnetic coupling between the copper centers of the paddle-wheel unit obtained by simulating the experimental data. This strong antiferromagnetic exchange interactions are a result of the congruent alignment of the square planar coordination environment of the two copper(II) centers in the complexes which are bridged by four aryl carboxylates. Nevertheless, the calculated coupling constants slightly overestimate the experimental values, where the largest deviation is found for **6** ($J_{exp} = -295\,\mathrm{cm}^{-1}$; $J_{calcd} = -351\,\mathrm{cm}^{-1}$). Moreover, only a small variation within the calculated coupling constants can be found ($|J| = 336-351\,\mathrm{cm}^{-1}$) indicating a negligible electronic effect of the different substituents present in the ligand backbone. In fact, the observed variation based on the structural disorder of the dmf co-ligands in **7** is with $10\,\mathrm{cm}^{-1}$ (**7**(A): -336; **7**(B): $-346\,\mathrm{cm}^{-1}$) in the same range as the observed variation overall complexes **5**−**8**. Spin density plots for the high-spin and broken-symmetry state of the complexes **5**−**8** (see Figures S11−S14) show that the spin density in all complexes is primarily localized on the paddle-wheel core, i.e. in the $d_{x^2-y^2}$ magnetic orbitals of the copper(II) ions. This further supports the idea of negligible electronic effects of the *para* substituents at the triphenylamine moiety.

To further investigate the effect of the triphenylamine moieties and their attached *para* substituents on the exchange coupling within the dicopper core unit two additional structurally reduced models have been used for BS-DFT calculations. In the medium model (**5**^{M}−**8**^{M}) the *para* substituted phenyl groups at the bridging aminobenzoates have been replaced by methyl groups, whereas in the small model (**5**^{S}−**8**^{S}) the amine substituent at the bridging benzoates have been completely removed and replaced by hydrogen atoms. For both reduced models the structural parameters are based on the crystal structures of the complexes **5**−**8**. The corresponding results summarized in Tables S7 and S8 show that both reduced models can reproduce the strong antiferromagnetic coupling obtained form the calculations for the full complexes. Interestingly, the results from both reduced models differ with a mean value less than $3\,\mathrm{cm}^{-1}$ from the values obtained for the calculations based on the original structure of the complexes **5**−**8**, with two slightly larger deviations observed for **6**^{S} ($6\,\mathrm{cm}^{-1}$) and **8**^{S} ($4\,\mathrm{cm}^{-1}$). This further indicates that neither the substitution pattern at the triphenylamine moieties nor the amino groups as such at the bridging benzoate groups have a significant effect on the exchange coupling between the copper(II) centers of the paddle-wheel unit.

Electrochemical properties

The cyclic voltammogram of ligand **1** is indicative for an irreversible process with a single peak in the anodic scan, corresponding to the oxidation of monomeric species to radical cations, which subsequently dimerize to from a tetraphenylbenzidine (TPB) dication.[32] In the following cathodic scan two reduction peaks were observed, which can be attributed to the reduction of the TPB dication to the monocation and then further to the neutral dimer (see Figure S15).[33] The same behavior was likewise seen for complex **5** and is consistent with reported triphenylamine systems that have an attached *para* substituent only at one of the phenyl rings.[34] The observed tendency to dimerize unfortunately hampered any further detailed studies on these systems.

For the analogous *para* substituted ligands **2**−**4** square-wave voltammetry measurements were carried out. The absence of the oxidative coupling reaction due to the occupied *para* positions allows for the observation of more detailed features related to the electron transfer process in these cases. The oxidation of the ligands **2**−**4** can be described in terms of single quasi-reversible one-electron oxidation steps. The underlying mechanism for the simulation of the recorded square-wave voltammetric data is given in Equations (1) and (2), where E° is the standard potential, k_s the heterogeneous rate constant, α the charge-transfer parameter, D the diffusion coefficient, and k_f the rate constant for the subsequent chemical reaction.

$$\text{HL}^+ + \text{e}^- \rightleftharpoons \text{HL} \qquad (E^\circ,\ k_s,\ \alpha,\ D) \tag{1}$$

$$\text{HL}^+ \rightarrow \text{P} \qquad\qquad (k_f) \tag{2}$$
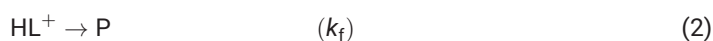
The data obtained from simulation are summarized in Table 2. The reported standard potentials E° are assigned to the half-wave potentials derived form square-wave voltammetry. This assignment is justified by approximately equal diffusion coefficients of the oxidized and reduced species,[35] which was confirmed by cyclic voltammetric studies at a platinum disk electrode ($\varnothing = 10\,\mu$m). Moreover, the charge-transfer parameter was assumed to be $\alpha = 0.5$, since varying this parameter over the range $0.45 \leq \alpha \leq 0.55$ has only a negligible small effect on the standard deviation between simulated and experimental curves. It should be noted that the k_f values reported in Table 2 are not only minimizing the difference between experimental and simulated square-wave voltammograms, but also the difference between experimental and simulated thin-layer cyclic voltammograms measured in the course of the spectroelectrochemical experiments (vide infra). A thorough analysis of the electrochemical data for the ligand systems **2**−**4** (see Figure S16) reveals that an error of 1 mV in the standard potential E° has approximately the same effect on the standard deviation as errors of about $0.3 \times 10^{-6}\,\text{cm}^2\,\text{s}^{-1}$ in the diffusion coefficient D and about $0.05\,\text{cm}\,\text{s}^{-1}$ in the heterogeneous rate constant k_s, respectively. In fact, with respect to the estimated errors the heterogeneous rate constant is essentially the same for all ligands, i.e. $k_s \approx 0.15 \pm 0.05\,\text{cm}\,\text{s}^{-1}$.

A comparison of the diffusion coefficients of the ligands **2**−**4** shows the expected trend with the bulky *tert*-butyl substituted ligand exhibiting the slowest diffusion followed by the methoxy and methyl analogues in that order. Similarly, the values of the standard potentials match the expected electronic

Table 2. Experimental parameters from simulating square wave voltammograms of the ligands **2**−**4**.

|	**2**	**3**	**4**
R	Me	*t*-Bu	OMe
D ($10^{-6}\,\text{cm}^2\,\text{s}^{-1}$)	8.5	6.9	7.8
E° (mV)	550	556	388
k_s (cm s^{-1})	0.13	0.16	0.14
k_f ($10^{-4}\,\text{s}^{-1}$)	≈ 4	≈ 4	≈ 4
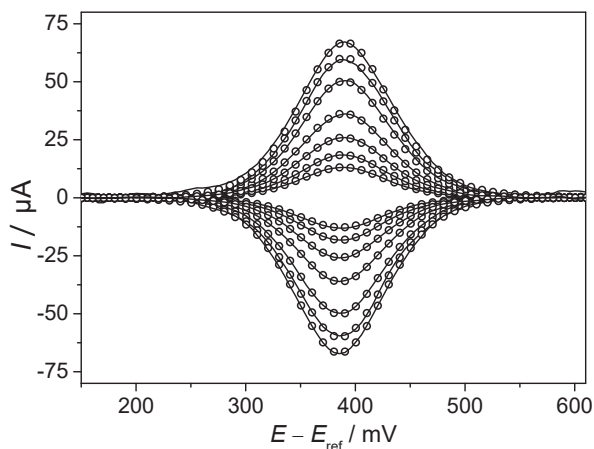
Figure 3. Square-wave voltammograms of the ligand **4** ($c = 1.95$ mM) in dichloromethane solution at square-wave frequencies of 25, 50, 100, 200, 400, 600, and 750 Hz. Open circles represent simulated and lines experimental data.

trend given by the *para* substituents at the triphenylamine moiety.[36] The representative square-wave voltammograms of ligand **4** are displayed in Figure 3 and show good agreement between simulated and experimental data (for **2** and **3** see Figure S17).

The square-wave voltammograms recorded for the complexes **6**−**8** show a rather similar behavior as those observed for their corresponding ligands. In Figure 4 the square-wave voltammograms of **8** are depicted as a representative example (for **6** and **7** see Figure S18). The oxidation of the complexes **6**−**8** can be described according the underlying mechanism given in Equations (3) to (6), where E_i° are the standard potentials for the individual one-electron steps.

$$[Cu_2(aba\text{-}R)_4]^+ + e^- \rightleftharpoons [Cu_2(aba\text{-}R)_4] \qquad (E_1^\circ) \qquad\qquad (3)$$

$$[Cu_2(aba\text{-}R)_4]^{2+} + e^- \rightleftharpoons [Cu_2(aba\text{-}R)_4]^+ \qquad (E_2^\circ) \qquad\qquad (4)$$

$$[Cu_2(aba\text{-}R)_4]^{3+} + e^- \rightleftharpoons [Cu_2(aba\text{-}R)_4]^{2+} \qquad (E_3^\circ) \qquad\qquad (5)$$

$$[Cu_2(aba\text{-}R)_4]^{4+} + e^- \rightleftharpoons [Cu_2(aba\text{-}R)_4]^{3+} \qquad (E_4^\circ) \qquad\qquad (6)$$
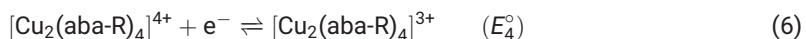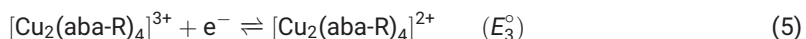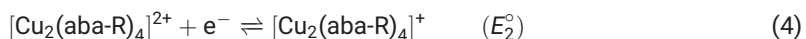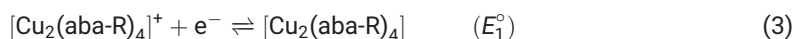
Consistent with the data presented for the ligands also for the complexes the charge-transfer parameter α was supposed to be 0.5 for all four charge-transfer reactions. Moreover, it was further assumed that the diffusion coefficient D and the heterogeneous rate constant k_s are related to the particular complex system and are independent of the charge of the individual species. The parameters obtained from simulation of the experimental square-wave voltammograms are presented in Table 3.

Qualitatively the diffusion coefficients of the complexes are following the same trend as observed for the related ligands. Nevertheless, the absolute values are as expected smaller than those of the corresponding ligands. Moreover, the voltammograms are only dependent on the ligand present, rather than being indicative of a metal ion centered process. The standard potentials observed for the complexes **6**−**8** show a slight shift which corresponds to the substitution pattern of the related ligand. The individual oxidation steps given in Equations (3) to (6) can be described as single one-electron processes despite

10
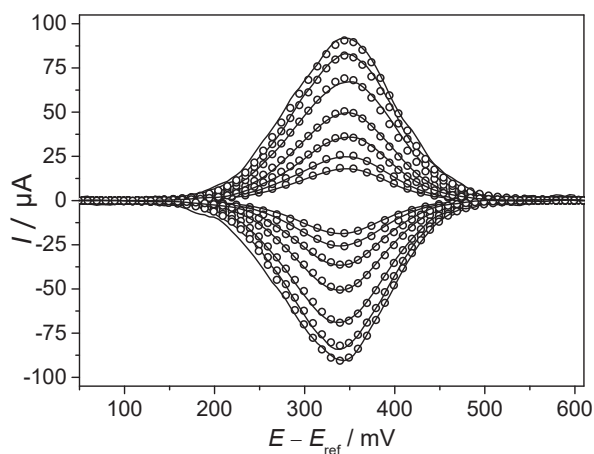
Figure 4. Square-wave voltammograms of the complex **8** ($c = 1.18$ mM) in dichloromethane solution at square-wave frequencies of 25, 50, 100, 200, 400, 600, and 750 Hz. Open circles represent simulated and lines experimental data.

the presence of four oxidizable centers. Such a behavior is theoretically expected if the interactions between the electrochemically active centers are negligibly small and the charge transfer process is virtually reversible.[37] Simulation of the experimental data allowed to determine the separation between the standard potential of the four oxidation steps which are summarized in Table 4 and compared to the corresponding values expected for a simple entropy effect with ΔE_S.[38]

An important observation to note is that experimental square-wave voltammograms are distinctly broader than expected from the pure entropy effect for a system containing four chemically identical oxidizable ligands. Moreover, this discrepancy also holds for the differences between the individual standard potentials of the four oxidation steps, for which significantly larger values are observed than those estimated from the presence of a solely entropy effect of four chemically equivalent oxidizable fragments in the system. Remarkably, the standard potential of the fourth oxidation step (Equation (6)) is close to the potential observed for the corresponding ligand (see Tables 2 and 3).

Table 3. Experimental parameters obtained from simulating square-wave voltammograms of complexes **6**–**8**.

	6	7	8
R	Me	*t*-Bu	OMe
D (10^{-6} cm^2 s^{-1})	4.8	3.2	4.0
E_1° (mV)	451	467	283
E_2° (mV)	497	503	329
E_3° (mV)	521	527	351
E_4° (mV)	558	562	389
k_s (cm s^{-1})	0.170	0.110	0.150

Table 4. Separations between the standard potential of individual one electron processes for complexes **6**−**8** as compared with value expected from a solely entropy related effect, ΔE_S.

	6	**7**	**8**	ΔE_S
R	Me	t-Bu	OMe	
$E_2^\circ - E_1^\circ$ (mV)	46	36	46	25
$E_3^\circ - E_2^\circ$ (mV)	24	24	22	21
$E_4^\circ - E_3^\circ$ (mV)	37	35	38	25

Spectroelectrochemistry

To further explore the electrochemical oxidation of the complexes **6**−**8** and to probe the electronic properties of oxidized species spectroelectrochemical investigations have been performed. In order to address this point we first performed spectroelectrochemical measurement for the corresponding ligands to examine their properties as a basis for the understanding of the related complexes. It has to be noted here that a general assumption is required for simulating electrochemical data recorded with an optically transparent thin-layer electrochemical (OTTLE) cell as used in our experiments. Generally, the theoretical model to simulate thin-layer cyclic voltammograms assumes a cell geometry for which one of the boundaries is a smooth optically transparent electrode, while the other being an optically transparent insulator. However, the experimental thin-layer cell consists of two optically transparent insulators having a platinum net electrode in between. Consequently, unlike in the case of the simulated cyclic voltammograms, the shape of the experimental ones does not only depend on diffusion processes occurring perpendicular to the electrode, but also on processes occurring within the meshes of the platinum net.

In Figure 5 the experimental and simulated thin-layer cyclic voltammograms for ligand **3** and complex **7** are depicted as representative examples (for ligands **2** and **4** as well as complexes **6** and **8** see Figure S19), indicating a suitable agreement and proving the validity of the assumption made to simulate the data (also cf. Table 2). In fact, it is obvious that the differences between both data sets are smaller for lower scan rates. This is consistent with the limiting condition that the shape of the thin-layer cyclic voltammograms becomes independent of the diffusion processes, if the scan rate and/or the cell thickness tends toward zero.

The UV/vis absorption spectra recorded for ligand **3** during the electrochemical forward and backward scan are depicted as a representative example in Figure 6 (for **2** and **4** see Figure S20). A factor analysis of the spectra obtained for the three ligands during thin-layer cyclic voltammetry experiments revealed that only a single optically active species is produced in the forward scan, while in the backward scan this species is completely consumed, which is consistent with the observed quasi-reversible one-electron oxidation steps for the ligands in the square-wave voltammetry measurements. Consequently, it was possible to determine the UV/vis absorption spectra of the corresponding oxidized ligands which are depicted in Figure 7. The values of the molar extinction coefficients are based on the assumption that the optical path length of the thin-layer cell is exactly 0.2 mm. However, the uncertainty estimated for the absolute value is about 10%, despite the fact, that the reproducibility of the individual species
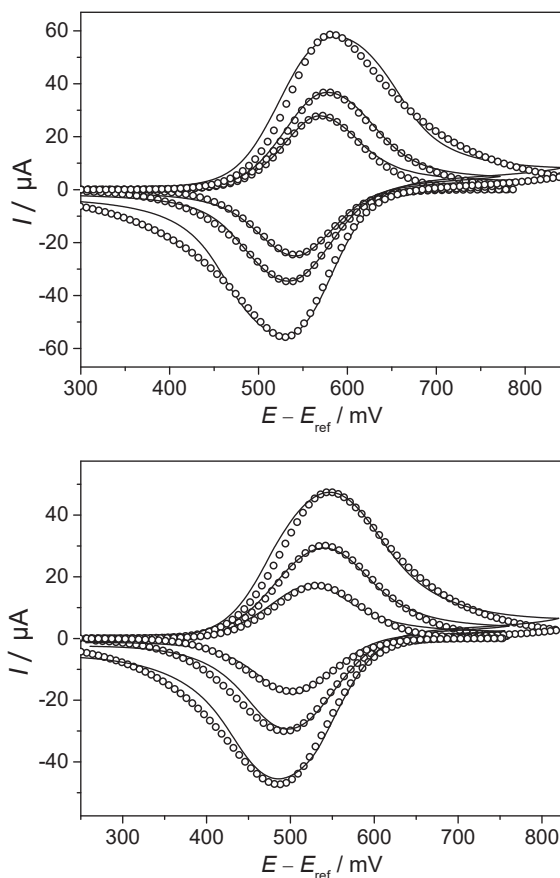
Figure 5. Thin-layer cyclic voltammograms of ligand **3** (top, $c = 2.40$ mM) and complex **7** (bottom, $c = 0.59$ mM) in dichloromethane solutions using scan rates of 1.25, 2.5, and 5 mV s^{-1}. Open circles represent simulated and lines experimental data.

spectra was distinctly better in a series of independent experiments.

The maxima in the observed UV/vis spectra of the oxidized ligands were found at 697, 709, and 774 nm for **2**, **3**, and **4**, respectively. This shows a clear trend for the ligands that the lowest energy absorption is shifted toward higher wavelengths within the series of methyl (**2**), *tert*-butyl (**3**), and methoxy (**4**) substitution, which is consistent with the variation of the electronic properties of *para* substituents and also reflects the trend observed for the standard potentials (cf. Table 2). Moreover, the observed trend is also consistent with the values reported for the corresponding symmetrically substituted triphenylamines.[39,40] Interestingly, the extinction coefficient of the absorption maximum for the methoxy substitute ligand **4** is significantly larger than those observed for ligands **2** and **3**.

Spectroelectrochemical investigations were also performed for the complexes **6**–**8** by recording UV/vis absorption spectra during the electrochemical forward and backward scan, which are shown for **7** as a representative example in Figure 8 (for **6** and **8** see Figure S21). As in the case of the ligands factor analysis of the spectra of the copper complexes reveals that only a single optically active species is produced in the forward scan of each thin-layer cyclic voltammetry experiment, which is consumed
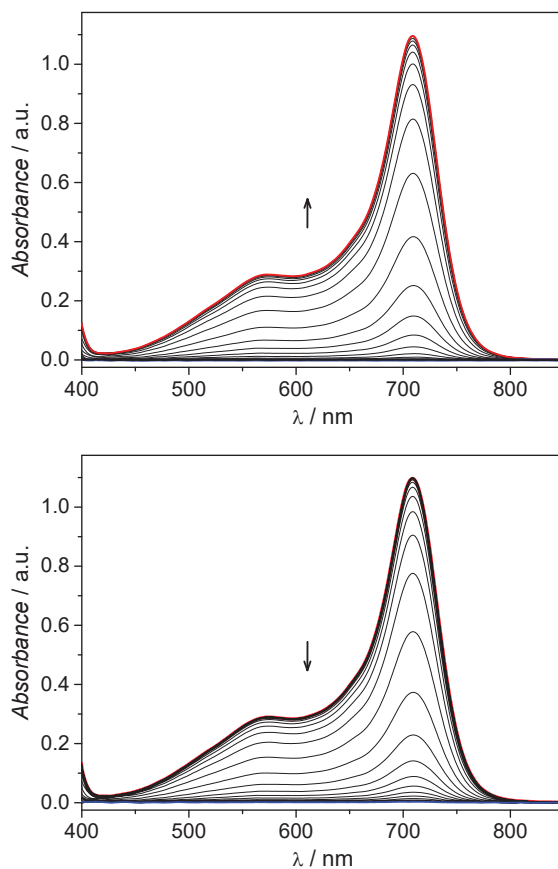
Figure 6. UV/vis spectra recorded during the electrochemical forward (top, blue to red line) and backward (bottom, red to blue line) scan for ligand **3** ($c = 2.40$ mM). The difference in potential between successive spectra is 20 mV.
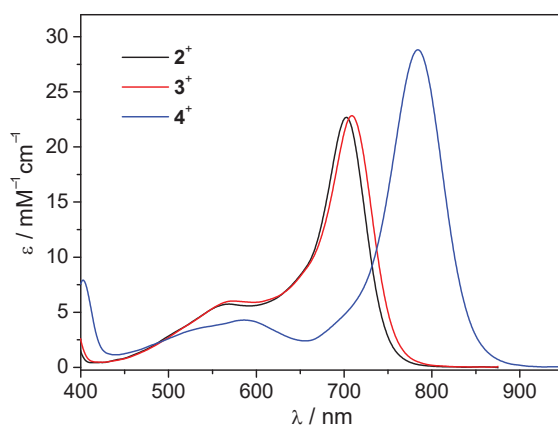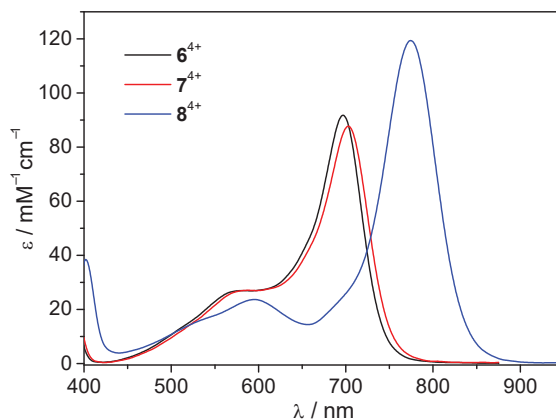

Figure 7. UV/vis spectra of the oxidized species for ligands **2** (black line), **3** (red line), and **4** (blue line) determined from spectroelectrochemical experiments.

during the following backward scan. Therefore, the absorption spectra of the oxidized copper complexes can be extracted from the data, again assuming an idealized optical path length as in the ligand case.
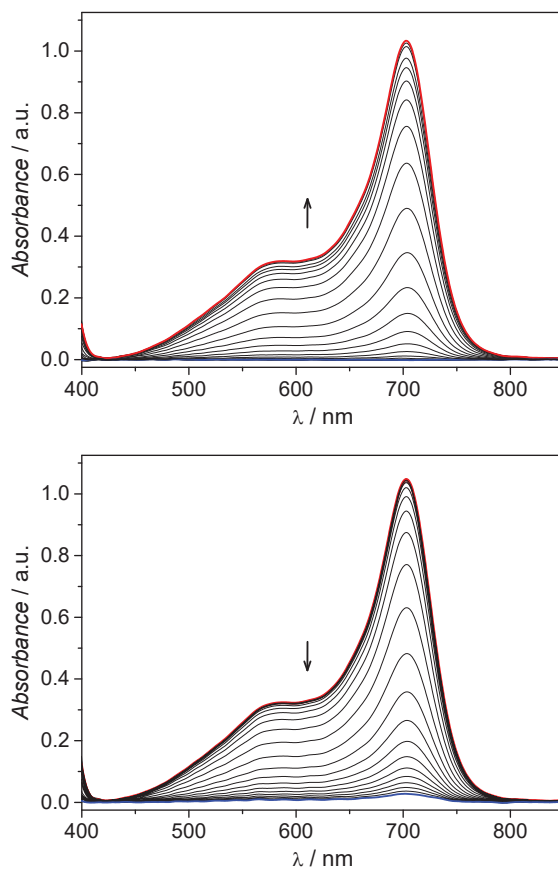
Figure 8. UV/vis spectra recorded during the electrochemical forward (top, blue to red line) and backward (bottom, red to blue line) scan for complex **7** ($c = 0.59$ mM). The difference in potential between successive spectra is 20 mV.

The obtained spectra of the complexes **6**−**8** are depicted in Figure 9.

For the absorption maxima of the complexes a similar basic trend as in the case of the corresponding ligands is observed, where again the highest wavelength is found for the methoxy derivative **8**. However, comparing the absorption maxima of the ligands and complexes a slight shift to lower wavelengths is observed for the complexes with about 5, 6, and 10 nm for **6**, **7**, and **8**, respectively (cf. Figures 7 and 9), indicative for only minor contributions of the copper paddle-wheel unit on the optical properties of the oxidized ligand moieties in the complexes. As in the case of the ligands the methoxy derivative shows the largest extinction coefficient for the absorption maximum. A comparison of the spectra obtained for the ligands and complexes reveals an approximately four-fold increase in the extinction coefficient (see Figure S22). Therefore, it is tempting to assume that the complex spectra can be viewed as a simple sum of four individual ligand spectra. This view is consistent with the fact that only one optically active species is generated during the oxidation of the complexes **6**−**8**. In fact, there is no indication for any difference in the spectra of the oxidized species obtained by successive oxidations steps, which means that all oxidized species $[Cu_2(aba\text{-}R)_4]^{n+}$ independent of their charge have the same spectra only related to the variation of the *para* substituents. This is further evidenced by the comparison of UV/vis

15

Figure 9. UV/vis spectra for the oxidized species of the complexes **6** (black line), **7** (red line), and **8** (blue line) determined from spectroelectrochemical experiments.

spectra recorded at different potentials during the spectroelectrochemical oxidation, which are related to different molar fractions of the possible charged species. The latter can be concluded from the fact that the difference in standard potentials of the four oxidation processes can not solely be related to the pure entropy term (cf. Table 4). Indeed, applying an appropriate scaling factor the spectra obtained for intermediate potentials can be superimposed with the spectrum of the fully oxidized complex cation (see Figure S23 for complex **6** as a representative case).

Chemical oxidation of ligands and complexes

Chemical oxidation of the ligands and complexes was carried out with silver tetrafluoroborate as an oxidant in dichloromethane solution. It was observed that the methoxy derivatives **4** and **8** showed greatest ease in oxidation, for which it was possible to obtain the oxidized species upon addition of stoichiometric amounts of oxidant. This is consistent with the appreciably lower standard potential observed for **4** and **8** with respect to the other derivatives (see Tables 2 and 3). The corresponding UV/vis absorption spectra recorded for the chemically oxidized species of the ligand **4** and complex **8** are depicted in Figure 10. However, due to their higher standard potentials, the methyl (**2** and **6**) and *tert*-butyl (**3** and **7**) counterparts required an excess of oxidant to obtain the radical species. The corresponding UV/vis spectra of their chemically oxidized species depicted in Figure S24 are in full agreement with the data obtained from the spectroelectrochemical experiments (vide supra). It is interesting to note here that the oxidized species of all ligands and complexes did generally show a remarkable stability, as their spectra did not change appreciably over time for at least several days, particularly when care was taken to prevent solvent evaporation. This even holds for samples which were appropriately stored in contact to ambient atmosphere.

To further characterize the oxidized species derived from the ligands **2**−**4** and complexes **6**−**8** room temperature X-band ESR spectra were recorded. The radicals were obtained by treating solutions of the ligands and complexes in dichloromethane with an excess of silver tetrafluoroborate, upon which the
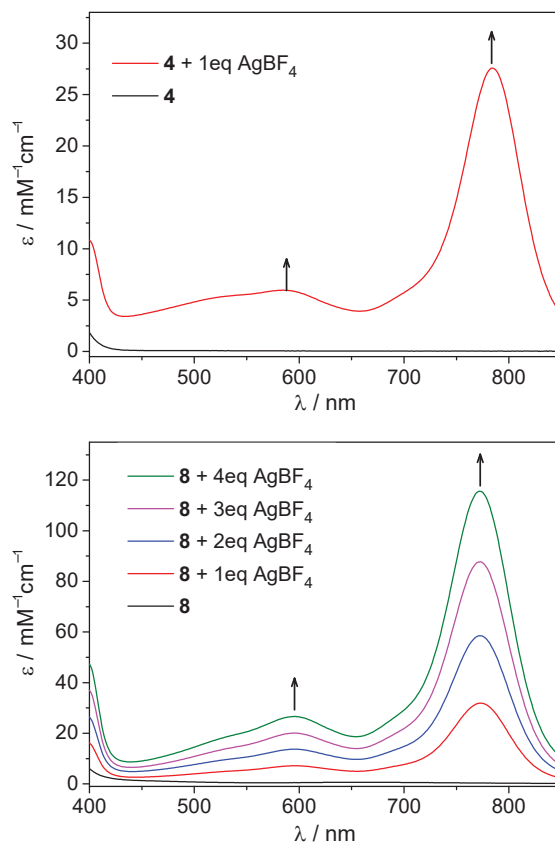
Figure 10. UV/vis spectra for the chemically oxidized species of ligand **4** (top) and complex **8** (bottom: different stoichiometric ratios of oxidant) measured in dichloromethane.

solutions turned deep blue-violet to give the corresponding radicals. The ESR spectra recorded for the chemically oxidized species of the ligand **4** and complex **8** are depicted in Figure 11 (for ESR spectra of **2**, **3**, **6**, and **7** see Figure S25).

The observed g factor for all compounds is close to the expected value for the free electron at about 2.003 as expected for triarylamine radicals. The ESR spectra for the oxidized radical species of the methoxy substituted ligand **4** and complex **8** show a well-resolved hyperfine coupling of the electron spin to the nuclear spin of the nitrogen atom (^{14}N: $I = 1$) of the triphenylamine moiety of 22 MHz (0.79 mT). This is well within the expected range usually reported for triarylamine radicals.[4,39,41] A similar behavior is observed for the compounds with *tert*-butyl substitution (**3** and **7**) for which the hyperfine coupling is found to be 25 MHz (0.89 mT). For the methyl derivatives the hyperfine coupling is not resolved in the spectra (cf. Figure S25). Therefore, the hyperfine coupling can only be estimated to about 22 MHz (0.79 mT). The observed values for the hyperfine coupling constants are consistent with a nearly planar geometry at the nitrogen atom of the triphenylamine moiety as observed in the crystal structures.[40] Moreover, all radicals exhibit an isotropic signal with g values typical for triarylamine radicals. Comparing the ESR spectra and the fit parameters obtained from simulation it is obvious that there is very little variation between the ligands and their corresponding complexes, indicative for an only minor influence
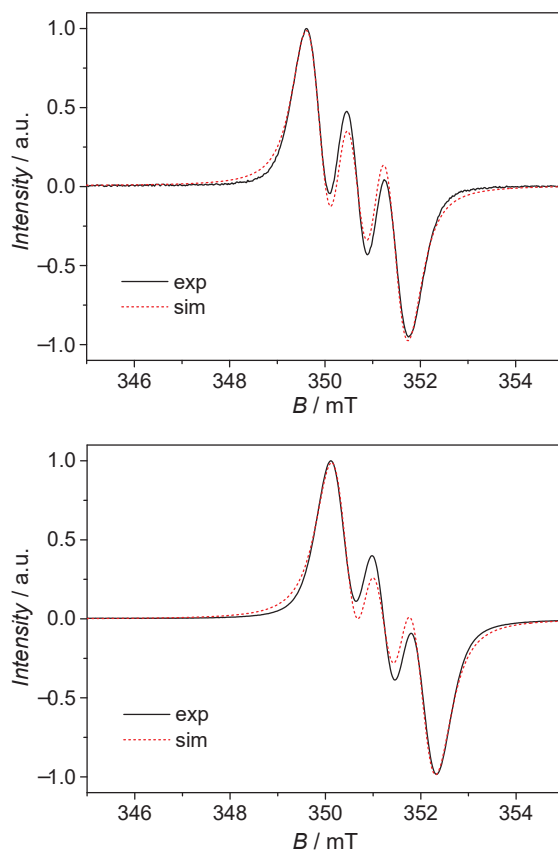
Figure 11. X-band ESR spectra for the oxidized ligand **4** (top) and complex **8** (bottom) measured in dichloromethane solution at room temperature ($c = 0.223$ mM for **4** and **8**; $c \approx 1$ mM for the oxidant).

of the central dicopper unit on the coordinated triphenylamine radicals.

To further elucidate the character of possible interactions between the oxidized ligand backbone and the central paddle-wheel core, BS-DFT calculations for the corresponding radical cations of the complexes $[Cu_2(aba\text{-}R)_4(dmf)_2]^{4+}$ with fully oxidized triphenylamine moieties have been performed based on the molecular structures of the neutral complexes **5**−**8** derived from crystallography. The results of these BS-DFT calculations are summarized in Table S9 and the corresponding spin density distributions of the cationic radical species $\mathbf{5^{4+}}$−$\mathbf{8^{4+}}$ are depicted in Figures S26−S29. The data confirms that the unpaired spin density of the radicals is mainly localized at the central nitrogen atoms of the triphenylamine ligand moieties, which is in agreement with the observed hyperfine coupling in the ESR experiments. The BS-DFT calculations reveal a rather small ferromagnetic exchange coupling between the organic radicals and the copper(II) ions of the core unit in the order of 2−3 cm^{-1}. This again is consistent with the observed ESR spectra indicative of independent nitrogen-centered radicals. It should be noted that the exchange coupling between the two copper(II) ions within the paddle-wheel core is two orders of magnitude larger than their coupling with the coordinated radical cations, a situation which has also been observed for dinuclear copper paddle-wheel complexes with coordinated radical ligands on the basis of magnetic susceptibility measurements.[42] This consequently leads to a situation where the radical

species can be regarded as virtually independent, which is consistent with the observations from ESR spectroscopy as well as electrochemistry.

Additional theoretical calculations to investigate the possible magnetic exchange between the organic radicals in the fully oxidized species have been performed utilizing the model systems $[Zn_2(aba\text{-}R)_4(dmf)_2]^{4+}$, where the copper ions have been replaced by zinc(II) ions. Generally, due to the arrangement of the four aryl carboxylates at the paddle-wheel core, two different magnetic couplings between the organic radicals are possible based on their relative position which can be *cis* or *trans* (J_{cis} and J_{trans}). The detailed results are summarized in Table S10 and the corresponding spin density distributions are depicted in Figures S30−S34. The BS-DFT calculations revealed an almost negligible antiferromagnetic coupling between the organic radicals for both possible type of interactions ($J_{cis} = -0.09$ to $-0.22\,\text{cm}^{-1}$; $J_{trans} = 0$ to $-0.09\,\text{cm}^{-1}$).

Conclusions

In summary, we have reported on four new monocarboxyl triphenylamine based ligands Haba-R (**1**−**4**) with varying substitution at the remaining *para* postilions of the phenyl rings and the corresponding dinuclear cooper(II) complexes (**5**−**8**). All complexes adopt the common paddle-wheel arrangement for the dinuclear core, where the remaining axial coordination site at the copper(II) ions is occupied by a dmf molecule. The four complexes **5**−**8** have been fully characterized toward their structural and magnetic properties. A strong antiferromagnetic coupling between the copper(II) ions of the paddle-wheel core was observed and could be confirmed by BS-DFT calculations. Moreover, the variation of the substitution at the triphenylamine moieties did not show a significant influence on the observed magnetic exchange. Although triphenylamine derivatives have been widely studied due to their electrical conductivity, electroluminescence, and hole-transport properties, reports on their redox behavior and the interactions of their corresponding radical species within metal bonded systems are scarce. In the present work detailed electrochemical and spectroelectrochemical investigations of the triphenylamine-based ligands and complexes have been performed. For the *para* substituted ligands (**2**−**4**) and complexes (**6**−**8**) electrochemistry demonstrates the expected behavior leading to highly stable oxidized species for both ligands and complexes. Spectroelectrochemical experiments allowed us to characterize the properties of these oxidized radical species and to elucidate their interactions with the central dicopper core. It was found that the UV/vis and ESR spectroscopic properties do not significantly vary between the oxidized radical species derived from the ligands and the complexes, indicating that only small interactions between the radical species and the copper(II) ions can be present. This was further confirmed by BS-DFT calculations which show that the exchange interactions of the coordinated radicals with the copper(II) ions of the core unit are weak ferromagnetically coupled, but about two orders of magnitude smaller than the magnetic coupling within the dinuclear paddle-wheel core. Moreover, BS-DFT calculations for the fully oxidized complexes further indicate a very weak antiferromagnetic coupling among the ligand radicals. In the case of the presented complexes this leads to the observation of virtually independent radical species in the full oxidized complex species $[Cu_2(aba\text{-}R)_4(dmf)_2]^{4+}$. As a consequence,

triphenylamine derivatives as linkers can be regarded as promising candidates for obtaining new coordinations polymers and MOFs that can lead to new magnetic materials via oxidation of the amine nitrogen leading to the generation of extra spin centers within the frameworks, which in turn can allow to transmit and trigger the magnetic exchange interactions between the paramagnetic metal ions of corresponding frameworks. However, this will preferentially require frameworks that contain metal ion building units, which are either based on mononuclear paramagnetic metal ions or exhibit magnetic interactions within the metal clusters that are in the same order of magnitude as those with the bridging linkers.

Experimental Section

Materials

All starting chemicals are commercially available and were used without further purification. The methyl 4-aminobenzoate was prepared as reported in literature.[43] Also the Buchwald−Hartwig coupling procedure utilized in the syntheses of the ligands **2**, **3**, and **4** was adapted from literature.[26] The syntheses of the complexes **5**, **6**, and **8** were carried out in Teflon-lined acid digestion vessels from Parr Instruments.

Physical measurements

^{1}H and ^{13}C NMR spectra were recorded with Bruker Avance 400 and 600 MHz spectrometers. ^{1}H NMR assignments and comparison of the data for **1**−**4** are presented in Figure S35 and Table S11. Thermogravimetric analysis (TGA) on powdered samples was performed using a Netzsch STA409PC Luxx apparatus under constant flow of air ranging from room temperature up to 1000 °C with a heating rate of 5 °C min^{-1}. Mass spectra were measured on a Bruker MAT SSQ 710 spectrometer. Elemental analyses were determined on a Leco CHNS/932 and a VARIO EL III elemental analyzer. The FT-IR spectra were measured using the Specac Diamond ATR optional accessory on an VERTEX70 spectrometer by Bruker Optics. The UV/vis spectra were obtained on a Varian Cary5000 UV/vis/NIR spectrometer, while the fluorescence spectra were measured on a JASCO FP-6300 spectrofluorometer.

Syntheses

4-(diphenylamino)benzaldehyde:[24] Triphenylamine (3.0 g, 12.2 mmol) was dissolved in dmf (150 mL) under stirring at 0 °C. The stirring was continued for 10 min and subsequently POCl$_3$ (1.2 mL) was added dropwise. After complete addition, the mixture was refluxed under N$_2$ atmosphere for 22 h. The dark mixture was then allowed to cool to room temperature and added into ice water (100 mL). The mixture was then neutralized with aqueous NaOH and extracted with CH$_2$Cl$_2$ (3 × 100 mL). The combined organic layers were washed with water (2 × 100 mL) and dried with anhydrous sodium sulphate. The product was then purified using flash column chromatography (hexane/ethyl acetate 5:1). Yield: 2.4 g, 72 %; ^{1}H NMR (400 MHz, CDCl$_3$, 25 °C): $\delta = 9.81$ (s, 1H, CHO), 7.68 (d, $J = 8.7$ Hz, 2H), 7.34 (t, $J = 7.8$ Hz, 2H), 7.15−7.19 (m, 6H), 7.02 ppm (d, $J = 8.7$ Hz, 2H); ^{13}C NMR (101 MHz, CDCl$_3$, 25 °C): $\delta = 190.6, 153.5, 146.3, 131.5,$

129.9, 129.3 126.5, 125.3, 119.5 ppm; IR (ATR, cm^{-1}): $\tilde{\nu}$ = 3063 (w), 1675 (s), 1581 (s), 1564 (m), 1487 (s), 1328 (s), 1285 (vs), 1218 (s), 1155 (m).

4-(diphenylamino)benzoic acid (Haba, 1): To a solution of 4-(diphenylamino)benzaldehyde (2.0 g, 7.3 mmol) in acetone (60 mL) was added dropwise an aqueous solution (80 mL) containing K_2CO_3 (0.7 g, 5.1 mmol) and $KMnO_4$ (4.56 g, 29.2 mmol). The mixture was refluxed for 12 h overnight and subsequently filtered over a celite pad while still hot. The filtrate was then acidified using concentrated aqueous HCl, upon which the solution turned cloudy. The light yellow precipitate obtained was then filtered off, washed and dried overnight in an oven at 80 °C. Yield: 1.56 g, 76 %; ^{1}H NMR (600 MHz, dmso-d$_6$, 25 °C): δ = 12.48 (s, 1H, COOH), 7.79 (d, J = 8.8 Hz, 2H), 7.39 (t, J = 7.9 Hz, 4H), 7.18 (t, J = 7.4 Hz, 2H), 7.13 (d, J = 7.6 Hz, 4H), 6.88 ppm (d, J = 8.8 Hz, 2H); ^{13}C NMR (151 MHz, dmso-d$_6$, 25 °C): δ = 166.9, 151.3, 146.1, 130.8, 129.9, 125.7, 124.7, 122.4, 119.1 ppm; IR (ATR, cm^{-1}): $\tilde{\nu}$ = 3063 (w), 1665 (s), 1608 (m), 1583 (s), 1510 (m), 1488 (s), 1430 (m), 1415 (m), 1316 (s), 1271 (vs), 1177 (s), 1074 (m), 1028 (w), 949 (m); UV/vis spectra see Figure S36; EI-MS: m/z (%): 289 (100) [M]$^+$; elemental analysis calcd (%) for $C_{19}H_{15}NO_2$ (289.33 g mol^{-1}): C 78.87, H 5.23, N 4.84; found: C 78.64, H 5.11, N 4.89.

4-(bis(4-tolylphenyl)amino)benzoic acid (Haba-Me, 2): To a solution of Pd(OAc)$_2$ (36 mg, 0.16 mmol) in degassed toluene (20 mL) P(t-Bu)$_3$ (0.19 mL, 0.48 mmol, 0.5 g mL^{-1} in hexane) was added, which was then stirred for 15 min at room temperature. Subsequently 4-bromotoluene (1.57 g, 9.6 mmol), methyl 4-aminobenzoate (0.48 g, 3.2 mmol), and Cs$_2$CO$_3$ (2.6 g, 8.0 mmol) were added to this solution. The resulting mixture was refluxed for 5 days. After this period the reaction mixture was allowed to cool to room temperature and poured into dichloromethane (60 mL). After filtration over a celite pad the filtrate was loaded onto silica gel by adding the silica (about 10 g) to the filtrate and evaporating all volatiles from the mixture. The loaded silica gel was used for flash column chromatography (chloroform/hexane 2:1) from which a yellow oil was obtained. A mixture of aqueous KOH solution (30 mL, 30 %) and methanol (30 mL) was added and the reaction mixture refluxed overnight. Subsequently, the resulting mixture was filtered over a celite pad while still hot. The filtrate was acidified with concentrated aqueous HCl to give a colorless precipitate, which was filtered off, washed, and dried overnight in an oven at 80 °C. Yield: 0.65 g, 64 %; ^{1}H NMR (400 MHz, dmso-d$_6$, 25 °C): δ = 7.73 (d, J = 8.9 Hz, 2H), 7.18 (d, J = 8.2 Hz, 4H), 7.02 (t, J = 8.3 Hz, 4H), 6.77 (d, J = 8.3 Hz, 2H), 2.28 ppm (s, 6H, Me); ^{13}C NMR (100 MHz, dmso-d$_6$, 25 °C): δ = 167.04, 151.67, 143.53, 134.21, 130.42, 126.04, 121.44, 117.75, 20.51 ppm; IR (ATR, cm^{-1}): $\tilde{\nu}$ = 3024 (w), 1667 (s), 1594 (s), 1505 (s), 1416 (m), 1315 (s), 1280 (vs), 1175 (s), 949 (w); UV/vis spectra see Figure S37; EI-MS: m/z (%): 317 (100) [M]$^+$; elemental analysis calcd (%) for $C_{21}H_{19}NO_2$ (317.38 g mol^{-1}): C 79.47, H 6.03, N 4.41; found: C 79.53, H 5.99, N 4.43.

4-(bis(4-*tert*-butylphenyl)amino)benzoic acid (Haba-tBu, 3): The procedure described for **2** was adopted for the coupling of 4-*tert*-butylbromobenzene (1.7 mL g, 9.9 mmol) utilizing the similar reaction conditions and compounds (Pd(OAc)$_2$: 37 mg, 0.17 mmol; P(t-Bu)$_3$: 0.20 mL, 0.5 mmol; methyl 4-aminobenzoate: 0.50 g, 3.3 mmol; Cs$_2$CO$_3$: 2.7 g, 8.3 mmol) as well as solvent (toluene: 20 mL). The final reaction mixture was allowed to cool to room temperature and poured into dichloromethane (60 mL). After filtration over a celite pad the filtrate was loaded onto silica gel by adding the silica (about 10 g) to the filtrate and evaporating all volatiles from the mixture. The loaded silica gel was used for flash column chromatography (chloroform/hexane 2:1) from which a brown solid was obtained. A mixture of aqueous

KOH solution (30 mL, 30 %) and methanol (60 mL) was added and the mixture refluxed overnight. The reaction mixture was then filtered hot over a celite pad and subsequently acidified with concentrated aqueous HCl to give a colorless precipitate, which was filtered off, washed, and dried overnight in an oven at 80 °C. Yield: 0.97 g, 91 %; ^{1}H NMR (400 MHz, dmso-d$_6$, 25 °C) $\delta = 7.74$ (d, $J = 8.9$ Hz, 2H), 7.38 (d, $J = 8.2$ Hz, 4H), 7.05 (d, $J = 8.3$ Hz, 4H), 6.78 (d, $J = 8.3$ Hz, 2H), 1.27 ppm (s, 18H, CMe$_3$); ^{13}C NMR (100 MHz, dmso-d$_6$, 25 °C) $\delta = 167.5$, 152.0, 147.7, 143.8, 131.3, 127.1, 125.1, 122.0, 118.3, 34.7, 31.6 ppm; IR (ATR, cm^{-1}): $\tilde{\nu} = 3024$ (w), 1667 (s), 1594 (s), 1505 (s), 1416 (m), 1315 (s), 1280 (vs), 1175 (s), 949 (w); UV/vis spectra see Figure S38; EI-MS: m/z (%): 401 (85) $[M]^+$; elemental analysis calcd (%) for C$_{27}$H$_{31}$NO$_2$ (401.54 g mol^{-1}): C 80.76, H 7.78, N 3.49; found: C 80.96, H 7.89, N 3.50.

4-(bis(4-methoxyphenyl)amino)benzoic acid (Haba-OMe, 4): The procedure described for **2** was adopted for the coupling of 4-bromoanisole (3 mL, 23.7 mmol) utilizing the similar reaction conditions and compounds (Pd(OAc)$_2$: 88 mg, 0.4 mmol; P(t-Bu)$_3$: 0.48 mL, 1.2 mmol; methyl 4-aminobenzoate: 1.2 g, 7.9 mmol; Cs$_2$CO$_3$: 6.6 g, 19.8 mmol) as well as solvent (toluene: 20 mL). The reaction mixture was allowed to cool to room temperature and poured into dichloromethane (150 mL). After filtration over a celite pad the filtrate was loaded onto silica gel by adding the silica (about 10 g) to the filtrate and evaporating all volatiles from the mixture. The loaded silica gel was used for flash column chromatography (chloroform/hexane 2:1) from which a colorless oil was obtained. A mixture of aqueous KOH solution (30 mL, 30 %) and methanol (30 mL) was added and the mixture refluxed overnight. The resulting mixture was filtered hot over a celite pad followed by acidification with concentrated aqueous HCl to give a light brown precipitate, which was filtered off, washed, and dried overnight in an oven at 80 °C. Yield: 1.22 g, 46 %; ^{1}H NMR (400 MHz, CDCl$_3$, 25 °C) $\delta = 7.84$ (d, $J = 8.9$ Hz, 2H), 7.12 (t, $J = 8.9$ Hz, 4H), 6.88 (d, $J = 8.9$ Hz, 4H), 6.81 (d, $J = 8.9$ Hz, 2H), 3.81 ppm (s, 6H, OMe); ^{13}C NMR (100 MHz, CDCl$_3$, 25 °C) $\delta = 171.1$, 157.0, 153.4, 139.3, 131.6, 127.9, 119.0, 116.8, 115.0, 55.3 ppm; IR (ATR, cm^{-1}): $\tilde{\nu} = 3394$ (w), 1666 (s), 1594 (m), 1502 (m), 1462 (m), 1317 (s), 1280 (vs), 1174 (s), 1126 (w), 1033 (w), 930 (w); UV/vis spectra see Figure S39; EI-MS: m/z (%): 349 (100) $[M]^+$; elemental analysis calcd (%) for C$_{21}$H$_{19}$NO$_4$ (349.38 g mol^{-1}): C 72.19, H 5.48, N 4.01; found: C 72.02, H 5.38, N 4.09.

[Cu$_2$(aba)$_4$(dmf)$_2$] (5): A mixture of the ligand Haba (**1**, 0.05 g, 0.173 mmol) and Cu(NO$_3$)$_2$·3H$_2$O (0.08 g, 0.34 mmol) in dmf (4 mL) was stirred for 1 h. The resulting green solution was transferred into a 23 mL Teflon-walled Parr acid digestion bomb. The reaction container was placed in an oven and heated at 110 °C for 24 h under autogenous pressure followed by cooling at a constant rate of 0.2 °C min^{-1}. Allowing the resulting reaction solution to stand for a few hours at room temperature led to the formation of green crystals from the brown mother liquor. The crystals were filtered off, washed with dmf until the wash fluid was no longer colored and dried in vacuo. Yield: 48 mg, 66 %; IR (ATR, cm^{-1}): $\tilde{\nu} = 1667$ (m), 1608 (s), 1587 (s), 1558 (w), 1488 (m), 1391 (vs), 1317 (m), 1274 (s), 1176 (m), 1100 (w), 1090 (w); UV/vis spectra see Figure S36; elemental analysis calcd (%) for **5** · 4 dmf, C$_{94}$H$_{98}$Cu$_2$N$_{10}$O$_{14}$ (1718.93 g mol^{-1}): C 65.68, H 5.75, N 8.15; found: C 66.10, H 5.74, N 8.05.

[Cu$_2$(aba-Me)$_4$(dmf)$_2$] (6): The ligand Haba-Me (**2**, 0.15 g, 0.476 mmol) and Cu(NO$_3$)$_2$·3H$_2$O (0.23 g, 0.952 mmol) were dissolved in dmf (4 mL) and stirred overnight. The resulting green solution was then transferred into a 23 mL Teflon-walled Parr acid digestion bomb. The reaction vessel was placed in an oven to heat at 110 °C for 24 h under autogenous pressure followed by cooling at a constant rate of

0.2 °C min^{-1}. The insoluble products were separated by centrifugation leading to a clear supernatant, which was separated and carefully layered by methanol (1 mL) on top. However, the solvent layer separation disappeared within about 15 min leading to a clear solution from which a light green precipitate was formed after a few hours. The precipitate was filtered off and washed with methanol. Additional product could be isolated from the filtrate as green block crystals after allowing it to stand for a few days. The combined product was dried in vacuo. Yield: 126 mg, 68 %; IR (ATR, cm^{-1}): $\tilde{\nu} = 1667$ (m), 1608 (s), 1599 (s), 1504 (s), 1394 (vs), 1316 (s), 1267 (s), 1169 (s); UV/vis spectra see Figure S37; elemental analysis calcd (%) for **6** $\cdot$ 1.5 H$_2$O, C$_{90}$H$_{89}$Cu$_2$N$_6$O$_{11.5}$ (1565.79 g mol^{-1}) C 69.04, H 5.73, N 5.37 found: C 68.73, H 5.46, N 5.43.

[Cu$_2$(aba-tBu)$_4$(dmf)$_2$] (7): A mixture of the ligand Haba-tBu (**3**, 0.05 g, 0.124 mmol) and Cu(NO$_3$)$_2$·3H$_2$O (0.03 g, 0.124 mmol) in dmf (2 mL) was stirred for 1 h followed by heating at 110 °C for 30 min. The resulting green solution was allowed to stand leading to green crystals being formed after a few days. The crystalline material was separated, washed with dmf, and dried in vacuo for 4 h to obtain the dried material. Yield: 39 mg, 16 %; IR (ATR, cm^{-1}): $\tilde{\nu} = 2962$ (m), 1671 (s), 1699 (s), 1506 (s), 1485 (s) 1397 (vs), 1321 (s), 1267 (m), 1176 (s), 1146 (w), 1063 (m); UV/vis spectra see Figure S38; elemental analysis calcd (%) for **7** $\cdot$ dmf $\cdot$ H$_2$O, C$_{117}$H$_{143}$Cu$_2$N$_7$O$_{12}$ (1966.51 g mol^{-1}): C 71.46, H 7.33, N 4.99; found: C 71.52, H 7.11, N 4.95.

[Cu$_2$(aba-OMe)$_4$(dmf)$_2$] (8): Solutions of the ligand Haba-OMe (**4**, 0.04 g, 0.114 mmol) in dmf (1.5 mL) and Cu(NO$_3$)$_2$·3H$_2$O (0.014 g, 0.057 mmol) in dmf (1.5 mL) were mixed in a 23 mL Teflon-walled Parr acid digestion bomb and stirred for 1 h at room temperature. Subsequently, the mixture was heated under autogenous pressure at 110 °C for 24 h followed by cooling at a constant rate of 0.2 °C min^{-1}. From the mother liquor which was allowed to stand undisturbed dark green micro-crystals were obtained. The micro-crystalline material was filtered off, washed with dmf until the wash fluid was no longer colored, and dried for 1 h in vacuo. Crystals suitable for X-ray studies were obtained by stirring a mixture of ligand and metal salt in dmf for about 20 min followed by slowly layering methanol on top of the mixture. Both solvents were allowed to slowly evaporate over 4 weeks to yield green crystals of **8**, which were dried in vacuo. Yield: 61 mg, 32 %; IR (ATR, cm^{-1}): $\tilde{\nu} = 1660$ (m), 1600 (s), 1557 (s), 1391 (vs), 1319 (s), 1274 (m), 1239 (vs), 1182 (s), 1144 (w), 1088 (m); UV/vis spectra see Figure S39; elemental analysis calcd (%) for C$_{90}$H$_{86}$Cu$_2$N$_6$O$_{18}$ (1666.77 g mol^{-1}): C 64.85, H 5.20, N 5.04; found: C 64.95, H 5.16, N 5.37.

Synthesis of radical cations

Excess of silver tetrafluoroborate (2 mM in CH$_2$Cl$_2$) was added into dilute solutions of the compounds in dichloromethane ($\approx 10^{-4}$ M) leading to deep blue-violet solutions which were centrifuged. The clear supernatant was decanted off and used for collection of ESR as well as UV/vis spectroscopic data. The obtained solutions of the oxidized radical cations were observed to be stable for several days, as no spectral changes could be detected within this period.

Voltammetry

CV measurements: Cyclic Voltammetry measurements were carried out at room temperature using a Reference 600 potentiostat (GAMRY Instruments). For the measurements of the ligand Haba (**1**) and its copper complex **5** in dichloromethane solution a Pt electrode was employed with 0.1 M tetrabutylammoniumperchlorate (TBAP) as co-electrolyte. A scan rate of 1 V s^{-1} was used and the reference electrode was a Ag/AgCl electrode.

Square-wave measurements: Square-wave voltammetric measurements were conducted on the substituted ligand analogues **2**–**4** and their copper complexes **6**–**8**, utilizing a three-electrode technique using the same potentiostat as above. The instrument was controlled by the DigiElch 8 software (available from GAMRY). This program provides not only routines for the digital simulation of electrochemical experiments but also those for performing the measurements in a consistent way making use of the GAMRY Electrochemical Toolkit library. The square-wave voltammograms were measured in dichloromethane (containing 0.25 M tetra-n-hexylammoniumperchlorate) under a blanket of solvent-saturated nitrogen gas using a square-wave signal with an amplitude of 25 mV and potential steps of 5 mV in all experiments. The ohmic resistance, which had to be compensated for, was determined by measuring the impedance of the system at potentials where the faradaic current was negligibly small. Background correction was accomplished by subtracting the current curves of the blank electrolyte (containing the same concentration of supporting electrolyte) from the experimental square-wave voltammograms. The working electrode was an 1.6 mm carbon disk electrode (ALS Japan). A Ag/AgCl electrode in acetonitrile containing 0.25 M tetra-n-butylammonium chloride served as reference electrode. All potentials reported in this paper refer to the ferrocenium/ferrocene couple, which was always measured at the end of a series of experiments.

Spectroelectrochemisty

Spectroelectrochemical experiments were performed using the Reference 600 potentiostat in combination with an AvaSpec 2048 spectrometer and an AvaLight-DHc light-source (both from Avantes, Apeldoorn, The Netherlands). The synchronization between potentiostat and spectrometer as well as the simultaneous recording of spectra and current curve was accomplished by the SPELCH software module included in DigiElch 8. A commercially available optically transparent thin-layer electrochemical (OTTLE) cell (University of Reading) with an optical path length of about 0.2 mm was used in all experiments. The cell consists of two platinum net electrodes serving as working and counter electrode. The (pseudo-) reference electrode is a silver wire. All spectra are difference spectra with respect to the spectrum of the starting material, which was taken as reference spectrum.

Magnetic measurements and ESR spectroscopy

The magnetic susceptibility was measured on bulk vacuum dried materials in the 4–300 K temperature range with a Quantum Design MPMS-5 superconducting SQUID magnetometer. The measured data were corrected for diamagnetism of the capsules used and the intrinsic diamagnetism of the constituent

atoms using Pascal constants. The ESR spectra were recorded at room temperature using an X-Band ELEXSYS E500 spectrometer from Bruker equipped with a SHQE resonator. The simulation of the experimental data was performed with EasySpin.[44]

X-ray Diffraction

The single crystal X-ray data for the compounds **5**−**8** were collected on a Nonius KappaCCD diffractometer, using graphite-monochromated Mo-K$_\alpha$ radiation ($\lambda = 71.073$ pm). Data were corrected for Lorentz and polarization effects, absorption was taken into account on a semi-empirical basis using multiple-scans.[45] The structures were solved by direct methods (SHELXS[46]) and refined by full-matrix least-squares techniques against $F_o{}^2$ (SHELXL-2014[46]). All hydrogen atoms were included at calculated positions with fixed thermal parameters. All non-disordered, non-hydrogen atoms were refined anisotropically.[46] The crystals of **5** and **7** contain large voids, filled with disordered solvent molecules, with a size of 821×10^6 pm^3/unit cell and 554×10^6 pm^3/unit cell for **5** and **7**, respectively. Their contribution to the structure factors were secured by back-Fourier transformation using the SQUEEZE routine of the program PLATON[47] resulting in 376 electrons/unit cell, respectively. Crystallographic data as well as structure solution and refinement details are summarized in Table S2. Diamond 4.2.2,[48] Olex 1.2.9,[49] and ORTEP-3[50] were used for structure representations. CCDC 1521017−1521020 contain the supplementary crystallographic data for complexes **5**−**8**. These data are provided free of charge by the Cambridge Crystallographic Data Centre (http://www.ccdc.cam.ac.uk). The powder measurements were performed on a Stoe Powder Diffractometer with a Mythen 1K detector at room temperature. Measurements were done using capillary tubes while the Debye−Scherrer Scan Mode was applied with a 2θ scan type. The X-ray tube was a Cu-long fine focus tube. The measurement was carried out between 2 and 50° with steps of 2.1° per 20 seconds.

Computational details

The structures used for calculations are based on the single-crystal structure data of **5**−**8** as all atomic positions of non-hydrogen atoms are concerned. The positions of all hydrogen atoms were optimized in the high-spin state ($S = 1$) at RI-DFT[51]/PBE[52]/def2-SVP[53] level of theory utilizing the TURBOMOLE 6.6 package of programs.[54] For broken-symmetry DFT (BS-DFT) calculations the PBE0 hybrid functional[52,55] was employed in combination with highly polarized triple-ζ def2-TZVPP basis sets.[53] The coupling constants were obtained by Yamaguchi's approach (Equation (7)) for an isotropic Heisenberg Hamiltonian ($\hat{H} = -J\hat{S}_1\hat{S}_2$).[56]

$$J = \frac{2\left(E_{\mathsf{BS}} - E_{\mathsf{HS}}\right)}{\left\langle S_{\mathsf{HS}}^2 \right\rangle - \left\langle S_{\mathsf{BS}}^2 \right\rangle} \tag{7}$$

25

Acknowledgements

Conflict of interest

The authors declare no conflict of interest.

References

[1] a) R. Rybakiewicz, M. Zagorska, A. Pron, *Chem. Pap.* **2017**, *71*, 243–268; b) A. Mahmood, *Chem. Soc. Rev.* **2016**, *123*, 127–144; c) M. Liang, J. Chen, *Chem. Soc. Rev.* **2013**, *42*, 3453–3488; d) Z. Ning, H. Tian, *Chem. Commun.* **2009**, 5483–5495; e) Y. Shirota, H. Kageyama, *Chem. Rev.* **2007**, *107*, 953–1010.

[2] a) R. A. Klenkler, G. Voloshin, *J. Phys. Chem. C* **2011**, *115*, 16777–16781; b) P. Cias, C. Slugovc, G. Gescheidt, *J. Phys. Chem. A* **2011**, *115*, 14519–14525; c) P. M. Borsenberger, E. H. Magin, *Macromol. Symp.* **1997**, *116*, 51–58; d) C. W. Tang, S. A. VanSlyke, *Appl. Phys. Lett.* **1987**, *51*, 913–915.

[3] a) U. Mitschke, P. Bäuerle, *J. Mater. Chem.* **2000**, *10*, 1471–1507; b) G. Wu, G. Zhao, C. He, J. Zhang, Q. He, X. Chen, Y. Li, *Sol. Energy Mater. Sol. Cells* **2009**, *93*, 108–113; c) O. Alévêque, P. Leriche, N. Cocherel, P. Frére, A. Cravino, J. Roncali, *Sol. Energy Mater. Sol. Cells* **2008**, *92*, 1170–1174; d) C. He, Q. He, X. Yang, G. Wu, C. Yang, F. Bai, Z. Shuai, L. Wang, Y. Li, *J. Phys. Chem. C* **2007**, *111*, 8661–8666; e) S. Roquet, A. Cravino, P. Leriche, O. Alévêque, P. Frére, J. Roncali, *J. Am. Chem. Soc.* **2006**, *128*, 3459–3466.

[4] E. T. Seo, R. F. Nelson, J. M. Fritsch, L. S. Marcoux, D. W. Leedy, R. N. Adams, *J. Am. Chem. Soc.* **1966**, *88*, 3498–3503.

[5] J.-H. Pan, H.-L. Chiu, L. Chen, B.-C. Wang, *Comput. Mater. Sci.* **2006**, *38*, 105–112.

[6] B. Adelizzi, I. A. W. Filot, A. R. A. Palmans, E. W. Meijer, *Chem. Eur. J.* **2017**, *23*, 6103–6110.

[7] a) H. Iden, W. Bi, J.-F. Morin, F.-G. Fontaine, *Inorg. Chem.* **2014**, *53*, 2883–2891; b) M. Zhu, Y. Li, C. Li, C. Zhong, C. Yang, H. Wu, J. Qin, Y. Cao, *J. Mater. Chem.* **2012**, *22*, 11128–11133; c) Y. Liu, Y. Wang, H. Guo, M. Zhu, C. Li, J. Peng, W. Zhu, Y. Cao, *J. Phys. Chem. C* **2011**, *115*, 4209–4216; d) J. Wang, C. He, P. Wu, J. Wang, C. Duan, *J. Am. Chem. Soc.* **2011**, *133*, 12402–12405; e) L. Zhang, B. Li, S. Yue, M. Li, Z. Hong, W. Li, *J. Lumin.* **2008**, *128*, 620–624; f) G. S. Maciel, K.-S. Kim, S.-J. Chung, J. Swiatkiewicz, G. S. He, P. N. Prasad, *J. Phys. Chem. B* **2001**, *105*, 3155–3157.

[8] a) L. Chen, S. Mallick, Y. N. Tan, M. Meng, C. Y. Liu, *Inorg. Chem.* **2017**, *56*, 7470–7481; b) M. H. Chisholm, C. B. Durr, S. A. Lewis, *Polyhedron* **2013**, *64*, 339–345.

[9] S. I. Vagin, A. K. Ott, B. Rieger, *Chem. Ing. Tech.* **2007**, *79*, 767–780.

[10] a) J. N. V. Niekerk, F. R. L. Schoening, *Acta Crystallogr.* **1953**, *6*, 227–232; b) B. Bleaney, K. D. Bowers, *Proc. R. Soc. A.* **1952**, *214*, 451–465; c) B. C. Guha, *Proc. R. Soc. A.* **1951**, *206*, 353–373; d) M. Melnik, *Coord. Chem. Rev.* **1982**, *42*, 259–293.

[11] S. S. Chui, S. M. F. Lo, J. P. H. Charmant, A. G. Orpen, I. D. William, *Science* **1999**, *283*, 1148–1150.

[12] a) X. X. Zhang, S. S.-Y. Chui, I. D. Williams, *J. Appl. Phys.* **2000**, *87*, 6007–6009; b) W. Böhlmann, A. Pöppl, M. Sabo, S. Kaskel, *J. Phys. Chem. B* **2006**, *110*, 20177–20181; c) S. Ketrat, T. Maihom,

S. Wannakao, M. Probst, S. Nokbin, J. Limtrakul, *Inorg. Chem.* **2017**, *56*, 14005–14012; d) M. K. Bhunia, J. T. Hughes, J. C. Fettinger, A. Navrotsky, *Langmuir* **2013**, *29*, 8140–8145; e) X.-S. Wang, S. Ma, P. M. Forster, D. Yuan, J. Eckert, J. J. López, B. J. Murphy, J. B. Parise, H.-C. Zhou, *Angew. Chem. Int. Ed.* **2008**, *47*, 7263–7266, *Angew. Chemie.* **2008**, *120*, 7373–7376; f) B. Chen, N. W. Ockwig, A. R. Millward, D. S. Contreras, O. M. Yaghi, *Angew. Chem. Int. Ed.* **2005**, *44*, 4745–4749, *Angew. Chemie.* **2005**, *117*, 4823–4827; g) M. Eddaoudi, J. Kim, J. B. Wachter, H. K. Chae, M. O'Keeffe, O. M. Yaghi, *J. Am. Chem. Soc.* **2001**, *123*, 4368–4369; h) K. Tan, N. Nijem, P. Canepa, Q. Gong, J. Li, T. Thonhauser, Y. J. Chabal, *Chem. Mater.* **2012**, *24*, 3153–3167; i) S. Rostamnia, H. Alamgholiloo, M. Jafari, R. Rookhosh, A. R. Abbasib, *Appl. Organometal. Chem.* **2016**, *30*, 954–958; j) S. Krause, V. Bon, I. Senkovska, U. Stoeck, D. Wallacher, D. M. Többens, S. Zander, R. S. Pillai, G. Maurin, F.-X. Coudert, S. Kaskel, *Nature* **2016**, *532*, 348–352.

[13] a) H. K. Chae, J. Kim, O. D. Friedrichs, M. O'Keeffe, O. M. Yaghi, *Angew. Chem. Int. Ed.* **2003**, *42*, 3907–3909, *Angew. Chemie.* **2003**, *115*, 4037–4039; b) E. Y. Lee, S. Y. Jang, M. P. Suh, *J. Am. Chem. Soc.* **2005**, *127*, 6376–6381; c) O. Akintola, D. Hornig, A. Buchholz, H. Görls, W. Plass, *Dalton Trans.* **2017**, *46*, 8037–8050; d) C. Livage, N. Guillou, A. Castiglione, J. Marrot, M. Frigoli, F. Millange, *Microporous Mesoporous Mater.* **2012**, *157*, 37–41; e) Y. Shen, X.-F. Yang, H.-B. Zhu, Y. Zhao, W.-S. Li, *Dalton Trans.* **2015**, *44*, 14741–14746; f) Q. Yao, A. B. Gómez, J. Su, V. Pascanu, Y. Yun, H. Zheng, H. Chen, L. Liu, H. N. Abdelhamid, B. Martín-Matute, X. Zou, *Chem. Mater.* **2015**, *27*, 5332–5339; g) J.-S. Hu, L. Zhang, L. Qin, H.-G. Zheng, X.-B. Zhang, *Chem. Commun.* **2015**, *51*, 2899–2902; h) X.-L. Hu, F.-H. Liu, C. Qin, K.-Z. Shao, Z.-M. Su, *Dalton Trans.* **2015**, *44*, 7822–7827; i) X.-L. Hu, C. Qin, X.-L. Wang, K.-Z. Shao, Z.-M. Su, *New J. Chem.* **2015**, *39*, 7858–7862; j) M. Venkateswarulu, A. Pramanik, R. R. Koner, *Dalton Trans.* **2015**, *44*, 6348–6352; k) Y. Li, Z. Weng, Y. Wang, L. Chen, D. Sheng, J. Diwu, Z. Chai, T. E. Albrecht-Schmitt, S. Wang, *Dalton Trans.* **2016**, *45*, 918–921; l) Y.-F. Niu, L.-T. Cui, J. Han, X.-L. Zhao, *J. Solid State Chem.* **2016**, *241*, 18–25; m) C. Qiao, X. Qu, Q. Yang, Q. Wei, G. Xie, S. Chen, D. Yang, *Green Chem.* **2016**, *18*, 951–956; n) Y.-J. Qu, J. Li, *Inorg. Chem. Commun.* **2017**, *76*, 77–80.

[14] a) P. Wu, J. Wang, C. He, X. Zhang, Y. Wang, T. Liu, C. Duan, *Adv. Funct. Mater.* **2012**, *22*, 1698–1703; b) Z. Peng, X. Yi, Z. Liu, J. Shang, D. Wang, *ACS Appl. Mater. Interfaces* **2016**, *8*, 14578–14585; c) X.-L. Hu, C. Qin, X.-L. Wang, K.-Z. Shao, Z.-M. Su, *Chem. Commun.* **2015**, *51*, 17521–17524; d) M. Zhang, J. Han, H. Wu, Q. Wei, G. Xie, S. Chen, S. Gao, *RSC Adv.* **2016**, *6*, 94622–94628; e) D.-M. Chen, J.-Y. Tian, C.-S. Liu, *Inorg. Chem. Commun.* **2016**, *68*, 29–32; f) L. Wen, X. Wang, H. Shi, K. Lv, C. Wang, *RSC Adv.* **2016**, *6*, 1388–1394; g) Y. Du, N. Song, X. Lv, B. Hu, W. Zhou, Q. Jia, *Dyes Pign.* **2017**, *138*, 15–22.

[15] a) P. Wu, J. Wang, Y. Li, C. He, Z. Xie, C. Duan, *Adv. Funct. Mater.* **2011**, *21*, 2788–2794; b) P. Wu, C. He, J. Wang, X. Peng, X. Li, Y. An, C. Duan, *J. Am. Chem. Soc.* **2012**, *134*, 14991–14999; c) P. Wu, X. Guo, L. Cheng, C. He, J. Wang, C. Duan, *Inorg. Chem.* **2016**, *55*, 8153–8159.

[16] Y. E. Cheon, M. P. Suh, *Angew. Chem. Int. Ed.* **2009**, *48*, 2899–2903, *Angew. Chemie.* **2009**, *121*, 2943–2947.

[17] a) P. M. Usov, C. Fabian, D. M. D'Alessandro, *Chem. Commun.* **2012**, *48*, 3945–3947; b) F. J. Rizzuto,

T. B. Faust, B. Chan, C. Hua, D. M. D'Alessandro, , C. J. Kepert, *Chem. Eur. J.* **2014**, *20*, 17597–17605; c) C. Hua, A. Baldansuren, F. Tuna, D. Collison, D. M. D'Alessandro, *Inorg. Chem.* **2016**, *55*, 7270–7280.

[18] a) C. F. Leong, T. B. Faust, P. Turner, P. M. Usov, C. J. Kepert, R. Babarao, A. W. Thorntonb, D. M. D'Alessandro, *Dalton Trans.* **2013**, *42*, 9831–9839; b) C. F. Leong, B. Chan, T. B. Faust, D. M. D'Alessandro, *Chem. Sci.* **2014**, *5*, 4724–4728; c) C. Hua, B. F. Abrahams, D. M. D'Alessandro, *Cryst. Growth Des.* **2016**, *16*, 1149–1159.

[19] a) K. Koh, A. G. Wong-Foy, A. J. Matzger, *J. Am. Chem. Soc.* **2010**, *132*, 15005–15010; b) A. Dutta, A. G. Wong-Foy, A. J. Matzger, *Chem. Sci.* **2014**, *5*, 3729–3734; c) L.-T. Cui, Y.-F. Niu, J. Han, X.-L. Zhao, *J. Solid State Chem.* **2015**, *227*, 155–164; d) L. Yang, S. Zhang, X. Qu, Q. Yang, X. Liu, Q. Wei, G. Xie, S. Chen, *J. Solid State Chem.* **2015**, *231*, 223–229; e) S. J. Lee, C. Doussot, A. Baux, L. Liu, G. B. Jameson, C. Richardson, J. J. Pak, F. Trousselet, F.-X. Coudert, S. G. Telfer, *Chem. Mater.* **2016**, *28*, 368–375; f) O. Akintola, S. Ziegenbalg, A. Buchholz, H. Görls, W. Plass, *CrystEngComm* **2017**, *19*, 2723–2732; g) S. J. Lee, C. Doussot, S. G. Telfer, *Cryst. Growth Des.* **2017**, *17*, 3185–3191.

[20] D. Sun, D. J. Collins, Y. Ke, J.-L. Zuo, H.-C. Zhou, *Chem. Eur. J.* **2006**, *12*, 3768–3776.

[21] a) Y. E. Cheon, J. Park, M. P. Suh, *Chem. Commun.* **2009**, 5436–5438; b) H. J. Park, Y. E. Cheon, M. P. Suh, *Chem. Eur. J.* **2010**, *16*, 11662–11669; c) R. Grünker, I. Senkovska, R. Biedermann, N. Klein, A. Klausch, I. A. Baburin, U. Müller, S. Kaskel, *Eur. J. Inorg. Chem.* **2010**, 3835–3841; d) R. Grünker, I. Senkovska, R. Biedermann, N. Klein, M. R. Lohe, P. Müller, S. Kaskel, *Chem. Commun.* **2011**, *47*, 490–492; e) X. Li, X. Chen, F. Jiang, L. Chen, S. Lu, Q. Chen, M. Wu, D. Yuan, M. Hong, *Chem. Commun.* **2016**, *52*, 2277–2280; f) X. Li, F. Jiang, L. Chen, M. Wu, S. Lu, J. Pang, K. Zhou, X. Chen, M. Hong, *CrystEngComm* **2016**, *18*, 2239–2243.

[22] a) P. Müller, F. M. Wisser, V. Bon, R. Grünker, I. Senkovska, S. Kaskel, *Chem. Mater.* **2015**, *27*, 2460–2467; b) P. Müller, V. Bon, I. Senkovska, J. Getzschmann, M. S. Weiss, S. Kaskel, *Cryst. Growth Des.* **2017**, *17*, 3221–3228; c) P. Müller, F. M. Wisser, P. Freund, V. Bon, I. Senkovska, S. Kaskel, *Inorg. Chem.* **2017**, *56*, 14164–14169.

[23] H. K. Chae, M. Eddaoudi, J. Kim, S. I. Hauck, J. F. Hartwig, M. O'Keeffe, O. M. Yaghi, *J. Am. Chem. Soc.* **2001**, *123*, 11482–11483.

[24] G. Lai, X. Bu, J. Santos, *Synlett* **1997**, 1275–1276.

[25] B. Liu, Q. Zhang, H. Ding, G. Hu, Y. Du, C. Wang, J. Wu, S. Li, H. Zhou, J. Y. et al, *Dyes Pigm.* **2012**, *95*, 149–160.

[26] R. Lartia, C. Allain, G. Bordeau, F. Schmidt, C. Fiorini-Debuisschert, F. Charra, M. P. Teulade-Fichou, *J. Org. Chem.* **2008**, *73*, 1732–1744.

[27] a) K. Sreenath, T. Thomas, K. Gopidas, *Org. Lett.* **2011**, *13*, 1134–1137; b) S. Sumalekshmy, K. Gopidas, *Chem. Phys. Lett.* **2005**, *413*, 294–299.

[28] B. A. Blight, A. F. Stewart, N. Wang, S. W. J.-S. Lu, *Inorg. Chem.* **2012**, *51*, 778–780.

[29] O. Kahn, *Molecular Magnetism*, Wiley-VCH Inc., Weinheim, **1993**.

[30] a) J. P. Naskar, C. Biswas, B. Guhathakurta, N. Aliaga-Alcalde, L. Lu, M. Zhu, *Polyhedron* **2011**, *30*, 2310–2319; b) A. Aijaz, E. C. Sanudo, P. K. Bharadwaj, *Inorg. Chim. Acta* **2009**, *362*, 4246–4250.

[31] N. F. Chilton, R. Anderson, L. Turner, A. Soncini, K. Murray, *J. Comput. Chem.* **2013**, *34*, 1164–1175.

[32] C.-C. Chang, M.-k. Leung, *Chem. Mater.* **2008**, *20*, 5816–5821.

[33] a) M. Oyama, K. Nozaki, S. Okazaki, *Anal. Chem.* **1991**, *63*, 1387–1392; b) T. Zhang, A. Brajter-Toth, *Anal. Chem.* **2000**, *72*, 2533–2540.; c) O. Yurchenko, D. Freytag, L. Z. Borg, R. Zentel, J. Heinze, S. Ludwigs, *J. Phys. Chem. B* **2012**, *116*, 30–39.

[34] a) C. Quinton, V. Alain-Rizzo, C. Dumas-Verdes, F. Miomandr, P. Audebert, *Electrochim. Acta* **2013**, *110*, 693–701; b) C.-J. Yao, Y.-W. Zhong, J. Yao, *Inorg. Chem.* **2013**, *52*, 10000–10008.

[35] J. M. Olmos, A. Molina, E. Laborda, F. Martínez-Ortiz, *Electrochim. Acta* **2015**, *176*, 1044–1053.

[36] S. Dapperheld, E. Steckhan, K.-H. Grosse Brinkhaus, T. Esch, *Chem. Ber.* **1991**, *124*, 2557–2567.

[37] a) B. Jin, P. Liu, Y. Wang, Z. Zhang, Y. Tian, J. Yang, S. Zhang, F. Cheng, *J. Phys. Chem. B* **2007**, *111*, 1517–1522; b) W. H. Morrison, S. Krogsrud, D. N. Hendrickson, *Inorg. Chem.* **1973**, *12*, 1998–2004.

[38] a) J. B. Flanagan, S. Margel, A. J. Bard, F. C. Anson, *J. Am. Chem. Soc.* **1978**, *100*, 4248–4253; b) F. Ammar, J. Savéant, *J. Electroanal. Chem. Interfacial Electrochem.* **1973**, *47*, 215–221.

[39] R. I. Walter, *J. Am. Chem. Soc.* **1966**, *88*, 1923–1930.

[40] F. A. Neugebauer, S. Bamberger, W. R. Groh, *Chem. Ber.* **1975**, *108*, 2406–2415.

[41] H. van Willigen, *J. Am. Chem. Soc.* **1967**, *89*, 2229–2230.

[42] a) M. Mikuriya, H. Azuma, J. Sun, D. Yoshioka, M. Handa, *Chem. Lett.* **2002**, *31*, 608–609; b) D. Maspoch, D. Ruiz-Molina, K. Wurst, C. Rovira, J. Veciana, *Chem. Commun.* **2002**, 2958–2959; c) D. Maspoch, D. Ruiz-Molina, K. Wurst, J. Vidal-Gancedo, C. Rovira, J. Veciana, *Dalton Trans.* **2004**, 1073–1082.

[43] D. Takamatsu, K.-i. Fukui, S. Arouac, Y. Yamakoshi, *Org. Biomol. Chem.* **2010**, *8*, 3655–3664.

[44] S. Stoll, A. Schweiger, *J. Magn. Reson.* **2006**, *178*, 42–55.

[45] a) B. Nonius, *COLLECT; Data Collection Software*, Delft, The Netherlands, **1998**; b) Z. Otwinowski, W. Minor, *Methods in Enzymology*, Academic Press, Vol. 276 of *Macromolecular Crystallography Part A*, Chap. Processing of X-ray Diffraction Data Collected in Oscillation Mode, **1997**, 307–326; c) Bruker AXS Inc., Madison, Wisconsin, USA., *SADABS 2.10.*, **2002**.

[46] G. M. Sheldrick, *Acta Crystallogr.* **2015**, *C71*, 3–8.

[47] A. L. Spek, *Acta Crystallogr.* **2015**, *C71*, 9–18.

[48] H. Putz, K. Brandenburg, *Diamond 4.2.2 - Crystal and Molecular Structure Visualization*, Crystal Impact, Kreuzherrenstr. 102, 53227 Bonn, Germany.

[49] O. Dolomanov, L. Bourhis, R. Gildea, J. Howard, H. Puschmann, *J. Appl. Cryst.* **2009**, *42*, 339–341.

[50] L. J. Farrugia, *J. Appl. Crystallogr.* **2012**, *45*, 849–854.

[51] a) E. Baerends, D. Ellis, P. Ros, *Chem. Phys.* **1973**, *2*, 41–51; b) B. I. Dunlap, J. Connolly, J. Sabin, *J. Chem. Phys.* **1979**, *71*, 3396–3402; c) C. Van Alsenoy, *J. Comput. Chem.* **1988**, *9*, 620–626.

[52] a) J. P. Perdew, Y. Wang, *Phys. Rev. B* **1992**, *45*, 13244–13249; b) J. P. Perdew, K. Burke, M. Ernzerhof, *Phys. Rev. Lett.* **1996**, *77*, 3865–3868.

[53] F. Weigend, R. Ahlrichs, *Phys. Chem. Chem. Phys.* **2005**, *7*, 3297–3305.

[54] TURBOMOLE V6.6 2014, a development of University of Karlsruhe and Forschungszentrum Karlsruhe GmbH, 1989-2007, TURBOMOLE GmbH, since 2007; available from http://www.turbomole.com.

[55] J. P. Perdew, M. Ernzerhof, K. Burke, *J. Chem. Phys.* **1996**, *105*, 9982–9985.

[56] a) K. Yamaguchi, Y. Takahara, T. Fueno, *Ab-initio molecular orbital studies of structure and reactivity of transition metal-oxo compounds*, Springer, **1986**, 155–184; b) T. Soda, Y. Kitagawa, T. Onishi, Y. Takano, Y. Shigeta, H. Nagao, Y. Yoshioka, K. Yamaguchi, *Chem. Phys. Lett.* **2000**, *319*, 223–230.

Metal Bonded Redox-Active Triarylamines and their Interactions: Synthesis, Structure, and Redox Properties of Paddle-Wheel Copper Complexes

Oluseun Akintola, Michael Böhme, Manfred Rudolph, Axel Buchholz,
Helmar Görls, and Winfried Plass

Supplementary Information

Contents

List of Figures

List of Tables

1 Thermogravimetric analysis

Figure S1: Thermogravimetric data for complexes **5** (top left), **6** (top right), **7** (bottom left), and **8** (bottom right).

Table S1: Analytical data based on thermogravimetric and elemental analysis for compounds **5**–**8**.

| | loss of solvent molecules[a] | | rest mass | | molecular weight ($g\,mol^{-1}$) | solvent molecules of crystallization |
	measured (%)	calcd (%)	measured (%)	calcd (%)		
5	24.1[b]	25.5	8.7	9.3	1718.93	4 dmf
6	10.3[c]	11.1	10.8	10.2	1565.90	1.5 H_2O
7	12.1[d]	12.1	8.7	8.1	1966.52	1 H_2O and 1 dmf
8	9.2[e]	8.8	9.6	9.5	1666.77	none

[a] Solvent molecules of crystallization and the two coordinated dmf molecules at the copper centers.
[b] Mass loss up to about 200 °C.
[c] Mass loss up to about 240 °C.
[d] Mass loss up to about 260 °C.
[e] Mass loss between about 190−250 °C.

2 Additional structural data
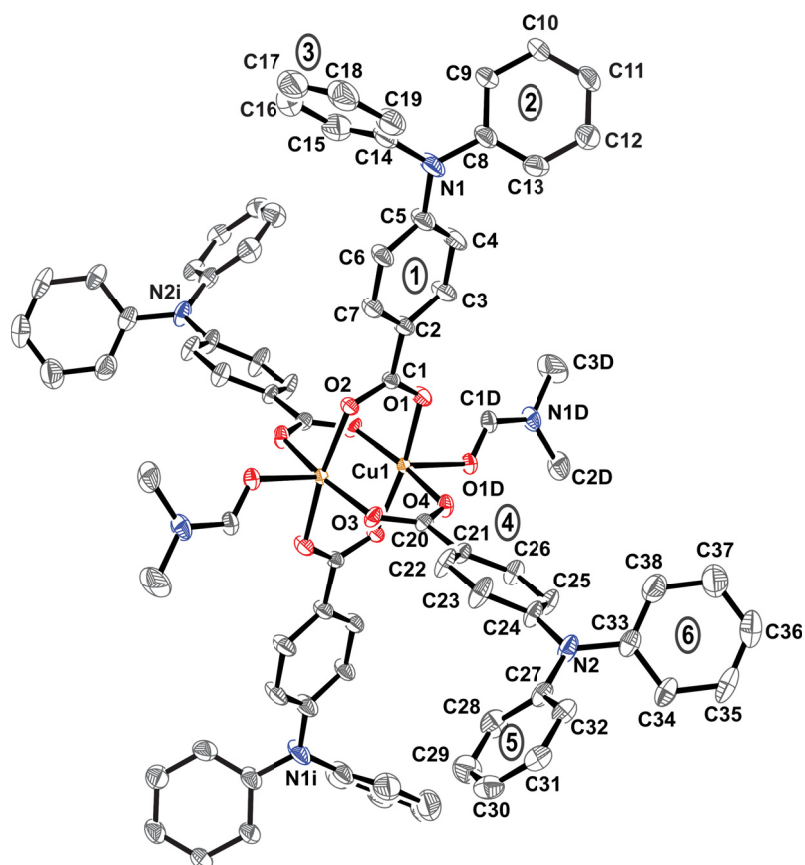
Figure S2: Molecular structure and numbering scheme of **5**. The ellipsoids are drawn at the 40% probability level. Hydrogen atoms are omitted for clarity. Individual phenyl rings of the triphenylamine fragments are labeled by numbers encased in ovals.

Table S2: Crystallographic data and structure refinement parameters for complexes **5–8**.

Complexes	5	6	7	8
Empirical formula	$C_{82}H_{70}Cu_2N_6O_{10}$[a]	$C_{93}H_{93}Cu_2N_7O_{11}$	$C_{114}H_{136}Cu_2N_6O_{11}$[a]	$C_{90}H_{86}Cu_2N_6O_{18}$
Formula weight	1426.52[a]	1611.82	1893.36[a]	1666.73
Temperature (°C)	−140(2)	−140(2)	−140(2)	−140(2)
Crystal system	triclinic	triclinic	triclinic	triclinic
Space group	$P\bar{1}$	$P\bar{1}$	$P\bar{1}$	$P\bar{1}$
a (pm)	1228.77(3)	1208.66(3)	1216.08(4)	1067.14(2)
b (pm)	1461.43(3)	1346.56(3)	1497.08(4)	1436.82(3)
c (pm)	1472.98(3)	1554.34(3)	1905.54(6)	1525.57(3)
α (°)	97.081(1)	112.957(1)	76.738(2)	66.695(1)
β (°)	97.587(1)	110.327(1)	89.783(1)	79.644(1)
γ (°)	113.323(1)	95.215(1)	68.387(2)	68.752(1)
V (10^6 pm^3)	2362.52(9)	2107.90(6)	3126.74(17)	2000.44(7)
Z	1	1	1	1
ρ (g cm^{-3})	1.003[a]	1.270	1.006[a]	1.384
μ (cm^{-1})	4.99[a]	5.68	3.91[a]	6.07
θ_{max} (°)	27.50	27.49	25.35	27.50
Measured data	14940	13696	19578	13239
Data with $I > 2\sigma(I)$	9530	8976	9126	7901
Unique data (R_{int})	10641(0.0201)	9580(0.0138)	11116(0.0338)	9036(0.0238)
wR_2 (all data)[b]	0.0936	0.0898	0.2326	0.1097
R_1 ($I > 2\sigma(I)$)[b]	0.0413	0.0371	0.0819	0.0520
S[c]	1.060	1.060	1.063	1.142
Residual electron density (10^6 pm^3)	0.523/−0.359	0.757/−0.654	1.747/−0.762	0.572/−0.365
Absorption method	multi-scan	multi-scan	multi-scan	multi-scan
Absorption corrections T_{min}/T_{max}	0.659/0.746	0.634/0.746	0.683/0.746	0.633/0.746

[a] Derived parameters do not contain the contribution of the disordered solvent molecules.
[b] $R_1 = \sum(||F_o| - |F_c||)/\sum|F_o|$ and $wR_2 = \{\sum[w(F_o{}^2 - F_c{}^2)^2]/\sum[w(F_o{}^2)^2]\}^{1/2}$; with $w^{-1} = \sigma^2(F_o{}^2) + (aP)^2 + bP$ and $P = [2F_c{}^2 + \mathrm{Max}(F_o{}^2)]/3$.
[c] $S = \{\sum[w(F_o{}^2 - F_c{}^2)^2]/(N_o - N_p)\}^{1/2}$.

Figure S3: Molecular structure and numbering scheme of **6**. The ellipsoids are drawn at the 40% probability level. Hydrogen atoms are omitted for clarity. Individual phenyl rings of the triphenylamine fragments are labeled by numbers encased in ovals.
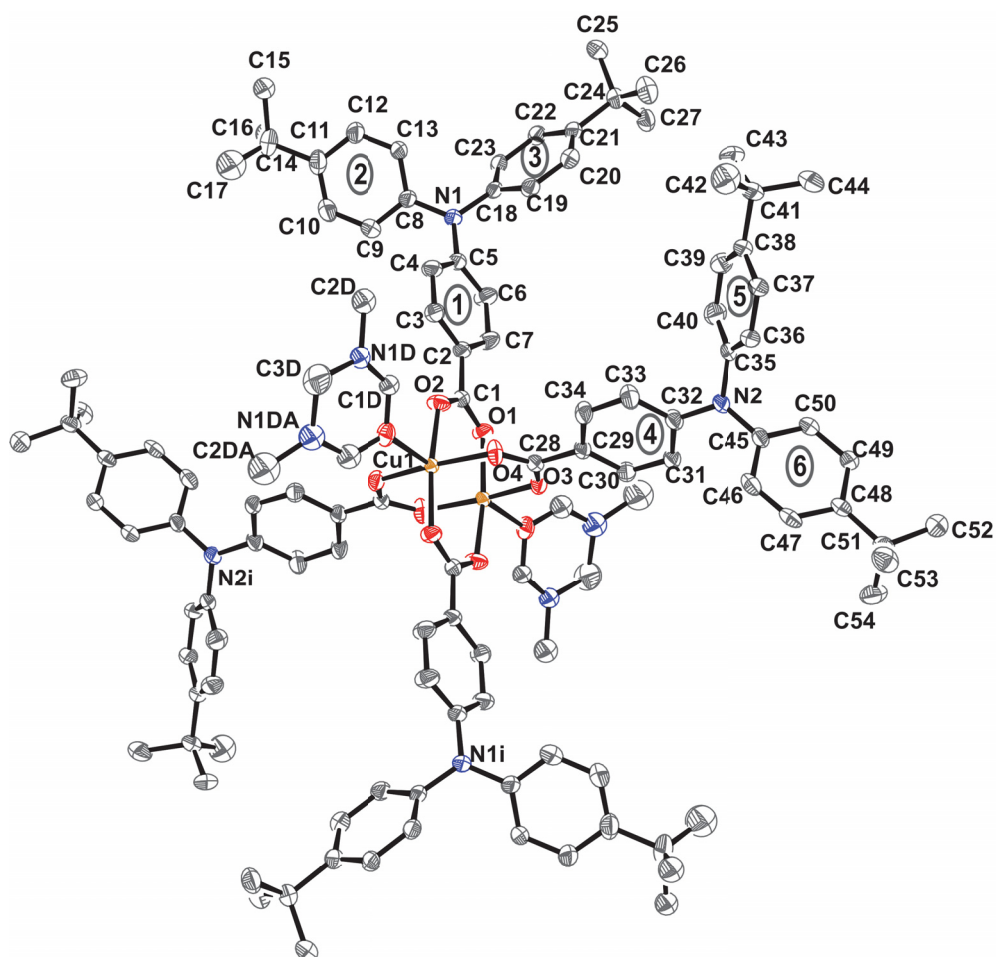
Figure S4: Molecular structure and numbering scheme of **7**. The ellipsoids are drawn at the 40% probability level. Hydrogen atoms are omitted for clarity. The dmf molecule coordinated at the copper center is disordered on two positions (1:1 ratio). Individual phenyl rings of the triphenylamine fragments are labeled by numbers encased in ovals.
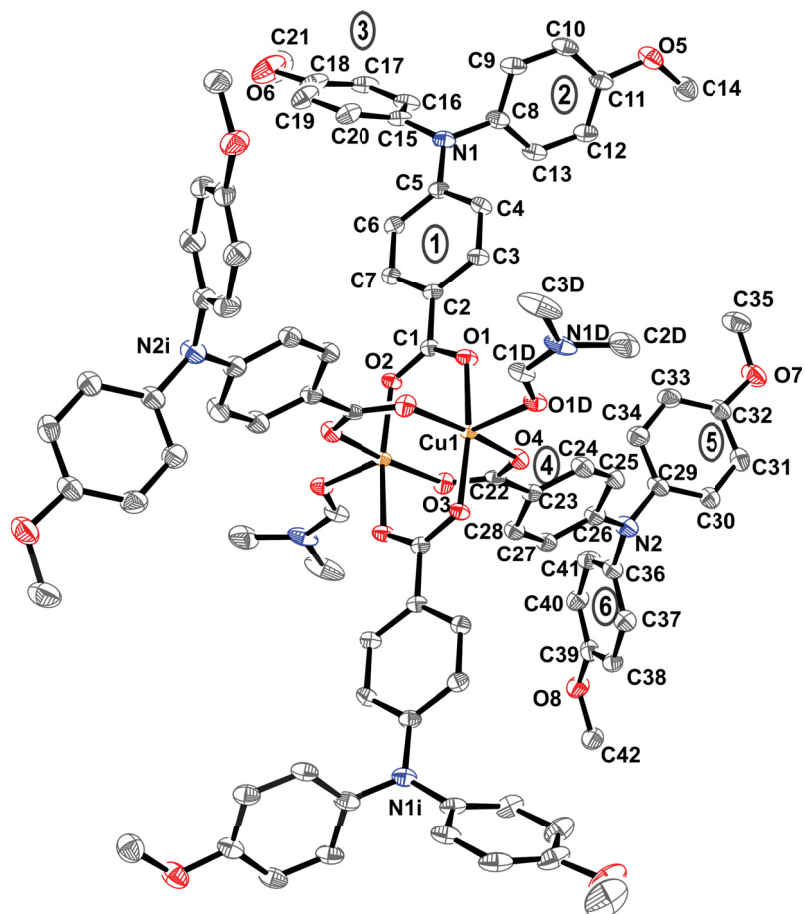
Figure S5: Molecular structure and numbering scheme of **8**. The ellipsoids are drawn at the 40% probability level. Hydrogen atoms are omitted for clarity. Individual phenyl rings of the triphenylamine fragments are labeled by numbers encased in ovals.

Table S3: Selected bond lengths and distances (in pm) for the Cu(II) ions in **5**–**8** compared with average values obtained from the CSD database.

	5	6	7	8	CSD_{av}
Cu1−O1	196.10(12)	195.67(12)	195.1(3)	195.26(18)	
Cu1−O2A	196.22(12)	197.42(12)	196.6(3)	196.91(17)	196.4(9)
Cu1−O3A	196.87(13)	196.32(12)	196.2(3)	196.53(18)	
Cu1−O4	195.40(12)	195.93(12)	195.5(3)	196.20(17)	
C1−O1	126.5(2)	126.3(2)	125.7(5)	126.6(3)	
C1−O2	126.6(2)	126.2(2)	126.7(5)	126.4(3)	126.1(8)
C20−O3	126.5(2)	126.3(2)	126.8(5)	125.8(3)	
C20−O4	126.3(2)	126.6(2)	125.3(5)	126.6(3)	
Cu1i···Cu1A	260.77(4)	258.97(4)	262.14(9)	260.84(6)	262.6(12)
Cu−O1D[a]	214.77(12)	215.77(12)	216.5(3)	218.66(18)	214.5(18)
Cui···[O4][b]	18.0(1)	17.2(1)	19.0(1)	18.2(1)	19.6(7)

[a] Oxygen donor of the apical dmf molecule.
[b] Displacement of the Cu(II) ions from the basal $[O_4]$ plane.
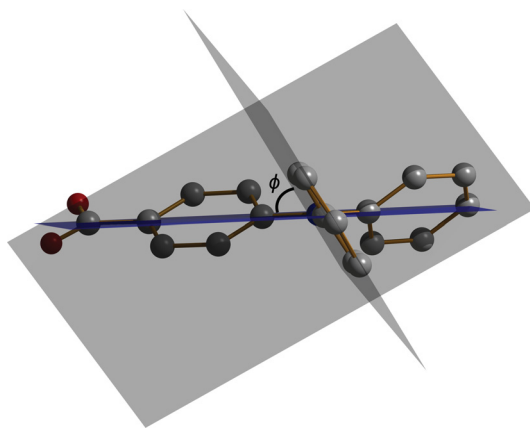
Figure S6: Representation of the dihedral angles ϕ between the plane given by the three carbon atoms at the amine nitrogen (violet) and phenyl rings (grey) in the complexes. See Table S4 for more details.
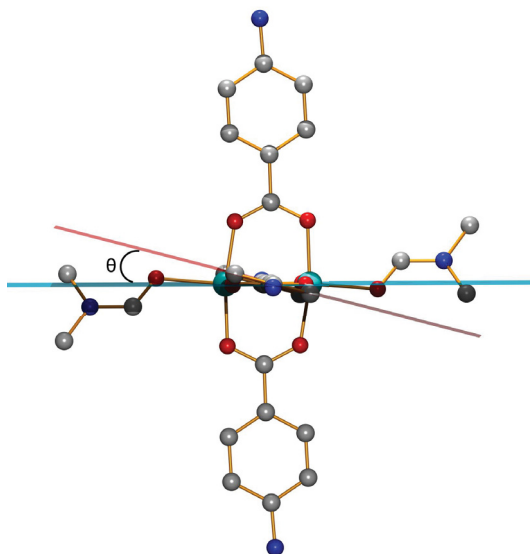
Figure S7: Representation of the dihedral angles θ between the plane given by the carboxylate group (blue) and the attached phenyl ring of the triphenylamine moiety (red) in the complexes. See Table S5 for more details.
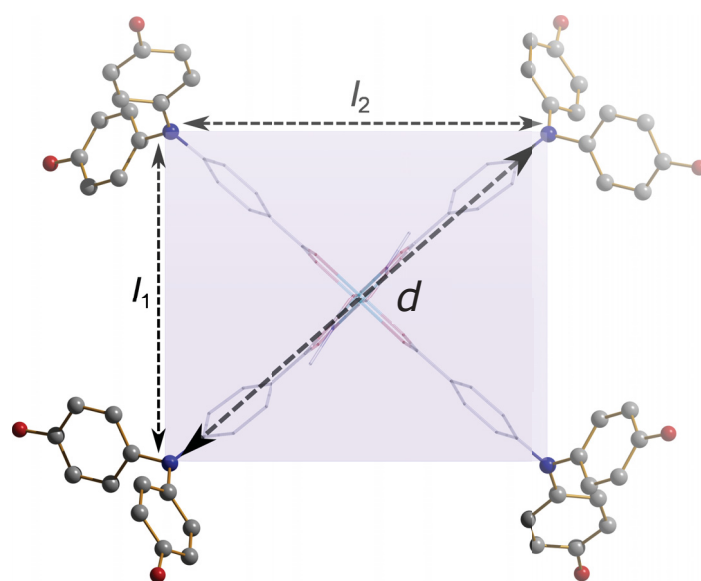
Figure S8: Representation of the N⋯N separations between the triphenylamine moieties within the complexes **5**−**8**. See Table S5 for more details.

Table S4: Dihedral angles ϕ (in °) between individual phenyl rings (for numbering see Figs. S2–S5) and the amine planes given by the mean plane defined by the three carbon atoms bound to the amine nitrogen for complexes **5**–**8** (see Fig. S6) as well as the displacement (in pm) of the nitrogen atom from the latter mean plane.

	R	$\phi(1)$ Ph–CO_2	$\phi(2)$ Ph–R	$\phi(3)$ Ph–R	N1$\cdots$[C_3][a]	$\phi(4)$ Ph–CO_2	$\phi(5)$ Ph–R	$\phi(6)$ Ph–R	N2$\cdots$[C_3][a]
5	H	41.9	41.2	36.3	5.5	28.2	60.2	38.9	1.3
6	Me	31.7	37.1	46.1	4.9	34.3	46.5	45.4	6.8
7	*t*-Bu	54.1	32.0	41.1	9.9	34.6	46.8	45.0	4.2
8	OMe	21.1	63.9	40.2	12.4	21.7	58.7	65.4	15.4

[a] Deviation of the nitrogen atom from the mean plane of the bonded carbon atoms.

Table S5: Dihedral angles θ (in °) between individual planes given by the mean plane defined by the carboxylate group and its attached phenyl ring of the triphenylamine moiety (see Fig. S7) as well as the distances (in pm) between the nitrogen atoms of the triphenylamine moieties (see Fig. S8) of complexes **5**–**8**.

	R	$\theta(1)$	$\theta(4)$	θ_{av}	l_1	l_2	d
5	H	15.0	6.7	10.9	1141.8	1184.7	1644.8
6	Me	5.2	9.0	7.1	1100.0	1226.1	1646.0
7	*t*-Bu	7.4	20.8	14.1	1145.4	1179.6	1645.7
8	OMe	8.8	27.8	18.3	1088.0	1234.6	1649.6

3 Powder diffraction data
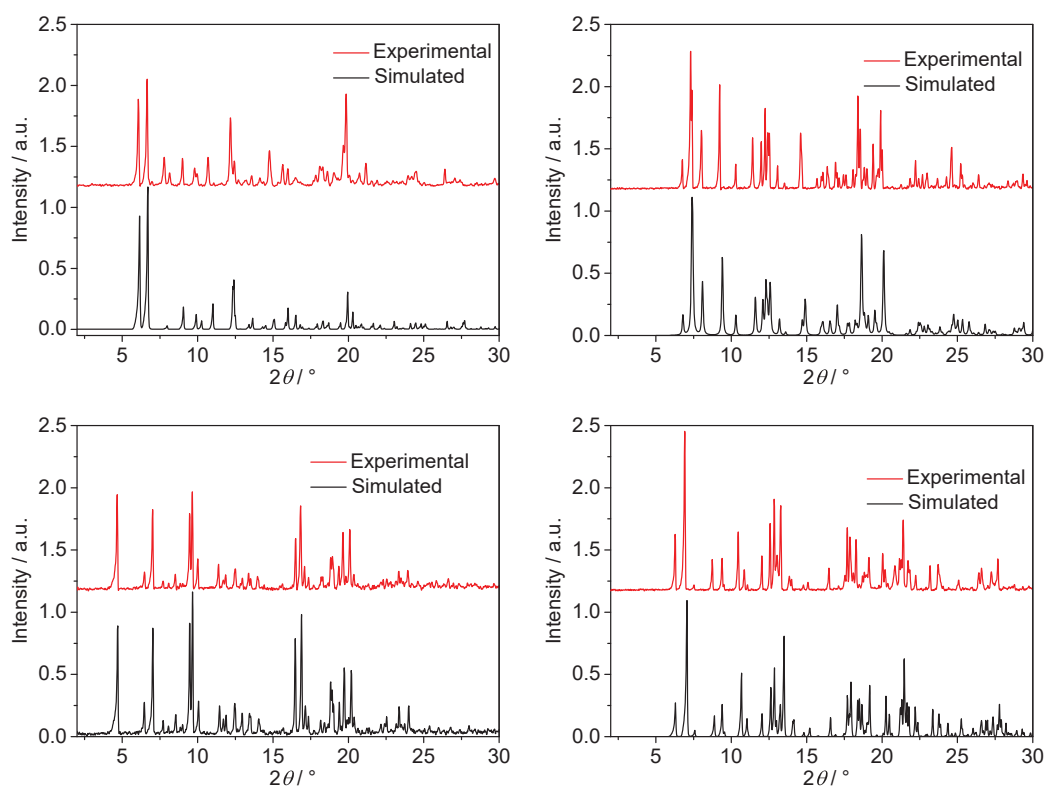
Figure S9: Powder diffraction data for the complexes **5** (top left), **6** (top right), **7** (bottom left), and **8** (bottom right).

4 Magnetic properties
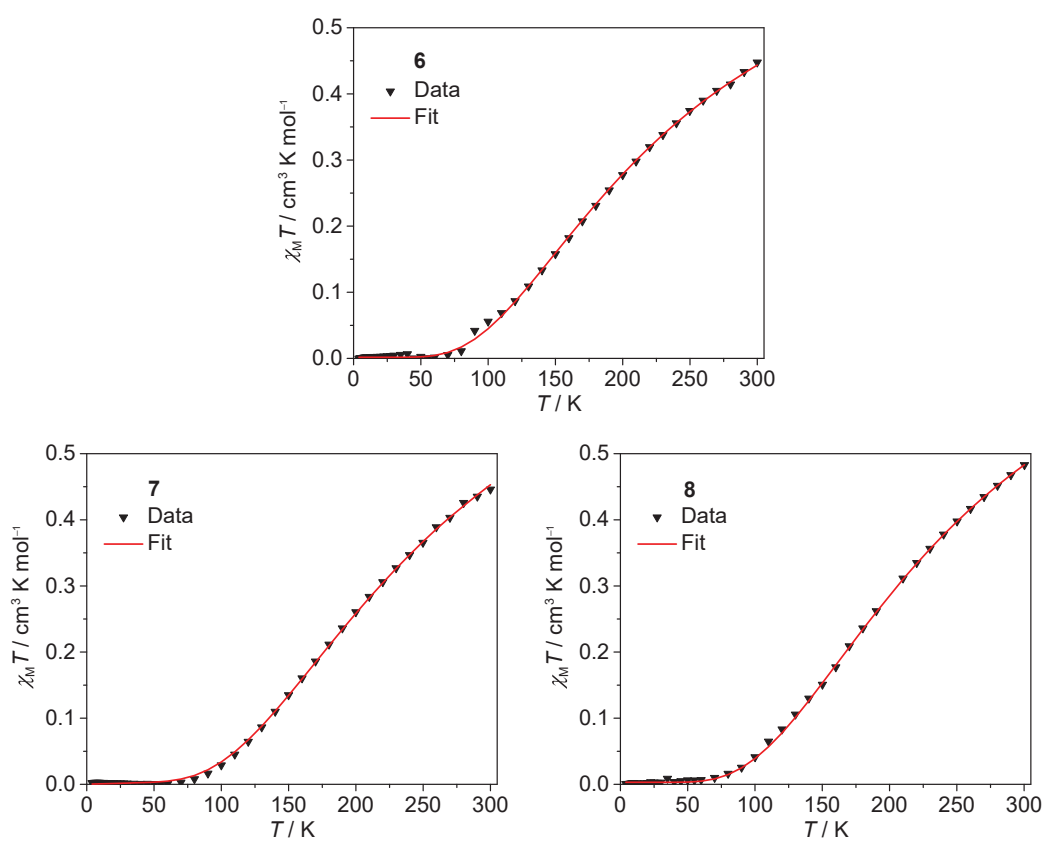
Figure S10: Temperature dependence of the magnetic susceptibility $\chi_M T$ for **6** (top), **7** (bottom left), and **8** (bottom right) at an applied field of 2 kOe. The solid red lines represent the best fit.

5   BS-DFT investigations on the complexes

Table S6: Detailed BS-DFT results for the complexes **5**–**8** (for further details see the computational details in the experimental section of the manuscript).

	state	$2S+1$	E_{elec} / au	$\left\langle S^2 \right\rangle$	J_{calcd} / cm^{-1}
5	HS	3	−7525.09675	2.00444	−345
	BS	1	−7525.09754	0.99636	
6	HS	3	−8087.67964	2.00449	−351
	BS	1	−8087.68045	0.99613	
7(A)^a	HS	3	−8781.93088	2.00438	−336
	BS	1	−8781.93165	0.99655	
7(B)^a	HS	3	−8781.92449	2.00442	−346
	BS	1	−8781.92528	0.99622	
8	HS	3	−8440.64954	2.00445	−345
	BS	1	−8440.65033	0.99622	

^{a} The structure of **7** contains a disorder of the dmf co-ligands on two positions (ratio 1:1).
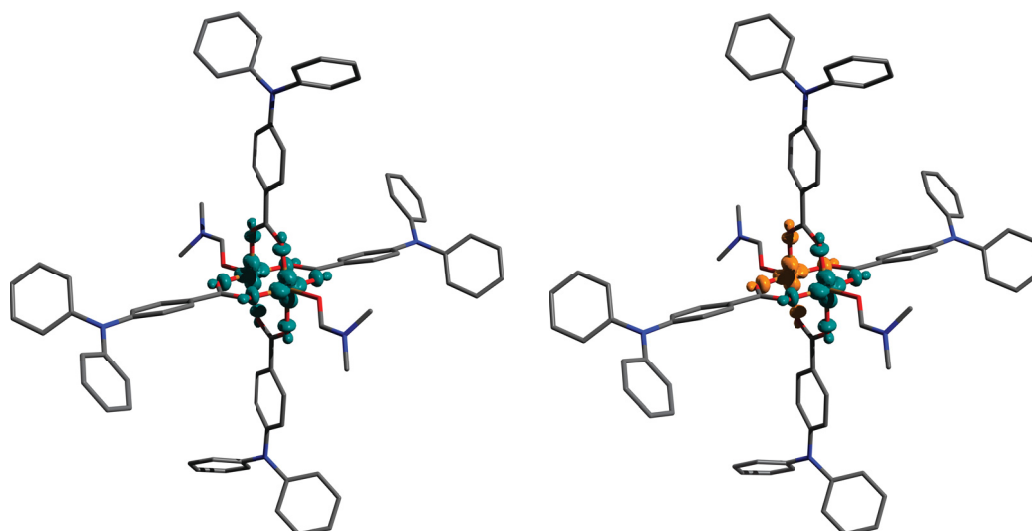
Figure S11: Spin-density isosurfaces (0.01 au; turquoise: net α density; orange: net β density) for the high-spin (left) and broken-symmetry (right) state of **5** obtained with DFT/PBE0/def2-TZVPP. Hydrogen atoms are omitted for clarity.
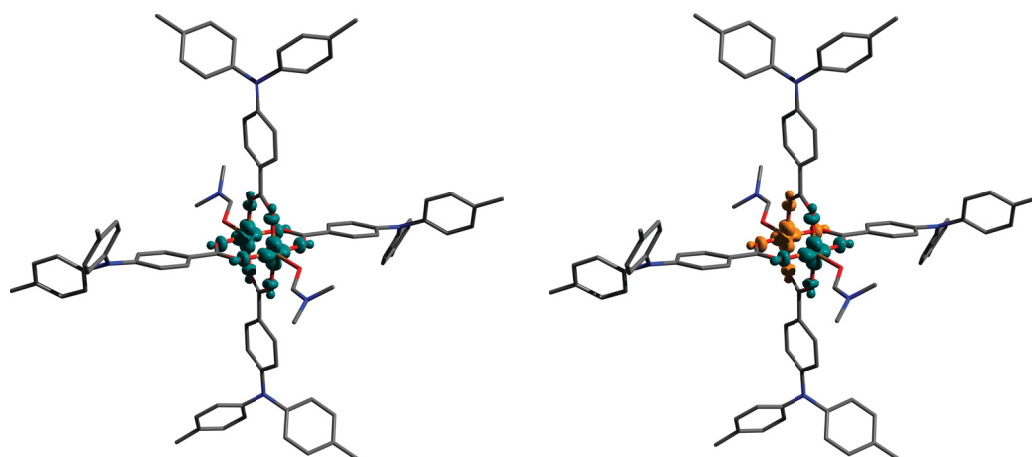
Figure S12: Spin-density isosurfaces (0.01 au; turquoise: net α density; orange: net β density) for the high-spin (left) and broken-symmetry (right) state of **6** obtained with DFT/PBE0/def2-TZVPP. Hydrogen atoms are omitted for clarity.
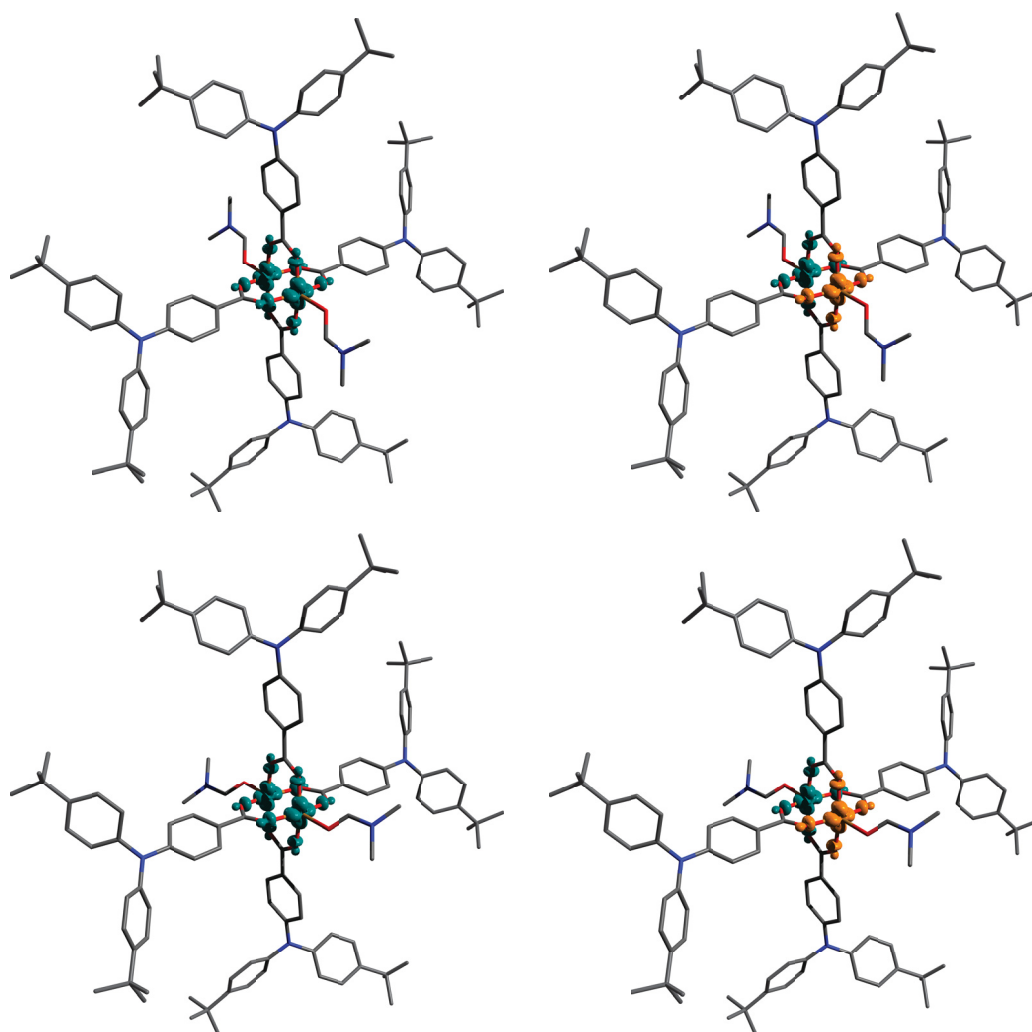
Figure S13: Spin-density isosurfaces (0.01 au; turquoise: net α density; orange: net β density) for the high-spin (left column) and broken-symmetry (right column) state of **7**(A) (top row) and **7**(B) (bottom row) obtained with DFT/PBE0/def2-TZVPP. Hydrogen atoms are omitted for clarity.
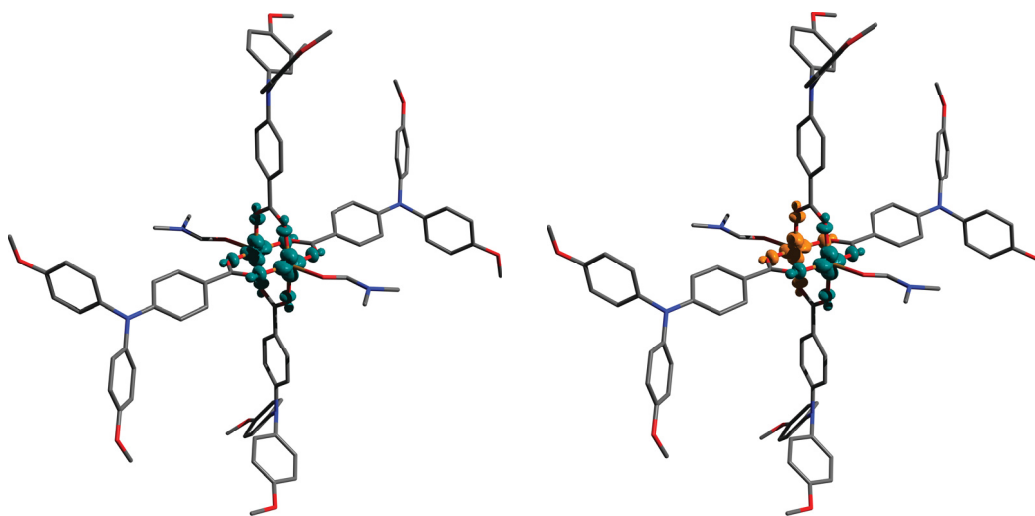
Figure S14: Spin-density isosurfaces (0.01 au; turquoise: net α density; orange: net β density) for the high-spin (left) and broken-symmetry (right) state of **8** obtained with DFT/PBE0/def2-TZVPP. Hydrogen atoms are omitted for clarity.

Table S7: Detailed BS-DFT results for the reduced structural models 5^M−8^M where the phenyl groups at the aminobenzoates have been replaced by methyl groups. Structural parameters are taken from the crystal structures of the complexes **5**−**8**.

|	state	$2S+1$	E_{elec} / au	$\langle S^2 \rangle$	J_{calcd} / cm^{-1}
5^M	HS	3	−5992.43785	2.00396	−348
	BS	1	−5992.43866	0.99607	
6^M	HS	3	−5992.43508	2.00445	−353
	BS	1	−5992.43588	0.99625	
7^M(A)^a	HS	3	−5992.39500	2.00439	−339
	BS	1	−5992.39578	0.99644	
7^M(B)^a	HS	3	−5992.38876	2.00443	−349
	BS	1	−5992.38956	0.99611	
8^M	HS	3	−5992.45512	2.00446	−346
	BS	1	−5992.45592	0.99619	

^{a} The structure of **7** contains a disorder of the dmf co-ligands on two positions (ratio 1:1).

Table S8: Detailed BS-DFT results for the reduced structural models 5^S−8^S where the amino substituent at the bridging benzoates have been replaced by hydrogen atoms. Structural parameters are taken from the crystal structures of the complexes **5**−**8**.

	state	$2S+1$	E_{elec} / au	$\langle S^2 \rangle$	J_{calcd} / cm^{-1}
5^S	HS	3	−5457.02275	2.00443	−344
	BS	1	−5457.02354	0.99643	
6^S	HS	3	−5457.01968	2.00448	−345
	BS	1	−5457.02047	0.99637	
7^S(A)^a	HS	3	−5456.98681	2.00442	−335
	BS	1	−5456.98760	0.99629	
7^S(B)^a	HS	3	−5456.99333	2.00438	−344
	BS	1	−5456.99410	0.99662	
8^S	HS	3	−5457.01951	2.00443	−341
	BS	1	−5457.02029	0.99642	

^{a} The structure of **7** contains a disorder of the dmf co-ligands on two positions (ratio 1:1).

6 Electrochemical properties
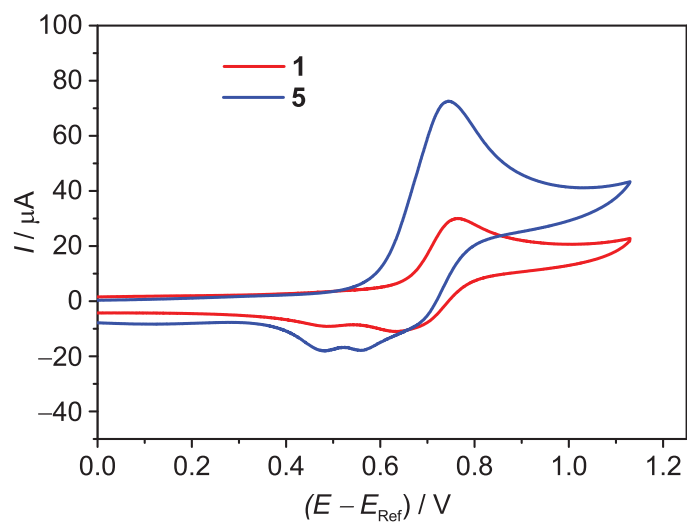
Figure S15: Cyclic voltammetry data for ligand **1** and complex **5** represented by red and blue lines, respectively.
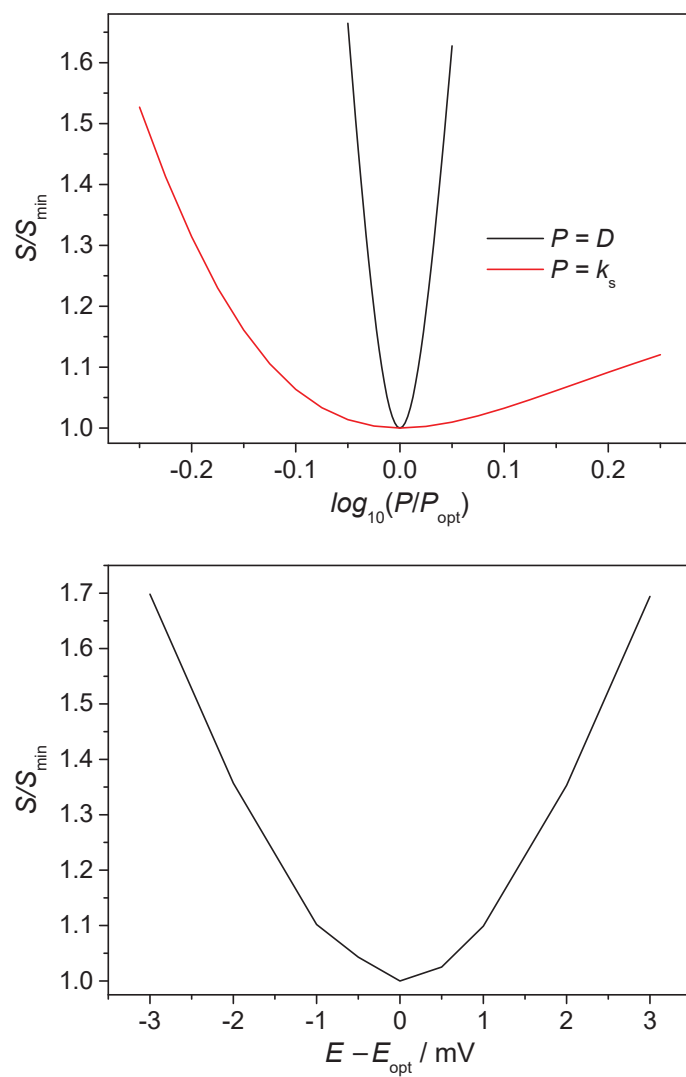
Figure S16: Error estimation for the parameters used for the simulation of the square-wave voltammograms of ligand **2** (see Figure S17): Effect of the variation of the standard potential (bottom) and the diffusion coefficient D as well as the heterogeneous rate constant k_s (top) on the overall standard deviation between experimental and simulated square-wave voltammograms. Similar results are obtained for the ligands **3** and **4**.
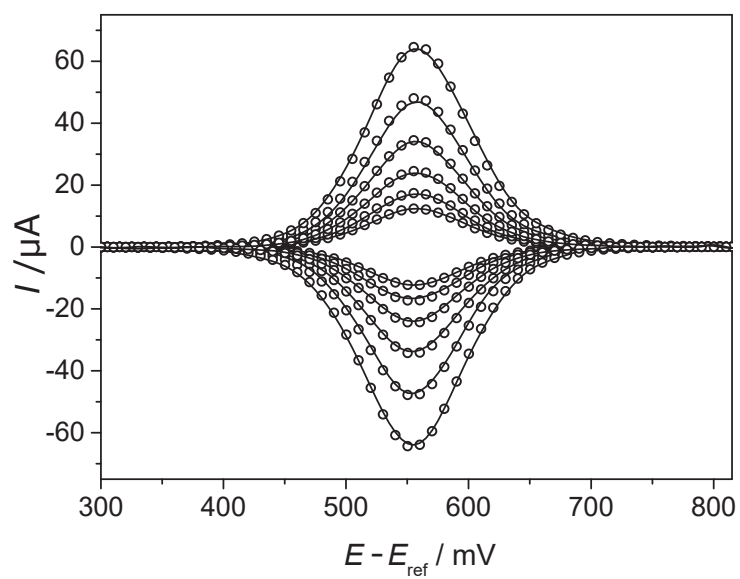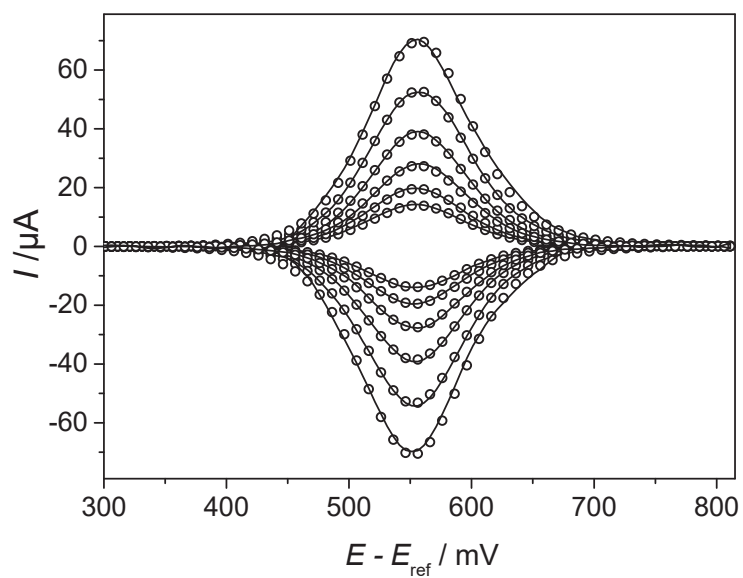
Figure S17: Square-wave voltammograms of the ligands **2** ($c = 2.00$ мм) and **3** ($c = 1.97$ мм) in dichloromethane solutions at square-wave frequencies of 25, 50, 100, 200, 400, and 600 Hz. Open circles represent simulated data, while lines represent experimental data.

24
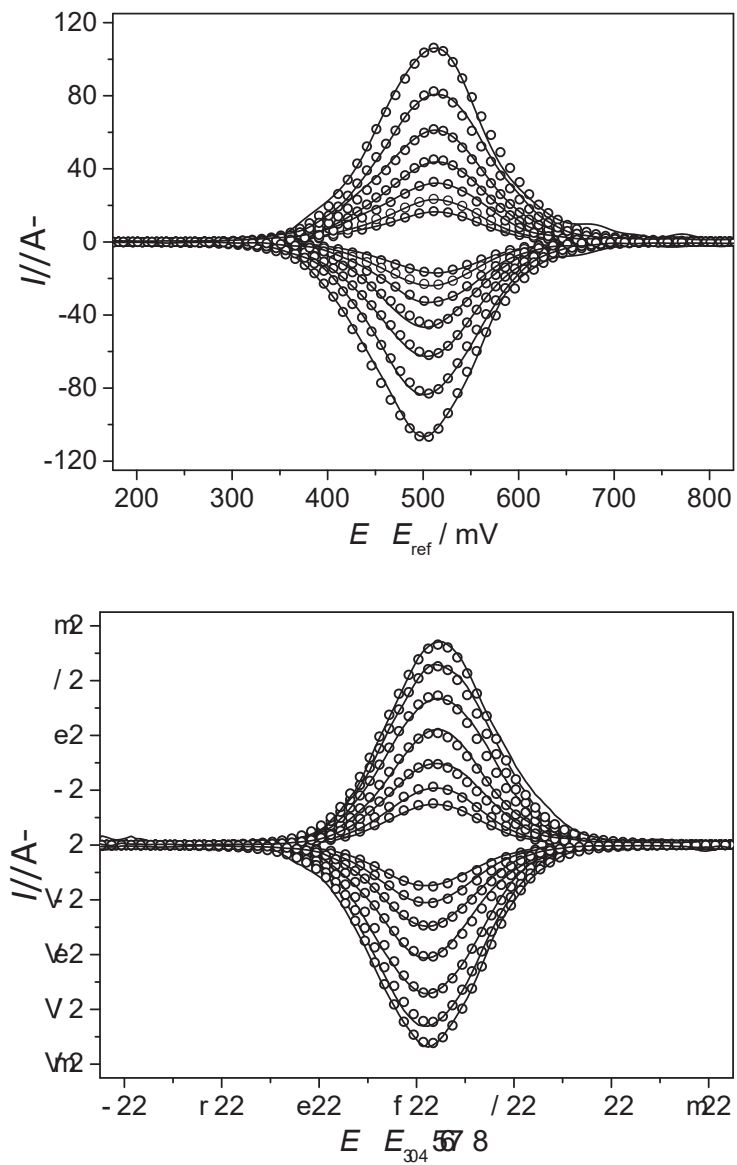
Figure S18: Square-wave voltammograms of the complexes **6** ($c = 1.01$ mᴍ) and **7** ($c = 1.05$ mᴍ) in dichloromethane solutions at square-wave frequencies of 25, 50, 100, 200, 400, 600, and 750 Hz. Open circles represent simulated data, while lines represent experimental data.

7   Spectroelectrochemistry
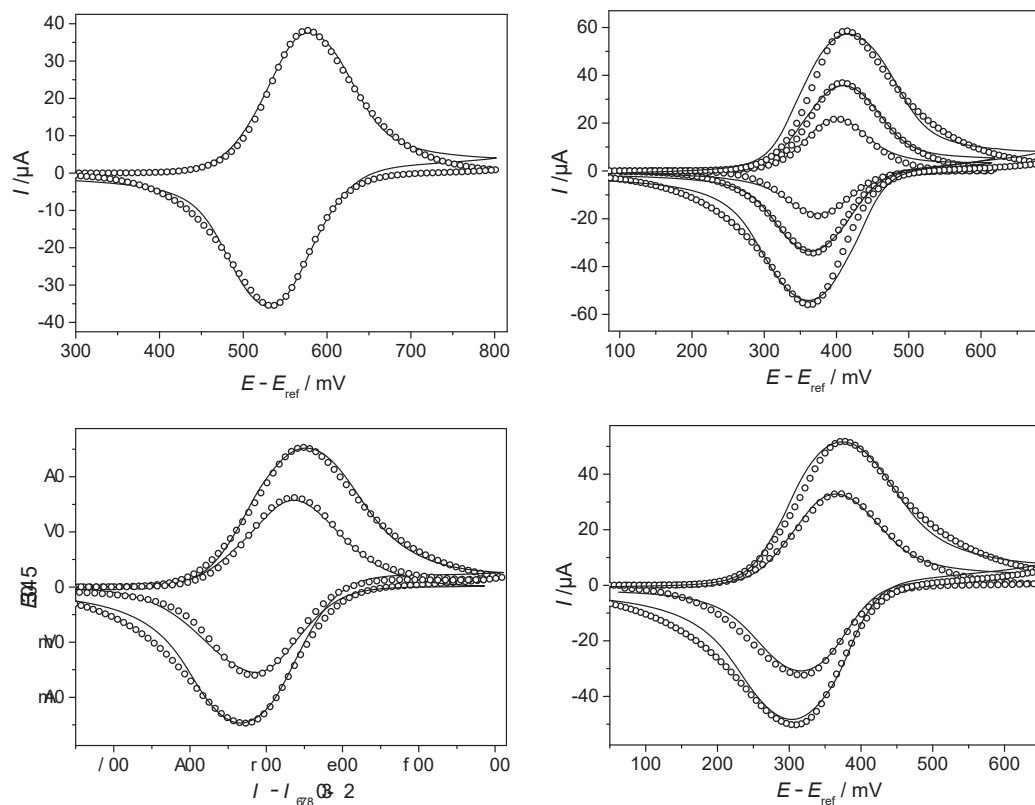
Figure S19: Thin-layer cyclic voltammograms in dichloromethane solutions.
(Top left): Ligand **2** ($c = 2.40$ mM) using a scan rate of 2.5 mV s^{-1}.
(Top right): Ligand **4** ($c = 2.40$ mM) using scan rates of 1.25, 2.5, and 5 mV s^{-1}.
(Bottom left): Complex **6** ($c = 0.59$ mM) using scan rates of 2.5 and 5 mV s^{-1}.
(Bottom right): Complex **8** ($c = 0.61$ mM) using scan rates of 2.5 and 5 mV s^{-1}.
Open circles represent simulated and lines experimental data.
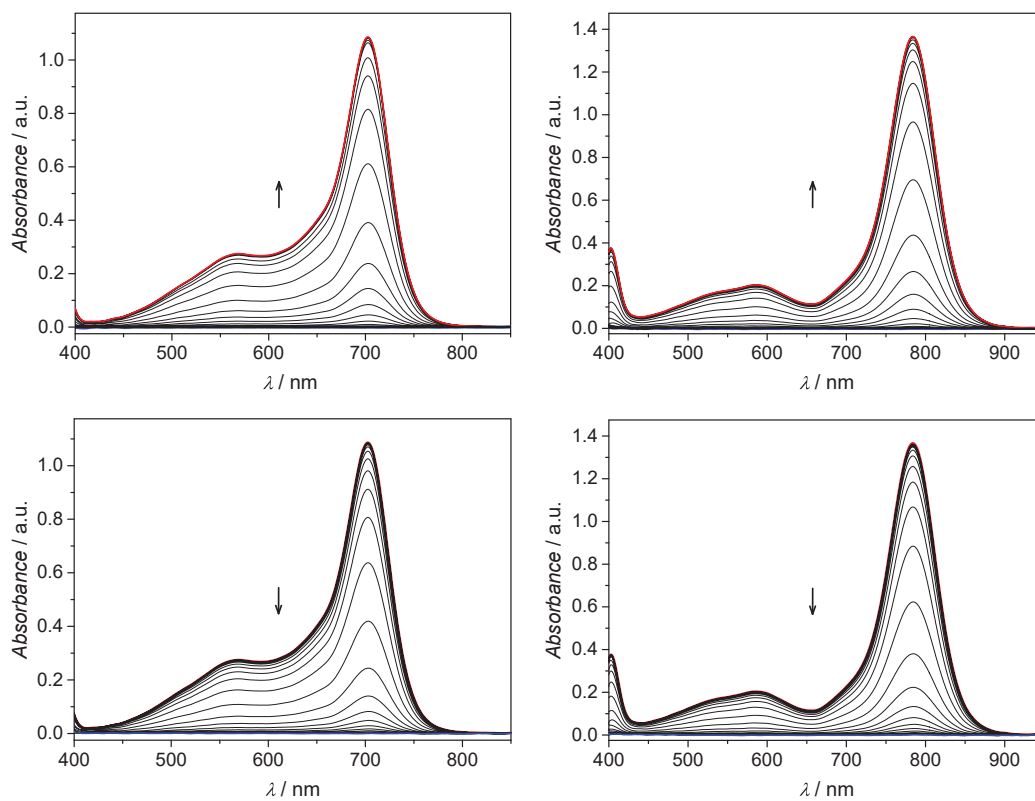
Figure S20: UV/vis spectra recorded during the forward (top row, blue to red line) and backward (bottom row, red to blue line) scans of the ligands **2** (left column) and **4** (right column). The difference in potential between successive spectra is 20 mV.
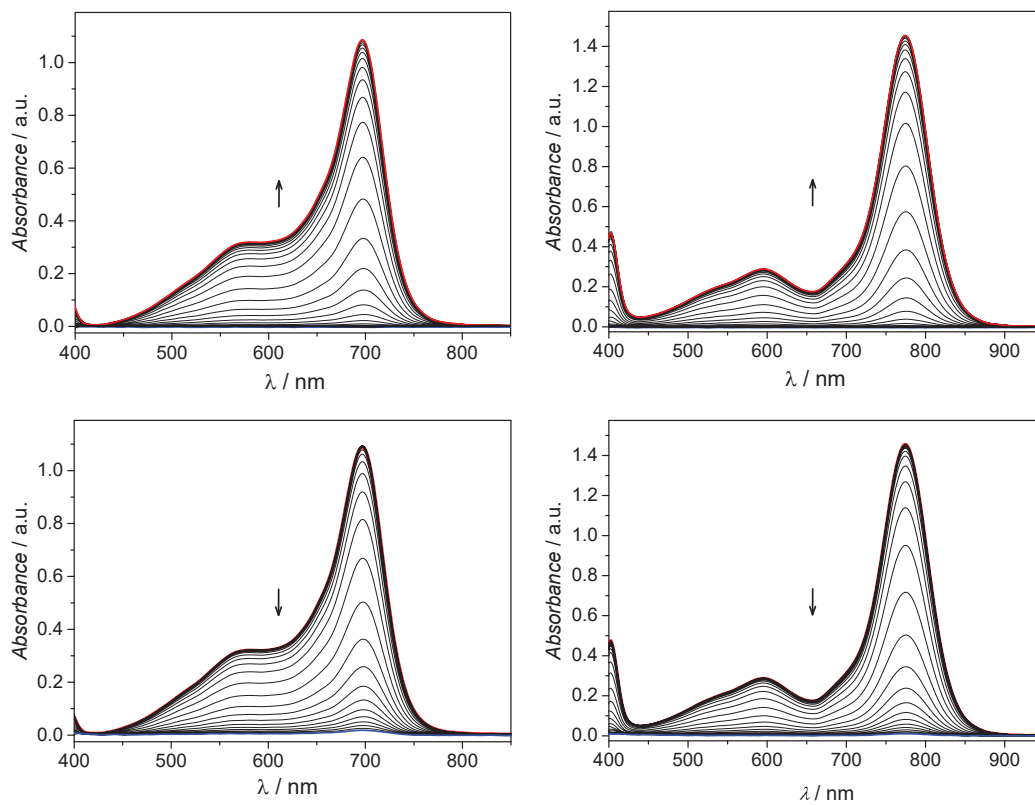
Figure S21: UV/vis spectra recorded during the forward (top row, blue to red line) and backward (bottom row, red to blue line) scans of the complexes **6** (left column) and **8** (right column). The difference in potential between successive spectra is 20 mV.
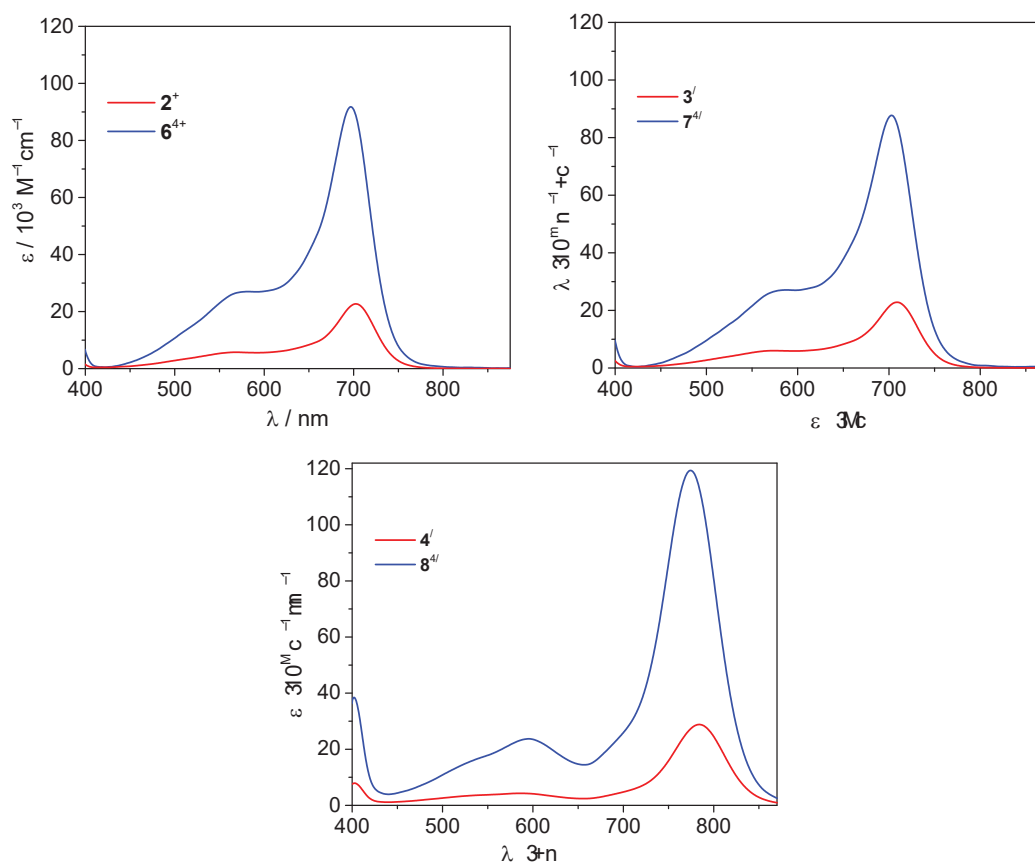
Figure S22: Comparison of the UV/vis spectra of the oxidized species of ligands and their corresponding complexes as determined from spectroelectrochemical experiments. (Top left): Methyl substitution, ligand **2** and complex **6**. (Top right): *tert*-Butyl substituent, ligand **3** and complex **7**. (Bottom): Methoxy substituent, ligand **4** and complex **8**.
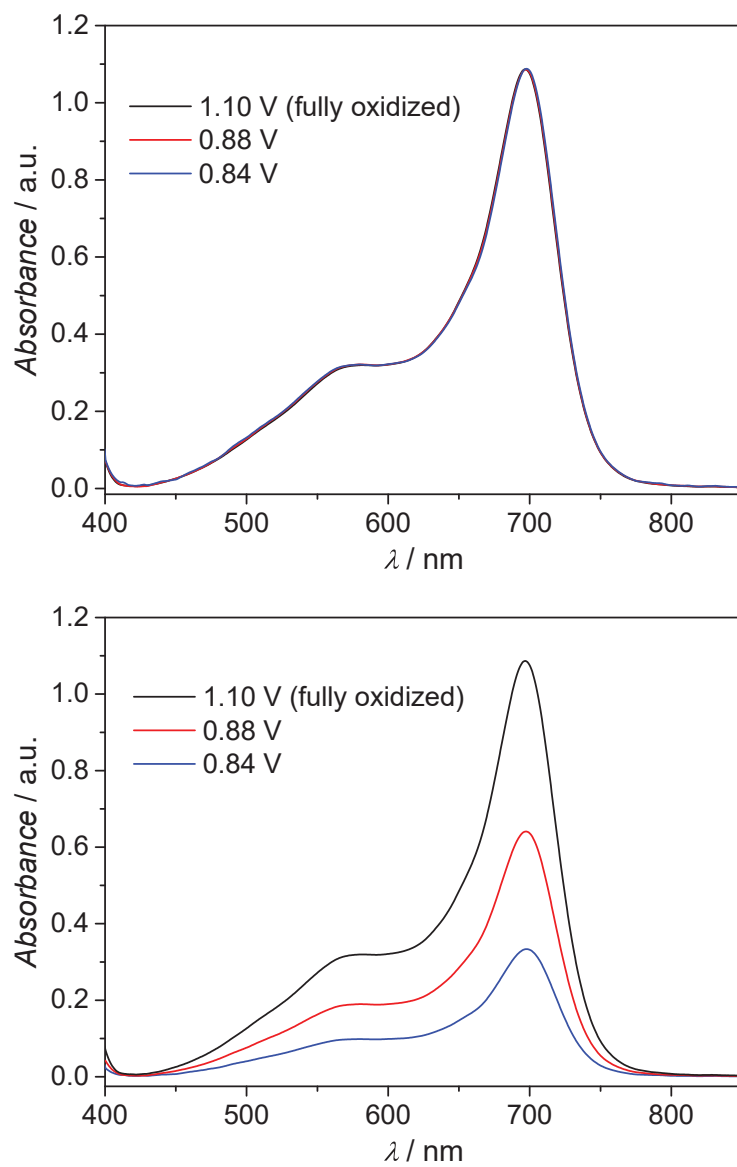
Figure S23: Superposition of scaled UV/vis spectra (top) for the oxidation of complex **6** measured at different potentials during the forward scan (bottom).

8　UV/vis spectra of chemically oxidized compounds
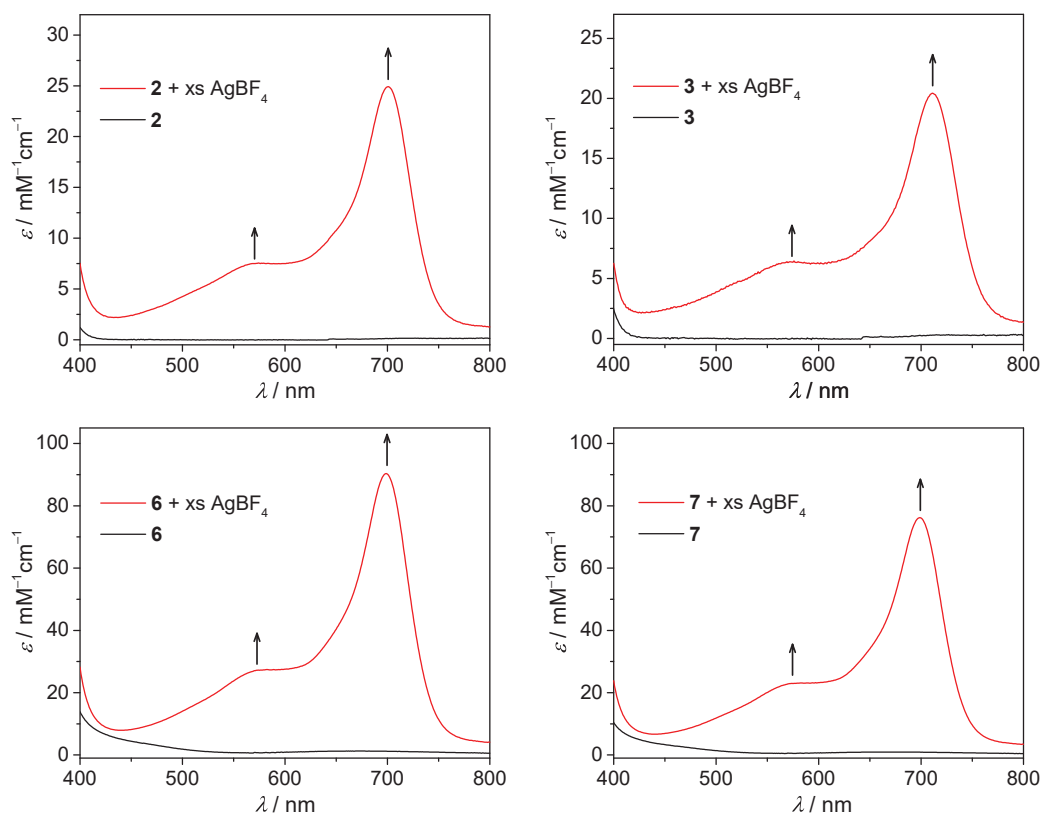
Figure S24: UV/vis spectra recorded after oxidation of the ligands **2** (top left) and **3** (top right) as well as the complexes **6** (bottom left) and **7** (bottom right) with an excess of AgBF$_4$ in dichloromethane solutions.

9 ESR spectra of chemically oxidized compounds
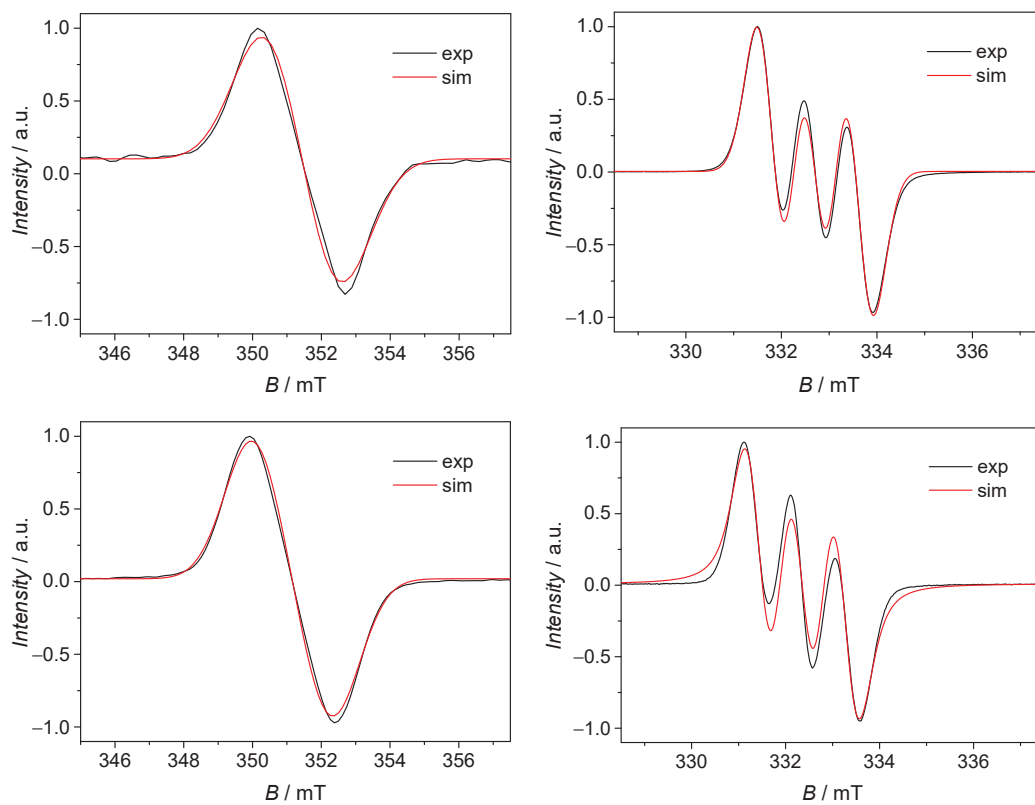
Figure S25: ESR spectra recorded at room temperature for the chemically oxidized ligands **2** (top left) and **3** (top right) as well as complexes **6** (bottom left) and **7** (bottom right) with an excess of AgBF$_4$ in dichloromethane solutions.

10 Theoretical investigations of chemically oxidized compounds

Table S9: Detailed BS-DFT results for the radical cations $\mathbf{5^{4+}}$–$\mathbf{8^{4+}}$; J'_{rad} refers to the individual coupling between a nitrogen-based organic radical and a copper(II) ion given as $J'_{rad} = J_{rad} / 8$.

	state	$2S + 1$	E_{elec} / au	$\left\langle S^2 \right\rangle$	J_{rad} / cm^{-1}	J'_{rad} / cm^{-1}
$\mathbf{5^{4+}}$	HS	7	−7523.88142	12.11291	22.6	2.8
	BS	3	−7523.88101	4.10727		
$\mathbf{6^{4+}}$	HS	7	−8086.50078	12.09917	22.9	2.9
	BS	3	−8086.50037	4.09465		
$\mathbf{7^{4+}(A)}^a$	HS	7	−8780.76716	12.09346	13.9	1.7
	BS	3	−8780.76690	4.08907		
$\mathbf{7^{4+}(B)}^a$	HS	7	−8780.76081	12.09343	13.8	1.7
	BS	3	−8780.76055	4.08897		
$\mathbf{8^{4+}}$	HS	7	−8439.47561	12.07713	14.4	1.8
	BS	3	−8439.47534	4.06909		

^{a} The structure of **7** contains a disorder of the dmf co-ligands on two positions (ratio 1:1).
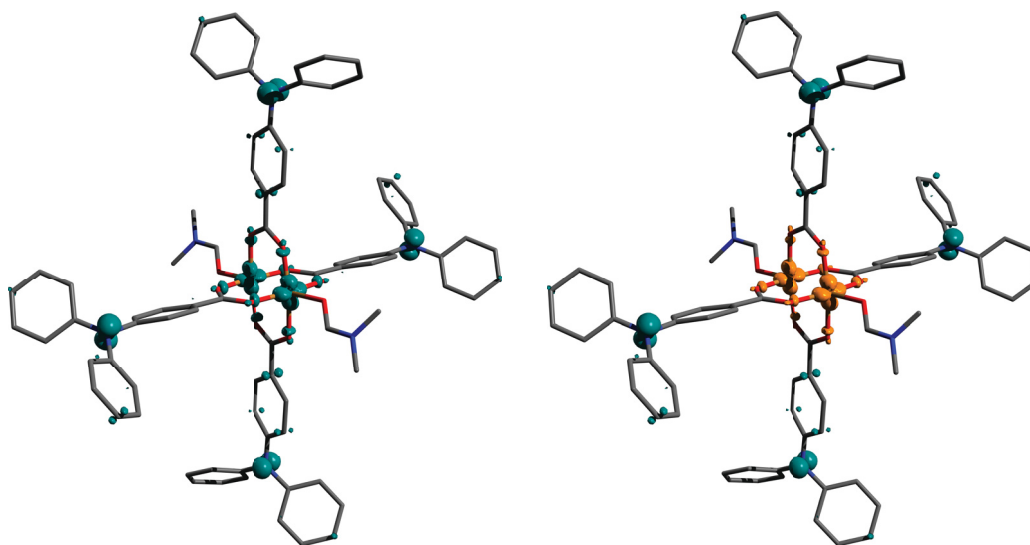
Figure S26: Spin-density isosurfaces (0.02 au; turquoise: net α density; orange: net β density) for the high-spin (left) and broken-symmetry (right) states of $\mathbf{5^{4+}}$ obtained with DFT/PBE0/def2-TZVPP. Hydrogen atoms are omitted for clarity.
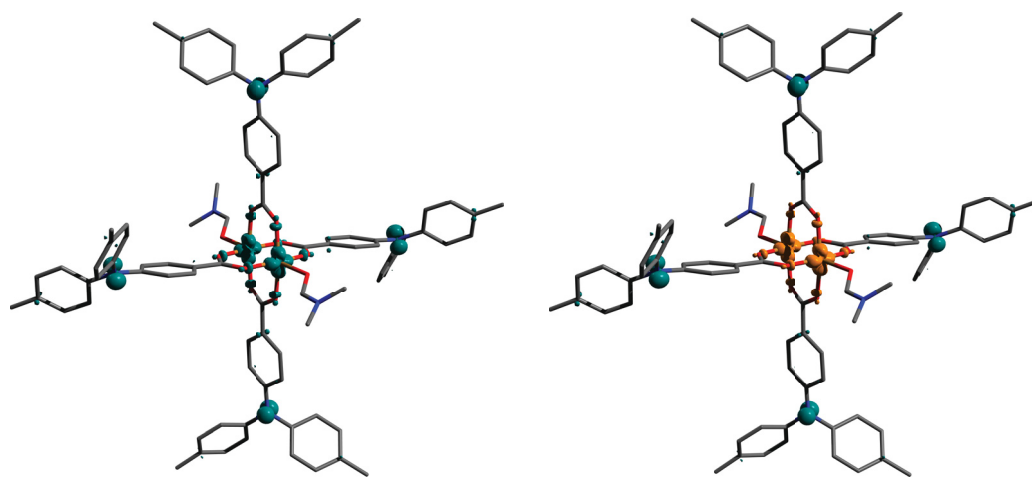
Figure S27: Spin-density isosurfaces (0.02 au; turquoise: net α density; orange: net β density) for the high-spin (left) and broken-symmetry (right) states of $\mathbf{6}^{4+}$ obtained with DFT/PBE0/def2-TZVPP. Hydrogen atoms are omitted for clarity.
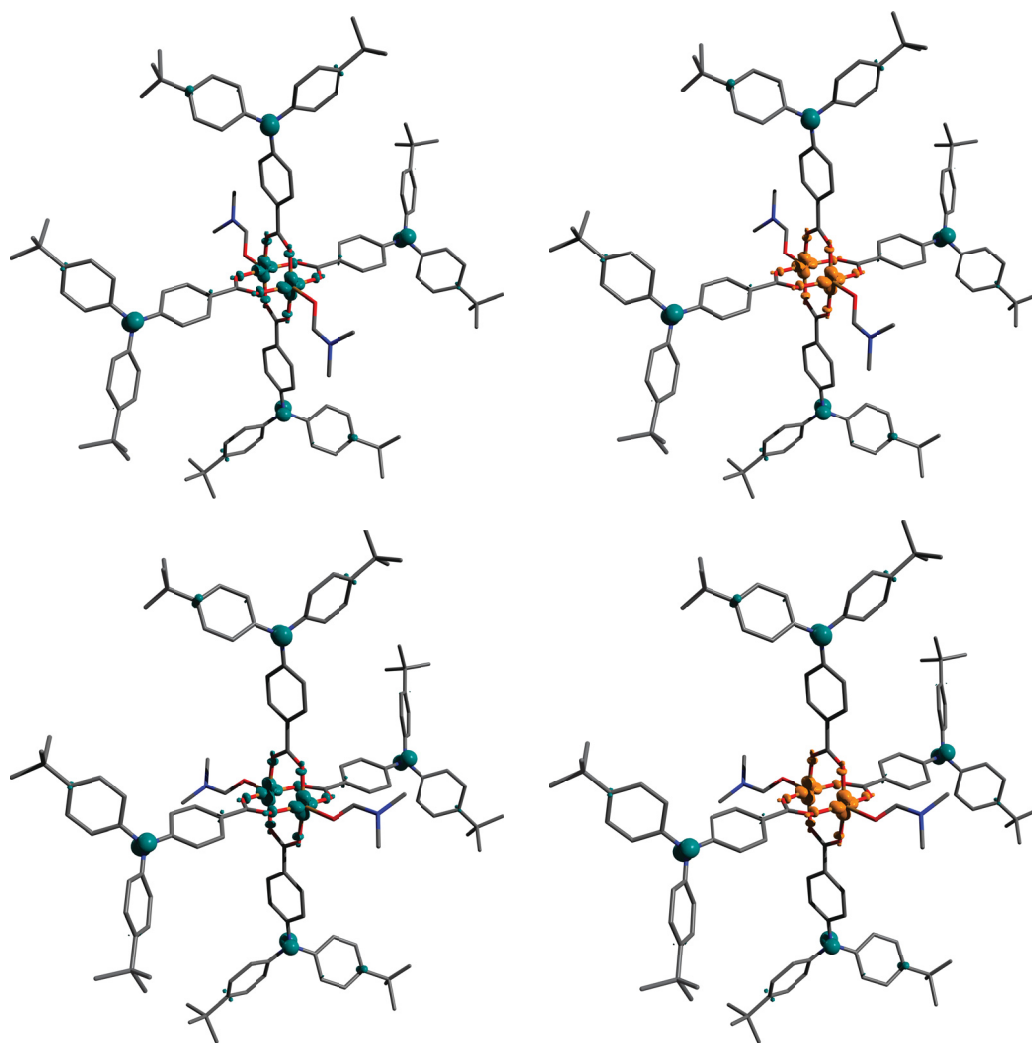
Figure S28: Spin-density isosurfaces (0.02 au; turquoise: net α density; orange: net β density) for the high-spin (left) and broken-symmetry (right) states of $\mathbf{7}^{4+}$(A) obtained with DFT/PBE0/def2-TZVPP. Hydrogen atoms are omitted for clarity.
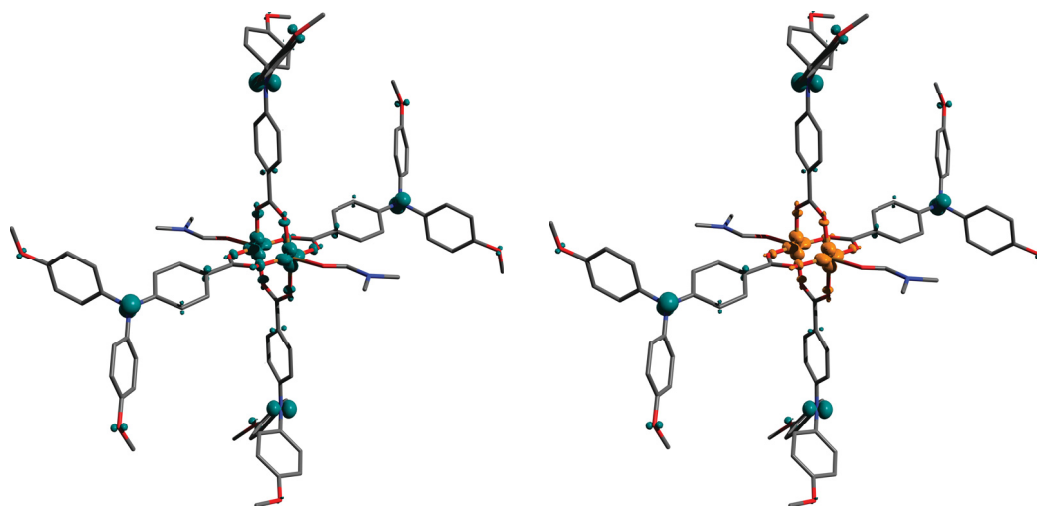
Figure S29: Spin-density isosurfaces (0.02 au; turquoise: net α density; orange: net β density) for the high-spin (left) and broken-symmetry (right) states of **8** obtained with DFT/PBE0/def2-TZVPP. Hydrogen atoms are omitted for clarity.

Table S10: Detailed BS-DFT results for the zinc(II) replaced models $[Zn_2(aba\text{-}R)_4(dmf)_2]^{4+}$ $\mathbf{5}_{Zn}^{4+}$– $\mathbf{8}_{Zn}^{4+}$ (ΔE_1 and ΔE_2 are determined according to Yamaguchi's approach and are based on the broken-symmetry states BS1 and BS2, respectively; the radical-radical coupling constants are defined as: $J_{cis} = \Delta E_1/4$; $J_{trans} = (\Delta E_2 - 2J_{cis})/2$).

	state	$2S+1$	E_{elec} / au	$\langle S^2 \rangle$	ΔE_1 / cm^{-1}	ΔE_2 / cm^{-1}	J_{cis} / cm^{-1}	J_{trans} / cm^{-1}
$\mathbf{5}_{Zn}^{4+}$	HS	5	-7801.664942	6.10649	-0.87	-0.51	-0.22	-0.04
	BS1	1	-7801.664950	2.10622				
	BS2	1	-7801.664947	2.10627				
$\mathbf{6}_{Zn}^{4+}$	HS	5	-8364.282992	6.09306	-0.78	-0.39	-0.20	0.00
	BS1	1	-8364.282999	2.09288				
	BS2	1	-8364.282996	2.09297				
$\mathbf{7}_{Zn}^{4+}(A)^a$	HS	5	-9058.552066	6.08787	-0.35	-0.20	-0.09	-0.01
	BS1	1	-9058.552069	2.08780				
	BS2	1	-9058.552068	2.08783				
$\mathbf{7}_{Zn}^{4+}(B)^a$	HS	5	-9058.543800	6.08783	-0.36	-0.20	-0.09	-0.01
	BS1	1	-9058.543803	2.08773				
	BS2	1	-9058.543802	2.08777				
$\mathbf{8}_{Zn}^{4+}$	HS	5	-8717.258269	6.07142	-0.72	-0.53	-0.18	-0.09
	BS1	1	-8717.258276	2.07128				
	BS2	1	-8717.258274	2.07132				

[a] The structure of **7** contains a disorder of the dmf co-ligands on two positions (ratio 1:1).
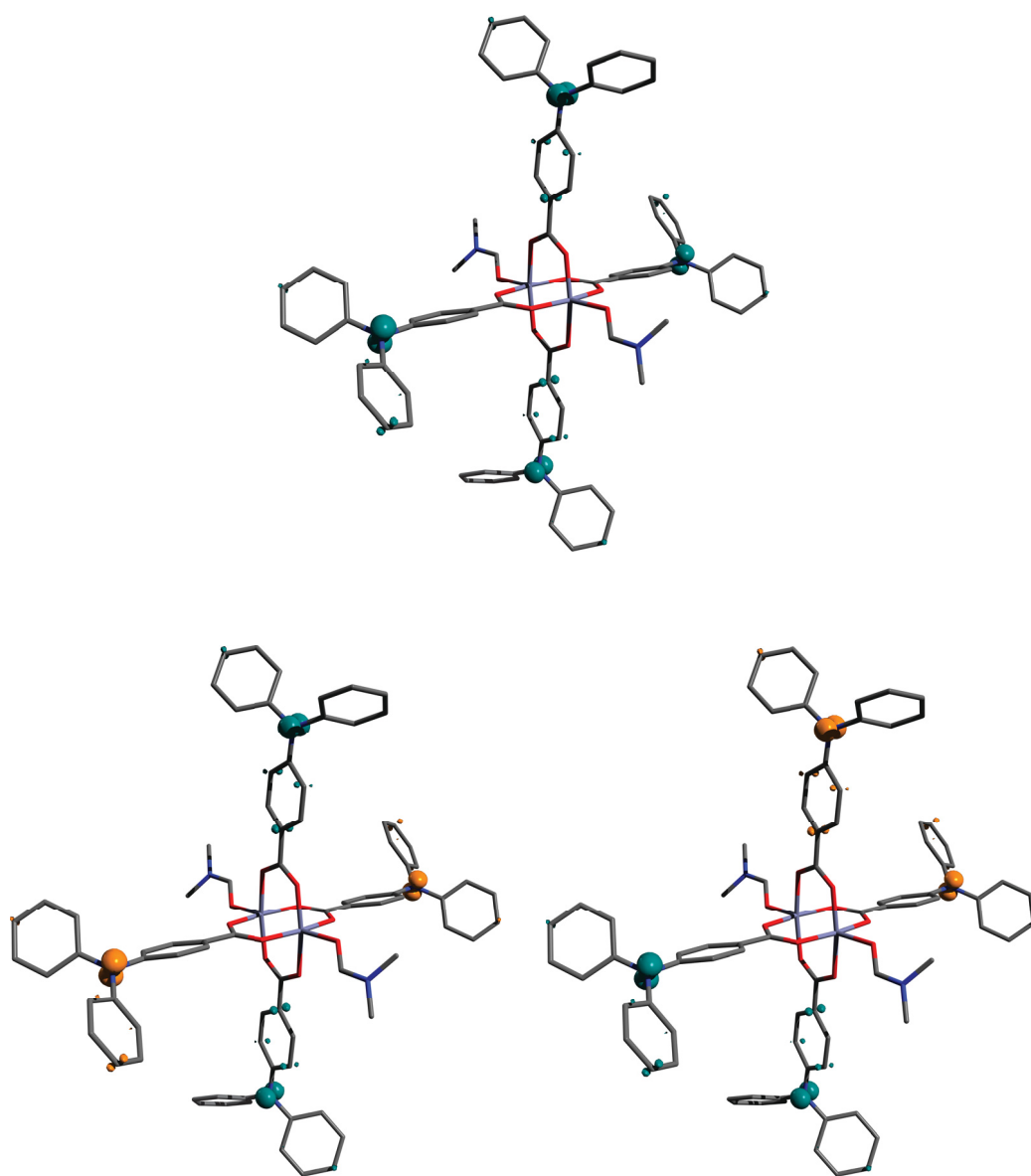
Figure S30: Spin-density isosurfaces (0.02 au; turquoise: net α density; orange: net β density) for the high-spin (top) and the two broken-symmetry states BS1 (bottom left) and BS2 (bottom right) of $\mathbf{5}_{Zn}^{4+}$. Hydrogen atoms are omitted for clarity.
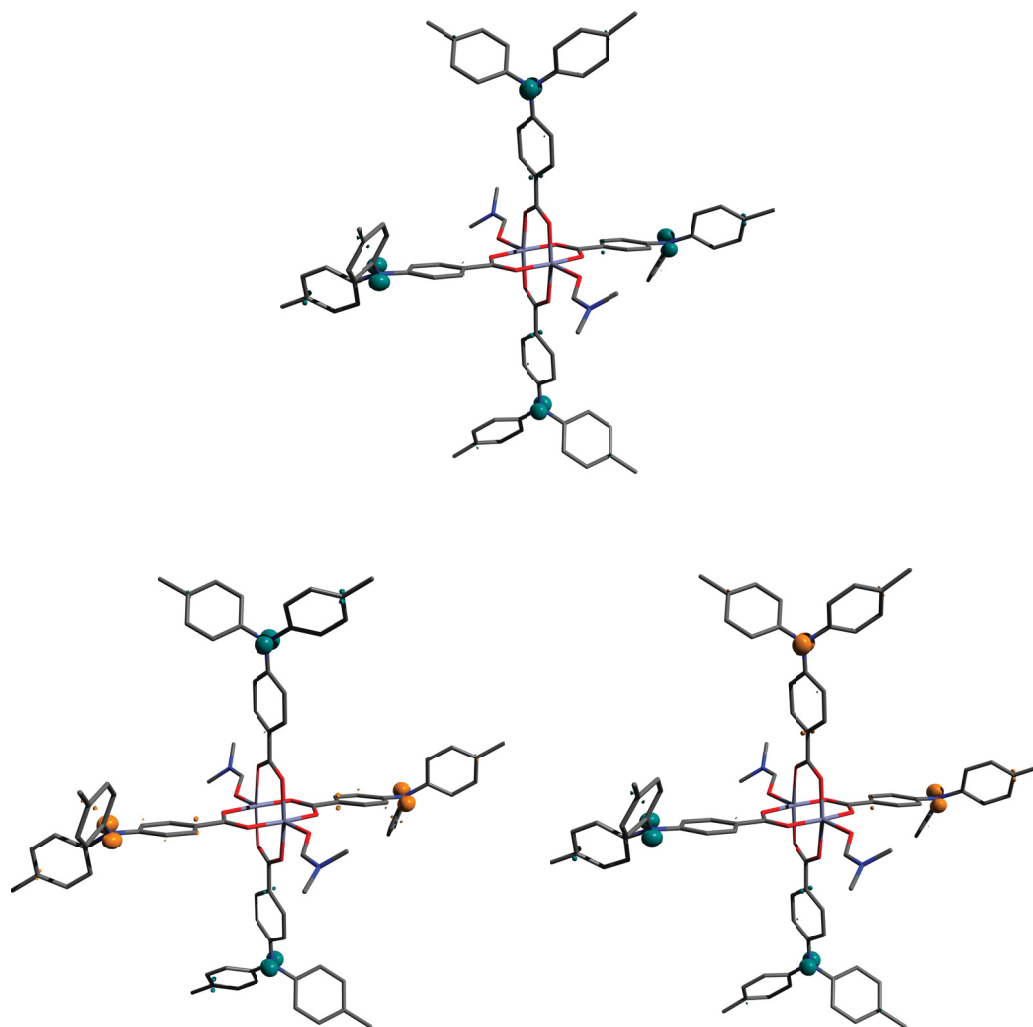
Figure S31: Spin-density isosurfaces (0.02 au; turquoise: net α density; orange: net β density) for the high-spin (top) and the two broken-symmetry states BS1 (bottom left) and BS2 (bottom right) of $\mathbf{6}_{Zn}^{4+}$. Hydrogen atoms are omitted for clarity.
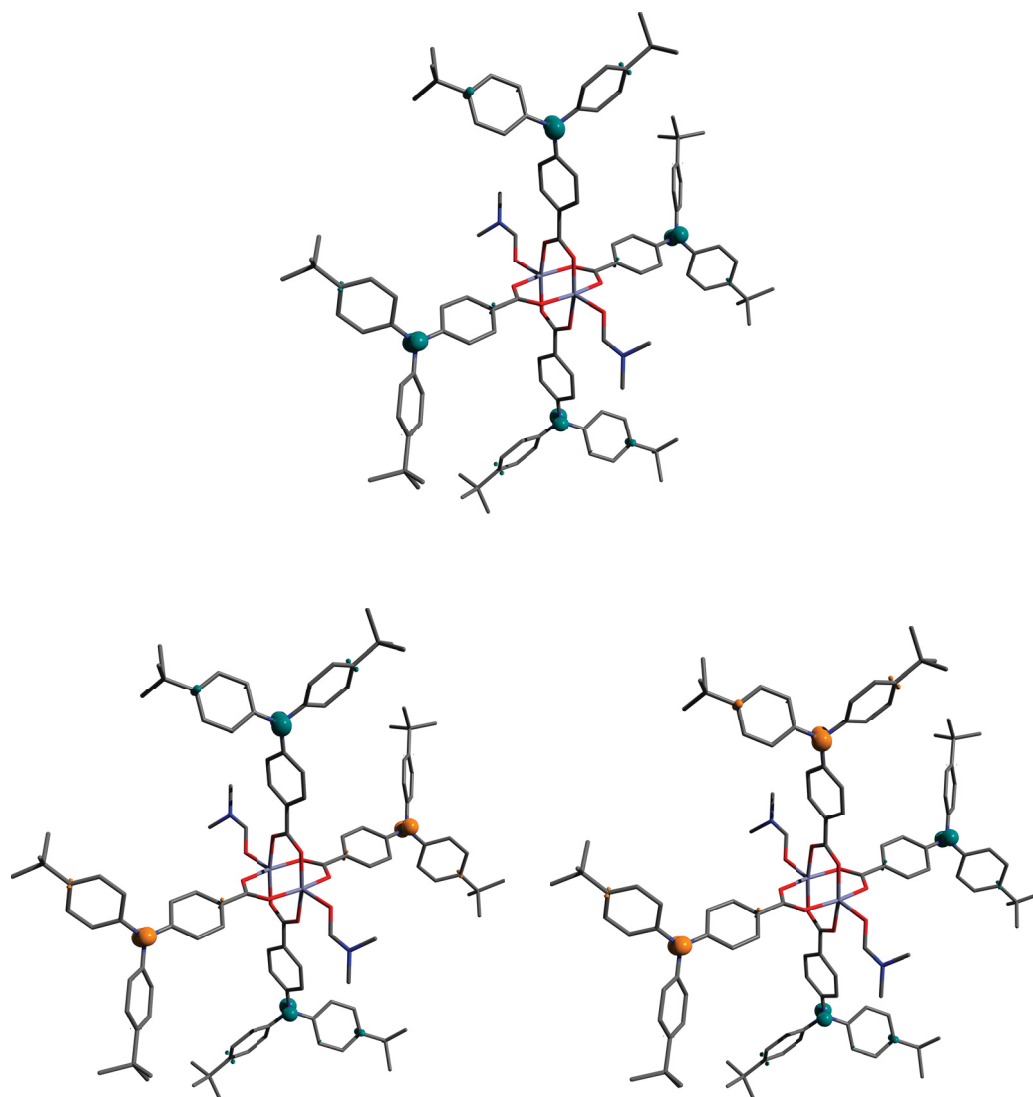
Figure S32: Spin-density isosurfaces (0.02 au; turquoise: net α density; orange: net β density) for the high-spin (top) and the two broken-symmetry states BS1 (bottom left) and BS2 (bottom right) of $\mathbf{7}^{4+}_{Zn}$(A). Hydrogen atoms are omitted for clarity.
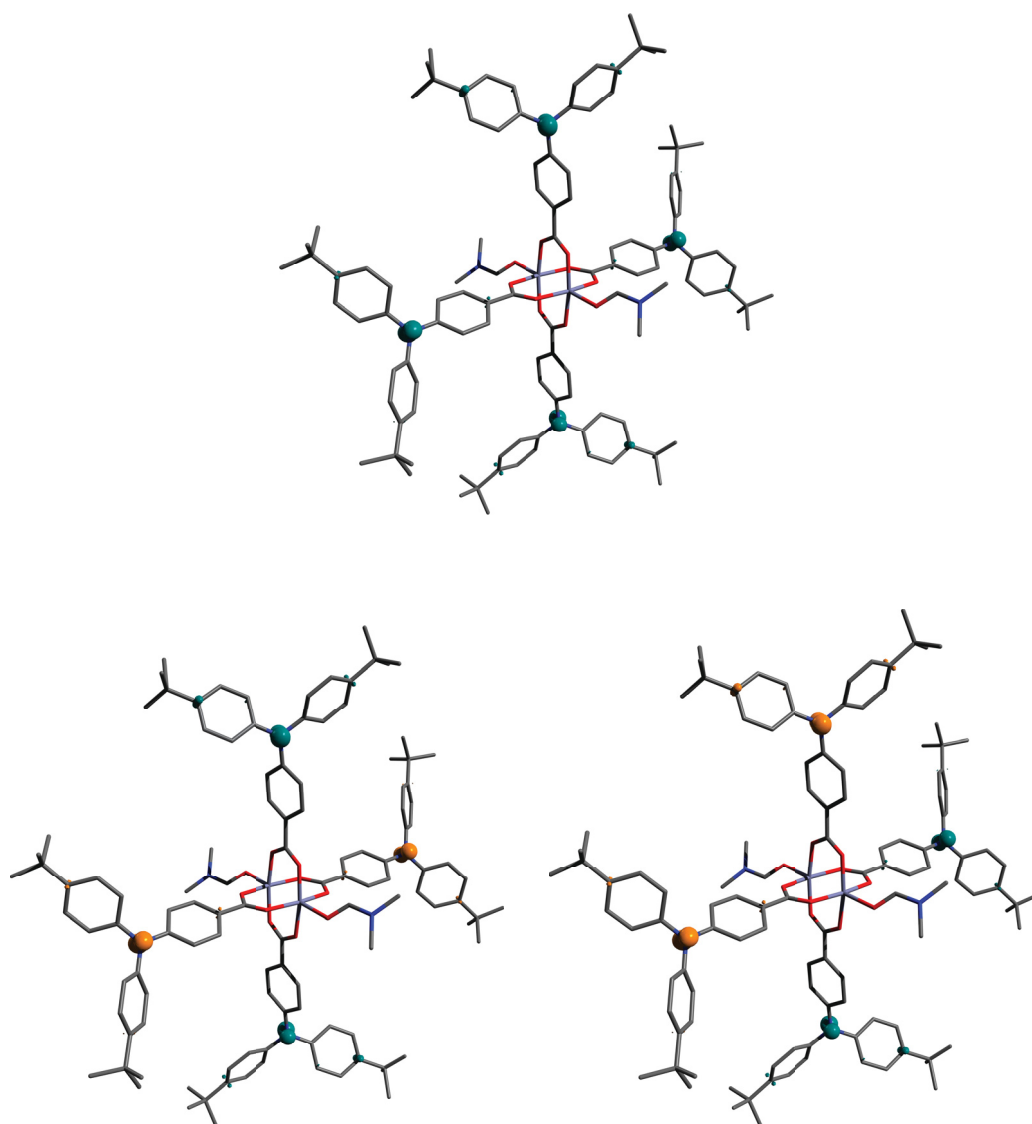
Figure S33: Spin-density isosurfaces (0.02 au; turquoise: net α density; orange: net β density) for the high-spin (top) and the two broken-symmetry states BS1 (bottom left) and BS2 (bottom right) of 7^{4+}_{Zn}(B). Hydrogen atoms are omitted for clarity.
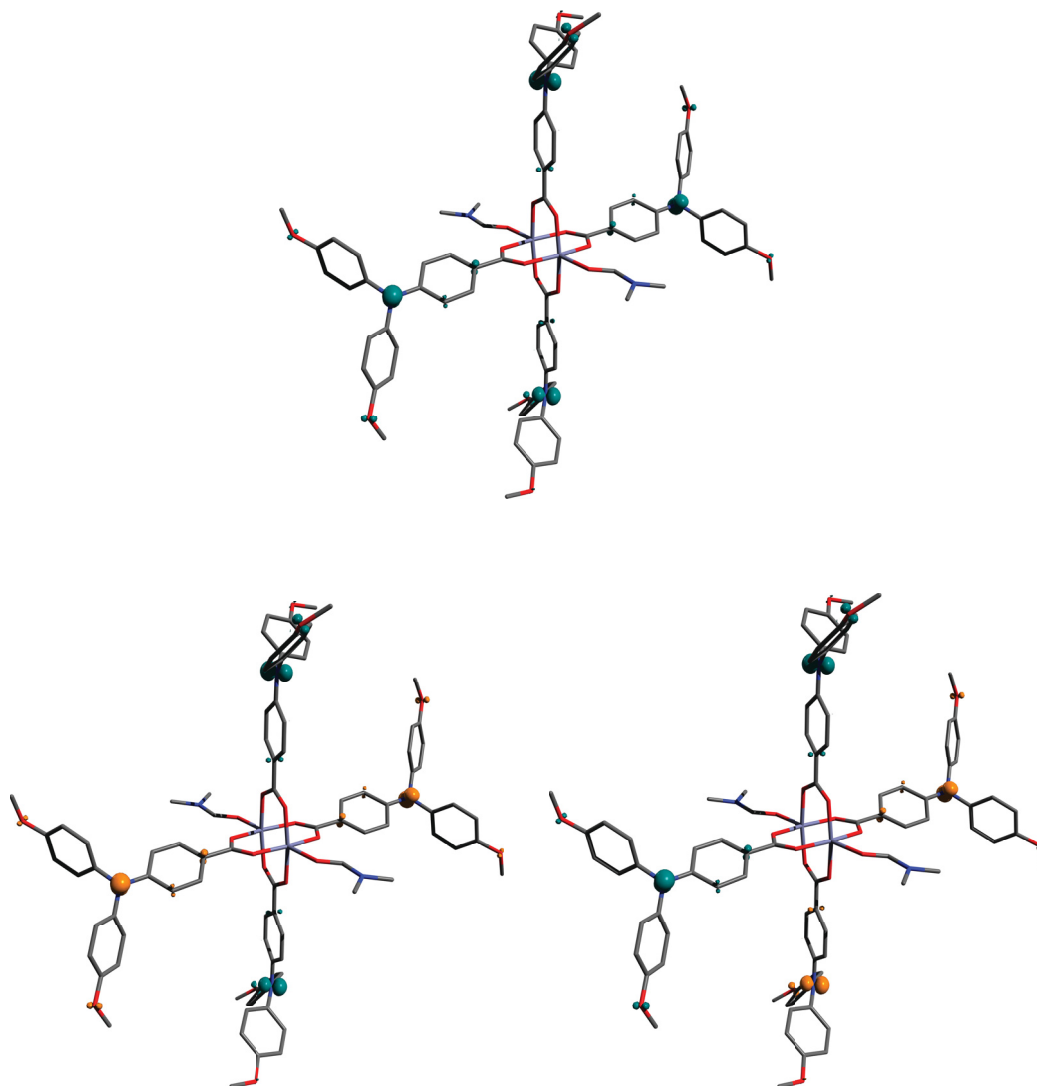
Figure S34: Spin-density isosurfaces (0.02 au; turquoise: net α density; orange: net β density) for the high-spin (top) and the two broken-symmetry states BS1 (bottom left) and BS2 (bottom right) of $\mathbf{8}_{Zn}^{4+}$. Hydrogen atoms are omitted for clarity.

11 Proton NMR spectral data of ligands
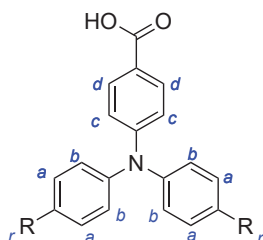
Figure S35: Labeling for assignment of protons in NMR spectra of the ligands **1**–**4**.

Table S11: Summary of proton NMR chemical shifts and their assignments for the ligands **1**–**4** measured in dmso-d$_6$.

Proton	1	2	3	4
a	7.13	7.02	7.05	6.96
b	7.39	7.18	7.18	7.14
c	7.18	6.77	6.78	6.65
d	7.79	7.73	7.74	7.70
r	6.88	2.28	1.27	3.75

12 UV/vis spectra of ligands and complexes
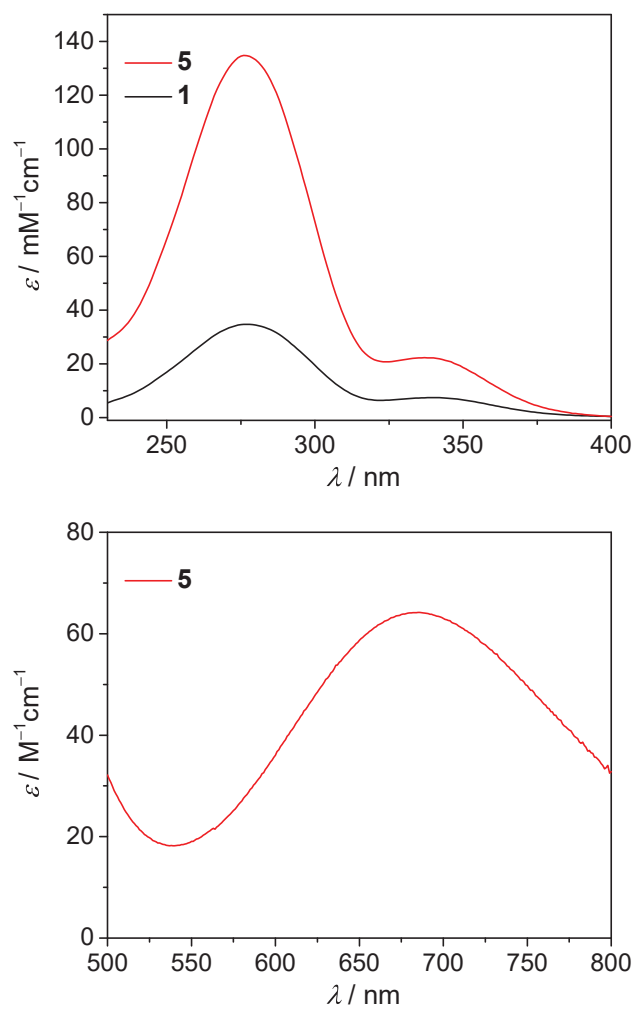
Figure S36: UV spectra of ligand **1** and complex **5** (top) and vis spectrum of complex **5** (bottom) in dichloromethane solutions.
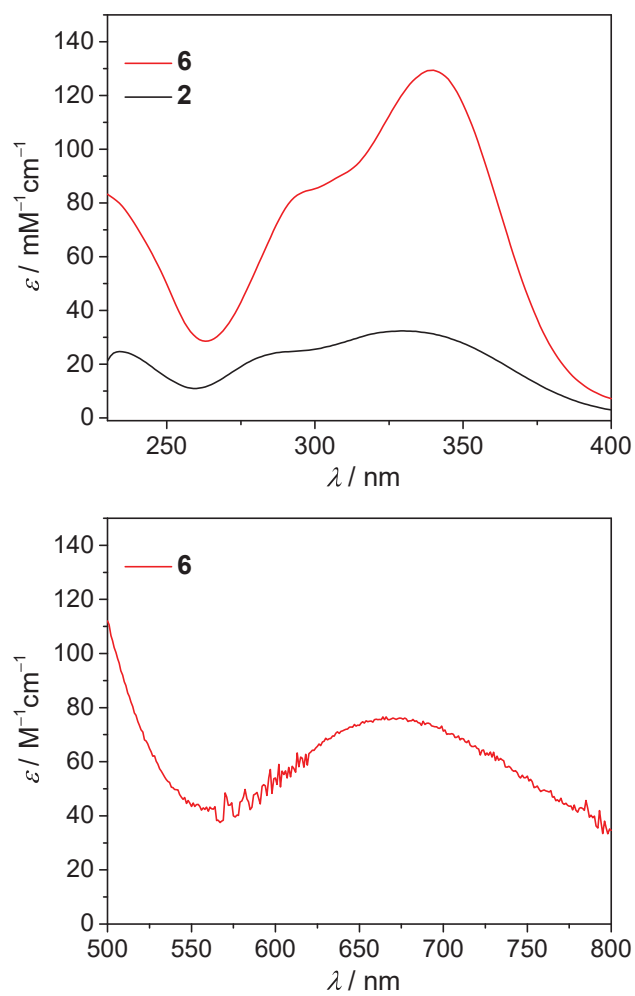
Figure S37: UV spectra of ligand **2** and complex **6** (top) and vis spectrum of complex **6** (bottom) in dichloromethane solutions.
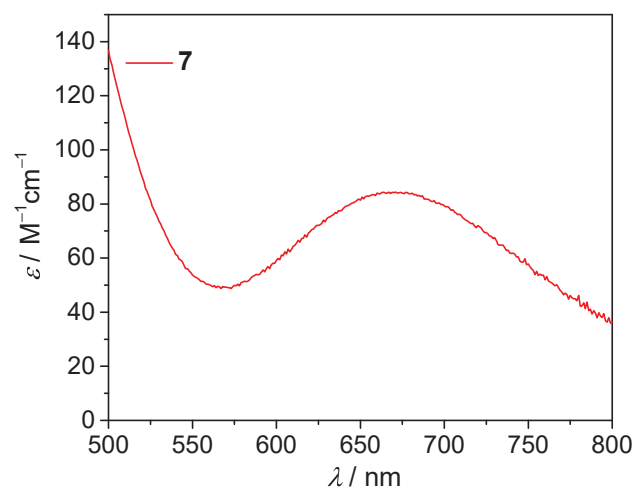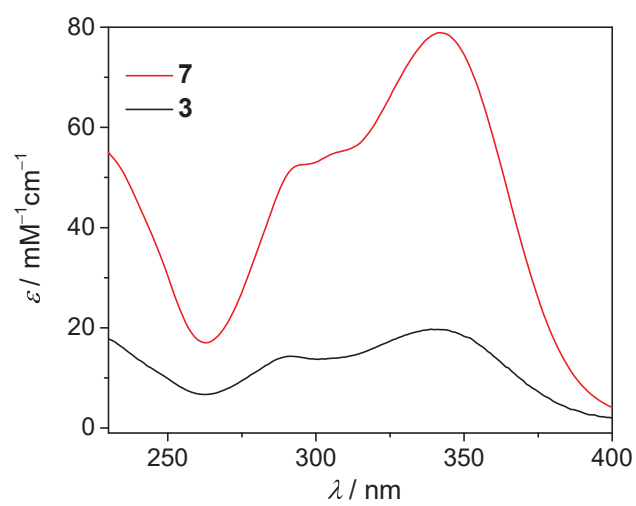
Figure S38: UV spectra of ligand **3** and complex **7** (top) and vis spectrum of complex **7** (bottom) in dichloromethane solutions.

Publication 2

Solvent-dependent selective cation exchange in anionic frameworks based on cobalt(II) and triphenylamine linkers: reactor-dependent synthesis and sorption properties

Oluseun Akintola, David Hornig, Axel Buchholz, Helmar Görls, and Winfried Plass *Dalton Trans.*, **2017**, 46, 8037−8050.
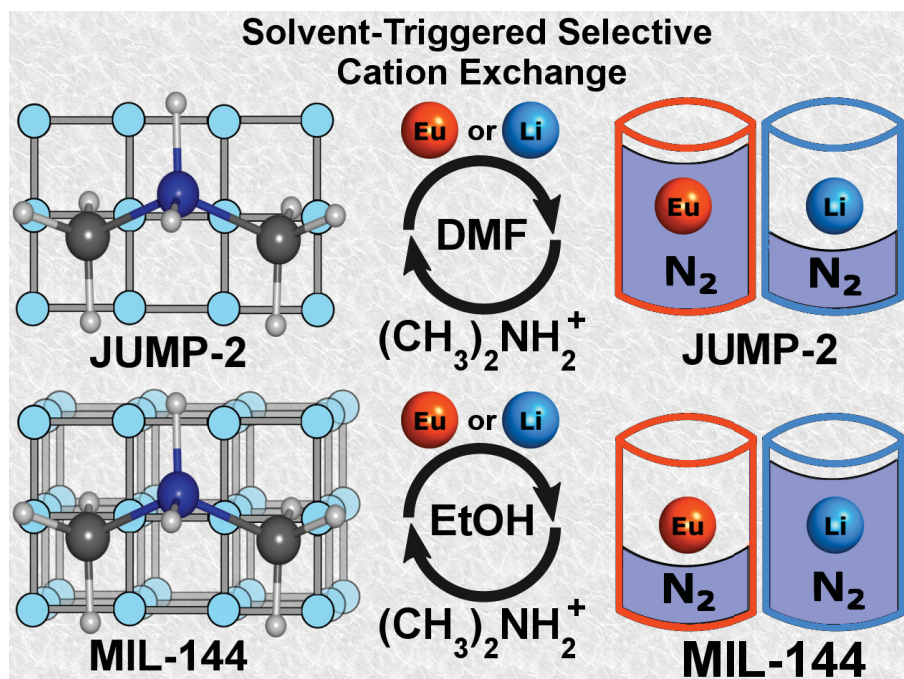
Dalton Transactions

An international journal of inorganic chemistry

rsc.li/dalton
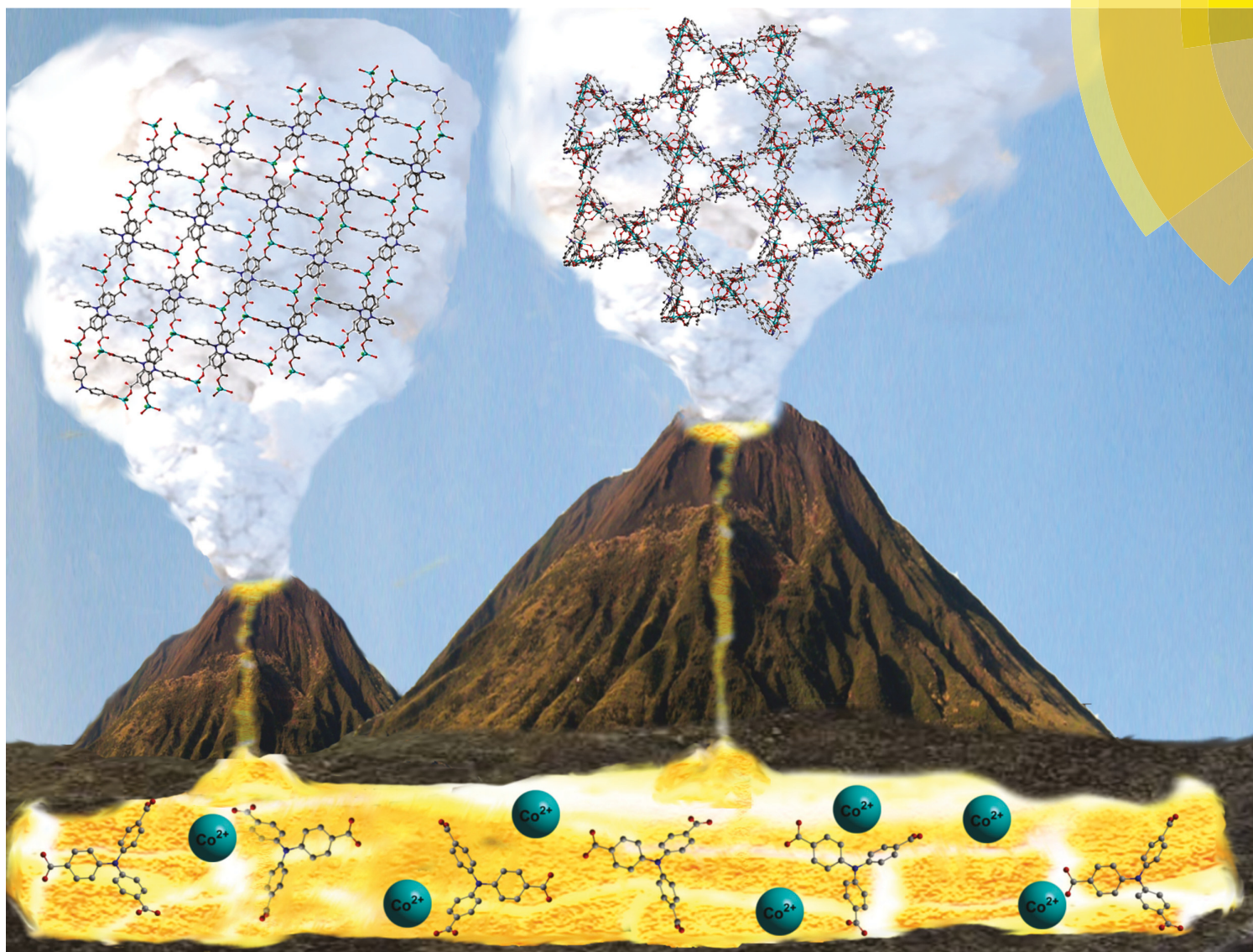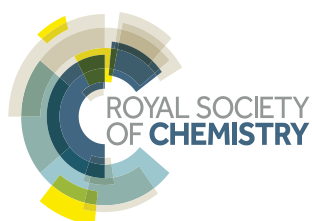
ROYAL SOCIETY
OF CHEMISTRY

Check for updates

Solvent-dependent selective cation exchange in anionic frameworks based on cobalt(II) and triphenylamine linkers: reactor-dependent synthesis and sorption properties†

Oluseun Akintola, [ID] David Hornig, Axel Buchholz, [ID] Helmar Görls and Winfried Plass [ID] *

Two cobalt(II) coordination polymers with anionic networks of formulae {(Me$_2$NH$_2$)$_2$[CoCl(ntb)]}$_n$ (JUMP-2) and {(Me$_2$NH$_2$)$_2$[Co$_5$(ntb)$_4$(H$_2$O)$_3$(Me$_2$NH)]}$_n$ (previously reported as MIL-144 by Livage *et al.*, *Microporous Mesoporous Mater.*, 2012, **157**, 37) have been obtained *via* a solvothermal reaction of cobalt chloride and 4,4′,4″-nitrilotribenzoic acid (H$_3$ntb) in DMF employing two differently-sized reactors, while using the same absolute amount of reactants. Structure analysis revealed that JUMP-2 crystallized in the monoclinic space group $P2_1/n$ and displays a two-dimensional (2D) network, which by topological analysis was characterized as a layered 3-connected hcb net. The topological analysis of MIL-144 revealed a 3,6-connected net with 3,6T80 topology. The magnetic properties of JUMP-2 are indicative of independent single-ion behavior of the tetrahedral cobalt(II) ions and showed an out-of-phase signal in the alternating-current (ac) magnetic susceptibility below 2.5 K, whereas for MIL-144 an overall antiferromagnetic interaction within the di- and trinuclear secondary building units is observed and no indication for slow magnetization dynamics. The organic cations in both frameworks could successfully be exchanged with inorganic cations under retention of the respective network structure. In the process of exchange, both compounds displayed cation selectivity based on which solvent was utilized for immersing the solids. JUMP-2 shows a preference for europium(III) ions in DMF, whereas MIL-144 preferentially takes up lithium ions when ethanol is used. The N$_2$ adsorption isotherms were measured before and after exchange and revealed a considerable improvement in the sorption properties of the exchanged samples.

Introduction

Since the last couple of decades, the study of metal–organic frameworks (MOFs) or porous coordination polymers (PCPs) as an area of research is attracting a greater share of attention. This can be attributed to their fascinating architectures and topologies in addition to their potential applications as functional materials in catalysis, gas storage and separation, fluorescent sensors, electroluminescent devices, drug-delivery and many more.[1] More than any other class of compounds, they exhibit structure-tunability based on the choice of both ligands and metal ions, thus implying that some form of control of the properties can be achieved. Carboxylate ligands have, in recent years, been extensively utilized in the design and construction of novel porous coordination polymers. In particular, aromatic polycarboxylates offer the advantage of imposing rigidity, which thus aids in stabilizing these porous polymers.[2] Furthermore, usage of polycarboxylates is expected to yield coordination polymers with higher dimensionality as well as open-frame networks with varying topologies.[3]

Generally, the structure and architecture adopted by a MOF is often dependent on the synthetic conditions under which it is prepared. Conditions, such as solvent mixture, pH value, counterion used, cooling rate, metal–ligand ratio *etc.*, have been found to play a role in the final topology adopted by the synthesized MOF.[4] This has been exploited in templated synthesis, where anionic frameworks have been obtained either by addition of large organic cations to the mixture or in most cases by *in situ* generation of the cation as a by-product of the decomposition of solvent molecules.[5] As a consequence, the finally obtained framework is able to undergo post-synthetic

Institut für Anorganische und Analytische Chemie, Friedrich-Schiller-Universität, Jena, Humboldtstr 8, 07743 Jena, Germany. E-mail: Sekr.Plass@uni-jena.de; Fax: +49 (0)3641 948132; Tel: +49 (0)3641 948130

modification *via* replacement of the counterion associated with it. This ability can allow tunability of the pore sizes by exploiting the size exclusion effect.[6] Furthermore, this could enable the use of MOFs to act as sensors for certain ions.[7,8]

To date, various factors have been reported to influence the final topology adopted by the framework, but there seems to be very little attention towards the influence of size/geometry of the reactor vessel on the final outcome.[9] The 4,4′,4″-nitrilotribenzoic acid (H_3ntb) ligand chosen for this study has been reported earlier for a few coordination polymers with zinc(II) ions and structural differences have been observed in each case depending on the solvent mixtures and temperature employed in their synthesis.[10] We have used this potentially redox-active ligand H_3ntb to generate the pillar-layer framework $\{(Me_2NH_2)_2[Co_3(ntb)_2(bdc)]\}_n$ (H_2bdc = terephthalic acid) denoted as JUMP-1 (JUMP = Jena University Magnetic Polymer), which showed interesting post-synthetic modification potential resulting in significantly increased sorption properties.[11] Along this line we obtained two cobalt(II) coordination polymers $\{(Me_2NH_2)_2[CoCl(ntb)]\}_n$ (JUMP-2) and $\{(Me_2NH_2)_2[Co_5(ntb)_4(Me_2NH)(H_2O)_3]\}_n$ (MIL-144), for which the structure of the latter had been previously reported.[12] Both JUMP-2 and MIL-144 are anionic polymers obtained simply by altering the reactor vessel while retaining the same absolute amount of reactants and solvents. Post-synthetic modification of the compounds will be performed by replacing the organic countercations. The influence of the solvent used in exchange will be studied to check for any solvent-dependent cation selectivity. The sorption properties of the resulting countercation-exchanged samples will then be studied and reported.

Experimental section

Materials

Triphenylamine (Alfa Aesar) and cobalt(II) chloride hexahydrate (Aldrich) were obtained commercially and used without further purification. All other chemicals were of AR grade. The tribromotriphenylamine used was prepared from triphenylamine by following a reported procedure.[13] The final ligand 4,4′,4″-nitrilotribenzoic acid (H_3ntb) was obtained in good yield following procedures already described in the literature.[12,14] The analytical data of H_3ntb is consistent with those reported earlier.[11]

Physical measurements

Simultaneous TG/DTA analyses were performed under a static air atmosphere using a Netzsch STA Luxx PC analyzer up to 1000 °C. The FT-IR spectra were measured on a VERTEX 70 IR spectrometer (Bruker Optics) using the Specac Diamond ATR optional accessory. Mass spectrometry was performed on a MAT SSQ710 mass spectrometer (Bruker). NMR spectra were recorded with a Bruker AVANCE400 spectrometer. The elemental analyses were done on a VARIO EL III analyzer. The magnetic susceptibilities were measured on the bulk vacuo dried materials in the 2–300 K temperature range with a Quantum

Design MPMS-5 superconducting SQUID magnetometer. The data were corrected for diamagnetic contributions. The N_2 physisorption isotherms were measured on an Autosorb-IQ instrument from Quantachrome Instruments Corporation. Solvothermal reactions were carried out in Teflon-lined acid digestion vessels from both Parr Instruments and PerkinElmer with volumes of 23 and 110 mL, respectively, utilizing a programmable oven (Binder). Supercritical CO_2 drying was carried out in a steel autoclave with a 100 mL inner glass chamber from Carl Roth. X-ray powder diffraction (XRPD) measurements were performed on a Stoe Powder Diffractometer with a Mython 1 K detector at room temperature. Measurements were carried out using capillary tubes while the Debye Scherrer Scan Mode was applied with a 2θ scan type. The X-ray tube was a Cu-long fine focus tube. The powdered samples were suspended in DMF in a 0.5 mm glass capillary and then measured. The measurement was carried out between 2 and 50° with steps of 2.1° per 20 seconds.

Syntheses

$\{(\mathbf{Me_2NH_2})_2[\mathbf{Co(ntb)Cl}]\}_n·1/2n\mathbf{DMF}·1/2n\mathbf{H_2O}$ (JUMP-2·1/ 2DMF·1/2H_2O). Cobalt(II) chloride hexahydrate (0.26 g, 1.06 mmol) and H_3ntb (0.10 g, 0.26 mmol) were dissolved in DMF (5 mL) in a 23 mL Parr acid digestion bomb (see Fig. S1†) and heated at 150 °C for 72 h under autogenous pressure. The reaction mixture was then allowed to cool within the vessel over 24 h using a pre-programmed temperature gradient (5.2 °C h^{-1}). Violet crystals were isolated after cooling and washed with DMF (4 × 2 mL). Yield: 91 mg, 0.139 mmol, 54%. Anal. Calcd for JUMP-2·1/2DMF·1/2H_2O $C_{26.5}H_{32.5}ClCoN_{3.5}O_8$ (606.45 g mol^{-1}): C 52.5, H 5.4, N 8.1%. Found: C 52.6, H 5.1, N 8.1%. Selected IR (ATR, cm^{-1}): 1651 m, 1593 s, 1559 sh, 1505 m, 1369 vs, 1313 s, 1271 s, 1172 s, 1103 m, 1023 m.

$\{(\mathbf{Me_2NH_2})_2[\mathbf{Co_5(ntb)_4(H_2O)_3(Me_2NH)}]\}_n·13n\mathbf{DMF}·2n\mathbf{H_2O}$ (MIL-144·13DMF·2H_2O). The above described procedure for JUMP-2·DMF·H_2O was employed utilizing exactly the same absolute amount of reactants (cobalt(II) chloride hexahydrate: 0.26 g, 1.06 mmol; H_3ntb: 0.10 g, 0.26 mmol) and solvents (DMF: 5 mL). However, a 110 mL PerkinElmer acid digestion bomb was used as a reactor (see Fig. S1†). After heating at 150 °C for 72 h under autogenous pressure the reactor was allowed to cool over 24 h using a pre-programmed temperature gradient (5.2 °C h^{-1}). Violet block crystals could be isolated after cooling which were washed with DMF (4 × 2 mL). Yield: 73 mg, 0.025 mmol, 39% based on a ligand. Anal. Calcd for MIL-144·13DMF·2H_2O $C_{129}H_{172}Co_5N_{20}O_{42}$ (2969.52 g mol^{-1}): C 52.2, H 5.8, N 9.4%. Found: C 51.8, H 5.5, N 9.7%. Selected IR (ATR, cm^{-1}): 1653 m, 1590 s, 1533 m, 1505 m, 1377 vs, 1312 s, 1272 s, 1174 m, 1103 m, 1013 w.

Post-synthetic cation exchange

Exchange with lithium ions. The organic dimethylammonium cations of JUMP-2 and MIL-144 were exchanged by soaking the as-synthesized materials (50–70 mg) in saturated solutions of $LiNO_3$, two different solvents were used namely DMF and ethanol (each 10 mL). Then $LiNO_3$ solutions were

decanted and replaced by fresh solution every day for a period of 10 days. After this period the saturated supernatant solutions were removed and the ion-exchanged crystals washed repeatedly with ethanol to ensure removal of any residual free $LiNO_3$ molecules. The corresponding lithium-exchanged samples derived from soaking in ethanol and DMF are further denoted as JUMP-2(Li)E, JUMP-2(Li)D, MIL-144(Li)E, and MIL-144(Li)D (where E and D connote ethanol and DMF as the solvent used in cation exchange), respectively. Their full analytical data are summarized in the ESI.†

Exchange with europium ions. In order to follow the process of europium exchange by fluorescence the as-synthesized samples of JUMP-2 and MIL-144 (each 25 mg) were immersed in solutions of DMF as well as ethanol (3 mL, 2 mM $Eu(NO_3)_3$). The exchange was then monitored by measuring the decrease in the fluorescence signal over a period of 48 h at a wavelength of λ_{ex} = 395 nm.

For the synthesis of the actual europium-exchanged samples the as-synthesized materials of JUMP-2 and MIL-144 (50–70 mg) were soaked in vials containing a 0.03 M $Eu(NO_3)_3$ solution in DMF (10 mL) over a period of 10 d during which the salt solutions were replaced with fresh solution every 24 h. The same experiment was repeated using a 0.03 M $Eu(NO_3)_3$ solution in ethanol (10 mL). At the end of the soaking period the salt solutions were decanted followed by repeated washing of the europium-exchanged samples with ethanol in order to remove any free residual $Eu(NO_3)_3$ molecules. The derived europium-exchanged samples are further denoted as JUMP-2(Eu)E, JUMP-2(Eu)D, MIL-144(Eu)E, and MIL-144(Eu)D (where E and D connote ethanol and DMF as the solvent used in cation exchange), respectively. Their full analytical data are summarized in the ESI.†

X-ray structure determination

The single crystal X-ray data were collected on a Nonius Kappa CCD diffractometer, using graphite-monochromated Mo-K_α radiation (λ = 0.71073 Å) at 133(2) K. Data were corrected for Lorentz and polarization effects, but not for absorption.[15] The structure was solved by direct methods (SHELXS) and refined by full-matrix least squares techniques against $F_o{}^2$ (SHELXL-97).[16] All hydrogen atoms were included at calculated positions with fixed thermal parameters. All non-disordered, non-hydrogen atoms were refined anisotropically. Olex 2.1[17] and Diamond 4.2[18] were used for structure representations. The identity of the crystals of MIL-144·13DMF·2H₂O with respect to the reported structure was verified by a comparison of the obtained cell parameters.[12]

Crystallographic and refinement parameters for JUMP-2. Formula $C_{26.5}H_{32.5}ClCoN_{3.5}O_7$, M = 606.45, monoclinic $P2_1/n$, a = 13.5527(3), b = 10.0016(10), c = 23.6872(6) Å, β = 94.24(10)°, V = 3201.98(11) Å³, Z = 4, ρ_{calc} = 1.256 g cm⁻³, μ = 0.663 mm⁻¹, 20911 reflections collected, θ_{max} = 27.57°, 7298 unique reflections (R_{int} = 0.0352) and 6258 observed reflections ($I > 2\sigma(I)$), 393 parameters, goodness-of-fit on F^2 S = 1.126, R_1 = 0.0684 (observed reflections), wR_2 = 0.2015 (all unique reflections).

Full details are given in the deposited cif file CCDC 1485391 which contains the supplementary crystallographic data.

Sample pretreatment and sorption measurements

Supercritical carbon dioxide activation. The as-synthesized samples (50–70 mg) were soaked in vials containing ethanol (10 mL) for one week during which the solvent was refreshed every 24 h by decanting the supernatant and replacing with a fresh solvent. For the drying with supercritical CO_2, the supernatant was decanted and the ethanol-immersed slurry (to prevent dry out of the sample during transfer) was transferred into an autoclave (100 mL capacity) and sealed. Liquid CO_2 was then introduced into the autoclave (final pressure of 60 bar) and allowed to stand 30 min. In order to remove any possible non-occluded ethanol from the materials, CO_2 was slowly removed over a period of 20 min. A second batch of liquid CO_2 was then introduced into the reactor (60 bar), but this time allowed to stand for 24 h. After 24 h the temperature of the autoclave was raised to 40 °C to bring the CO_2 to supercritical conditions and maintained at this temperature for one hour. The CO_2 was then slowly released over 30 min with the temperature continuously maintained at 40 °C so as to prevent any cooling that might ensue from the expansion of the gas during evaporation. The supercritical drying procedure was applied to the as-synthesized materials of JUMP-2 and MIL-144 to generate the products JUMP-2^{scd} and MIL-144^{scd} (where the superscript "scd" abbreviates the term "supercritical drying"), respectively. In addition, selected cation-exchanged samples also were subjected to supercritical drying with CO_2. The samples were chosen based on the solvent in which the best cation exchange performance was observed, *i.e.* DMF for JUMP-2 and ethanol for MIL-144. The corresponding lithium and europium samples are JUMP-2(Li)D and MIL-144(Li)E as well as JUMP-2(Eu)D and MIL-144(Eu)E, respectively. The resulting materials are further denoted as JUMP-2(Li)D^{scd}, MIL-144(Li)E^{scd}, JUMP-2(Eu)D^{scd}, and MIL-144(Eu)E^{scd}.

Sorption measurements. The isotherms of all pretreated and dried products were measured immediately after degassing the samples for 30 min at room temperature. Pore size distribution curves were calculated by fitting the experimental data using a quenched solid density functional theory (QSDFT) kernel based on adsorption models for N_2 on carbon at 77 K, which was provided by QUANTACHROME Instruments.[19] The Brunauer–Emmett–Teller (BET) surface areas were determined from the adsorption data over different relative pressure ranges all between 0.005–0.300 while ensuring compliance with the consistency criteria.[20]

Results and discussion

Synthesis

The compounds JUMP-2 and MIL-144 were obtained by the solvothermal reaction of the ligand H₃ntb with cobalt(II) chloride hexahydrate in DMF. For both syntheses the same stoichiometry and absolute amount of reactants were used. Moreover,

both syntheses were performed with exactly the same reaction temperature program. However, the reaction in the case of JUMP-2 was performed in a 23 mL Teflon-lined Parr acid digestion vessel, whereas MIL-144 was prepared using a 110 mL PerkinElmer acid digestion vessel. The two products show clear dissimilarities in their appearance; while the crystals of JUMP-2 were violet plates, those of MIL-144 could be isolated as light violet blocks. The only obvious difference between the performed reactions is related to the size and type of reaction container used for the syntheses. However, this may lead to changes of the internal reaction conditions. At first, the variation in design of the two reactors (see Fig. S1†) may cause differences as far as the temperature profile is concerned at least during heating and cooling periods. Secondly, the difference in the internal size of the reactor is likely to cause variations as the phase distribution and concentration conditions are concerned. To exclude seeding effects responsible for the observed reactor dependence of the obtained reaction products, we repeated the syntheses for both cases with fresh but not previously used teflon liners and observed the same results as described above. This clearly indicates that a seeding effect is not operative in the case of the reactor dependent synthesis of JUMP-2 and MIL-144.

X-ray crystal structures

The single-crystal X-ray diffraction study performed on JUMP-2 revealed that it crystallizes in the space group $P2_1/n$ and exhibits an anionic two-dimensional (2D) network. The asymmetric repeating unit of the network consists of a cobalt(II) ion coordinated by one ntb^{3-} ligand and one chlorido ligand leading to $[CoCl(ntb)]_n^{2n-}$ as an overall formula for the charged 2D framework. The framework charge is compensated by two dimethylammonium cations. As frequently observed for reactions in DMF, the dimethylammonium cations are believed to be a by-product of the thermal decomposition of the DMF solvent during the synthesis.[21] Moreover, additional solvent molecules of water and DMF are found to be disordered in the crystal structure leading to half a molecule of water and DMF per asymmetric unit.

The cobalt(II) ion is found to be tetrahedrally coordinated by one terminal chlorido ligand and three carboxylate oxygen atoms from three different ntb^{3-} ligands as illustrated in Fig. 1. The Co–O bond lengths are approximately the same at about 199 pm while the Co–Cl distance is found to be 230 pm. Besides the difference in bond lengths the distortion from the tetrahedral geometry at the cobalt(II) ion can clearly be seen by the variation of the corresponding bond angles. Although four of the angles are rather close to the expected tetrahedral angle, two bond angles deviate significantly, with the smallest at about 94 and the largest at 121° corresponding to O4B–Co–O6A and O1–Co–O6A, respectively.

The structure is built up as a 2D coordination network with the tetrahedral cobalt center serving as the secondary building unit (SBU) resulting in a honeycombed structure which is oriented along the crystallographic (010) plane as depicted in Fig. 2. The overall crystal structure is composed of a packing of
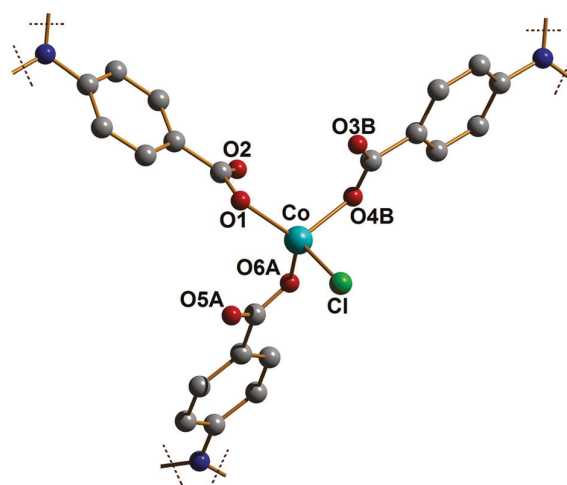
Fig. 1 Cutout view from the anionic 2D network of JUMP-2 showing the pseudo-tetrahedral geometry around the cobalt(II) ion. Hydrogen atoms are omitted for clarity. Symmetry codes: $A = -1/2 + x$, $1/2 - y$, $-1/2 + z$; $B = -1 + x$, $+y$, $+z$. Pertinent bond lengths (pm) and angles (°): Co–O1 198.5(3), Co–O4B 198.2(3), Co–O6A 198.9(3), Co–Cl 230.32(10), Cl–Co–O1 109.70(9), Cl–Co–O4B 103.39(9), Cl–Co–O6A 111.95(9), O1–Co–O4B 113.83(12), O1–Co–O6A 121.49(13), O4B–Co–O6A 94.28(13).

these unconnected undulating 2D layers with the chlorido ligands at the cobalt ions being alternately positioned up and down along the [001] direction (see Fig. 2). The resulting pseudo-hexagonal voids within the honeycombed layers are estimated to be about 10–13 Å wide. However, due to the staggered arrangement of succeeding layers these voids are shifted with respect to each other preventing the formation of corresponding 1D channels (see Fig. S2†). Nevertheless, the voids are interconnected in an undulated manner along the [010] direction. Moreover, the voids are further interconnected by additional 1D channels formed along the [12$\bar{1}$] direction (see Fig. S3†). The void within the anionic framework is estimated to be 1546.6 Å^3 per unit cell which represents about 48% of its total volume.[22] In the crystal structure of the as-synthesized JUMP-2 this void is filled by the two dimethylammonium cations compensating the charge of the 2D network as well as the disordered solvent molecules (water and DMF). The two dimethylammonium cations are hydrogen bonded to the noncoordinating oxygen atoms O2 and O3 of the deprotonated carboxylate groups of the ntb^{3-} linkers at N···O distances of about 271 pm. Further hydrogen bonding is observed for one of the dimethylammonium cations towards the disordered guest DMF molecule at a distance of 277 pm (see Fig. S4†). However, there is no interconnection between the 2D layers by hydrogen bonding (see Fig. S5†). Moreover, no evidence for potential π···π interactions between the 2D layers can be found.

To further characterize the network structure a topological analysis has been performed using TOPOS 5.0 (see Tables S1 and S2†).[23] Considering the cobalt center as one node, it connects to three ligands giving a three-connected node. The
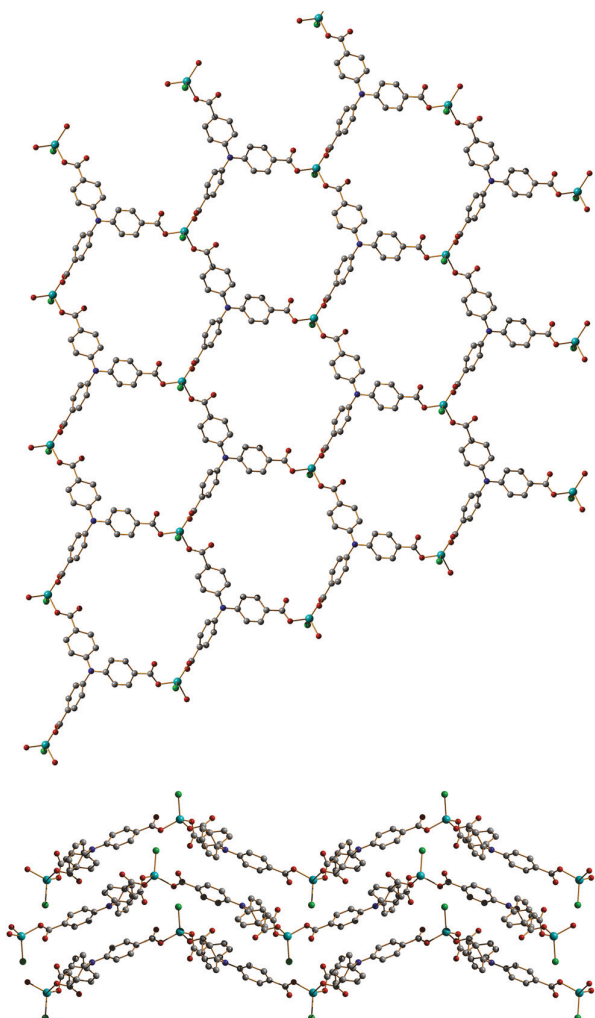
Fig. 2 2D layered structure of the anionic framework in JUMP-2: (top) view along the [010] direction showing a honeycombed structure; (bottom) view along the [100] direction representing stacked undulating layers.
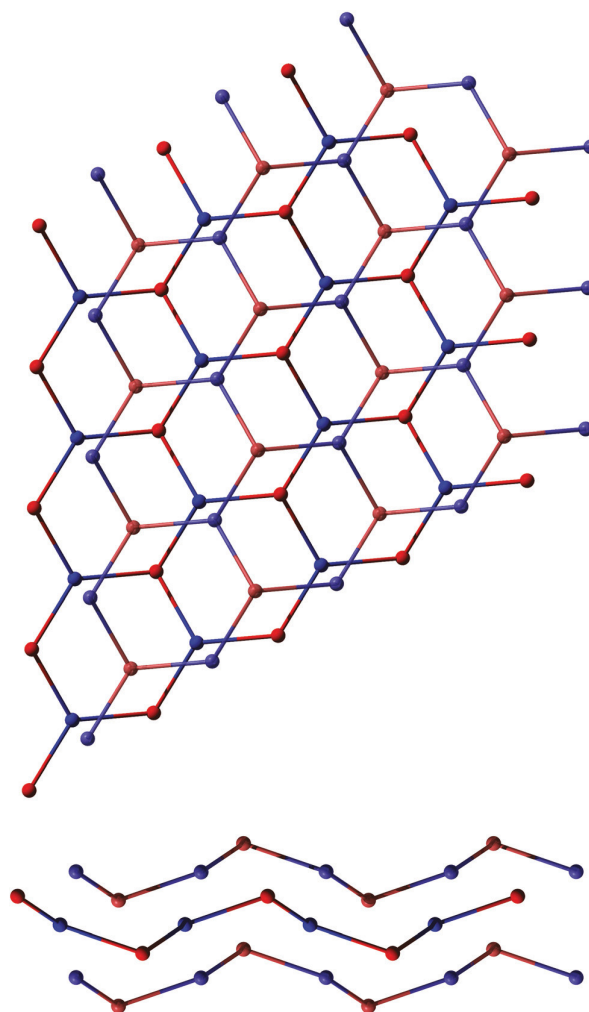

Fig. 3 Topological representation of the staggered hcb nets of JUMP-2. (Top) View along the [010] direction. (Bottom) View along the [$\bar{1}$00] direction. Blue and red balls represent the nodes given by the nitrogen atoms at the center of the amine ligands and the cobalt atoms, respectively.

central nitrogen atom of the ntb^{3-} ligand can likewise be viewed as the other node, which is then also 3-connected. The analysis shows that the framework is a 2-periodic, 3-connected net with hcb topology and the point symbol 6^3 (see Fig. 3).

Although already reported in the literature,[12] we briefly describe here the crystal structure of MIL-144 as a basis for the further analysis and discussion of its properties. The identity of the crystal structure of MIL-144 was ascertained by comparing its cell parameters with those of the reported structure. It crystallizes in the space group $R\bar{3}$ with three symmetry independent cobalt atoms in the asymmetric unit, one of which is located at a special position. In addition, two ntb^{3-} ligands and two water molecules (one of which is disordered with a dimethylamine molecule, both with half occupancies) are found on general positions. Moreover, a disordered dimethylammonium cation and four uncoordinated DMF molecules

(one of which is disordered) are present in the structure. This leads to the overall formula of $\{(Me_2NH_2)_2[Co_5(ntb)_4(H_2O)_3(Me_2NH)] \cdot 7DMF\}_n$.

In contrast to JUMP-2, MIL-144 is a 3D coordination network which is based on two types of inorganic building units (see Fig. 4) one of which is a dinuclear cobalt unit which adopts the classic paddle-wheel motif often seen in copper(II) carboxylates (Co⋯Co distance 291 pm). The second inorganic building unit is a trinuclear cobalt moiety commonly encountered in cobalt–carboxylate systems.[24–26] All cobalt ions within the trinuclear moiety possess an octahedral geometry and the carboxylates show syn–syn-μ_2-η^1:η^1 and μ_2-η^2:η^1 coordination modes. The overall result is a 3D framework consisting of a mixture of triangular and hexagonal channels oriented along the [001] direction (Fig. 5). However, as in the case of JUMP-2,
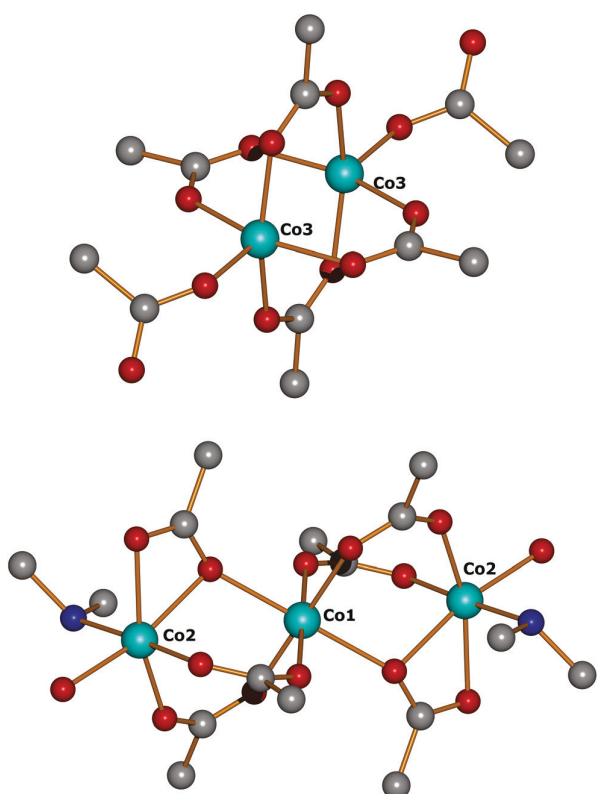
Fig. 4 SBUs found in MIL-144: (top) dinuclear paddle-wheel unit. (Bottom) Trinuclear cobalt(II) cluster linked by carboxylate groups of the ntb^{3-} ligands. For the disordered position dimethylamine is shown.

an anionic framework is obtained, for which the charge is compensated by dimethylammonium cations generated by thermal decomposition of the DMF solvent.

In contrast to the previously assigned topology of interconnected NbO subnets,[12] our analysis utilizing the TOPOS 5.0 program[23] revealed a 3D framework consisting of a 3,6-connected net with 3,6T80 topology and the point symbol $(4^2 \cdot 6)_2(4^4 \cdot 6^2 \cdot 8^8 \cdot 10)$ (see Tables S3 and S4†). Three different vertices can be identified, two of which are based on cobalt clusters and can be considered as the di- and trinuclear cobalt SBUs depicted in Fig. 4. Both of these cobalt-based units are 6-connected nodes, as they are linked to six different carboxylate moieties. The third node is formed by the nitrogen atom at the center of the triphenylamine ligand (ntb^{3-}) giving rise to the 3-connection of the net (Fig. 6). This again shows the presence of hexagonal channels and the alternating occurrence of the two cobalt based nodes (di- and trinuclear SBUs) along the crystallographic [001] direction within the overall framework. A tile representation of the MIL-144 framework is given in Fig. S6.†
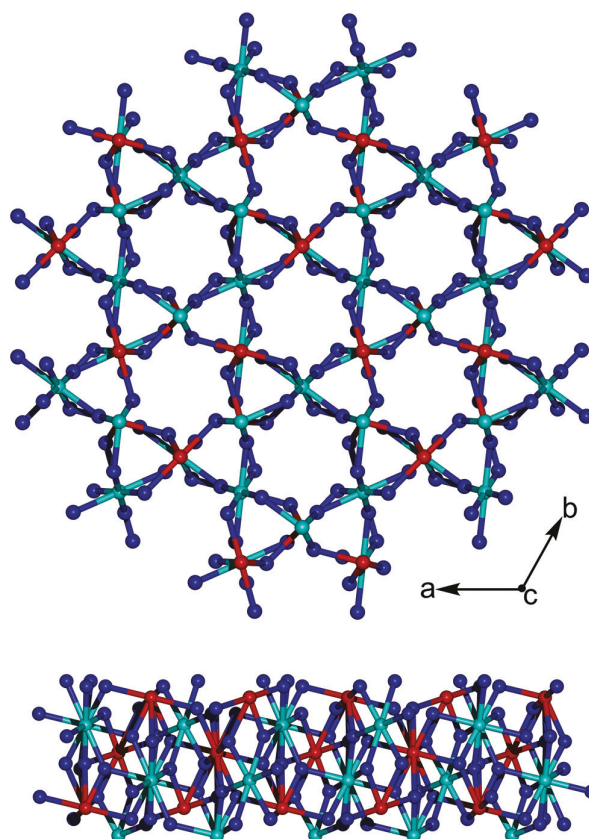
Fig. 6 Topological representation of the 3,6-connected net of MIL-144: (top) view along the [001] direction. (Bottom) View along the [010] direction. Blue balls represent nitrogen atoms at the center of the amine ligand, whereas red and cyan balls represent the centers of the tri- and dinuclear SBUs, respectively (for details see the text).

Fig. 5 Representation of the crystal structure of MIL-144 viewed along the [001] direction showing the arrangement of triangular and hexagonal channels.

Powder diffraction and thermal analysis

To confirm the phase purity of the bulk materials, X-ray powder diffraction (XRPD) experiments were carried out for both as-synthesized compounds JUMP-2 and MIL-144. The experimental XRPD patterns are in close agreement with the corresponding simulations based on the single crystal data, except for the relative intensity variations which might be due to the presence of extra framework species within the pores (see Fig. S7 and S8†).[27]

The thermal analysis of JUMP-2, for a vacuo dried sample at room temperature for 1 h, showed its thermal stability up to about 200 °C. However, the first structured mass loss step up to about 350 °C of 32.5% already indicates a partial degradation of the 2D frameworks as it cannot be solely related to the loss of the guest molecules (DMF and water: calcd 7.5%), but rather suggests the additional loss of the dimethyl-ammonium counterions and that of the chlorido ligand (calcd 33.2%). This indicates that the decomposition of the framework already sets in at rather low temperatures. Additional weight loss steps found up to about 600 °C lead to a rest mass of 12.7%, which nicely compares to the theoretical value of 12.4% expected for CoO (see Fig. S9†).

The thermal analysis of a predried sample of MIL-144 (1 h at room temperature) revealed two major weight loss steps. The first step up to about 220 °C corresponds to about 34% and can be attributed to the loss of guest molecules (DMF and water: calcd 33.2%). The further weight loss of about 6% up to a temperature of about 350 °C can be attributed to the loss of the donor molecules linked to the trinuclear cobalt SBUs (water and dimethylamine) as well as the dimethylammonium cations (calcd 6.4%) indicating the onset of the decomposition of the framework. The remaining mass after full combustion of the organic moieties is found to be 13.6%, which is in agreement with the theoretical value of 12.6% expected for CoO (see Fig. S10†).

Magnetic properties

The magnetic properties of JUMP-2 were investigated by susceptibility measurements at an applied dc field of 1 kOe in the temperature range of 2 to 300 K. The corresponding data are depicted in Fig. 7 as temperature-dependent plots of $\chi_M T$ and χ_M^{-1}. For JUMP-2 a $\chi_M T$ value of 2.34 cm^3 K mol^{-1} is observed at room temperature, which is considerably larger than the spin-only value expected for a high-spin cobalt(II) ion (1.88 cm^3 K mol^{-1}, 3/2, g = 2) indicating the presence of significant spin–orbit coupling.[28] However, this value is well within the range typically observed for similar tetracoordinate cobalt (II) complexes.[29,30] Upon cooling the $\chi_M T$ value decreases only slightly and a significant decrease is only seen to begin below 50 K to reach a value of about 1.6 cm^3 K mol^{-1} at 2 K. This decrease can be attributed to the magnetic anisotropy of the cobalt(II) ion rather than antiferromagnetic exchange consistent with the structural information in which the cobalt(II) ions are well separated from each other. For temperatures above 50 K JUMP-2 behaves as a Curie–Weiss paramagnet with a Curie constant of 2.35 cm^3 K mol^{-1} and a Weiss constant of
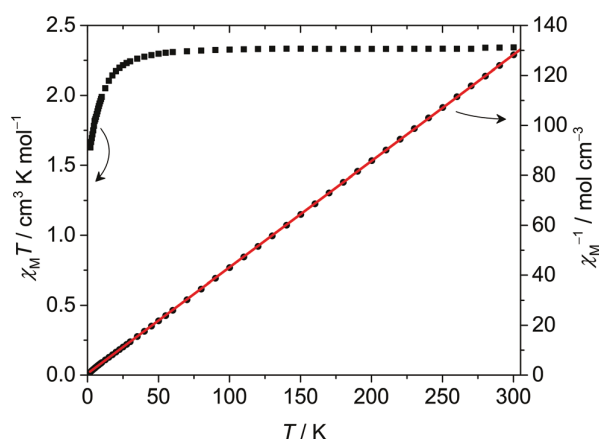

Fig. 7 Temperature dependence of the magnetic susceptibility $\chi_M T$ (black squares) and χ_M^{-1} (black circles) for JUMP-2. The solid line represents the best fit (see the text for parameters).

−1.43 K, which is consistent with only small exchange interactions between individual cobalt(II) ions. Consequently, zero-field splitting (ZFS) needs to be considered for the description of the electronic structure, which however cannot be extracted in a meaningful manner from the susceptibility data, in particular as far as the sign of the corresponding ZFS parameter D is concerned.[28]

ZFS parameters can generally be determined from field-dependent magnetization data which are depicted in Fig. 8. Fitting of the magnetization data with the Hamiltonian given in eqn (1) using the program PHI[31] leads to the parameters D = −16.4 cm^{-1} and g = 2.29. Attempts to include the rhombic ZFS parameter E in the fitting procedure were unsuccessful due to strong parameter dependencies.

$$\hat{H} = g\mu_B B \hat{S} + D\left[\hat{S}_z^2 - \frac{1}{3}S(S+1)\right] \qquad (1)$$
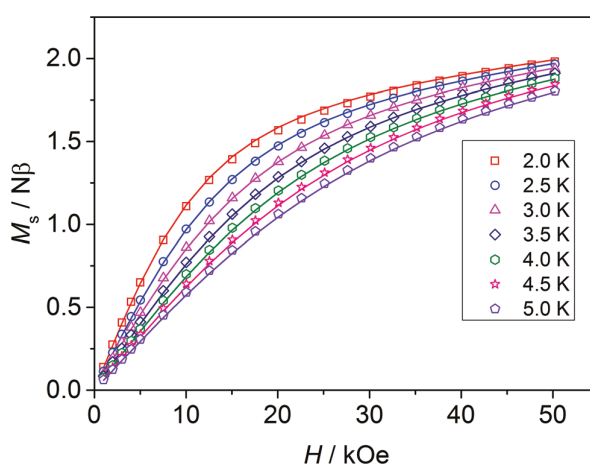

Fig. 8 Temperature- and field-dependent magnetization data for JUMP-2. Lines represent best fit, see the text for details.

There was no evidence of a hysteresis loop down to temperatures of 2 K. Nevertheless, an out-of-phase signal for the ac magnetic susceptibility could be detected at temperatures below 2.5 K when a static dc field was applied (see Fig. S11–S14†), which indicates the presence of slow magnetic relaxation. However, a thermal barrier related to this process could not be determined from the data down to 2 K suggesting very efficient relaxation processes to be operative such as quantum tunneling of magnetization (QTM). This is further supported by quantum mechanical investigations on the electronic structure of the single cobalt(II) ions in JUMP-2 (see data given in the ESI†).

The magnetic susceptibility data obtained for MIL-144 in the temperature range from 2 to 300 K are depicted in Fig. 9. At room temperature a $\chi_M T$ value of 12 cm^3 K mol^{-1} is observed which is much higher than the spin-only value expected for five non-interacting high-spin cobalt(II) ions (9.38 cm^3 K mol^{-1}, 3/2, $g = 2$).[28] This leads to an approximated averaged g value of about 2.26 for the five octahedral cobalt(II) centers. A steady decrease of the $\chi_M T$ value is observed upon cooling reaching a value of 5.4 cm^3 K mol^{-1} at 2 K. For temperatures above 100 K MIL-144 behaves as a Curie–Weiss paramagnet with a Curie constant of 14.0 cm^3 K mol^{-1} and a Weiss constant of −47.3 K. The latter is indicative of the presence of significant antiferromagnetic exchange interactions between the cobalt(II) ions of the di- and trinuclear units found in MIL-144. Field-dependent magnetization data for MIL-144 were recorded at different temperatures and show that saturation is not reached up to 50 kOe (Fig. S15†). Moreover, ac magnetic susceptibility measurements were lacking any out-of-phase signals which indicates the absence of any magnetic ordering and is consistent with magnetically isolated clusters as suggested by the crystal structure. However, any attempt to simulate the experimental data by an appropriate Hamiltonian failed.
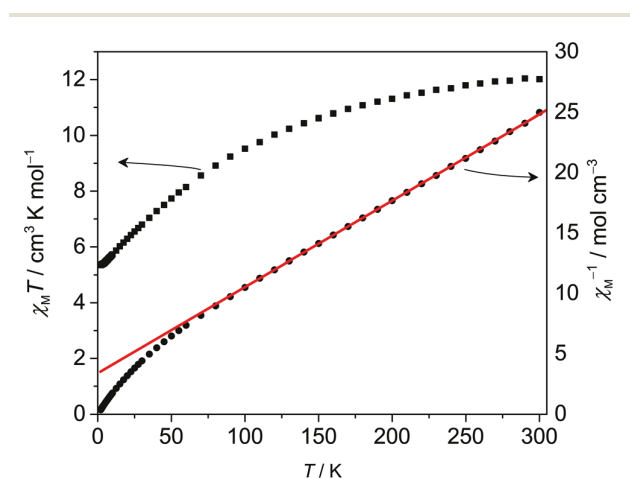
Fig. 9 Temperature dependence of the magnetic susceptibility $\chi_M T$ (black squares) and χ_M^{-1} (black circles) for MIL-144.

Cation exchange studies

To probe the possibility of exchanging the dimethylammonium cations incorporated in the void generated by the frameworks of JUMP-2 and MIL-144 soaking experiments were performed with cations of different sizes and charges in combination with the variation of the applied solvent. At first, the lithium ion was selected for its small size, which should take up considerably less space when compared with the large organic cation. The as-synthesized materials of JUMP-2 and MIL-144 were immersed in saturated solutions of LiNO$_3$ in either ethanol or DMF, to probe the influence of the used solvent on the cation exchange behavior. In order to prevent mechanical stress on the MOF materials during the exchange process no stirring was applied. However, simple convection and diffusion processes were found to be sufficient to maintain the cation exchange. The exchanged materials were then thoroughly washed with ethanol. The corresponding lithium-exchanged samples for JUMP-2 and MIL-144 are further denoted as JUMP-2(Li)E and JUMP-2(Li)D as well as MIL-144(Li)E and MIL-144(Li)D, respectively (where E and D connote ethanol and DMF as the solvents used in cation exchange).

In ethanol as solvent JUMP-2 displays intake of the lithium cations as seen from the analytical data obtained for JUMP-2(Li)E (see the ESI†), which shows agreement with the uptake of one lithium cation per formula unit indicating that only half of the dimethylammonium cations can be replaced under these conditions. In terms of appearance, the material does not undergo a change in color as a result of the ion exchange. Repeating the ion exchange in DMF as solvent has little effect on its performance as judged from the analytical data for JUMP-2(Li)D thereby mirroring the same behavior observed in ethanol. However, for the exchange experiment of MIL-144 in ethanol a distinctly different behavior is observed, as the violet crystals immediately turn to light pink upon the transformation. The elemental analysis for the resulting material MIL-144(Li)E shows agreement with the full replacement of the organic cations. The behavior in DMF as solvent is however contrastingly different as in this case the material retains its appearance. This again goes along with a partial exchange of organic cations, which is consistent with the corresponding analytical data (see the ESI†) indicating that only one of the dimethylammonium cations per formula unit is exchanged by a lithium ion. Moreover, the analytical data for MIL-144(Li)E and MIL-144(Li)D indicate that the dimethylamine ligand coordinated at the trinuclear SBU (see Fig. 4) is replaced by ethanol during the overall exchange process. Extending the soaking period had no impact in increasing uptake of cations in all samples.

The XRPD patterns obtained for the samples after lithium ion exchange show good agreement with the patterns measured for the as-synthesized bulk materials in all cases with the exception of MIL-144(Li)E, for which the disappearance of clearly defined Bragg reflections was observed indicating the loss of crystallinity (see Fig. S16†). Nonetheless, this confirms that the networks generally undergo little

change in response to the replacement of the organic cations. In fact, the observation of persisting broad diffraction peaks at low angles in the case of MIL-144(Li)E suggests the presence of remnant short-range order in the material.[32] It should be noted here that the observed loss of crystallinity is not expected to have a negative impact on the porosity of MIL-144 (Li)E, as it has been previously established that crystallinity does not necessarily translate into high adsorptive capacity.[33]

To further probe the cation-exchange ability of JUMP-2 and MIL-144 we also used the higher charged europium(III) ions, which in addition are fluorescent and allow to easily follow the progression of the exchange process by fluorescence spectroscopy. Both as-synthesized materials were immersed in europium(III) nitrate solutions in both DMF and ethanol as solvent at room temperature. The depletion of europium ions in the supernatant solutions was monitored by the decrease of the corresponding fluorescence signal. The exchange process was monitored over a period of two days and fluorescence spectra were taken at intervals of 1 h (see Fig. 10 and S17†). The decrease in the fluorescence signal related to the free europium(III) ions in solution over time clearly indicates the occurrence of exchange of the dimethylammonium cations within the framework by the europium(III) ions from the solution. In particular, for JUMP-2 a rapid uptake of the europium(III) ions was observed in DMF solution, which is evident from the near depletion of the fluorescence signal in the supernatant solution after a period of 12 h. Moreover, there was a change in the appearance of JUMP-2 under these conditions, as the originally violet crystals turned brown after continuous submersion for 48 h. Also for MIL-144 in DMF solution the europium(III) ions were seen to exchange for the dimethylammonium cations of the framework, although at a comparatively higher remnant fluorescence intensity after 48 h. For the related exchange experiments of JUMP-2 and MIL-144 carried out in ethanol as the solvent similar observations were made (see Fig. S17†). However, the overall uptake was found to be considerably slower. In general, it is apparent that both frameworks also undergo exchange of their countercations with europium(III) ions, although to a varying extent depending on the solvent used.

Based on these results, we also performed the cation exchange with europium(III) ions on a preparative scale following the above described procedure for the exchange with lithium ions utilizing solutions of 0.03 M $Eu(NO_3)_3$ in either ethanol or DMF. The corresponding europium(III) ion exchanged samples for JUMP-2 and MIL-144 are further denoted as JUMP-2(Eu)E and JUMP-2(Eu)D as well as MIL-144 (Eu)E and MIL-144(Eu)D, respectively (where E and D connote ethanol and DMF as the solvents used in cation exchange). The general behavior of JUMP-2 and MIL-144 in the fluorescence experiments was confirmed by the analytical data obtained for the preparative samples after europium(III) ion exchange (see the ESI†). In particular, JUMP-2 shows full replacement of the dimethylammonium cations in DMF as solvent, while only undergoing partial replacement in ethanol. On the other hand, MIL-144 shows generally only partial replacement
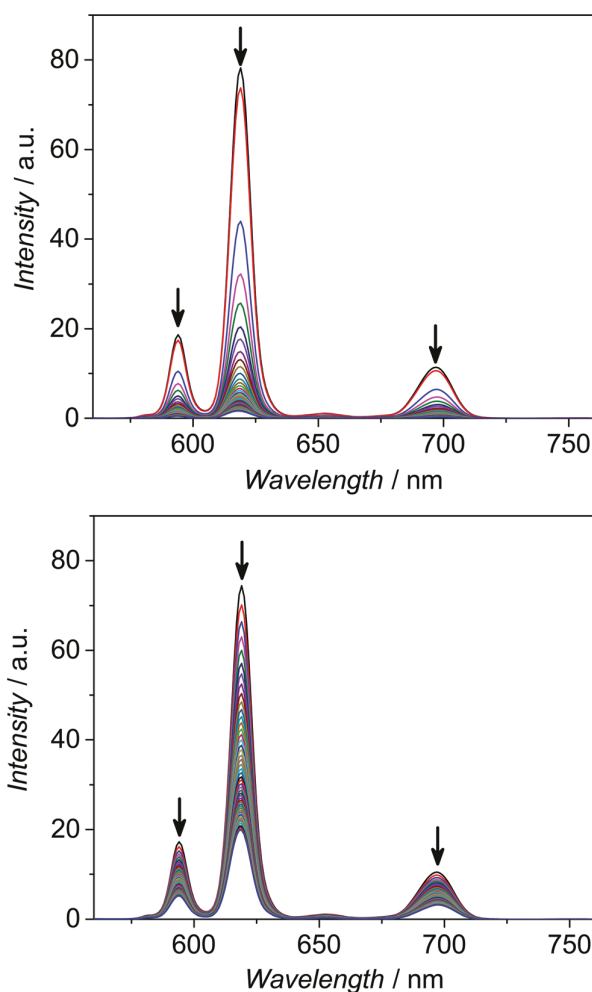

Fig. 10 Cation exchange experiment for JUMP-2 (top) and MIL-144 (bottom) with europium(III) nitrate in DMF solution. Fluorescence spectra depicted were measured in time intervals of 1 h over a period of 48 h at an excitation wavelength of 395 nm.

of the organic cations irrespective of the solvent used, with only one organic cation per framework unit being replaced. Moreover, the analytical data for MIL-144(Eu)E and MIL-144 (Eu)D indicate, similarly to what was observed for the corresponding lithium ions exchanged samples MIL-144(Li)E and MIL-144(Li)D, that the coordinated dimethylamine ligand at the cobalt centers of the trinuclear SBU (see Fig. 4) can easily be replaced by ethanol during the overall exchange process. All XRPD patterns measured for the samples after europium(III) ion exchange are in very good agreement with the patterns obtained for the as-synthesized bulk materials (see Fig. S16†), indicating that the frameworks undergo very little structural change upon exchange of the organic counterions. This nicely proves that the post-synthetic replacement (partial or complete) of the countercations with the europium(III) ions for JUMP-2 and MIL-144 is possible without any observable detrimental impact on the frameworks.

Overall, the porous frameworks JUMP-2 and MIL-144 clearly demonstrate solvent-based cation selectivity in the exchange of the organic countercations present in the as-synthesized materials. A summary of the cation-exchange and solvent selectivity is presented in Table 1. Specifically, JUMP-2 only shows full replacement of the dimethylammonium cations with europium(III) ions and only when DMF is used as the solvent. On the other hand, MIL-144 shows a clear bias towards undergoing full cation exchange only with lithium

ions. This clearly shows that the overall exchange process is triggered by the employed solvent.

Gas-sorption properties

Sorption properties of JUMP-2. The N_2 isotherms measured for samples pretreated by supercritical carbon dioxide activation of the as-synthesized JUMP-2^{scd} and the corresponding cation-exchanged materials JUMP-2(Li)D^{scd} and JUMP-2(Eu)D^{scd} are presented in Fig. 11 and relevant data are summarized in Table 2. The DMF based ion-exchanged samples were selected as they showed the best exchange behavior in the case of JUMP-2. For JUMP-2^{scd} no significant BET surface area was observed with a value of only 13 m^2 g^{-1} (*cf.* Table S5†) and a total pore volume of about 0.02 cm^3 g^{-1}. Upon lithium ion exchange in DMF, the resulting JUMP-2(Li)D^{scd} material showed approximately a doubled BET surface area of 24 m^2 g^{-1} and a corresponding increase in its total pore volume to 0.05 cm^3 g^{-1}. The observed non-porous nature of JUMP-2(Li)D^{scd} is in agreement with the observed cation-exchange behavior as only a partial replacement of the dimethylammonium cations occurred. However, the situation is significantly different for the europium(III) ion exchanged sample for which a complete exchange of the cations had been observed. In the case of JUMP-2(Eu)D^{scd} an almost 17-fold increase of the BET surface area to 216 m^2 g^{-1} as well as 14-fold increase in the total pore volume to 0.27 cm^3 g^{-1} was obtained. In comparison with the overall void given by the anionic framework (0.38 cm^3 g^{-1}, as calculated from the crystal structure of JUMP-2) the total pore volume obtained for JUMP-2^{scd}, JUMP-2(Li)D^{scd}, and JUMP-2(Eu)D^{scd} corresponds to about 5, 13, and 71%, respectively.

Table 1 Solvent dependent selectivity of cation exchange in JUMP-2 and MIL-144

Sample	Exchange	Solvent
JUMP-2(Li)E	Partial	Ethanol
JUMP-2(Li)D^a	Partial	DMF
JUMP-2(Eu)E	Partial	Ethanol
JUMP-2(Eu)D^a	Complete	DMF
MIL-144(Li)E^a	Complete	Ethanol
MIL-144(Li)D	Partial	DMF
MIL-144(Eu)E^a	Partial	Ethanol
MIL-144(Eu)D	Partial	DMF

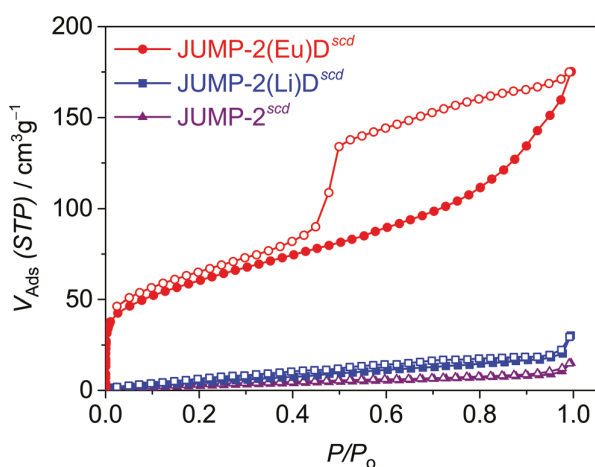^{a} Selected for investigation of its sorption behavior.

Fig. 11 N_2 adsorption isotherms measured at 77 K for samples derived from JUMP-2, open symbols denote the desorption process (for notation details see the text).

The isotherm for JUMP-2(Eu)D^{scd} depicted in Fig. 11 can be described as Type II isotherm based on IUPAC classification and shows a pronounced hysteresis loop of Type H2[34] while for the other two cases of JUMP-2^{scd} and JUMP-2(Li)D^{scd} no significant adsorption is observed, which is in agreement with the non-porous nature of these materials. This can be ascribed to the presence of the dimethylammonium cations in these materials, as these cations can be assumed to restrict the access to the pores. Consequently, there is only a slight increase observed in porosity when comparing JUMP-2^{scd} and JUMP-2(Li)D^{scd}, as the organic cations have only been partially exchanged in the latter. On the other hand, the full cation exchange observed for JUMP-2(Eu)D^{scd} leads to a distinct

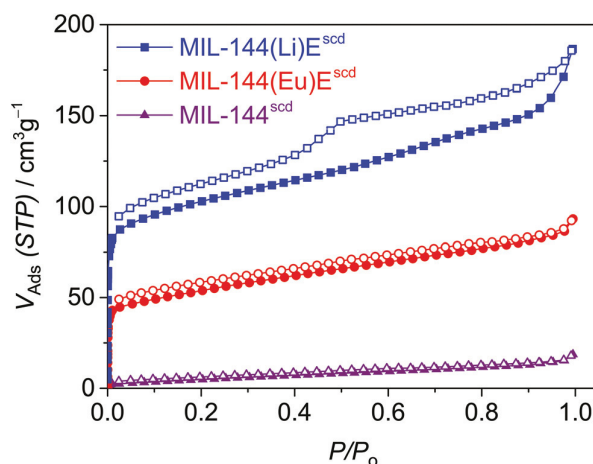**Table 2** Characteristic adsorption parameters for the as-synthesized as well as the lithium and europium ion exchanged samples of both JUMP-2 and MIL-144 after application of supercritical drying with CO_2

Parameter	JUMP-2^{scd}	JUMP-2(Li)D^{scd}	JUMP-2(Eu)D^{scd}	MIL-144^{scd}	MIL-144(Eu)E^{scd}	MIL-144(Li)E^{scd}
a(BET) (m^2 g^{-1})	13	24	216	21	194	380
Total pore volume (cm^3 g^{-1})	0.02	0.05	0.27	0.03	0.14	0.29
Rel. calcd pore volume^a (%)	5	13	71	6	26	54
Mean pore width (nm)	7.1	8.0	5.0	5.5	3.0	3.1
Modal pore width (nm)	4.1	4.5	0.5	4.1	0.6	0.6

^{a} Based on the crystallographic void of 0.38 and 0.54 cm^3 g^{-1} for JUMP-2 and MIL-144, respectively.

increase in the surface area, as the overall lesser steric demand of the europium(III) cations should allow for a considerably better access to the micropores.[35]

To further elucidate this point a pore size analysis of the pretreated samples JUMP-2[scd], JUMP-2(Li)D[scd], and JUMP-2(Eu)D[scd] was performed. The corresponding pore size distribution plots are displayed in Fig. 12. The comparison clearly indicates a massive increase in the population of micropores for the europium(III) ion exchanged sample JUMP-2(Eu)D[scd], with a particular emphasis in the range around 1 nm. The overall observed differences are consistent with the variation in cation exchange behavior, i.e. complete exchange of the dimethylammonium cations was only found for JUMP-2(Eu)D[scd]. This is consistent with the stabilization of the mesopore structure by gentle pretreatment with the supercritical CO_2 drying,[36] and clearly shows that the accessibility to micropores within an anionic framework can be adjusted via the variation of the size of cations residing in the pores.[8]

Sorption properties of MIL-144. The N_2 isotherms for the as-synthesized and ethanol based cation-exchanged samples of

Fig. 13 N_2 adsorption isotherms measured at 77 K for samples derived from MIL-144, open symbols denote the desorption process (for notation details see the text).
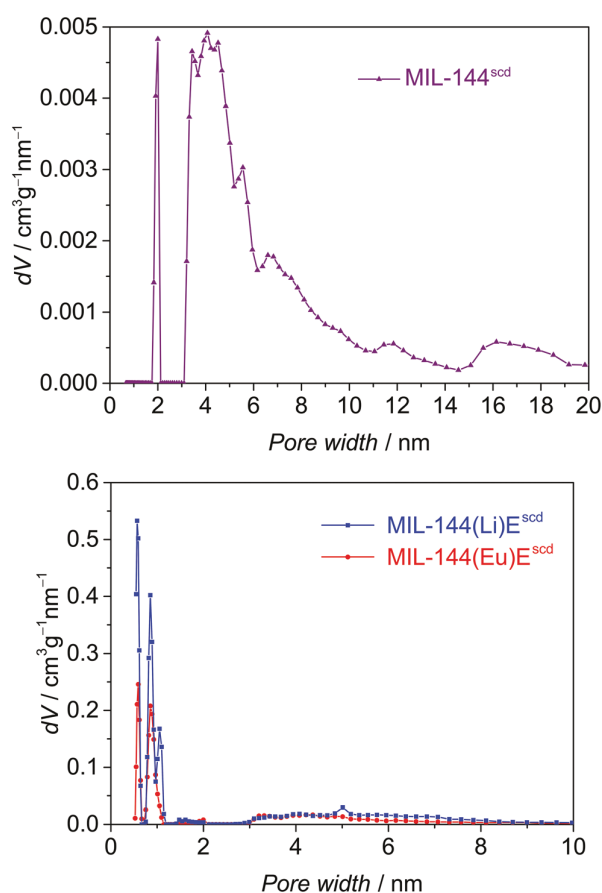

Fig. 12 Pore size distribution data for the as-synthesized and cation-exchanged samples of JUMP-2 after application of supercritical drying with CO_2: JUMP-2[scd] and JUMP-2(Li)D[scd] (top) as well as JUMP-2(Eu)D[scd] (bottom) were fitted using N_2 at 77 K on carbon (slit/cylindrical pores, QSDFT adsorption branch model) (see the text for notation).

MIL-144 are presented in Fig. 13 and relevant data are summarized in Table 2. Here the ethanol based ion-exchanged samples were selected as they showed the best exchange behavior in the case of MIL-144. As in the case of JUMP-2[scd], the N_2 adsorption isotherm measured for the as-synthesized sample MIL-144[scd] shows non-porosity with only a BET surface area of about 21 m^2 g^{-1} (cf. Table S5†) and a total pore volume of about 0.03 cm^3 g^{-1}. However, for the lithium ion exchanged material MIL-144(Li)E[scd] an approximately 20-fold increase in its BET surface area to 380 m^2 g^{-1} together with a ten-fold increase in its total pore volume of 0.29 cm^3 g^{-1} was observed. This can be attributed to the complete replacement of the dimethylammonium cations by the smaller lithium ions leading to significantly improved access to the internal pores. On the other hand, for the europium-exchanged material MIL-144(Eu)E[scd], for which only a partial exchange of the organic cations occurred, a significantly smaller increase only about half in size is observed for both the BET surface area and the pore volume. Based on the overall void given by the anionic framework (0.54 cm^3 g^{-1}, as calculated from the crystal structure of MIL-144) the total pore volume obtained for MIL-144[scd], MIL-144(Eu)E[scd], and MIL-144(Li)E[scd] corresponds to 6, 26, and 54%, respectively.

The isotherms for MIL-144(Eu)E[scd] and MIL-144(Li)E[scd] depicted in Fig. 13 can be classified Type II isotherms,[34] while for the as-synthesized sample MIL-144[scd] no significant adsorption was measured. The hysteresis loops observed for MIL-144(Eu)E[scd] and MIL-144(Li)E[scd] can be described as a Type H4 with a clearly more pronounced characteristic found in the isotherm of MIL-144(Li)E[scd]. As in the case of the JUMP-2 based materials, this is a clear indication that the presence of the dimethylammonium cations in the void of the anionic framework structures is restricting the access to the pores. This becomes evident by the improved sorption behavior upon exchange of the counterions present in the anionic

framework, which in turn allows improved micropore access. In fact, the complete exchange observed in the case of MIL-144 (Li)E^{scd} leads to a remarkable increase in both the BET surface area as well as the total pore volume (see Table 2).

The notable changes observed for the sorption behavior upon cation exchange also reflect in the pore size-distribution plots depicted in Fig. 14. The basic trends of the data follow those seen for the patterns already derived for the corresponding samples based on JUMP-2. The most striking feature is certainly the massive increase in the population of micropores in the range of 0.6 to 2 nm for the exchanged materials MIL-144(Eu)E^{scd} and MIL-144(Li)E^{scd} which are virtually absent in the non-exchanged as-synthesized sample MIL-144^{scd}. Again the complete ion exchange, as observed in the case of MIL-144(Li)E^{scd}, leads to the most pronounced effect. This provides additional evidence that the ion exchange enabled access to the mesopores, which in turn made the micropores accessible.[36]

The overall result of the sorption measurements nicely shows that for JUMP-2 and MIL-144 the access to the pores can be tuned *via* the cation size and consequently depends on a suitable choice of the cation.[8]

Conclusions

Two anionic cobalt(II) based coordination polymers with triphenylamine bridging ligand H$_3$ntb were synthesized in a solvothermal process. The anionic frameworks of JUMP-2 and MIL-144 are charge balanced by organic cations which were formed *in situ* from the employed solvent and take part in the templated synthesis. Despite using the same reaction conditions, it was observed that changing the size of the reaction vessel was decisive for the final product obtained. The topological analyses of the coordination polymers revealed JUMP-2 to be a 3-connected 2D network with hcb topology, while MIL-144 represents a 3D framework with a 3,6-connected net with 3,6T80 topology. The magnetic properties of JUMP-2 and MIL-144 have been examined. Both coordination polymers behave like paramagnets with no relevant magnetic interactions between their cobalt(II) based building blocks. The dimethylammonium countercations present in the as-synthesized compounds could be successfully exchanged by both lithium and europium(III) ions, of which the latter could be monitored by fluorescence measurements. Notably, both compounds also show a clear bias towards different ions depending on the solvent used for the exchange, leading to complete exchange only for the case of JUMP-2(Eu)D and MIL-144(Li)E. In fact, as adsorption measurements show, the lack of accessibility of the micropores in the as-synthesized materials, which can be attributed to the presence of the rather large organic cations in the void space of the frameworks, can be removed by both lithium and europium ion exchange. Both cation exchange and sorption experiments conclusively show that the properties of these anionic frameworks can be tuned by post-synthetic manipulations.

Fig. 14 Pore size distribution data for the as-synthesized and cation-exchanged samples of MIL-144 after the application of supercritical drying with CO$_2$: MIL-144^{scd} (top) as well as MIL-144(Eu)E^{scd} and MIL-144(Li)E^{scd} (bottom) were fitted using N$_2$ at 77 K on carbon (slit/cylindrical pores, QSDFT adsorption branch model) (see the text for notation).

References

1 (*a*) P. Mahata, G. Madras and S. Natarajan, *J. Phys. Chem. B*, 2006, **110**, 13759–13768; (*b*) A. Dhakshinamoorthy, M. Opanasenko, J. Cejka and H. Garcia, *Adv. Synth. Catal.*, 2013, **355**, 247–268; (*c*) A. Santra, I. Senkovska, S. Kaskel and P. K. Bharadwaj, *Inorg. Chem.*, 2013, **52**, 7358–7366;

(d) Z. Chang, D.-S. Zhang, Q. Chen and X.-H. Bu, *Phys. Chem. Chem. Phys.*, 2013, **15**, 5430–5442; (e) Y.-W. Li, J.-R. Li, L.-F. Wang, B.-Y. Zhou, Q. Chen and X.-H. Bu, *J. Mater. Chem. A*, 2013, **1**, 495–499; (f) M. Guo and Z.-M. Sun, *J. Mater. Chem.*, 2012, **22**, 15939–15946; (g) M. M. Wander-ley, C. Wang, C.-D. Wu and W. Lin, *J. Am. Chem. Soc.*, 2012, **134**, 9050–9053; (h) K. Koh, A. Wong-Foy and A. Matzger, *J. Am. Chem. Soc.*, 2010, **132**, 15005–15010; (i) A. Dutta, A. G. Wong-Foya and A. J. Matzger, *Chem. Sci.*, 2014, **5**, 3729–3734; (j) M. Tonigold, Y. Lu, A. Mavrandonakis, A. Puls, R. Staudt, J. Möllmer, J. Sauer and D. Volkmer, *Chem. – Eur. J.*, 2011, **17**, 8671–8695; (k) M. Tonigold, Y. Lu, B. Bredenkötter, B. Rieger, S. Bahnmüller, J. Hitzbleck, G. Langstein and D. Volkmer, *Angew. Chem., Int. Ed.*, 2009, **48**, 7546–7550; (l) M. Alvaro, E. Carbonell, B. Ferrer, F. X. L. I. Xamena and H. Garcia, *Chem. – Eur. J.*, 2007, **13**, 5106–5112; (m) L. Croitor, E. B. Coropceanu, D. Chisca, S. G. Baca, J. van Leusen, P. Kögerler, P. Bourosh, V. C. Kravtsov, D. Grabco, C. Pyrtsac and M. S. Fonari, *Cryst. Growth Des.*, 2014, **14**, 3015–3025; (n) O. Botezat, J. van Leusen, V. C. Kravtsov, I. G. Filippova, J. Hauser, M. Speldrich, R. P. Hermann, K. W. Krämer, S.-X. Liu, S. Decurtins, P. Kögerler and S. G. Baca, *Cryst. Growth Des.*, 2014, **14**, 4721–4728; (o) A. McKinlay, R. Morris, P. Horcajada, G. Férey, R. Gref, P. Couvreur and C. Serre, *Angew. Chem., Int. Ed.*, 2010, **49**, 6260–6266.

2 (a) J. Hong, M. Cheng, Q. Liu, W. Han, Y. Zhang, Y. Ji, X. Jia and Z. Li, *Transition Met. Chem.*, 2013, **38**, 385–392; (b) X.-N. Cheng, W. Xue and X.-M. Chen, *Eur. J. Inorg. Chem.*, 2010, 3850–3855; (c) H. J. Choi and M. P. Suh, *J. Am. Chem. Soc.*, 2004, **126**, 15844–15851; (d) X. X. Zhang, S. S.-Y. Chui and I. D. Williams, *J. Appl. Phys.*, 2000, **87**, 6007–6009.

3 A. Das, G. Pilet, D. Luneau, M. S. E. Fallah, J. Ribas and S. Mitra, *Inorg. Chim. Acta*, 2005, **358**, 4581–4587.

4 (a) L. Hou, B. Liu, L.-N. Jia, L. Wei, Y.-Y. Wang and Q.-Z. Shi, *Cryst. Growth Des.*, 2013, **13**, 701–707; (b) A. M. P. Peedikkal, Y.-M. Song, R.-G. Xiong, S. Gao and J. J. Vittal, *Eur. J. Inorg. Chem.*, 2010, 3856–3865; (c) P.-Z. Li, X.-J. Wang, Y. Li, Q. Zhang, R. H. D. Tan, W. Q. Lim, R. Ganguly and Y. Zhao, *Microporous Mesoporous Mater.*, 2013, **176**, 194–198; (d) D. Kim, X. Song, J. H. Yoon and M. S. Lah, *Cryst. Growth Des.*, 2012, **12**, 4186–4193.

5 (a) S. Chen, J. Zhang, T. Wu, P. Feng and X. Bu, *J. Am. Chem. Soc.*, 2009, **131**, 16027–16029; (b) X.-R. Hao, X.-L. Wang, Z.-M. Su, K.-Z. Shao, Y.-H. Zhao, Y.-Q. Lana and Y.-M. Fu, *Dalton Trans.*, 2009, 8562–8566; (c) K. Akhbari and A. Morsali, *Dalton Trans.*, 2013, **42**, 4786–4789; (d) J. Zhang, R. Liu, P. Feng and X. Bu, *Angew. Chem., Int. Ed.*, 2007, **46**, 8388–8391; (e) D. Banerjee, S. J. Kim, H. Wu, W. Xu, L. A. Borkowski, J. Li and J. B. Parise, *Inorg. Chem.*, 2011, **50**, 208–212.

6 (a) E. Quartapelle Procopio, F. Linares, C. Montoro, V. Colombo, A. Maspero, E. Barea and J. A. R. Navarro, *Angew. Chem, Int. Ed.*, 2010, **122**, 7466–7469; (b) S. Yang, G. S. B. Martin, J. J. Titman, A. J. Blake, D. R. Allan, N. R. Champness and M. Schröder, *Inorg. Chem.*, 2011, **50**, 9374–9384; (c) S. Yang, X. Lin, A. J. Blake, G. S. Walker, P. Hubberstey, N. R. Champness and M. Schröder, *Nat. Chem.*, 2009, **1**, 487–493.

7 (a) J.-S. Qin, S.-R. Zhang, D.-Y. Du, P. Shen, S.-J. Bao, Y.-Q. Lan and Z.-M. Su, *Chem. – Eur. J.*, 2014, **20**, 5625–5630; (b) W.-G. Lu, L. Jiang, X.-L. Feng and T.-B. Lu, *Inorg. Chem.*, 2009, **48**, 6997–6999; (c) J. An, C. M. Shade, D. A. Chengelis-Czegan, S. Petoud and N. L. Rosi, *J. Am. Chem. Soc.*, 2011, **133**, 1220–1223.

8 (a) J. An and N. L. Rosi, *J. Am. Chem. Soc.*, 2010, **132**, 5578–5579; (b) S. Yang, X. Lin, A. J. Blake, K. M. Thomas, P. Hubberstey, N. R. Champness and M. Schröder, *Chem. Commun.*, 2008, 6108–6110.

9 N. Stock and S. Biswas, *Chem. Rev.*, 2012, **112**, 933–969.

10 (a) H. K. Chae, J. Kim, O. D. Friedrichs, M. O'Keeffe and O. M. Yaghi, *Angew. Chem., Int. Ed.*, 2003, **42**, 3907–3909; (b) E. Y. Lee, S. Y. Jang and M. P. Suh, *J. Am. Chem. Soc.*, 2005, **127**, 6374–6381; (c) M. P. Suh, Y. E. Cheon and E. Y. Lee, *Chem. – Eur. J.*, 2007, **13**, 4208–4215.

11 O. Akintola, S. Ziegenbalg, A. Buchholz, H. Görls and W. Plass, *CrystEngComm*, 2017, **19**, 2723–2732.

12 C. Livage, N. Guillou, A. Castiglione, J. Marrot, M. Frigoli and F. Millange, *Microporous Mesoporous Mater.*, 2012, **157**, 37–41.

13 X. Cao, Y. Wen, Y. Guo, G. Yu, Y. Liu and L.-M. Yang, *Dyes Pigm.*, 2010, **84**, 203–207.

14 S. Dapperheld, E. Steckhan, K.-H. G. Brinkhaus and T. Esch, *Chem. Ber.*, 1991, **124**, 2557–2567.

15 (a) B. V. Nonius, *COLLECT; Data Collection Software*, Delft, The Netherlands, 1998; (b) Z. Otwinowski and W. Minor, in *Methods in Enzymology*, ed. C. W. Carter and R. M. Sweet, Academic Press, 1997, vol. 276, ch. Processing of X-ray Diffraction Data Collected in Oscillation Mode, pp. 307–326.

16 G. M. Sheldrick, *Acta Crystallogr., Sect. A: Fundam. Crystallogr.*, 2008, **64**, 112–122.

17 O. Dolomanov, L. Bourhis, R. Gildea, J. Howard and H. Puschmann, *J. Appl. Crystallogr.*, 2009, **42**, 339–341.

18 H. Putz and K. Brandenburg, *Diamond 4.2.2 - Crystal and Molecular Structure Visualization*, Crystal Impact, Kreuzherrenstr. 102, 53227 Bonn, Germany.

19 QUANTACHROME, Application of QSDFT (Quenched Solid Density Functional Theory) – A novel density functional theory for an accurate pore size analysis of disordered porous carbons.

20 J. Rouquerol, P. Llewellyn and F. Rouquerol, *Stud. Surf. Sci. Catal.*, 2007, **160**, 49–56.

21 (a) S. M. Hawxwell and L. Brammer, *CrystEngComm*, 2006, **8**, 473–476; (b) A. D. Burrows, K. Cassar, R. M. W. Friend, M. F. Mahon, S. P. Rigby and J. E. Warren, *CrystEngComm*, 2005, **7**, 548–550; (c) B. Cheng, F. Z. Karizi, M.-L. Hu and A. Morsali, *Mater. Lett.*, 2014, **137**, 88–91; (d) Z.-J. Li,

S. K. Khani, K. Akhbari, A. Morsali and P. Retailleau, *Microporous Mesoporous Mater.*, 2014, **199**, 93–98.

22 A. L. Spek, *Acta Crystallogr., Sect. D: Biol. Crystallogr.*, 2009, **65**, 148–155.

23 (*a*) V. A. Blatov, A. P. Shevchenko and D. M. Proserpio, *Cryst. Growth Des.*, 2014, **14**, 3576–3586; (*b*) O. Delgado-Friedrichs, M. O'Keeffe and O. Yaghi, *Phys. Chem. Chem. Phys.*, 2007, **9**, 1035–1043; (*c*) M. O'Keeffe and O. M. Yaghi, *Chem. Rev.*, 2012, **112**, 675–702.

24 (*a*) L.-F. Ma, Y.-Y. Wang, L.-Y. Wang, D.-H. Lu, S. R. Batten and J.-G. Wang, *Cryst. Growth Des.*, 2009, **9**, 2036–2038; (*b*) W.-X. Chen, G.-L. Zhuang, H.-X. Zhao, L.-S. Long, R.-B. Huang and L.-S. Zheng, *Dalton Trans.*, 2011, **40**, 10237–10241.

25 (*a*) Z. Su, Y. Song, Z.-S. Bai, J. Fan, G.-X. Liu and W.-Y. Sun, *CrystEngComm*, 2010, **12**, 4339–4346; (*b*) B. Xua, B. Liu, H.-M. Hu, Y. Cheng, Z. Chang and G. Xue, *Polyhedron*, 2015, **96**, 88–94.

26 (*a*) Z. Chen, X. Liu, C. Zhang, Z. Zhang and F. Liang, *Dalton Trans.*, 2011, **40**, 1911–1918; (*b*) T.-F. Liu, J. Lü, C. Tian, M. Cao, Z. Lin and R. Cao, *Inorg. Chem.*, 2011, **50**, 2264–2271.

27 J. Hafizovic, M. Bjorgen, U. Olsbye, P. D. C. Dietzel, S. Bordiga, C. Prestipino, C. Lamberti and K. P. Lillerud, *J. Am. Chem. Soc.*, 2007, **129**, 3612–3620.

28 O. Kahn, *Molecular Magnetism*, Wiley-VCH Inc., Weinheim, 1993.

29 S. Ziegenbalg, D. Hornig, H. Görls and W. Plass, *Inorg. Chem.*, 2016, **55**, 4047–4058.

30 A. Buchholz, A. O. Eseola and W. Plass, *C. R. Chim.*, 2012, **15**, 929–936.

31 N. F. Chilton, R. Anderson, L. Turner, A. Soncini and K. Murray, *J. Comput. Chem.*, 2013, **34**, 1164–1175.

32 B. Bueken, F. Vermoortele, M. J. Cliffe, M. T. Wharmby, D. Foucher, J. Wieme, L. Vanduyfhuys, C. Martineau, N. Stock, F. Taulelle, V. V. Speybroeck, A. L. Goodwin and D. D. Vos, *Chem. – Eur. J.*, 2016, **22**, 3264–3267.

33 J. L. C. Rowsell and O. M. Yaghi, *J. Am. Chem. Soc.*, 2006, **128**, 1304–1315.

34 (*a*) M. Thommes, K. Kaneko, A. V. Neimark, J. P. Olivier, F. Rodriguez-Reinoso, J. Rouquerol and K. S. W. Sing, *Pure Appl. Chem.*, 2015, **87**, 1051–1069; (*b*) K. S. W. Sing, D. H. Everett, R. A. W. Haul, L. Moscou, R. A. Pierotti, J. Rouquerol and T. Siemieniewska, *Pure Appl. Chem.*, 1985, **57**, 603–619.

35 M. Thommes and K. A. Cychosz, *Adsorption*, 2014, **20**, 233–250.

36 A. Nelson, O. Farha, K. Mulfort and J. Hupp, *J. Am. Chem. Soc.*, 2009, **131**, 458–460.

Solvent-dependent selective cation exchange in anionic frameworks based on cobalt(II) and triphenylamine linkers: reactor-dependent synthesis and sorption properties

Oluseun Akintola, David Hornig, Axel Buchholz, Helmar Görls, Winfried Plass

Supplementary Information

Contents

1 Reactor vessels

Fig. S1: Reactor vessels utilized in MOF syntheses: (Left) 110 mL Perkin Elmer acid digestion bomb for MIL-144. (Right) 23 mL Parr acid digestion bomb for JUMP-2.

2 Analytical data for cation-exchanged samples

2.1 Exchange with lithium ions

JUMP-2(Li)E

Analytical Data for [(Me$_2$NH$_2$)Li[Co(ntb)Cl] $\cdot$ C$_2$H$_5$OH $\cdot$ 1.5 DMF]$_n$

Anal. Calcd for C$_{29.5}$H$_{36.5}$ClCoLiN$_{3.5}$O$_{8.5}$ (677.45 g mol^{-1}):

C 52.30, H 5.43, N 7.24 %. Found: C 52.10, H 5.35, N 7.39 %.

Selected IR (ATR, cm^{-1}): 1651w, 1591s, 1506m, 1370s, 1313s, 1271s, 1174s, 1103m, 1045m.

JUMP-2(Li)D

Analytical Data for [(Me$_2$NH$_2$)Li[Co(ntb)Cl] $\cdot$ C$_2$H$_5$OH $\cdot$ DMF $\cdot$ H$_2$O]$_n$

Anal. Calcd for C$_{28}$H$_{35}$ClCoLiN$_3$O$_9$ (658.92 g mol^{-1}):

C 51.04, H 5.35, N 6.38 %. Found: C 51.10, H 5.61, N 6.17 %.

Selected IR (ATR, cm^{-1}): 1652w, 1591s, 1506m, 1372s, 1313s, 1270s, 1173s, 1088m, 1045m.

MIL-144(Li)E

Analytical Data for [Li$_2$[Co$_5$(ntb)$_4$(H$_2$O)$_3$(C$_2$H$_5$OH)] $\cdot$ 17 H$_2$O]$_n$

Anal. Calcd for C$_{86}$H$_{94}$Co$_5$Li$_2$N$_4$O$_{45}$ (2212.21 g mol^{-1}):

C 46.69, H 4.28, N 2.53 %. Found: C 46.67, H 4.20, N 2.36 %.

Selected IR (ATR, cm^{-1}): 1589s, 1535m, 1506m, 1378vs, 1313s, 1270s, 1176s, 1087m, 1045m.

MIL-144(Li)D

Analytical Data for [(Me$_2$NH$_2$)Li[Co$_5$(ntb)$_4$(H$_2$O)$_3$(C$_2$H$_5$OH)]$_n$ $\cdot$ 3 C$_2$H$_5$OH $\cdot$ 2 H$_2$O]

Anal. Calcd for C$_{94}$H$_{90}$Co$_5$LiN$_5$O$_{33}$ (2119.34 g mol^{-1}):

C 53.27, H 4.28, N 3.30 %. Found: C 53.18, H 4.41, N 3.20 %.

Selected IR (ATR, cm^{-1}): 1589s, 1536m, 1505m, 1376vs, 1312s, 1269s, 1175s, 1088m, 1043m.

2.2 Exchange with europium(III) ions

JUMP-2(Eu)E
Analytical Data for [(MeNH$_2$)$_3$Eu([Co(ntb)Cl])$_3$] · 3 C$_2$H$_5$OH · 6 DMF
Anal. Calcd for C$_{93}$H$_{120}$Cl$_3$Co$_3$EuN12O$_{27}$ (2273.13 g mol^{-1}):
C 49.14, H 5.32, N 7.39 %. Found: C 49.52, H 5.03, N 7.22 %.
Selected IR (ATR, cm^{-1}): 1653w, 1594s, 1505m, 1367s, 1313s, 1268s, 1170s, 1103m.

JUMP-2(Eu)D
Analytical Data for [Eu$_2$([Co(ntb)Cl])$_3$] · 9 C$_2$H$_5$OH · 3 DMF
Anal. Calcd for C$_{90}$H$_{111}$Cl$_3$Co$_3$Eu$_2$N$_6$O$_{30}$ (2343.95 g mol^{-1}):
C 46.12, H 4.77, N 3.59 %. Found: C 46.08, H 4.91, N 3.77 %.
Selected IR (ATR, cm^{-1}): 1591s, 1535m, 1506m, 1376vs, 1313s, 1271s, 1174s, 1088m, 1043s.

MIL-144(Eu)E
Analytical Data for [(Me$_2$NH$_2$)$_3$Eu[Co$_5$(ntb)$_4$(H$_2$O)$_3$(C$_2$H$_5$OH)]$_3$] · 54 H$_2$O · 18 C$_2$H$_5$OH
Anal. Calcd for C$_{300}$H$_{420}$Co$_{15}$EuN$_{15}$O$_{156}$ (7768.51 g mol^{-1}):
C 46.38, H 5.45, N 2.70 %. Found: C 46.37, H 5.68, N 2.44 %.
Selected IR (ATR, cm^{-1}): 1589s, 1529m, 1504m, 1382vs, 1312s, 1270s, 1175s, 1086m, 1042s.

MIL-144(Eu)D
Analytical Data for [(Me$_2$NH$_2$)$_3$Eu[Co$_5$(ntb)$_4$(H$_2$O)$_3$(C$_2$H$_5$OH)]$_3$] · 42 H$_2$O · 18 C$_2$H$_5$OH
Anal. Calcd for C$_{300}$H$_{396}$Co$_{15}$EuN$_{15}$O$_{144}$ (7552.33 g mol^{-1}):
C 47.71, H 5.29, N 2.78 %. Found: C 47.75, H 5.20, N 2.94 %.
Selected IR (ATR, cm^{-1}): 1590s, 1535m, 1505m, 1382vs, 1312s, 1271s, 1175s, 1087m, 1043s.

3 Additional structure information for JUMP-2
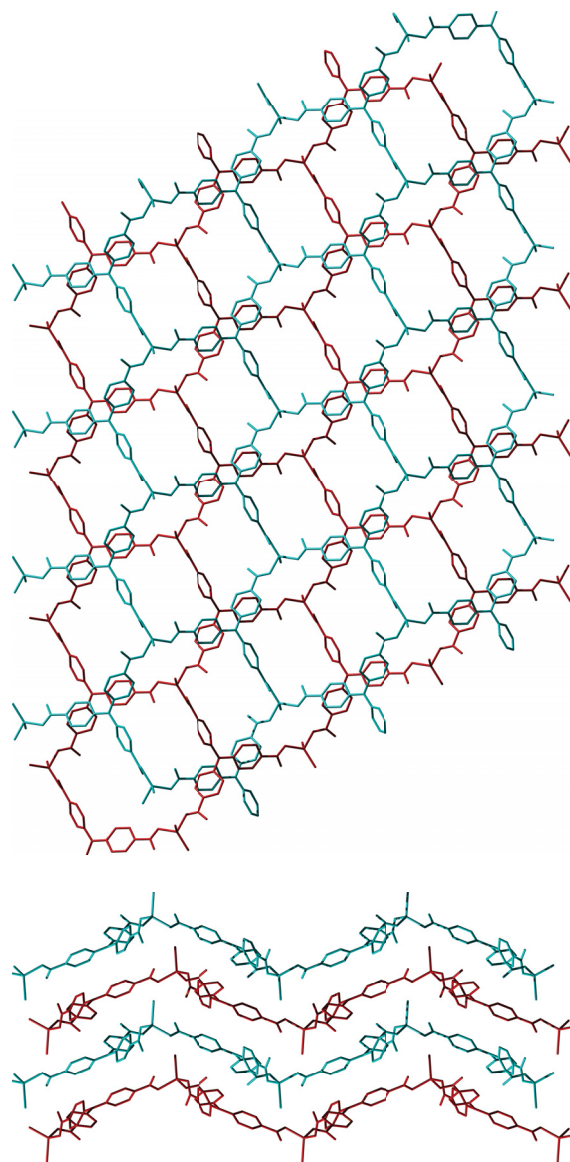
Fig. S2: 2D layered arrangement of the anionic framework in JUMP-2 showing the staggered arrangement: (Top) View along the [010] direction. (Bottom) Side view along the [$\bar{1}$00] direction.
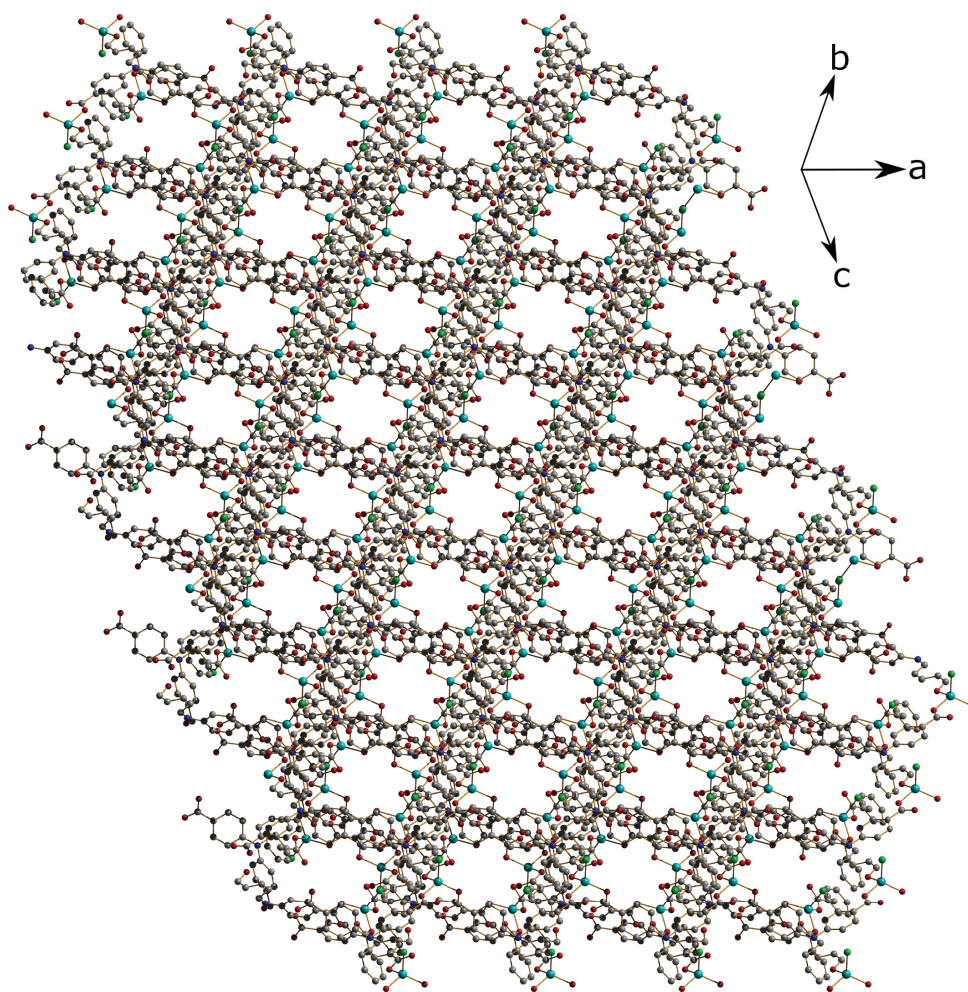
Fig. S3: 1D channels in the anionic framework of JUMP-2 viewed along [12$\bar{1}$] direction.
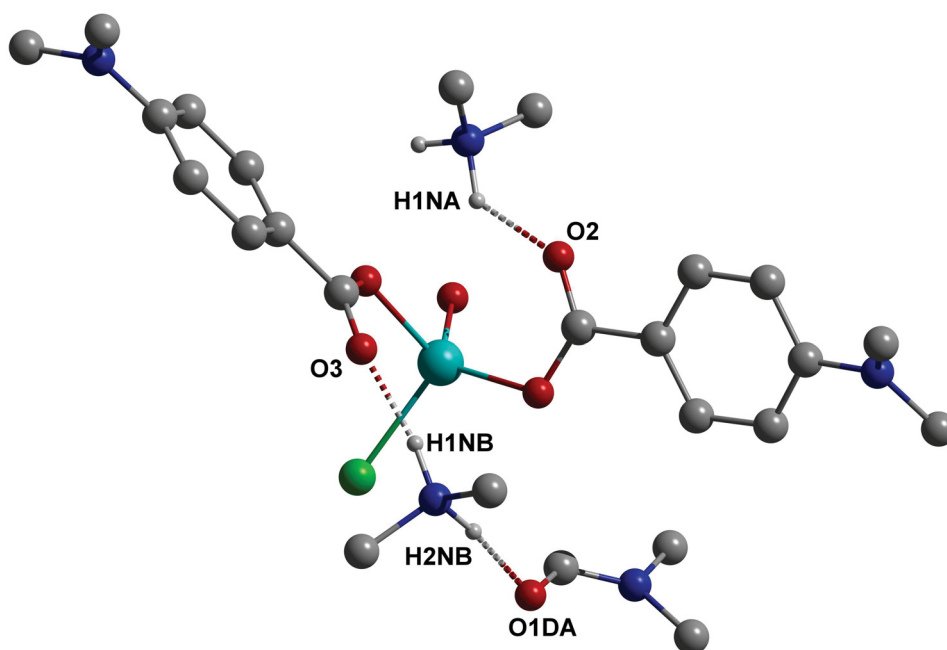
Fig. S4: Representation of the hydrogen bonding interactions for a cutout of the anionic framework of JUMP-2. Pertinent data: $O_2 \cdots N_1EA$ 271.7(5), $O_3 \cdots N_1EB$ 271.1(5), $O_1DA \cdots N_1EB$ 277.0(9) pm.
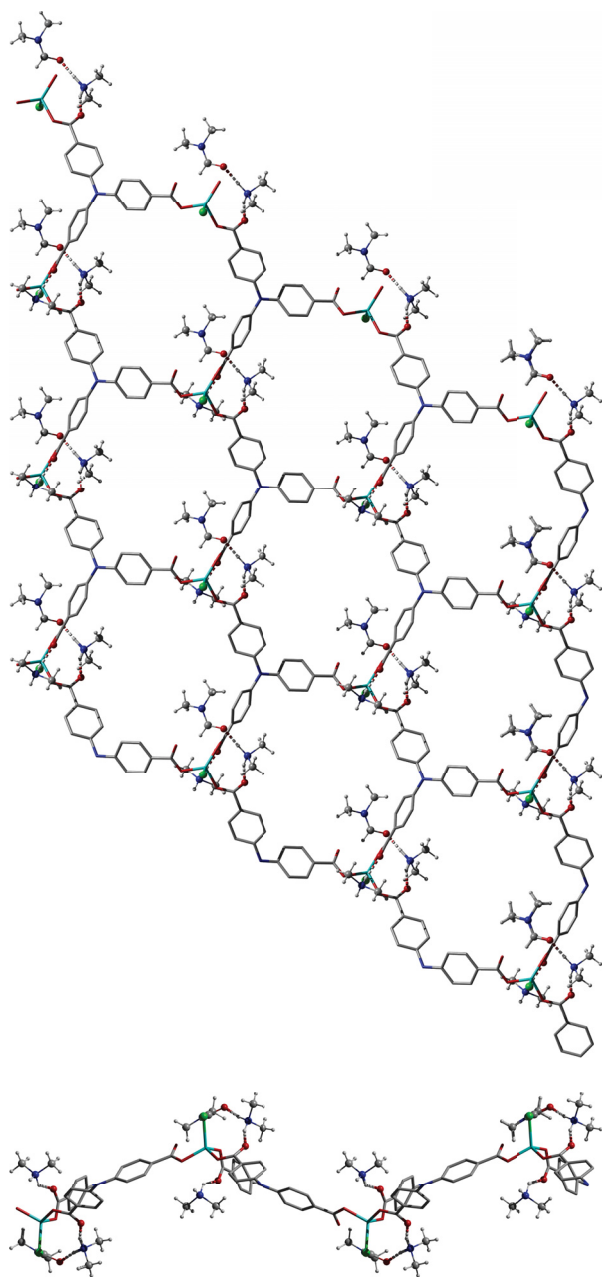
Fig. S5: Representation of the hydrogen bonding around the 2D layers in JUMP-2 viewed along [010] direction: (Top) View along the [010] direction. (Bottom) Side view of one layer along the [$\bar{1}$00] direction.

9

4 Topological analysis

4.1 Topological analysis for JUMP-2

Ideal space group is $P6mm$.

Table S1: Coordination sequences for JUMP-2 (topological density $TD_{10} = 166$)

Vertex	CS_1	CS_2	CS_3	CS_4	CS_5	CS_6	CS_7	CS_8	CS_9	CS_{10}
V1	3	6	9	12	15	18	21	24	27	30
V2	3	6	9	12	15	18	21	24	27	30

Table S2: Vertex Symbols for JUMP-2

Vertex	Vertex symbol	Extended Point Symbol
V1	$[6^3]$	[6.6.6]
V2	$[6^3]$	[6.6.6]

4.2 Topological analysis for MIL-144

Ideal space group: $R\bar{3}c$.

Table S3: Coordination sequences for MIL-144 (topological density $TD_{10} = 1192$)

Vertex	CS_1	CS_2	CS_3	CS_4	CS_5	CS_6	CS_7	CS_8	CS_9	CS_{10}
V1	3	13	16	52	45	134	103	257	171	418
V2	6	8	32	30	90	76	206	140	342	218

Table S4: Vertex Symbols for MIL-144

Vertex	Vertex symbol	Extended Point Symbol
V1	$[4^2.6]$	[4.4.6]
V2	$[4^4.6^2.8^8.10]$	$[4.4.4.4.6.6.8_2.8_3.8_3.8_4.8_7.8_7.8_7.8_7.10_{14}]$

4.3 Tiling of MIL-144
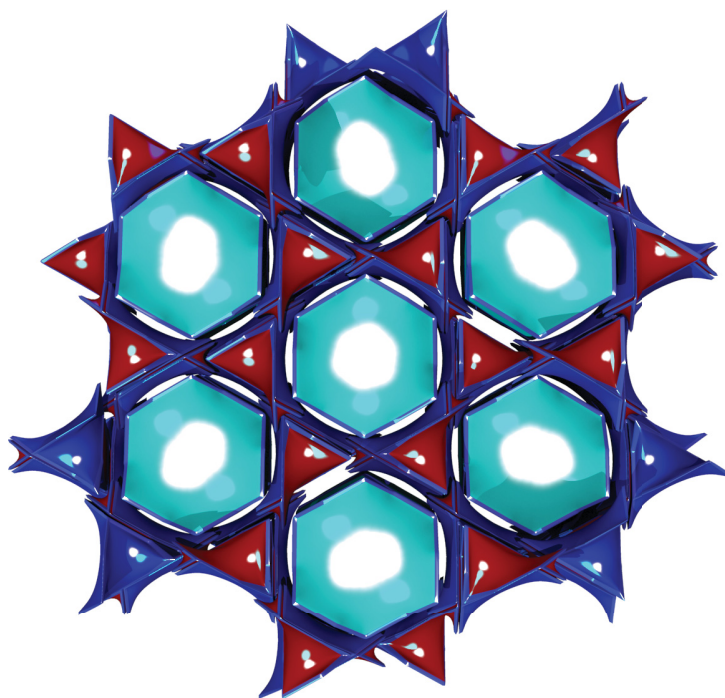
Fig. S6: Tiling of MIL-144 viewed along [001]. Tiles: $3[4^2.8^{2\cdot}]+3[4.8^3]+[4^3.8^{3\cdot}.12^2]$. Transitivity: [2353].

5 XRPD patterns of as-synthesized samples
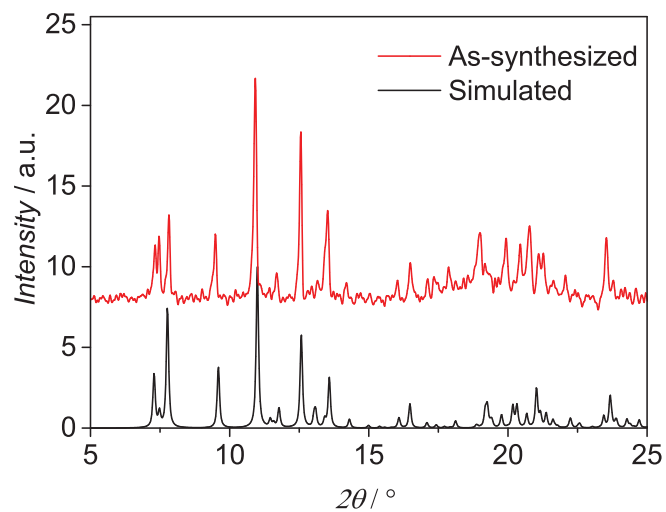
Fig. S7: XRPD pattern for JUMP-2.
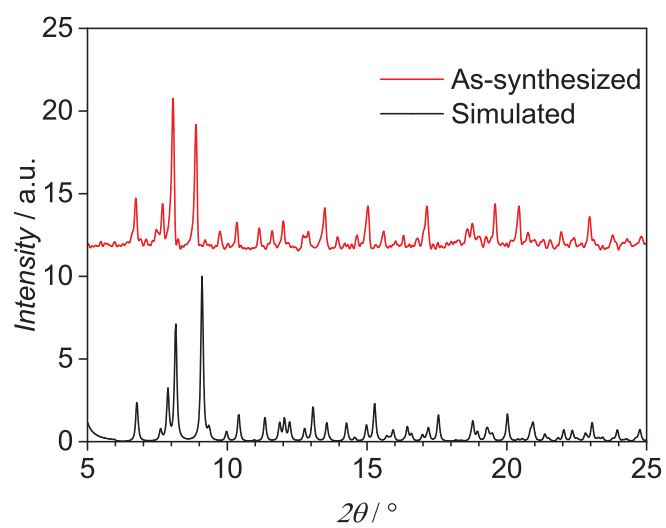
Fig. S8: XRPD pattern for MIL-144.

6   TGA profiles
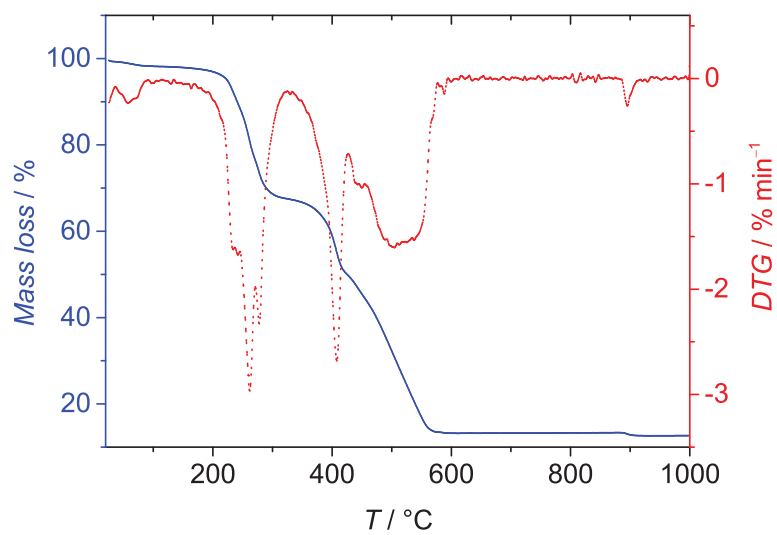
Fig. S9: TGA profile for JUMP-2.
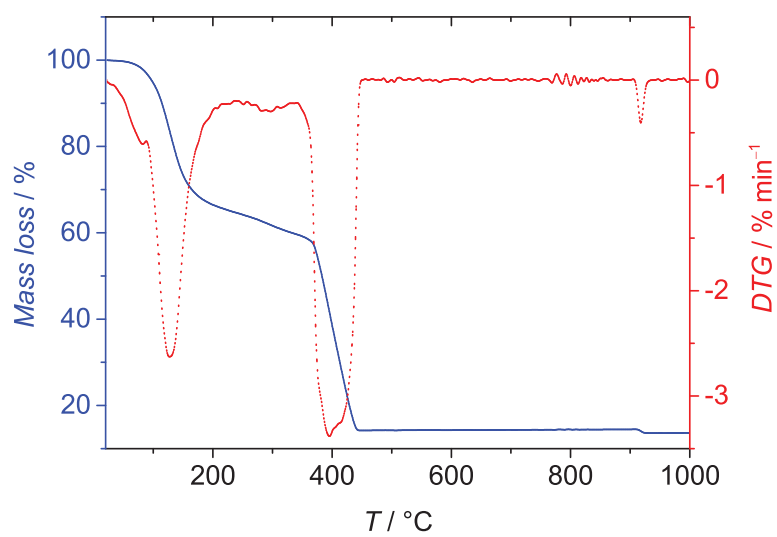
Fig. S10: TGA profile for MIL-144.

7 Alternating current (ac) magnetic measurements for JUMP-2
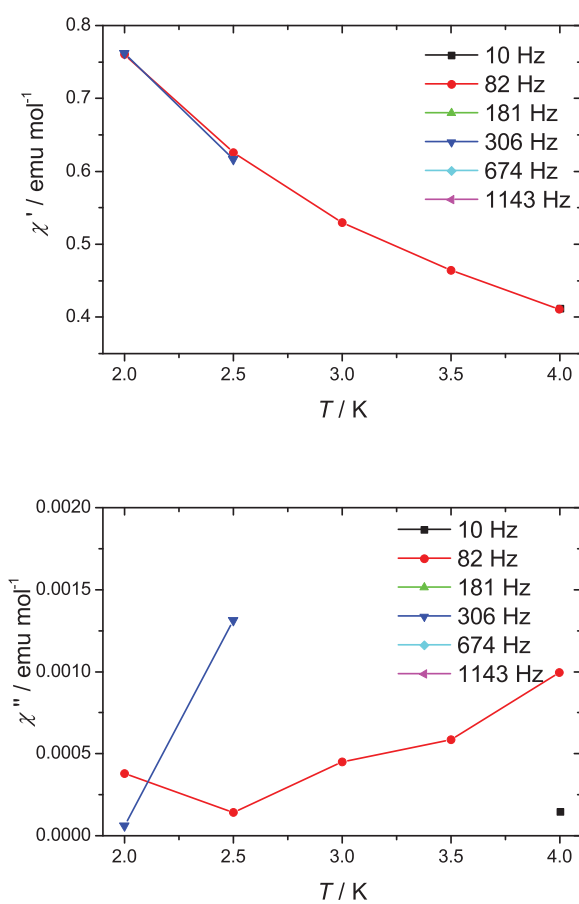
Fig. S11: Temperature dependence of the real (top) and imaginary (bottom) part of the susceptibility for JUMP-2 at a dc filed of 0 Oe.
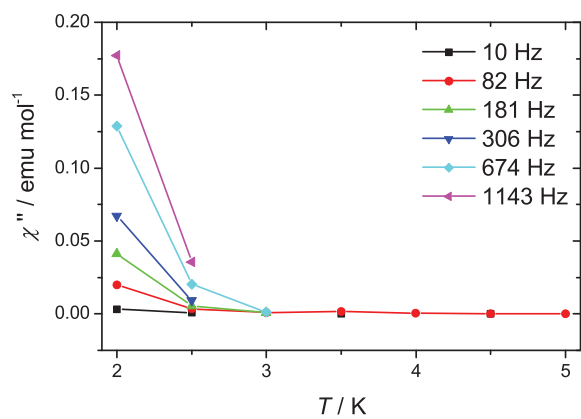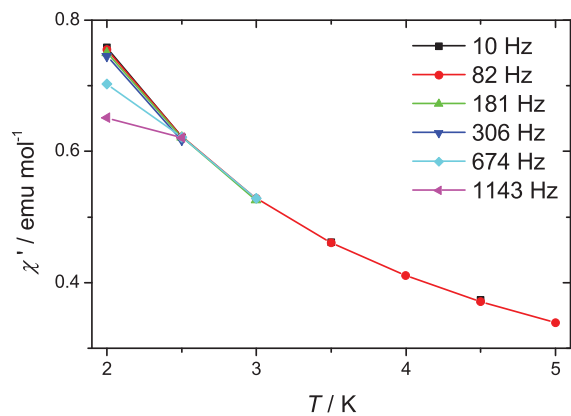
Fig. S12: Temperature dependence of the real (top) and imaginary (bottom) part of the susceptibility for JUMP-2 at a dc filed of 400 Oe.
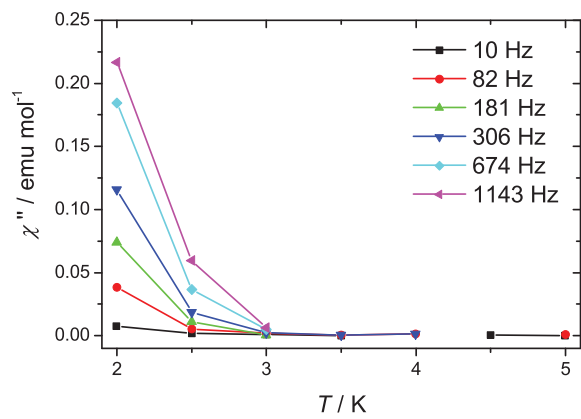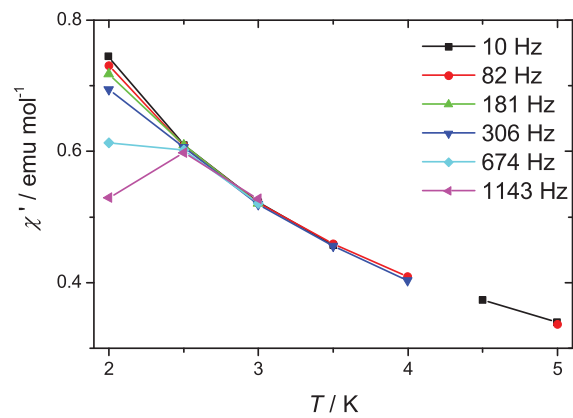
Fig. S13: Temperature dependence of the real (top) and imaginary (bottom) part of the susceptibility for JUMP-2 at a dc filed of 1000 Oe.
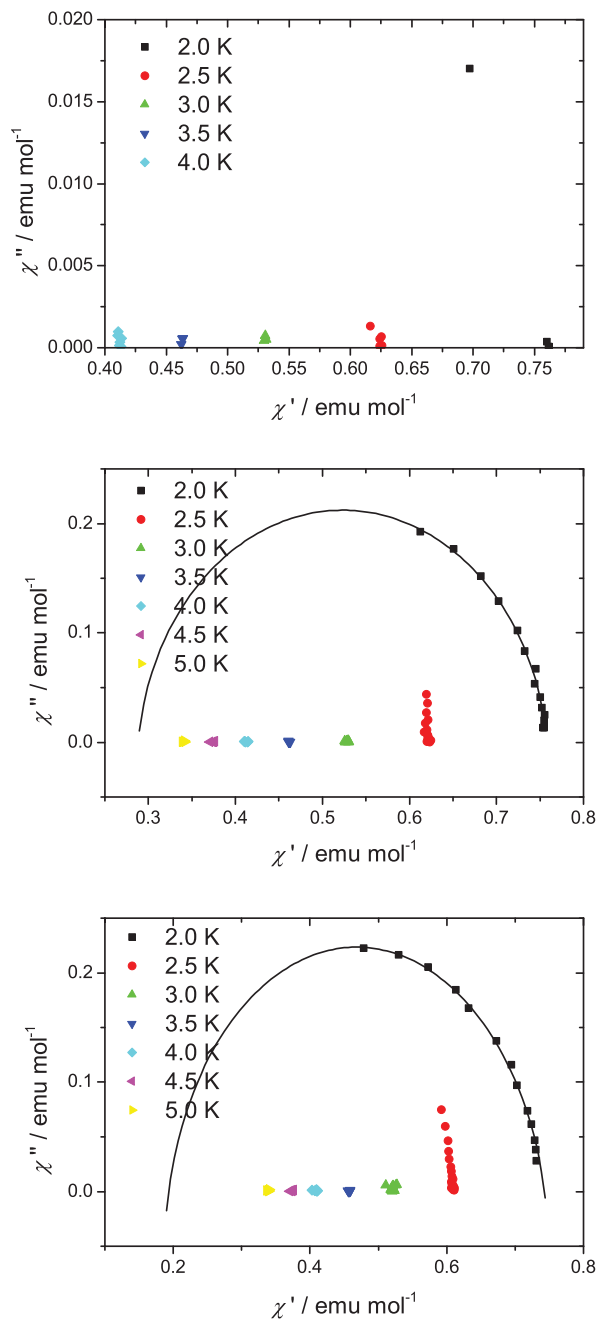
Fig. S14: Cole-cole plots for JUMP-2 at 0 Oe (top) 400 Oe (middle), and 1000 Oe (bottom).

8 Magnetization data for MIL-144
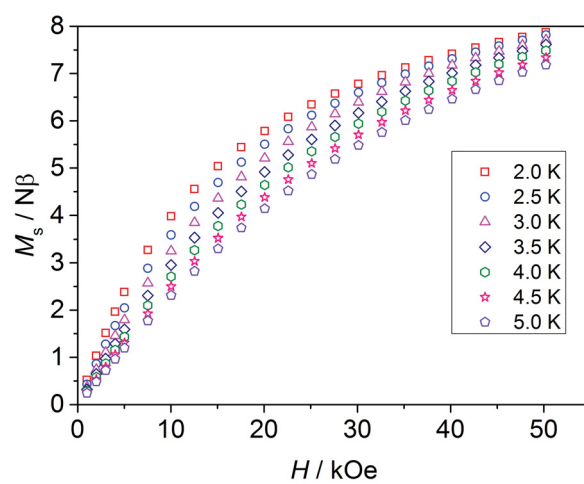
Fig. S15: Temperature- and field-dependent magnetization data for MIL-144.

9 XRPD patterns for cation exchanged samples
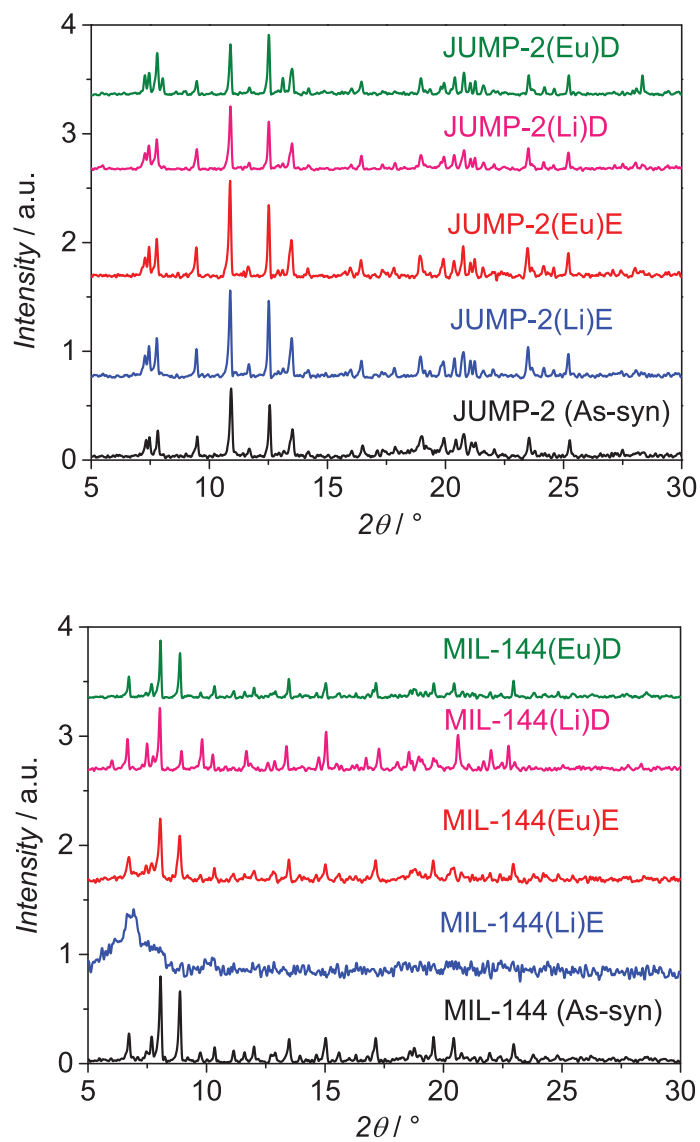
Fig. S16: XRPD patterns for the as-synthesized and cation exchanged samples of both JUMP-2 (top) and MIL-144 (bottom).

10 Fluorescence monitored europium(III) exchange
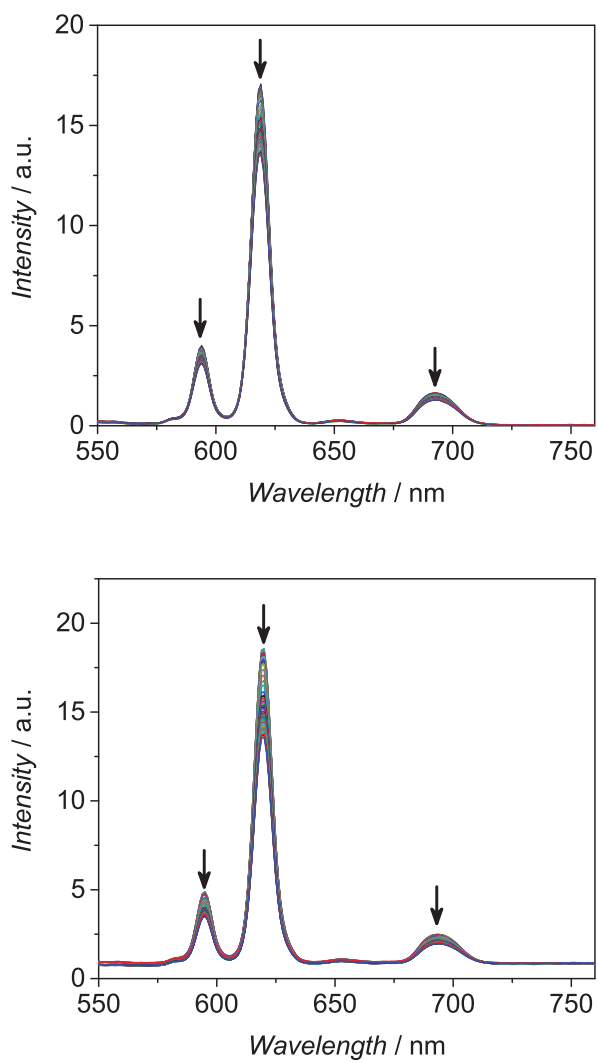
Fig. S17: Cation exchange experiment for JUMP-2 (top) and MIL-144 (bottom) with europium(III) nitrate in ethanol. Fluorescence spectra depicted were measured in time intervals of 1 h over a period of 48 h at an excitation wave length of 395 nm.

11 Sorption data

Table S5: Consistency criteria derived from measured BET Data for the as-synthesized and lithium ion exchanges samples of JUMP-2 and MIL-144 after application of supercritical drying with CO_2

	P/P_o range	C	V_m [cm³/g]	$1/\sqrt{C}+1$	$P/P_\mathrm{o}(V_\mathrm{m})$	a(BET) [m²/g]	R
JUMP-2^{scd}	0.13 - 0.28	7	2.99	0.27	0.27	13	0.999
JUMP-2(Li)D^{scd}	0.13 - 0.30	7	5.40	0.27	0.27	24	0.997
JUMP-2(Eu)D^{scd}	0.05 - 0.15	147	49.64	0.08	0.08	216	0.999
MIL-144^{scd}	0.13 - 0.28	16	4.84	0.20	0.20	21	0.999
MIL-144(Li)E^{scd}	0.005 - 0.08	1491	86.96	0.03	0.03	380	0.999
MIL-144(Eu)E^{scd}	0.005 - 0.08	1911	44.43	0.02	0.02	194	0.999

12 Quantum mechanical calculations

12.1 Computational details.

For all atoms the triple-ζ basis set def2-TZPV proposed by Ahlrichs et al.[1] was used. Calculations were performed for molecular models with the position of the non-hydrogen atoms taken from the crystal structures and the positions of the hydrogen atoms were optimized. These optimizations were carried out using the B88 exchange functional[2] and the correlation functionals VWN(V)[3] and P86.[4] The geometry optimizations were accelerated further by employing the resolution of identity approximation. The CASSCF,[5] CASPT2,[6] and RASSI-SO[7] calculations were carried out for the aforementioned model systems with optimized hydrogen atoms employing the MOLCAS 7.8 package.[8] ANO-RCC type basis sets[9] were used for all atoms (contractions: Co–6s5p4d2f1g, coordinating O and N–4s3p2d1f, peripheral N and C–3s2p, H–2s). To save computational time and disk space, the Choleski decomposition was used. Calculations for cobalt(II) involved a (7,10) active space with a double d-set of orbitals. 10 quartet states and 40 doublet states were calculated within the CASSCF procedure to account for all states arising from the d^7 configuration. CASPT2 calculations were done on all quartet states and on the 12 lowest doublet states. Otherwise, intruder states were regularly encountered. RASSI-SO calculations were performed on the CASPT2 wave functions for the states calculated. Calculations of the magnetic properties for mononuclear complexes were performed using the SINGLE_ANISO module.[10]

12.2 Magnetic anisotropy for JUMP-2

Quantum mechanical investigations on the electronic structure of the single cobalt(II) ions in JUMP-2 were performed by utilizing multiconfigurational wave function theory within the CASSCF/CASPT2/RASSI-SO methodology. For these calculations the approximation of the cobalt(II) environment is based on a cutout of the infinite two-dimensional layer from the crystal structure of JUMP-2 which is depicted in Figure S18. The CASSCF and CASPT2 energies summarized in Table S6 and their comparison shows only moderate changes upon inclusion of dynamic correlation. The ground state is separated by $3260\,\mathrm{cm}^{-1}$ from the first excited spin-free state and resembles the expected A_2 ground term, while the excited T_2 and T_1 term are split due to the deviation from T_d symmetry. Doublet states are found to follow above $16000\,\mathrm{cm}^{-1}$, which confirms the high-spin ground state suggested by experiment. Calculations of the spin-orbit states furthermore show a rather weak mixing of the spin-free ground state with excited states, with a leading weight of over 0.97. This also leads to a small energy gap of $25\,\mathrm{cm}^{-1}$ with respect to the first excited Kramers doublet (KD). In addition the g elements obtained for the ground state KD show considerable rhombic
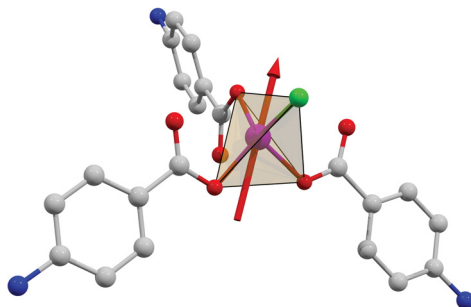
Fig. S18: Representation of the main anisotropy axis of the ground state Kramers doublet derived from multiconfigurational calculations on JUMP-2 for the depicted model structure. Hydrogen atoms are omitted for clarity.

components of over 0.8 (Table S7). Zero-field splitting (ZFS) parameters calculated with the SINGLE_ANISO program reveal easy-axis anisotropy ($D = -11.9\,\text{cm}^{-1}$), however, with a significant rhombic distortion of $E = -1.7\,\text{cm}^{-1}$. In fact, these parameters can reproduce the experimental magnetization data as shown in Figure S19 and are consistent with the presence of efficient relaxation processes already seen from the experimental absence of a relevant single-ion magnet behavior for JUMP-2.

Table S6: Spin-free CASSCF and CASPT2 energies (cm^{-1}) of the quartet and doublet states for JUMP-2. To avoid intruder states, only the 12 lowest doublet states were included in the CASPT2 calculations

	CASSCF	CASPT2
	0	0
	2853	3260
	3841	4018
	4536	4419
	5254	5621
quartet states	7303	8093
	7925	8905
	20589	17524
	21853	18829
	22544	19663
	19376	16914
	19664	17202
	20149	17637
	20215	17661
	20567	18121
doublet states	21277	18953
	22204	19849
	22492	20424
	22985	20823
	25420	22817
	25774	23198
	26152	23758
	...	

Table S7: Energies and g values of the lowest KDs of JUMP-2 calculated with the CASPT2/RASSI-SO procedure

KD		E (cm^{-1})	g value
	g_1		0.8605
1	g_2	0	1.0064
	g_3		7.0316
	g_1		2.2564
2	g_2	25	3.5240
	g_3		5.3774
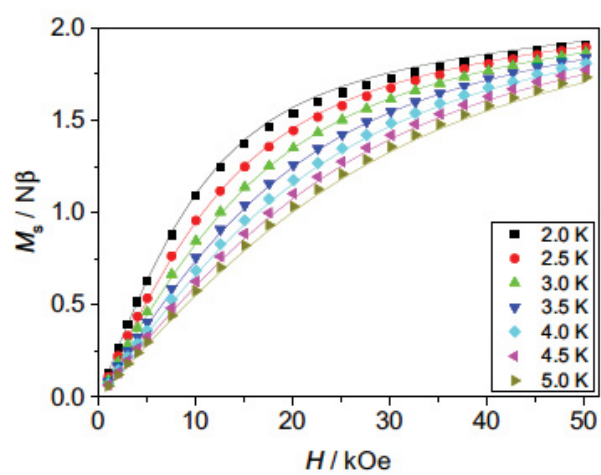
Fig. S19: Temperature- and field-dependent magnetization data for JUMP-2. Lines represent the simulated data based on the parameters obtained from CASPT2/RASSI-SO calculations.

Bibliography

[1] F. Weigend and R. Ahlrichs, *Phys. Chem. Chem. Phys.*, 2005, **7**, 3297–3305.

[2] A. D. Becke, *Phys. Rev. A*, 1988, **38**, 3098–3100.

[3] S. H. Vosko, L. Wilk and M. Nusair, *Can. J. Phys.*, 1980, **58**, 1200–1211.

[4] J. P. Perdew and W. Yue, *Phys. Rev. B*, 1986, **33**, 8800–8802.

[5] B. O. Roos, P. R. Taylor and P. E. Siegbahn, *Chem. Phys.*, 1980, **48**, 157–173.

[6] J. Finley, P.-A. Malmqvist, B. O. Roos and L. Serrano-Andrés, *Chem. Phys. Lett.*, 1998, **288**, 299–306.

[7] P. Å. Malmqvist, B. O. Roos and B. Schimmelpfennig, *Chem. Phys. Lett.*, 2002, **357**, 230–240.

[8] F. Aquilante, L. De Vico, N. Ferré, G. Ghigo, P.-Å. Malmqvist, P. Neogrády, T. B. Pedersen, M. Pitoňák, M. Reiher, B. O. Roos, L. Serrano-Andrés, M. Urban, V. Veryazov and R. Lindh, *J. Comput. Chem.*, 2010, **31**, 224–247.

[9] (*a*) B. O. Roos, R. Lindh, P.-Å. Malmqvist, V. Veryazov and P.-O. Widmark, *J. Phys. Chem. A*, 2004, **108**, 2851–2858; (*b*) B. O. Roos, R. Lindh, P.-A. Malmqvist, V. Veryazov and P.-O. Widmark, *J. Phys. Chem. A*, 2005, **109**, 6575–6579; (*c*) B. O. Roos, R. Lindh, P.-A. Malmqvist, V. Veryazov, P.-O. Widmark and A. C. Borin, *J. Phys. Chem. A*, 2008, **112**, 11431–11435.

[10] L. F. Chibotaru and L. Ungur, *J. Chem. Phys.*, 2012, **137**, 064112.

Publication 3

Robust anionic pillared-layer framework based on triphenylamine-based linkers: ion exchange and counterion dependent sorption properties

Oluseun Akintola, Sven Ziegenbalg, Axel Buchholz, Helmar Görls, and Winfried Plass
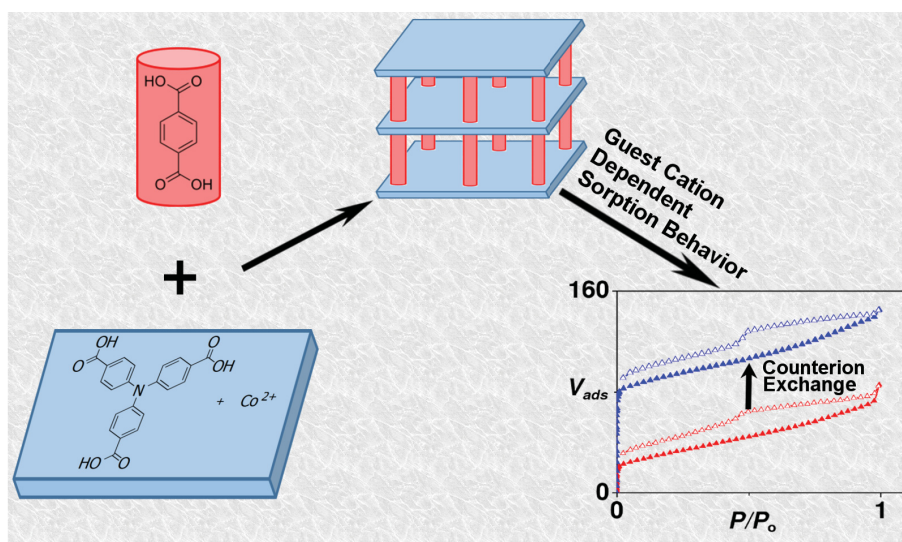
CrystEngComm

ROYAL SOCIETY
OF **CHEMISTRY**

CrystEngComm
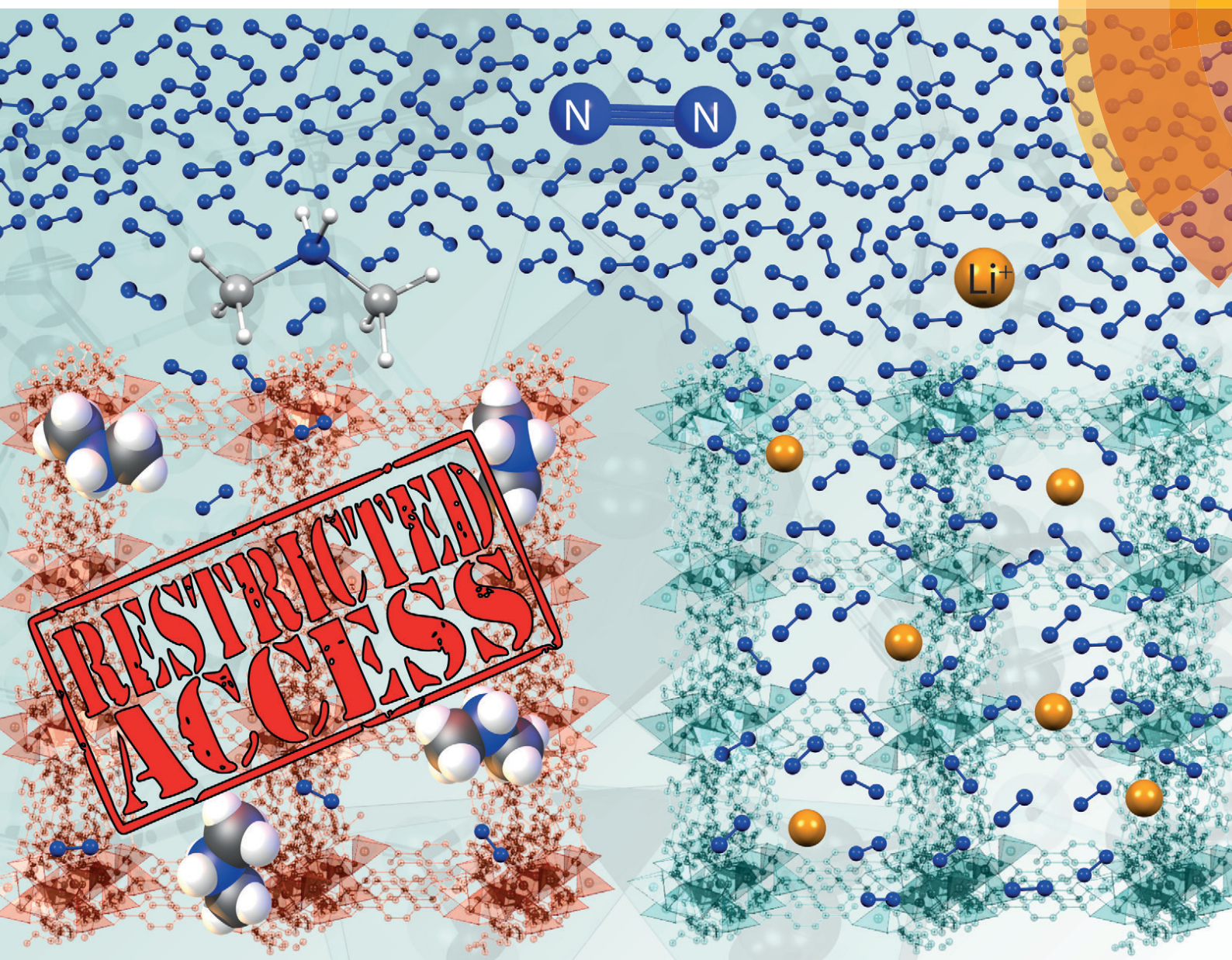
Check for updates

A robust anionic pillared-layer framework with triphenylamine-based linkers: ion exchange and counterion-dependent sorption properties†

Oluseun Akintola, [iD] Sven Ziegenbalg, Axel Buchholz, Helmar Görls and Winfried Plass [iD] *

A new anionic pillared-layer cobalt(II) metal–organic framework combining 4,4′,4″-nitrilotribenzoic acid (H_3ntb) as a linker and terephthalic acid (H_2bdc) as a pillar-ligand with the formula {$((CH_3)_2NH_2)_2[Co_3(ntb)_2(bdc)]$}$_n$ (JUMP-1, JUMP = Jena University Magnetic Polymer) has been solvothermally synthesized and characterized. The crystal structure of JUMP-1 was determined to belong to the orthorhombic space group *Cmca*. It displays a three-dimensional (3D) framework for which the topological analysis revealed a 3,8-connected net with a tfz-d topology. The 3-connected organic node is linked to an 8-connected secondary building unit composed of a linear trinuclear cobalt(II) cluster with a mixed arrangement of coordination geometries ($T_d–O_h–T_d$) leading to two-dimensional layers which are further linked by terephthalic acid to give the pillared-layer arrangement. The magnetic properties are characterized by an antiferromagnetic coupling between a central octahedrally coordinated cobalt(II) ion and two outer tetrahedral cobalt(II) centers, whereas only a very weak inter-cluster coupling is observed. Moreover, a moderate zero-field splitting is detected for the tetrahedral cobalt(II) ions. The organic counterions could successfully be exchanged by lithium ions under retention of the anionic 3D network leading to JUMP-1(Li). For both compounds JUMP-1 and JUMP-1(Li), N_2 and CO_2 adsorption isotherms were measured. The pore distribution analyses revealed improved microporosity for the lithium exchanged MOF.

Introduction

The field of coordination polymers and in particular that of metal–organic frameworks (MOFs) has become an ever more popular area of interest in recent years. This is, no doubt, due to the many applications of this class of compounds some of which include catalysis, gas storage, separation and sequestration, ion exchange, magnetism and sensing.[1] The most common strategy in obtaining them, so far, has been the simple combination of metals and polytopic ligands mostly under solvothermal conditions in a process of self-assembly with emphasis on slim organic linkers to provide access to high porosity.[2] As the functional groups concerned are polycarboxylate linkers, particularly aromatic based, they have been subjected to frequent use since they confer rigidity and stability on the obtained frameworks.[3] This approach has even been extended by use of spacer groups to expand the existing ligands thus increasing potential for better surface properties such as in the case of the isoreticular series.[4] While this method has worked quite well to date, it has also had its drawbacks such as in the case of interpenetrated or even fragile structures due to the frameworks being poorly reinforced.[5]

Even so total control over the synthesis of MOFs still remains an elusive goal in particular the ability to tune properties such as the pore sizes which is most desirable. One of the attempts to achieve this level of controllability has been the construction of pillared-layer structures.[6] A major advantage of this strategy is that it offers new levels of functionality in addition to avoiding the stress of searching for new linkers while at the same time making the most of existing ones. This approach has subsequently led to the discovery of MOFs with some of the highest reported surface areas currently known such as the UMCM-1[5,7] and MOF-210[2] of which the latter was only surpassed by the discovery of the NU-110 with over 7000 $m^2 g^{-1}$.[8]

The use of these pillared-layer systems has been found to be an effective route in obtaining three-dimensional frameworks in addition to offering the possibility of chemically functionalizing the channels for a selective adsorption behavior *via* modification of the pillar ligands.[9] Selecting

Institut für Anorganische und Analytische Chemie, Friedrich-Schiller-Universität, Jena, Humboldtstr 8, 07743 Jena, Germany. E-mail: Sekr.Plass@uni-jena.de; Fax: +49 (0)3641 948132; Tel: +49 (0)3641 948130

† Electronic supplementary information (ESI) available: Structural figures, PXRD patterns, TGA curves, topological data and sorption data are included in the ESI. CCDC 1508581. For ESI and crystallographic data in CIF or other electronic format see DOI: 10.1039/c7ce00369b

appropriate pillared ligands can be used to generate flexible MOFs which have the ability to undergo structural changes during adsorption and desorption of guests and are interesting for applications in selective gas adsorption/separation or chemical sensing.[10] This approach has also been used to facilitate the interconnection of layered structures with interesting magnetic properties[11] and, moreover, to introduce redox-active organic linkers in relevant frameworks.[12]

A common approach in synthesizing such mixed-ligand frameworks has been the coordination copolymerization route usually involving mixing two different linkers.[7,13] When combined, the organic linkers tend to cooperate thus avoiding formation of two separate single ligand MOFs.[14] Subtle changes in reaction conditions such as reactant ratios, temperature or even solvent often lead to slight variations in the final structure obtained.[15] Common ligands acting as pillars include the dicarboxylates like terephthalate or its derivatives and nitrogen based ligands such as imidazoles or bipyridines.[16]

We herein report the construction of a new anionic pillared-layer MOF, named JUMP-1 (JUMP = Jena University Magnetic Polymer), which is based on the redox-active ligand 4,4′,4″-nitrilotribenzoic acid (H$_3$ntb) with the inclusion of terephthalic acid as a pillar ligand containing a linear trinuclear cobalt(II) cluster as a secondary building unit (SBU). The anionic nature of the resulting framework will be used for post-synthetic modification *via* cation exchange and the resulting sorption properties before and after exchange will be reported.

Experimental section

Materials

Triphenylamine (Alfa Aesar) and cobalt(II) chloride hexahydrate (Aldrich) were obtained commercially and used without further purification. All other chemicals were of AR grade. The tribromotriphenylamine used was prepared from triphenylamine by a reported procedure.[17] The final ligand 4,4′,4″-nitrilotribenzoic acid (H$_3$ntb) was obtained in good yield following procedures already described in the literature.[18,19]

Analytical data for H$_3$ntb. ^{1}H NMR (400 MHz, [D$_6$]DMSO, 25 °C, δ in ppm): 7.13 (d, $^3J_{H,H}$ = 8.7 Hz, 6H), 7.89 (d, $^3J_{H,H}$ = 8.7 Hz, 6H), 12.76 (s, 3H). ^{13}C NMR (100 MHz, [D$_6$]DMSO, 25 °C, δ in ppm): 123.7, 125.9, 131.2, 149.8, 166.7. Selected IR data (ATR, cm^{-1}): 1672s, 1591s, 1509m, 1417s, 1314s, 1275vs, 1173s, 1129m, 932m. EI-MS: *m/z* 377 (M$^+$, 100%).

Physical measurements

Simultaneous TG/DTA analyses were performed under static air atmosphere using a Netzsch STA Luxx PC analyzer up to 1000 °C. The FT-IR spectra were measured on a VERTEX 70 IR spectrometer by Bruker Optics using the Specac Diamond ATR optional accessory. Mass spectrometry was performed on a MAT SSQ710 mass spectrometer made by Bruker. NMR spectra were recorded with a Bruker AVANCE400 spectrome-

ter. The elemental analyses were done on a VARIO EL III analyzer. The magnetic susceptibilities were measured on the bulk vacuum dried materials in the 2–300 K temperature range with a Quantum Design MPMS-5 superconducting SQUID magnetometer. The data were corrected for diamagnetic contributions. The N$_2$ and CO$_2$ physisorption isotherms were measured on an Autosorb-IQ instrument from Quantachrome Instruments Corporation. Solvothermal reactions were carried out in a 23 mL Teflon-lined acid digestion vessel from Parr Instruments, utilizing a programmable oven by Binder. Powder X-ray diffraction (PXRD) measurements were performed on a Stoe Powder Diffractometer with a Mythen 1 K detector at room temperature. Measurements were done using capillary tubes while the Debye Scherrer Scan Mode was applied with a 2θ scan type. The X-ray tube was a Cu-long fine focus tube. The powdered samples were suspended in DMF and transferred in a 0.5 mm glass capillary for measurement, which was carried out between 2 and 50° with steps of 2.1° per 20 seconds.

Synthesis

{((CH$_3$)$_2$NH$_2$)$_2$[Co$_3$(ntb)$_2$(bdc)]}$_n$·4DMF·2H$_2$O   (JUMP-1 ·4DMF·2H$_2$O). Terephthalic acid (H$_2$bdc, 33 mg, 0.199 mmol) and H$_3$ntb (50 mg, 0.13 mmol) were dissolved and stirred in DMF (5 mL) for 15 min. Cobalt(II) chloride hexahydrate (126 mg, 0.52 mmol) was then added and stirred for a further 15 min after which all solid was dissolved. The solution was then placed in a Parr acid digestion vessel and heated at 140 °C for 72 h under autogenous pressure. It was then allowed to cool at a rate of 5 °C h^{-1}. Deep blue-violet crystals could be seen in the room temperature sample which were washed repeatedly with DMF (3 × 5 mL) and subsequently dried *in vacuo* for 1 h, yielding the further denoted as-synthesized material JUMP-1·4DMF·2H$_2$O. Employing extended periods for the drying process led to a lower solvent content of the resulting material, as evidenced by CHN elemental analysis and TG measurements. Yield for JUMP-1 ·4DMF·2H$_2$O: 71.0 mg, 0.047 mmol, 72% based on the ligand. CHN elemental analysis calcd. for JUMP-1·4DMF·2H$_2$O, C$_{66}$H$_{76}$Co$_3$N$_8$O$_{22}$ (*M* = 1510.34): C, 52.5; H, 5.1; N, 7.4%. Found: C, 52.35; H, 5.0; N, 7.7%. Selected IR data ($\tilde{v}_{max}$/cm^{-1}): 1657s, 1592s, 1504w, 1385vs, 1312s, 1275s, 1171m, 1130m, 1092w, 834w, 779s, 675m.

Cation exchange

{Li$_2$[Co$_3$(ntb)$_2$(bdc)]}$_n$·4EtOH·8H$_2$O (JUMP-1(Li)·4EtOH·8H$_2$O). The as-synthesized JUMP-1·4DMF·2H$_2$O was immersed in a saturated ethanolic LiNO$_3$ solution for 10 d. During this period, the soaking solution was replaced every 24 h. After the 10 d period, the lithium ion exchanged material was subsequently soaked for one week in ethanol to remove any residual free LiNO$_3$ molecules. According to the elemental analysis of the final product the organoammonium cations present in the as-synthesized JUMP-1·4DMF·2H$_2$O were fully replaced by the lithium cations. The obtained lithium ion exchanged

framework is further denoted as JUMP-1(Li). CHN elemental analysis calcd. for $C_{58}H_{68}Co_3Li_2N_2O_{28}$ (M = 1431.84): C, 48.65; H, 4.8; N, 2.0%. Found: C, 48.3; H, 4.95; N, 1.8%. Selected IR data ($\tilde{v}_{max}$/cm^{-1}): 3326br, 1589s, 1506w, 1378vs, 1313s, 1273s, 1174m, 1147m, 1087w, 1045m, 833w, 780 s, 675m.

X-ray structure determination

The intensity data were collected on a Nonius KappaCCD diffractometer, using graphite-monochromated Mo-K$_\alpha$ radiation. Data were corrected for Lorentz and polarization effects, but not for absorption.[20] The structure was solved by direct methods (SHELXS)[21] and refined by full-matrix least squares techniques against F_o^2 (SHELXL).[21] The crystal structure of JUMP-1 contains large voids, filled with disordered dimethylammonium cations and solvent molecules. The total size of the voids is 13 846 Å^3 per unit cell. Their contribution to the structural factors was secured by back-Fourier transform using the SQUEEZE routine of the program PLATON[22] resulting in 2787 electrons per unit cell. All hydrogen atoms were included at calculated positions with fixed thermal parameters. All non-disordered, non-hydrogen atoms were refined anisotropically.[21] Diamond 4.2.2 was used for structure representations.[23]

Crystallographic and refinement parameters for JUMP-1. Formula $C_{50}H_{28}Co_3N_2O_{16}$, M = 1089.53, orthorhombic $Cmca$, a = 33.6004(6), b = 26.9604(5), c = 23.2138(5) Å, V = 21028.9(7) Å^3, T = 133 K, Z = 8, ρ_{calc} = 0.688 g cm^{-3}, μ = 0.501 mm^{-1}, 69 315 measured reflections, θ_{max} = 27.34°, 11 978 unique reflections (R_{int} = 0.0856) and 7595 observed reflections ($I > 2\sigma(I)$), 321 parameters, goodness of fit on F^2 S = 1.020, R_1 = 0.0649 (observed reflections), wR_2 = 0.1984 (all unique reflections). More details can be found in the deposited cif file CCDC 1508581 which contains additional crystallographic data.

Sample pretreatment and sorption measurements

Dichloromethane activation. The as-synthesized JUMP-1 was activated by carrying out solvent exchange with dichloromethane. This was done by soaking the sample (50–70 mg) in dichloromethane (10 mL) for 7 d during which the solvent was replaced by decanting every 24 h. Finally the supernatant liquid was removed and the sample dried in air. The final resulting product is further denoted as JUMP-1^{dcm}.

Supercritical carbon dioxide activation. In an alternative pretreatment procedure, the as-synthesized JUMP-1 (50–70 mg) was soaked in ethanol (10 mL) for one week during which the solvent was replaced every 24 h by decanting the supernatant. Subsequently this was followed by a drying process using supercritical CO_2. For this drying procedure the ethanol-immersed samples were decanted and the resulting slurry was transferred into an autoclave (100 mL volume) and sealed. Liquid CO_2 was then introduced into the autoclave at a final pressure of 60 bar and allowed to stand 30 min. To ensure removal of any possible non-occluded ethanol, the liquid CO_2 was slowly removed over a period of 20 min. A sec-

ond batch of liquid CO_2 was then introduced into the reactor (60 bar), but this time allowed to stand for 24 h. The temperature of the reactor was subsequently raised to 40 °C to bring the CO_2 to supercritical conditions and maintained at this temperature for one hour. The CO_2 was then slowly released over 30 min with the temperature continuously maintained at 40 °C in order to prevent any cooling that might result from expansion of the gas during evaporation. This supercritical drying (scd) procedure was applied to the as-synthesized JUMP-1 and the lithium ion exchanged JUMP-1(Li) samples resulting in the products JUMP-1^{scd} and JUMP-1(Li)^{scd}, respectively.

Sorption measurements. The isotherms of all pretreated and dried products were measured immediately after degassing the samples for 30 min at room temperature. Pore size distribution curves were calculated by fitting the experimental data using a quenched solid density functional theory (QSDFT) kernel based on adsorption models for N_2 on carbon at 77 K with cylindrical/slit pores, which was provided by QUANTACHROME Instruments.[24] The Brunauer–Emmett–Teller (BET) surface areas for both materials were determined from the adsorption data over different relative pressure ranges all between 0.005–0.28 while ensuring compliance with the consistency criteria.[25]

Results and discussion

Synthesis

The title compound JUMP-1 was prepared utilizing the copolymerization technique. It was shown earlier that this reaction technique requires a subtle balance between geometry and statistics.[5] To evaluate these conditions, it was found that the geometric ratio between the length of the ditopic (L_d) and tritopic (L_t) linkers is an important parameter (see Scheme 1). It was reported that the ratio L_d/L_t should not be too high with the ideal value of just around one, as using a higher ratio might lead to the formation of two distinct coordination polymers based on the individual linkers rather than the expected copolymer. Moreover, when using a mixture of ditopic and tritopic linkers, reported results show that an excess of the ditopic linker is beneficial for the generation of the desired copolymerization product.[5]
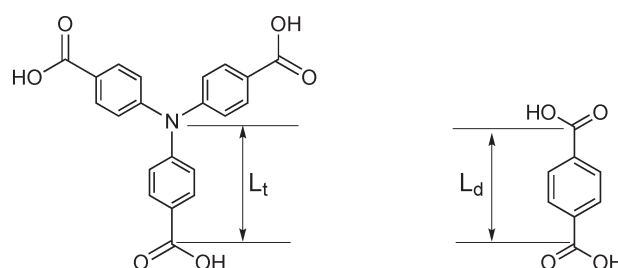
Scheme 1 Linkers used for the synthesis of JUMP-1. L_d and L_t define the characteristic lengths for the ditopic and tritopic linkers, respectively (L_d/L_t = 1.01).

The tritopic linker 4,4′,4″-nitrilotribenzoic acid being utilized in our synthesis leads to an almost ideal L_d/L_t ratio when combined with terephthalic acid (see Scheme 1). The ditopic linker was used in slight excess of approximately 6 : 4 (M_d/M_t). The linkers were predissolved in DMF solution followed by the addition of four equivalents of cobalt(II) chloride hexahydrate, all under continuous stirring. The solvent DMF was deliberately chosen to provide a source for the *in situ* generation of organic cations to stabilize the desired anionic framework. Solvothermal treatment of the resulting solution at 140 °C for 3 days followed by slow cooling (5 °C h^{-1}) leads to the formation of a violet crystalline material in rather high yields. Based on elemental and thermal analyses performed on samples dried *in vacuo*, the composition of the final material corresponds to the dimethylammonium salt $\{((CH_3)_2NH_2)_2[Co_3(ntb)_2(bdc)]\}_n$ (JUMP-1) which contains additional four molecules of DMF and two molecules of water per formula unit.

X-ray crystal structure

Crystals suitable for structural analysis were obtained directly from the solvothermal synthesis and are found to crystallize in the orthorhombic space group *Cmca*. The data reveals the presence of a 3D network with a pillared-layer structural arrangement. The crystallographic asymmetric unit contains two independent cobalt atoms, one ntb^{3-} linker and a half of a terephthalic acid moiety (see Fig. S1†). One of the cobalt(II) ions (Co1) is located on a crystallographic inversion center leading to the overall formula $\{[Co_3(ntb)_2(bdc)]\}_n^{2n-}$ for the anionic 3D framework.

The two crystallographically independent cobalt(II) ions show distinct differences in their coordination geometry. The atom Co1 is situated on an inversion center and shows an octahedral coordination provided by six carboxylate oxygen atoms each from a different ntb^{3-} linkers. Whereas the Co2 center possesses a distorted tetrahedral coordination geometry and is surrounded by three oxygen atoms from three different ntb^{3-} ligands with the fourth position being taken up by an oxygen atom (O7) from the terephthalic acid. The central Co1 ion together with the two crystallographically equivalent Co2 and Co2A ions at the terminal positions gives rise to a linear trinuclear cluster, which can be regarded as an SBU (see Fig. 1). Although linear trinuclear arrangements have been reported as SBUs in coordination frameworks,[26,27] the observed mixed coordination geometries at the cobalt(II) ions (T_d–O_h–T_d) in JUMP-1 are unusual with respect to the carboxylate ligand environment.[28–30] The trinuclear cluster SBUs are linked together *via* the ntb^{3-} ligands leading to the formation of neutral 2D networks with the formula $\{[Co_3(ntb)_2]\}_n$. These layers are then in turn connected with each other *via* the terephthalic acid linkers, which serve as pillars holding up the structure. A representation of the resulting anionic 3D framework structure is depicted in Fig. 2 (see also Fig. S2 and S3†).
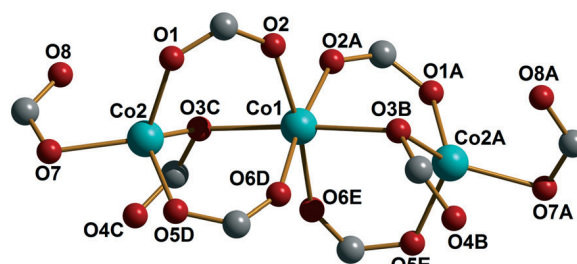

Fig. 1 Cut-out view of the trinuclear SBU showing the coordination environments around the cobalt(II) ions. Only carboxylate groups are depicted for clarity. Symmetry codes: A = $-\frac{1}{2} - x$, $+y$, $\frac{3}{2} - z$; B = $-\frac{1}{2} - x$, $\frac{3}{2} - y$, $1 - z$; C = $+x$, $\frac{3}{2} - y$, $\frac{1}{2} + z$; D = $\frac{1}{2} - x$, $\frac{1}{2} + y$, $+z$; E = $+x$, $\frac{1}{2} + y$, $\frac{3}{2} - z$.

The Co1 and Co2 ions within the trinuclear cluster are solely bridged by the carboxylate groups of the ntb^{3-} linkers. Overall there are three carboxylate bridges, one in a monodentate $\mu_{1,1}$ mode (O3) and two in a bidentate *syn–syn* $\mu_{1,3}$ mode (O1/O2 and O5/O6), leading to a Co1–Co2 distance of 327 pm. The bridging angle Co1–O3–Co2 at the monodentate carboxylate is found to be 103°. This leads to only slight distortions from the octahedral coordination at the central Co1 ion with bond lengths and angles within the expected range (see Tables S1 and S2†). On the other hand a significant distortion from the tetrahedral coordination is observed for the Co2 ions which is evident from the bond angles. In fact, the largest O–Co2–O bond angle is found to be about 133°, whereas the smallest is only about 96°. This is caused by steric effects of the non-coordinated oxygen atoms of the monodentate carboxylate ligands.
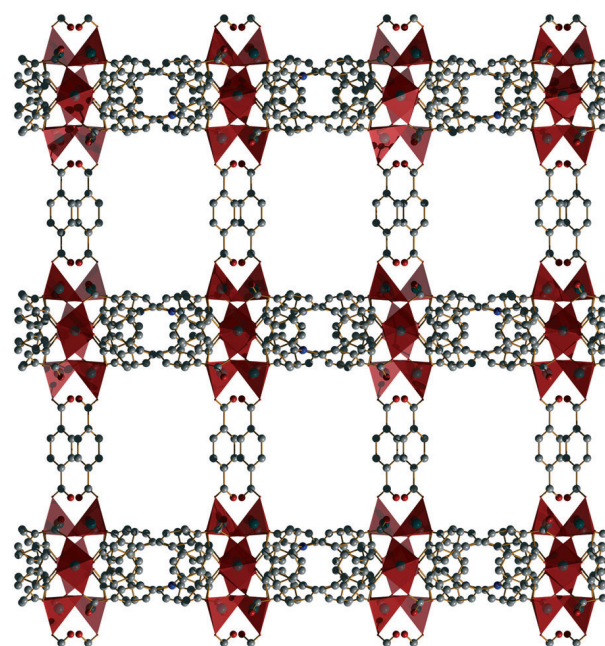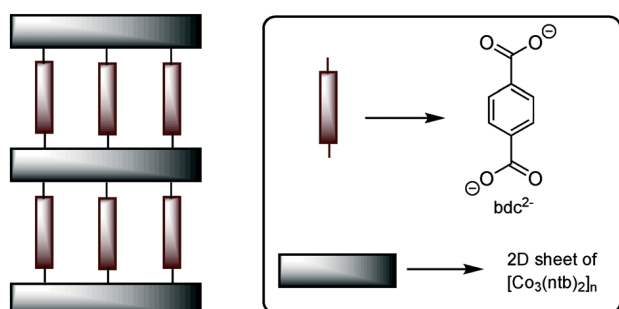

Fig. 2 3D framework of JUMP-1 viewed along the [010] direction. 2D networks composed of linear trinuclear cobalt(II) SBUs and ntb^{3-} ligands are arranged along the (100) plane and interconnected by the bdc^{2-} pillars. Red polyhedra represent cobalt(II) centers.

The linear trinuclear SBUs within the 2D networks are well separated with distances of about 1350 pm between their central Co1 centers. For the SBUs also a large interlayer separation is observed with a distance of about 1076 pm between the terminal Co2 centers of corresponding SBUs bridged by a terephthalate ligand. The charge of the resulting anionic 3D framework (see Scheme 2) needs to be balanced. This is attributed to the presence of two dimethylammonium cations in the void formed by the well-known thermal decomposition of DMF under the given reaction conditions.[31] Although these counterions could not be located in the crystal structure, due to the presence of large amounts of diffuse solvent molecules in the void of the framework structure, their formation is evidenced by elemental and thermogravimetric analyses.

The overall anionic 3D framework can be described as a stack of 2D sheets separated by terephthalic acid ligands to give the 3D cage-structure as shown in Fig. 2 (see also Fig. S2 and S3†). The topological analysis of the crystal structure of JUMP-1 utilizing TOPOS 5.0[32] revealed a binodal net (Tables S3 and S4†). The simplification of the network results in two different types of nodes, which are eight- and three-connected. The corresponding topological net is depicted in Fig. 3 (cf. Fig. S4 and S5†). The eight-connected node represents the linear trinuclear cobalt cluster, i.e. the SBU with eight attached carboxylate groups. Six of these connecting carboxylate groups originate from the ntb[3−] ligands. The central nitrogen atom of the latter can be regarded as the three-connected node (see also Fig. S5†). The other two carboxylate groups belong to the terephthalic acid pillars solely linking the eight-connected nodes. The analysis of the topology thus reveals a 3,8-connected net with a tfz-d topology and the point symbol $(4^3)_2(4^6 \cdot 6^{18} \cdot 8^4)$.

Powder diffraction and thermal analysis

The phase purity of the bulk material of JUMP-1 was confirmed by powder X-ray diffraction (PXRD) measurements. There is close agreement of the experimental data with the simulations based on the single crystal structure, except for intensity differences that might be attributed to the presence of extra framework species within the pores (see Fig. S6†).[33]

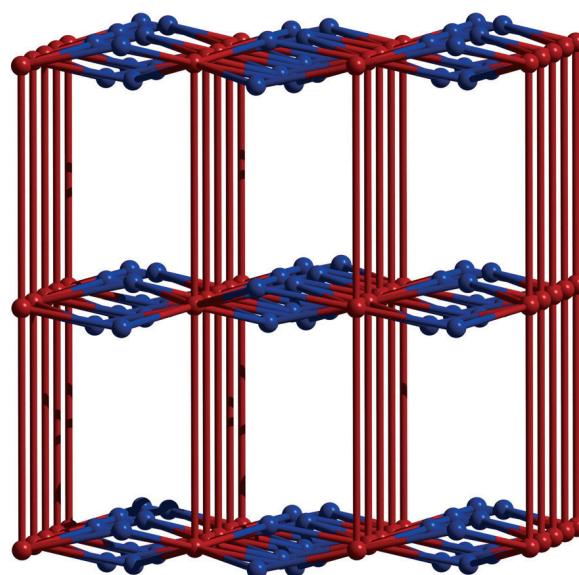Scheme 2 Schematic representation showing the build-up of the anionic 3D framework of JUMP-1.

Fig. 3 Representation of the tfz-d topology of the network of JUMP-1 viewed approximately along the crystallographic [010] direction. The red and blue spheres represent the trinuclear cobalt clusters (8-connected nodes) and the nitrogen atoms of the ntb[3−] ligands (3-connected nodes), respectively.

The thermal analysis of JUMP-1 showed a gradual weight loss up to about 380 °C before the compound starts to thermally decompose (see Fig. S7†). The first step consists of two individual partially overlapping events as indicated by the differential thermal gravimetric analysis, which can be attributed to the loss of solvent molecules. The lower mass loss at the first event (about 3.7%) suggests that the water molecules are more loosely bonded than the DMF molecules. The overall mass loss of 21.9% for the temperature range up to about 200 °C compares well to the calculated value for two water and four DMF molecules (21.7%). The following temperature range up to the onset of the decomposition of the organic ligand framework at about 380 °C corresponds to a weight loss of about 7% and can be attributed the loss of the two dimethylammonium counterions (calcd. 6.1%). The further decomposition of the organic ligand framework consists of several steps, which finally led to a rest mass of 15.0% at 600 °C which is in good agreement with the theoretical value of 14.9% expected for CoO.

Magnetic properties

The magnetic susceptibility data for JUMP-1 were measured in the temperature range from 2 to 300 K with an applied field of 2 kOe and is depicted in Fig. 4 as a temperature-dependent plot of $\chi_M T$ and χ_M^{-1}. The room temperature $\chi_M T$ value of 8.5 cm[3] K mol^{−1} is significantly higher than the corresponding spin-only value for three magnetically isolated cobalt(II) ions (5.63 cm[3] K mol^{−1}, $S = \frac{3}{2}$, $g = 2$) which clearly indicates strong spin–orbital coupling.[34] Upon decreasing the temperature the $\chi_M T$ value slowly decreases down to a temperature of 8 K with a slightly increasing slope below 100 K

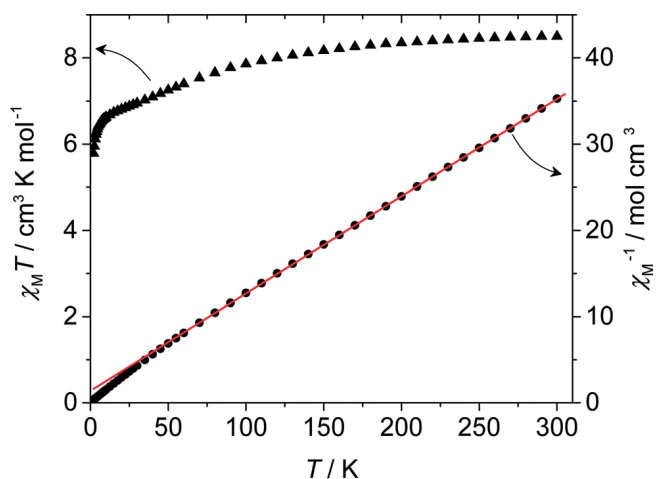**Fig. 4** Temperature dependence of the magnetic susceptibility $\chi_M T$ (black squares) and χ_M^{-1} (black circles) for JUMP-1. The solid line represent the best fits (see the text for parameters).

and a further significant drop down to a value of 5.8 cm³ K mol⁻¹ at 2 K. The observed behavior can basically be attributed to spin–orbit coupling as well as the presence of antiferromagnetic exchange interactions between the cobalt(II) ions.[27–29] As indicated by the χ_M^{-1} vs. T data JUMP-1 displays a paramagnetic behavior for temperatures above 50 K with a Curie constant of 8.86 cm³ K mol⁻¹ and a Weiss constant of −12.3 K. The latter is consistent with the presence of antiferromagnetic coupling.

The field-dependent magnetization was measured in the temperature range from 2 to 5 K and up to fields of 5 T (see Fig. S8†). The expected behavior for increasing field strength is observed with a value of about $6.3N\beta$ at 2 K and 5 T. The data indicate that saturation has not been reached under the given conditions. Nevertheless, this value is consistent with the presence of an octahedral[35] and two distorted tetrahedral cobalt(II) ions[36,37] as found in the crystal structure for the central and the two terminal cobalt centers, respectively.

The trinuclear cobalt(II) SBUs are found to be well-separated from each other within the framework structure, which suggests that the magnetic data of JUMP-1 can be analyzed based on the treatment of these isolated units. Nevertheless, additional exchange coupling between these SBUs through the bridging carboxylate ligands cannot be fully excluded. However, a full treatment for the in turn resulting extended three-dimensional exchange coupled system is not feasible. Moreover, the occurrence of two geometries (O_h and T_d) within the trinuclear clusters requires a multi-parameter approach including spin–orbit coupling to allow a consistent description of the distinct magnetic properties of the corresponding cobalt(II) ions,[34,35,38] i.e. individual sets of zero-field splitting (ZFS) parameter D and g-factor for both the octahedral and the tetrahedral cobalt(II) centers. Corresponding attempts to fit the susceptibility data over the entire temperature range were unsuccessful due to an overparameterization and led to an inadequate description of the system.

On the other hand, it is well-known that octahedral cobalt(II) ions can be treated as effective spin $S' = \frac{1}{2}$ systems at low temperatures.[35] This in turn should allow the analysis of the corresponding field-dependent magnetization data, which is measured at sufficiently low temperatures, by a simplified interaction model for the trinuclear cobalt(II) units. Since an effective spin of $S' = \frac{1}{2}$ is assumed for the central octahedral cobalt(II) ion, only the ZFS effects of the two terminal tetrahedral cobalt(II) centers are to be considered within this model by including an axial ZFS parameter D in the fit.[28] The resulting Hamiltonian utilized in fitting the field-dependent magnetization data is given in eqn (1).

$$H = J\left(S_1 S_2 + S_1 S_{2A}\right) + 2D\left[S_2(z)^2 - \frac{1}{3}S_2(S_2 + 1)\right] \tag{1}$$

The fitting of the magnetization data was performed with the routine MagProp included in the software package DAVE.[39] An additional self-consistent mean-field approximation as implemented in MagProp[40] was introduced in the fitting to account for possible intercluster exchange within the framework. To avoid overparameterization, only a single g-factor was used for both types of cobalt(II) ions. The experimental data are reproduced with the following fit parameters $g = 2.75$, $D = −2.9$ cm⁻¹, $J = −6.5$ cm⁻¹, and $zJ' = −0.06$ cm⁻¹ (see Fig. S8†).

The obtained intercluster exchange is consistent with the previous assumption of only weakly interacting trinuclear units. The exchange coupling constants J within the trinuclear SBU are comparable to values reported for similar trinuclear systems.[29] Moreover, the antiferromagnetic coupling between the central and the terminal cobalt(II) ions is consistent with the observed syn–syn and μ_2-η^2 carboxylate bridging modes. This is based on the observation that syn–syn and anti–anti conformations generally favor antiferromagnetic coupling, while syn–anti promotes ferromagnetic coupling.[41] On the other hand, for μ_2-η^2 carboxylate bridges, a dependence on the Co–O–Co bridging angle is reported with values above 100° related to antiferromagnetic interactions between the adjacent cobalt(II) ions.[42] This, in fact, is consistent with the corresponding angle of about 103° observed for JUMP-1 (see Table S2†).

To further address the magnetic properties of JUMP-1, alternating-current susceptibility measurements as well as a set of zero-field cooled and field cooled magnetization measurements have been performed. However, neither a signature for slow magnetization dynamics nor any kind of ordering could be detected.

Cation exchange studies

The possibility of replacing the organic cations present within the void of the framework was probed by immersing samples of JUMP-1 in solutions of the salt of a small monovalent cation such as lithium. This was done by soaking a

sample of JUMP-1 in saturated ethanolic lithium nitrate solution for a period of 10 d followed by washing with ethanol. In order to remove any residual free lithium salt from the sample the resulting material was further soaked in ethanol for another 7 d. The corresponding lithium ion exchanged sample is further denoted as JUMP-1(Li). Post-exchange PXRD spectra obtained for JUMP-1(Li) are in good agreement with the patterns observed for the as-synthesized bulk material indicating that the framework was left intact even upon exchange of the organic counterions (see Fig. S9†). The uptake of the lithium cation was further confirmed by CHN elemental analysis (see the Experimental section), which is consistent with the presence of two lithium ions per formula unit of the anionic framework. Additional evidence for a full exchange of the organic counterions comes from the thermal analysis of lithium ion exchanged sample JUMP-1(Li), which lacks a corresponding mass loss (see Fig. S10†). This confirms well the possibility of post-synthetic replacement of the counterions within the anionic framework of JUMP-1 without any detectable impact on the stability of the framework.

Gas-sorption properties

The porosity of the anionic framework JUMP-1 was studied by measuring the N_2 and CO_2 adsorption isotherms of the as-synthesized and lithium ion exchanged materials. The activation of the as-synthesized sample was first attempted by a solvent-exchange process utilizing dichloromethane followed by gentle outgassing of the air-dried sample at room temperature to obtain JUMP-1[dcm] (see the Experimental section for more details). However, this treatment led to the collapse of the accessible pores with a very low available surface area for gas sorption (see Table S5†), as indicated by the N_2 isotherm and the corresponding pore size distribution (Fig. S11 and S12†). We therefore explored an alternative activation procedure which is based on the treatment of the samples with supercritical CO_2 to obtain JUMP-1[scd] and JUMP-1(Li)[scd] from the as-synthesized and the lithium ion exchanged samples, respectively (see the Experimental section for more details). This has been reported earlier to be a milder form of treating materials, which is attributed to a more gentle evacuation of the pores preventing mesopore collapse and thereby ensuring the accessibility of micropores.[43]

The N_2 isotherms for the materials JUMP-1[scd] and JUMP-1(Li)[scd] are presented in Fig. 5 and the relevant data are summarized in Table 1. For JUMP-1[scd], an appreciable BET surface area of about 113 m^2 g^{-1} together with a total pore volume of 0.13 cm^3 g^{-1} was obtained. Upon replacement of the organic cations by the lithium ions, a more than threefold increase in the BET surface area to a value of 355 m^2 g^{-1} was observed. However, this is related with only a slight gain in the total pore volume to a value of 0.22 cm^3 g^{-1}. With respect to the overall void given by the anionic framework (0.96 cm^3 g^{-1} calculated from the crystal structure of JUMP-1), the total pore volume determined for JUMP-1[scd] and JUMP-1(Li)[scd] corresponds to about 14 and 23%, respectively.
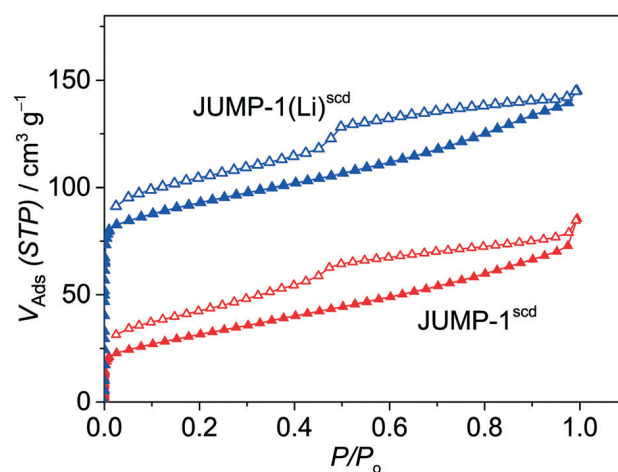

Fig. 5 N_2 isotherms of JUMP-1[scd] (red) and JUMP-1(Li)[scd] (blue) at 77 K. Open shapes denote desorption.

The isotherms shown in Fig. 5 can be classified as type II isotherms according to IUPAC rules.[44] The hysteresis loops observed can be described as type H4, which are somewhat characteristic for the presence of slit-shaped pores. The lower surface area of the as-synthesized material can be attributed to the steric demand of the organic cations when present in the framework, as they should hamper the accessibility of the internal pores for incoming guest molecules. Interestingly, the lithium ion exchange led to a considerable increase in porosity, as it is indicated by both the significant increase in the BET surface area and the larger total pore volume. This can be attributed to a reduced steric demand of the counterions upon replacement of the organic by the smaller lithium ions, thereby enabling greater access to the micropores.[45]

To further elucidate this point, a pore size analysis of the pretreated samples JUMP-1[scd] and JUMP-1(Li)[scd] was performed. The resulting pore size distribution plots are displayed in Fig. 6. The comparison clearly indicates a massive increase in the population of micropores for the lithium ion exchanged sample JUMP-1(Li)[scd], especially in the range below 1 nm. This is consistent with the above indicated stabilization of the mesopore structure by the gentle pretreatment with the supercritical CO_2 drying.[43] This clearly shows that the accessibility to micropores within an anionic framework can be adjusted *via* the variation of the size of cations residing in the pores.[46]

A similar basic trend can be seen from the CO_2 adsorption isotherms of the pretreated samples JUMP-1[scd] and JUMP-1(Li)[scd] (see Fig. S13†), as for the latter a slightly higher

Table 1 Characteristic adsorption parameters for the as-synthesized and lithium ion exchanged samples JUMP-1[scd] and JUMP-1(Li)[scd] after pretreatment by supercritical drying with CO_2

Parameter	JUMP-1[scd]	JUMP-1(Li)[scd]
a(BET) (m^2 g^{-1})	113	355
Total pore volume (cm^3 g^{-1})	0.13	0.22
Pore width (mean) (nm)	4.7	2.5
Pore width (mode) (nm)	1.0	0.6

Fig. 6 Pore size distribution data for JUMP-1^{scd} (top) and JUMP-1(Li)^{scd} (bottom).

ions. For the 3D framework, this leads to a 3,8-coordinated net with a tfz-d topology. The linear trinuclear SBUs observed in JUMP-1 exhibit mixed coordination geometries for the three cobalt(II) ions, *i.e.* octahedral for the central and tetrahedral for the two terminal ions. Such mixed geometries are uncommon for a solely carboxylate based coordination environment as observed in JUMP-1. The trinuclear SBUs were found to be magnetically well-separated and show an antiferromagnetic exchange coupling between the octahedral and the tetrahedral cobalt(II) ions. The porous material JUMP-1 is susceptible to exchange of the counterions present in the void of the 3D network indicating the robust nature of the anionic framework. Pretreatment prior to the gas-sorption experiments with supercritical CO_2 turned out to be very effective in making micropores accessible. The comparison of the as-synthesized and the lithium ion exchanged sample clearly shows that the accessibility to micropores within the anionic framework can be adjusted by variation of the cation size residing within the pores. In fact, this led to a massive increase in the population of micropores for the lithium ion exchanged material JUMP-1(Li)^{scd}.

Acknowledgements

References

1 (*a*) P. Mahata, G. Madras and S. Natarajan, *J. Phys. Chem. B*, 2006, **110**, 13759–13768; (*b*) A. Dhakshinamoorthy, M. Opanasenko, J. Cejka and H. Garcia, *Adv. Synth. Catal.*, 2013, **355**, 247–268; (*c*) A. Santra, I. Senkovska, S. Kaskel and P. K. Bharadwaj, *Inorg. Chem.*, 2013, **52**, 7358–7366; (*d*) Z. Chang, D.-S. Zhang, Q. Chen and X.-H. Bu, *Phys. Chem. Chem. Phys.*, 2013, **15**, 5430–5442; (*e*) Y.-W. Li, J.-R. Li, L.-F. Wang, B.-Y. Zhou, Q. Chen and X.-H. Bu, *J. Mater. Chem. A*, 2012, **1**, 495–499; (*f*) M. Guo and Z.-M. Sun, *J. Mater. Chem.*, 2012, **22**, 15939–15946; (*g*) M. M. Wanderley, C. Wang, C.-D. Wu and W. Lin, *J. Am. Chem. Soc.*, 2012, **134**, 9050–9053; (*h*) M. Tonigold, Y. Lu, A. Mavrandonakis, A. Puls, R. Staudt, J. Möllmer, J. Sauer and D. Volkmer, *Chem. – Eur. J.*, 2011, **17**, 8671–8695; (*i*) M. Tonigold, Y. Lu, B. Bredenkötter, B. Rieger, S. Bahnmüller, J. Hitzbleck, G. Langstein and D. Volkmer, *Angew. Chem., Int. Ed.*, 2009, **48**, 7546–7550; (*j*) M. Alvaro, E. Carbonell, B. Ferrer, F. X. L. i Xamena and H. Garcia, *Chem. – Eur. J.*, 2007, **13**, 5106–5112.

2 H. Furukawa, N. Ko, Y. Go, N. Aratani, S. Choi, E. Choi, A. Yazaydin, R. Snurr, M. O'Keeffe, J. Kim and O. Yaghi, *Science*, 2010, **329**, 424–428.

3 J. Hong, M. Cheng, Q. Liu, W. Han, Y. Zhang, Y. Ji, X. Jia and Z. Li, *Transition Met. Chem.*, 2013, **38**, 385–392.

4 M. Eddaoudi, J. Kim, N. Rosi, D. Vodak, J. Wachter, M. O'Keeffe and O. M. Yaghi, *Science*, 2002, **295**, 469–472.

volume in total adsorbed CO_2 is observed. However, the ratio of adsorbed CO_2 does not follow that obtained in the case of the N_2 isotherms. This can be attributed to characteristics of the CO_2 adsorption process which does neither generally scale with the pore volume nor with the available BET surface area as obtained from N_2 adsorption. In fact, the CO_2 adsorption rather tends to prefer smaller pores, which is due to the possibility of increasing adsorbate–adsorbent interactions.[46] Furthermore, as indicated from the N_2 adsorption data there is only a moderate difference in the total pore volume between JUMP-1^{scd} and JUMP-1(Li)^{scd}. A combination of both factors is assumed to be responsible for the absence of appreciable variations in the amount of adsorbed CO_2 for the pretreated as-synthesized and lithium ion exchanged materials.

Conclusions

A pillared-layer cobalt(II) MOF JUMP-1 based on the redox-active triphenylamine linker H$_3$ntb was synthesized by a solvothermal reaction. The structure of JUMP-1 can be viewed as constructed from neutral 2D networks $\{[Co_3(ntb)_2]\}_n$, which in turn are linked by terephthalic acid as an anionic pillar ligand. The charge of the resulting anionic 3D framework is compensated by *in situ* generated dimethylammonium cat-

5 K. Koh, A. Wong-Foy and A. Matzger, *J. Am. Chem. Soc.*, 2010, **132**, 15005–15010.

6 X.-L. Hu, F.-H. Liu, H.-N. Wang, C. Qin, C.-Y. Sun, Z.-M. Su and F.-C. Liu, *J. Mater. Chem. A*, 2014, **2**, 14827–14834.

7 K. Koh, A. Wong-Foy and A. Matzger, *Angew. Chem., Int. Ed.*, 2008, **47**, 677–680.

8 O. K. Farha, I. Eryazici, N. C. Jeong, B. G. Hauser, C. E. Wilmer, A. A. Sarjeant, R. Q. Snurr, S. T. Nguyen, A. Ö. Yazaydın and J. T. Hupp, *J. Am. Chem. Soc.*, 2012, **134**, 15016–15021.

9 (*a*) B.-B. Ding, Y.-Q. Weng, Z.-W. Mao, C.-K. Lam, X.-M. Chen and B.-H. Ye, *Inorg. Chem.*, 2005, **44**, 8836–8845; (*b*) Z.-H. Xuan, D.-S. Zhang, Z. Chang, T.-L. Hu and X.-H. Bu, *Inorg. Chem.*, 2014, **53**, 8985–8990; (*c*) B. Arstad, H. Fjellvog, K. O. Kongshaug, O. Swang and R. Blom, *Adsorption*, 2008, **14**, 755–762.

10 (*a*) S. Henke, A. Schneemann, A. Wütscher and R. A. Fischer, *J. Am. Chem. Soc.*, 2012, **134**, 9464–9474; (*b*) J. T. Culp, M. R. Smith, E. Bittner and B. Bockrath, *J. Am. Chem. Soc.*, 2008, **130**, 12427–12434.

11 (*a*) M.-H. Zeng, Y.-L. Zhou, M.-C. Wu, H.-L. Sun and M. Du, *Inorg. Chem.*, 2010, **49**, 6436–6442; (*b*) Y.-L. Zhou, M.-C. Wu, M.-H. Zeng and H. Liang, *Inorg. Chem.*, 2009, **48**, 10146–10150.

12 (*a*) N. Sikdar, K. Jayaramulu, V. Kiran, K. V. Rao, S. Sampath, S. J. George and T. K. Maji, *Chem. – Eur. J.*, 2015, **21**, 11701–11706; (*b*) Y. Takashima, S. Furukawa and S. Kitagawa, *CrystEngComm*, 2011, **13**, 3360–3363; (*c*) P. Wu, C. He, J. Wang, X. Peng, X. Li, Y. An and C. Duan, *J. Am. Chem. Soc.*, 2012, **134**, 14991–14999; (*d*) Y. E. Cheon and M. P. Suh, *Angew. Chem., Int. Ed.*, 2009, **48**, 2899–2903.

13 (*a*) H. Chun, D. N. Dybtsev, H. Kim and K. Kim, *Chem. – Eur. J.*, 2005, **11**, 3521–3529; (*b*) T.-H. Park, K. Koh, A. G. Wong-Foy and A. J. Matzger, *Cryst. Growth Des.*, 2011, **11**, 2059–2063.

14 Z. Yin, Y.-L. Zhou, M.-H. Zeng and M. Kurmoo, *Dalton Trans.*, 2015, **44**, 5258–5275.

15 L. Luo, K. Chen, Q. Liu, Y. Lu, T. A. Okamura, G.-C. Lv and Y. Zhao, *Cryst. Growth Des.*, 2013, **13**, 2312–2321.

16 (*a*) H. Chevreau, T. Devic, F. Salles, G. Maurin, N. Stock and C. Serre, *Angew. Chem., Int. Ed.*, 2013, **52**, 5056–5060; (*b*) H. J. Park and M. P. Suh, *Chem. – Eur. J.*, 2008, **14**, 8812–8821; (*c*) Y.-W. Li, D.-C. Li, J. Xu, H.-G. Hao, S.-N. Wang, J.-M. Dou, T.-L. Hu and X.-H. Bu, *Dalton Trans.*, 2014, **43**, 15708–15712.

17 X. Cao, Y. Wen, Y. Guo, G. Yu, Y. Liu and L.-M. Yang, *Dyes Pigm.*, 2010, **84**, 203–207.

18 C. Livage, N. Guillou, A. Castiglione, J. Marrot, M. Frigoli and F. Millange, *Microporous Mesoporous Mater.*, 2012, **157**, 37–41.

19 S. Dapperheld, E. Steckhan, K.-H. G. Brinkhaus and T. Esch, *Chem. Ber.*, 1991, **124**, 2557–2567.

20 B. V. Nonius, *COLLECT; Data Collection Software*, Delft, The Netherlands, 1998; Z. Otwinowski and W. Minor, in *Methods in Enzymology*, ed. C. W. Carter and R. M. Sweet, Academic Press, 1997, ch. Processing of X-ray Diffraction Data Collected in Oscillation Mode, vol. 276, pp. 307–326.

21 G. M. Sheldrick, *Acta Crystallogr., Sect. A: Found. Crystallogr.*, 2008, **64**, 112–122.

22 A. L. Spek, *Acta Crystallogr., Sect. D: Biol. Crystallogr.*, 2009, **65**, 148–155.

23 H. Putz and K. Brandenburg, *Diamond 4.2.0 - Crystal and Molecular Structure Visualization*, Crystal Impact, Kreuzherrenstr. 102, 53227 Bonn, Germany, 2016.

24 QUANTACHROME, *Application of QSDFT (Quenched Solid Density Functional Theory) - A novel density functinal theory for an accurate pore size analysis of disordered porous carbons*.

25 J. Rouquerol, P. Llewellyn and F. Rouquerol, *Stud. Surf. Sci. Catal.*, 2007, **160**, 49–56.

26 H. Wang, D. Zhang, D. Sun, Y. Chen, L.-F. Zhang, L. Tian, J. Jiang and Z.-H. Ni, *Cryst. Growth Des.*, 2009, **9**, 5273–5282.

27 L.-F. Ma, Y.-Y. Wang, L.-Y. Wang, D.-H. Lu, S. R. Batten and J.-G. Wang, *Cryst. Growth Des.*, 2009, **9**, 2036–2038.

28 P. Kapoor, A. P. S. Pannu, G. Hundal, R. Kapoor, M. Corbella, N. Aliaga-Alcalde and M. S. Hundal, *Dalton Trans.*, 2010, **39**, 7951–7959.

29 M.-X. Yao, M.-H. Zeng, H.-H. Zou, Y.-L. Zhou and H. Liang, *Dalton Trans.*, 2008, 2428–2432.

30 (*a*) W.-J. Huang, C.-J. Hsu, S.-K. Tsai, H.-Y. He, J.-J. Ding, T.-W. Hsu, C.-C. Yang and J.-D. Chen, *RSC Adv.*, 2015, **5**, 23374–23382; (*b*) D. Kim, X. Song, J. H. Yoon and M. S. Lah, *Cryst. Growth Des.*, 2012, **12**, 4186–4193; (*c*) S. Su, Z. Guo, G. Li, R. Deng, S. Song, C. Qin, C. Pan, H. Guo, F. Cao, S. Wanga and H. Zhang, *Dalton Trans.*, 2010, **39**, 9123–9130.

31 A. D. Burrows, K. Cassar, R. M. W. Friend, M. F. Mahon, S. P. Rigby and J. E. Warren, *CrystEngComm*, 2005, **7**, 548–550.

32 V. A. Blatov, A. P. Shevchenko and D. M. Proserpio, *Cryst. Growth Des.*, 2014, **14**, 3576–3586.

33 J. Hafizovic, M. Bjørgen, U. Oslbye, P. D. C. Dietzel, S. Bordiga, C. Prestipino, C. Lamberti and K. P. Lillerud, *J. Am. Chem. Soc.*, 2007, **129**, 3612–3620.

34 O. Kahn, *Molecular Magnetism*, Wiley-VCH Inc., Weinheim, 1993.

35 F. Lloret, M. Julve, J. Cano, R. Ruiz-García and E. Pardo, *Inorg. Chim. Acta*, 2008, **361**, 3432–3435.

36 A. Buchholz, A. O. Eseola and W. Plass, *C. R. Chim.*, 2012, **15**, 929–936.

37 S. Ziegenbalg, D. Hornig, H. Görls and W. Plass, *Inorg. Chem.*, 2016, **55**, 4047–4058.

38 M. Murrie, *Chem. Soc. Rev.*, 2010, **39**, 1986–1995.

39 R. Azuah, L. Kneller, Y. Qiu, P. Tregenna-Piggott, C. Brown, J. Copley and R. Dimeo, *J. Res. Natl. Inst. Stand. Technol.*, 2009, **114**, 341–358.

40 P. L. W. Tregenna-Piggott, D. Sheptyakov, L. Keller, S. I. Klokishner, S. M. Ostrovsky, A. V. Palii, O. S. Reu, J. Bendix, T. Brock-Nannestad, K. Pedersen, H. Weihe and H. Mutka, *Inorg. Chem.*, 2009, **48**, 128–137.

41 (*a*) T.-F. Liu, H.-L. Sun, S. Gao, S.-W. Zhang and T.-C. Lau, *Inorg. Chem.*, 2003, **42**, 4792–4794; (*b*) S.-J. Liu, L. Xue, T.-L. Hu and X.-H. Bu, *Dalton Trans.*, 2012, **41**, 6813–6819.

42 (*a*) M.-H. Zeng, X.-L. Feng, W.-X. Zhang and X.-M. Chen, *Dalton Trans.*, 2006, 5294–5303; (*b*) Y. Liu, H. Li, Y. Han, X.

Lv, H. Hou and Y. Fan, *Cryst. Growth Des.*, 2012, **12**, 3505–3513.

43 A. Nelson, O. Farha, K. Mulfort and J. Hupp, *J. Am. Chem. Soc.*, 2009, **131**, 458–460.

44 (*a*) M. Thommes, K. Kaneko, A. V. Neimark, J. P. Olivier, F. Rodriguez-Reinoso, J. Rouquerol and K. S. W. Sing, *Pure Appl. Chem.*, 2015, **87**, 1051–1069; (*b*) K. S. W. Sing, D. H. Everett, R. A. W. Haul, L. Moscou, R. A. Pierotti, J. Rouquerol and T. Siemieniewska, *Pure Appl. Chem.*, 1985, **57**, 603–619.

45 M. Thommes and K. A. Cychosz, *Adsorption*, 2014, **20**, 233–250.

46 (*a*) J. An and N. L. Rosi, *J. Am. Chem. Soc.*, 2010, **132**, 5578–5579; (*b*) S. Yang, X. Lin, A. J. Blake, K. M. Thomas, P. Hubberstey, N. R. Champness and M. Schroeder, *Chem. Commun.*, 2008, 6108–6110.

Robust anionic pillared-layer framework with triphenylamine-based linkers: ion exchange and counterion-dependent sorption properties

Oluseun Akintola, Sven Ziegenbalg, Axel Buchholz, Helmar Görls, Winfried Plass

Supplementary Information

Crystal and framework structure of JUMP-1 with topology

Table S1: Bond lengths for the cobalt(II) ions in the crystal structure of JUMP-1 (in pm). For notation see Fig. 1 in the main text

Co1–O2	2.0380(18)
Co1–O3	2.1536(19)
Co1–O6	2.056(2)
Co2–O1	1.978(2)
Co2–O3	2.020(2)
Co2–O5	1.996(2)
Co2–O7	2.001(3)

Table S2: Bond angles at the cobalt(II) ions in the crystal structure of JUMP-1 (in deg). For notation see Fig. 1 in the main text

O2–Co1–O2A	86.51(11)	O1–Co2–O5D	102.81(9)
O2–Co1–O3B	95.03(7)	O1–Co2–O7	106.59(11)
O2–Co1–O3C	87.70(7)	O5D–Co2–O7	95.81(12)
O2–Co1–O6D	96.00(10)	O1–Co2–O3C	101.07(8)
O2–Co1–O6E	172.50(8)	O5D–Co2–O3C	114.15(8)
O3B–Co1–O3C	176.25(10)	O7–Co2–O3C	133.10(11)
O3B–Co1–O6D	85.03(8)		
O3B–Co1–O6E	92.14(8)		
O6D–Co1–O6E	82.40(15)		
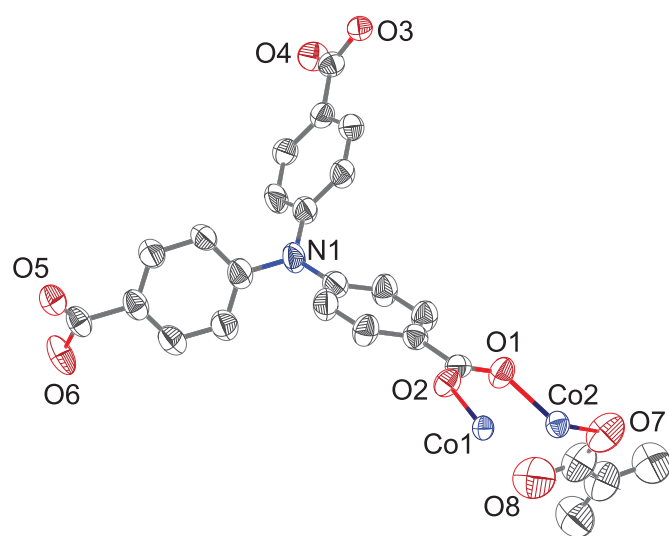
Fig. S1: Asymmetric unit of JUMP-1 with thermal ellipsoids at the 50 % probability level. Hydrogen atoms are omitted for the sake of clarity.
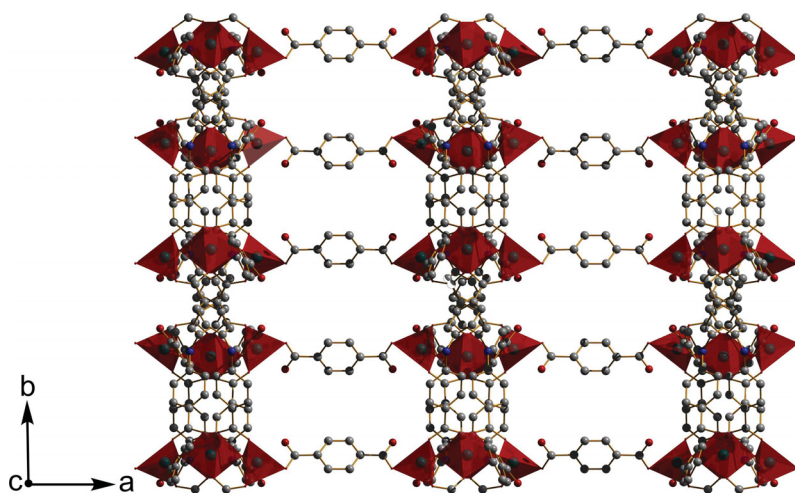
Fig. S2: 3D framework of JUMP-1 viewed along the crystallographic [001] direction. 2D networks composed of linear trinuclear cobalt(II) SBUs and ntb^{3-} ligands are arranged along the (100) plane and interconnected by the bdc^{2-} pillars. Red polyhedra represent cobalt(II) centers.
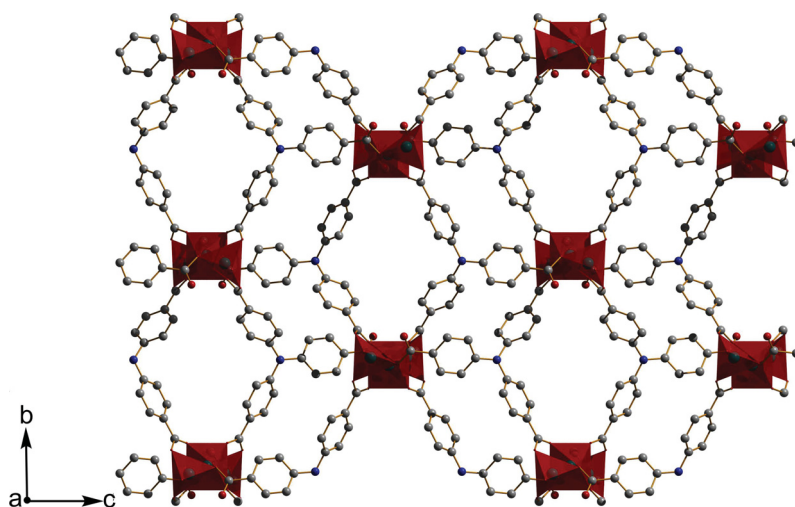
Fig. S3: Representation of the 2D network composed of linear trinuclear cobalt(II) SBUs and ntb^{3-} ligands within the 3D framework of JUMP-1 viewed along the crystallographic [100] direction.

Topological analysis for JUMP-1
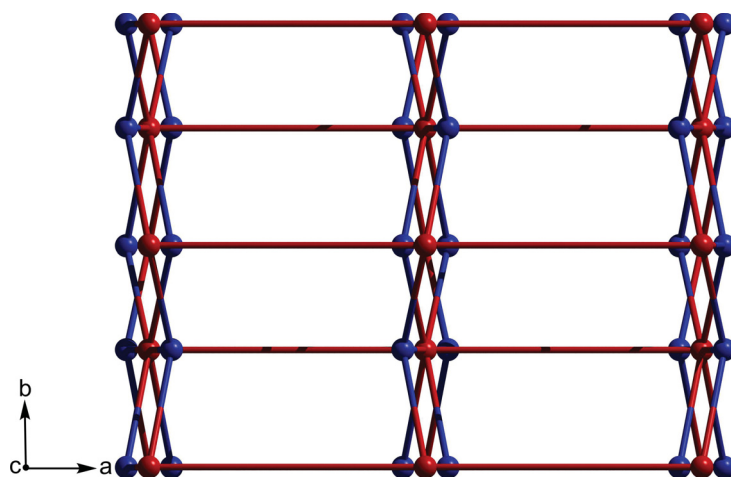
Fig. S4: Representation of the tfz-d topology of the network of JUMP-1 viewed along the negative crystallographic [001] direction. The red and blue spheres represent the trinuclear cobalt clusters (8-connected nodes) and the nitrogen atoms of the ntb^{3-} ligands (3-connected nodes), respectively.

Fig. S5: Representation of the tfz-d topology of the network of JUMP-1 viewed along the crystallographic [100] direction. The red and blue spheres represent the trinuclear cobalt clusters (8-connected nodes) and the nitrogen atoms of the ntb^{3-} ligands (3-connected nodes), respectively.

Table S3: Coordination sequences for JUMP-1 (topological density $TD_{10} = 1748$)

Vertex	CS_1	CS_2	CS_3	CS_4	CS_5	CS_6	CS_7	CS_8	CS_9	CS_{10}
V1	3	18	41	74	113	164	221	290	365	452
V2	8	20	44	74	116	164	224	290	368	452

Table S4: Vertex Symbols for JUMP-1

Vertex	Vertex symbol	Extended Point Symbol
V1	$[4^3]$	$[4.4.4]$
V2	$[4^6.6^{18}.8^4]$	$[4.4.4.4.4.4.6_2.6_2.6_2.6_2.6_2.6_2.6_4.6_4.6_4.6_4.6_4.6_4.6_4.6_4.6_4.6_4.6_4.6_4.8_8.8_8.8_8.8_{24}]$

5
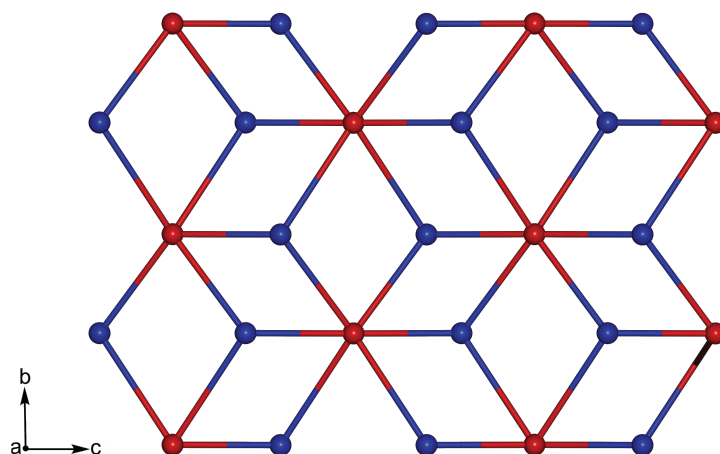
XRPD patterns for JUMP-1
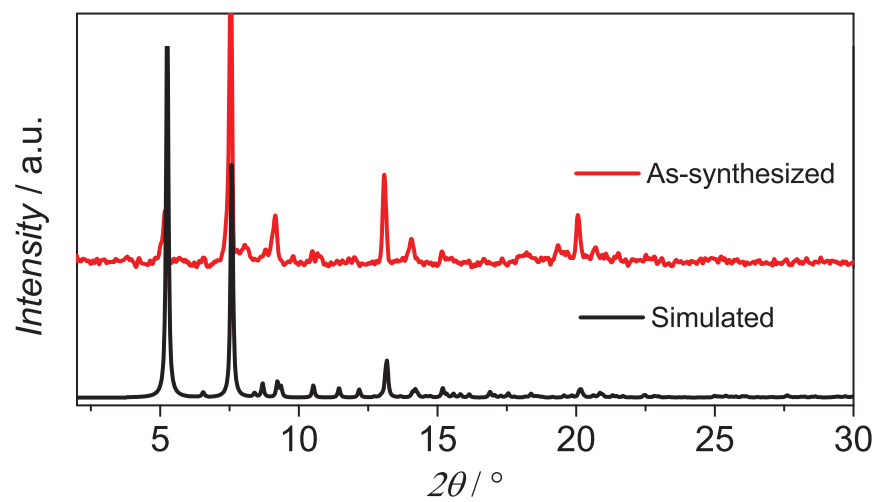
Fig. S6: XRPD pattern for JUMP-1: simulated pattern (bottom, black) and experimental pattern (top, red).

TGA profile for JUMP-1
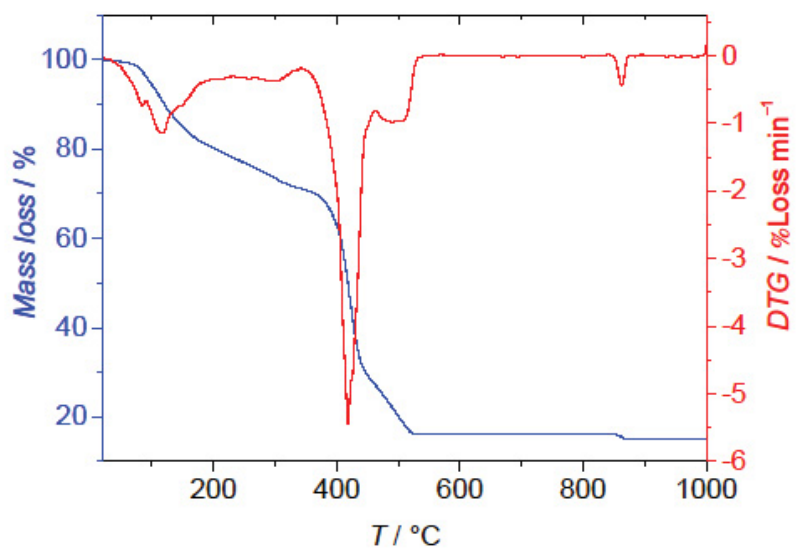
Fig. S7: Thermogravimetric data of JUMP-1: TG curve in blue and differential TG curve (DTG) in red.

Magnetic data for JUMP-1
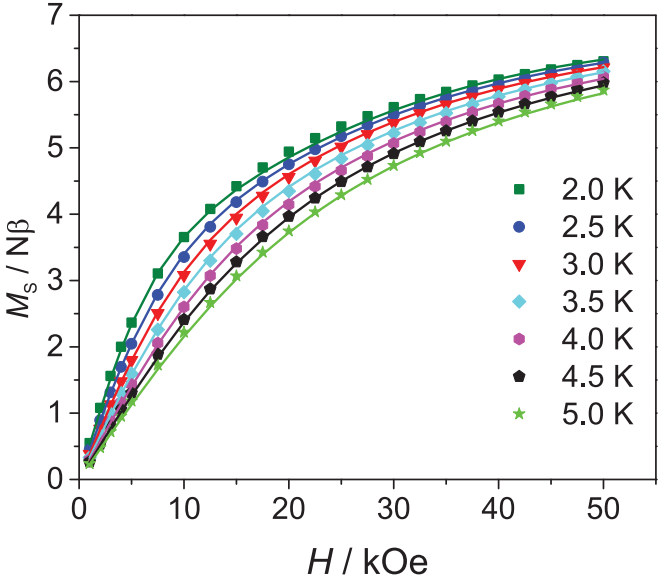
Fig. S8: Field-dependent magnetization for JUMP-1. Lines represent best fit (see text in main manuscript for parameters).

XRPD patterns for ion exchanged samples
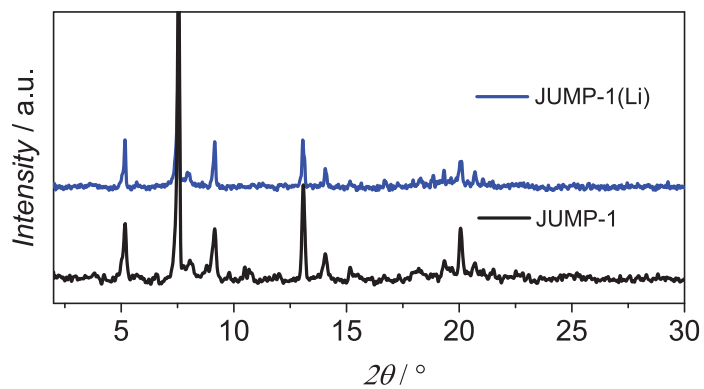
Fig. S9: XRPD pattern for lithium ion exchanged sample JUMP-1(Li) (top); for comparison also the pattern of the as-synthesized sample JUMP-1 is displayed (bottom).

TGA profile for ion exchanged sample
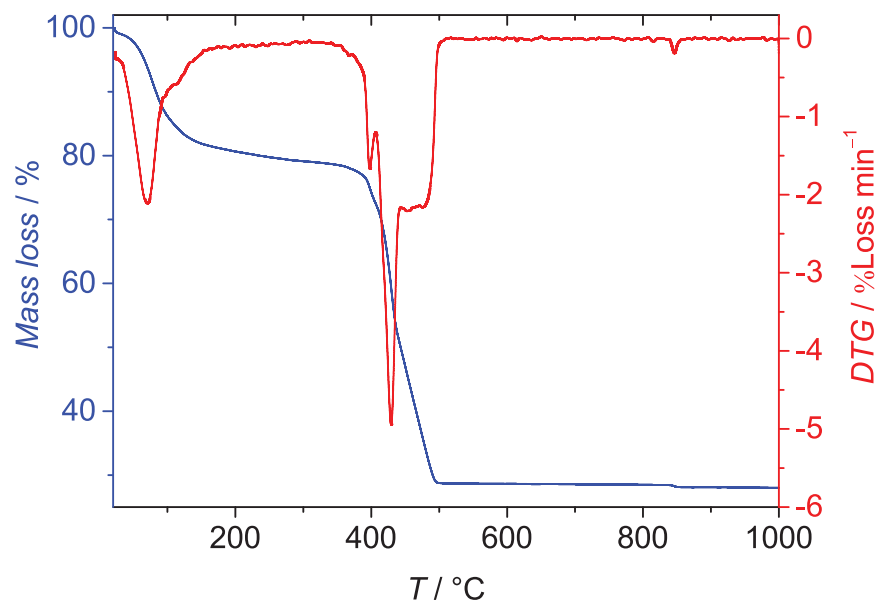
Fig. S10: Thermogravimetric data for lithium ion exchanged sample JUMP-1(Li): TG curve in blue and differential TG curve (DTG) in red.

Sorption data

Table S5: Consistency criteria derived from measured BET Data for activated samples of the as-synthesized (JUMP-1$^{\mathrm{dcm}}$ and JUMP-1$^{\mathrm{scd}}$) and lithium ion exchanged (JUMP-1(Li)$^{\mathrm{scd}}$) materials (for notation see text in main manuscript)

	P/P_o range	C	V_m [cm³/g]	$1/\sqrt{C}+1$	$P/P_\mathrm{o}(V_\mathrm{m})$	a(BET) [m²/g]	R
JUMP-1$^{\mathrm{dcm}}$	0.13 - 0.28	8.16	6.34	0.26	0.26	28	0.999
JUMP-1$^{\mathrm{scd}}$	0.08 - 0.23	134	25.96	0.08	0.08	113	0.999
JUMP-1(Li)$^{\mathrm{scd}}$	0.005 - 0.026	3025	81.52	0.018	0.018	355	0.999
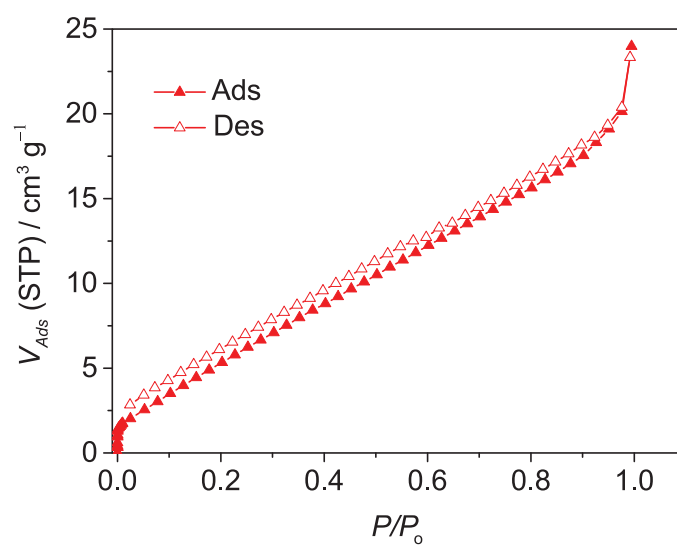
Fig. S11: N$_2$ isotherm for JUMP-1$^{\mathrm{dcm}}$ measured at 77 K, which is the as-synthesized sample activated by solvent-exchange with dichloromethane.
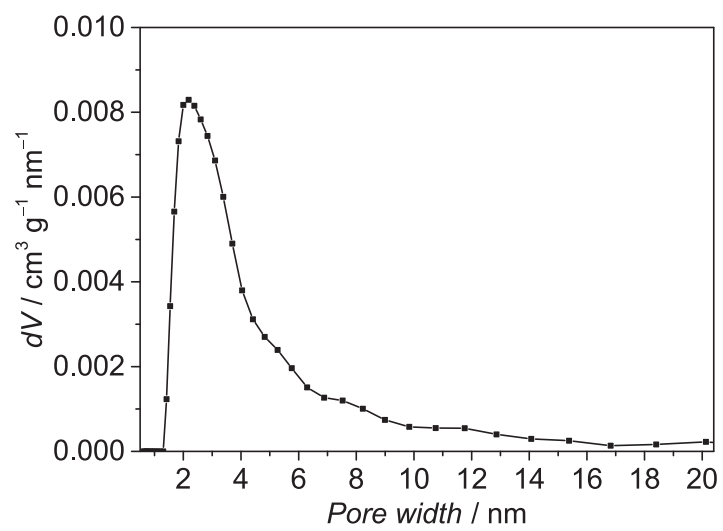
Fig. S12: Simulated pore distribution data for JUMP-1$^{\mathrm{dcm}}$ fitted using N$_2$ on carbon at 77 K (slit pores QSDFT equilibrium model).
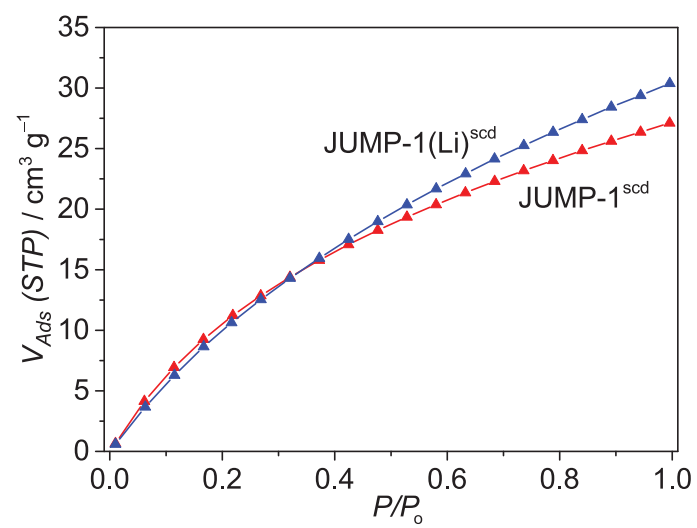
Fig. S13: CO_2 isotherms measured at 273 K for samples derived from the as-synthesized (red) and lithium ion exchanged (blue) samples of JUMP-1.

Publication 4

Isophthalic acid modulated synthesis of a neutral Co(II) nitrilotribenzoic acid MOF: Magnetic and sorption properties

Oluseun Akintola, Axel Buchholz, Helmar Görls, Winfried Plass *Eur. J. Inorg. Chem.* **2017** *To be submitted.*
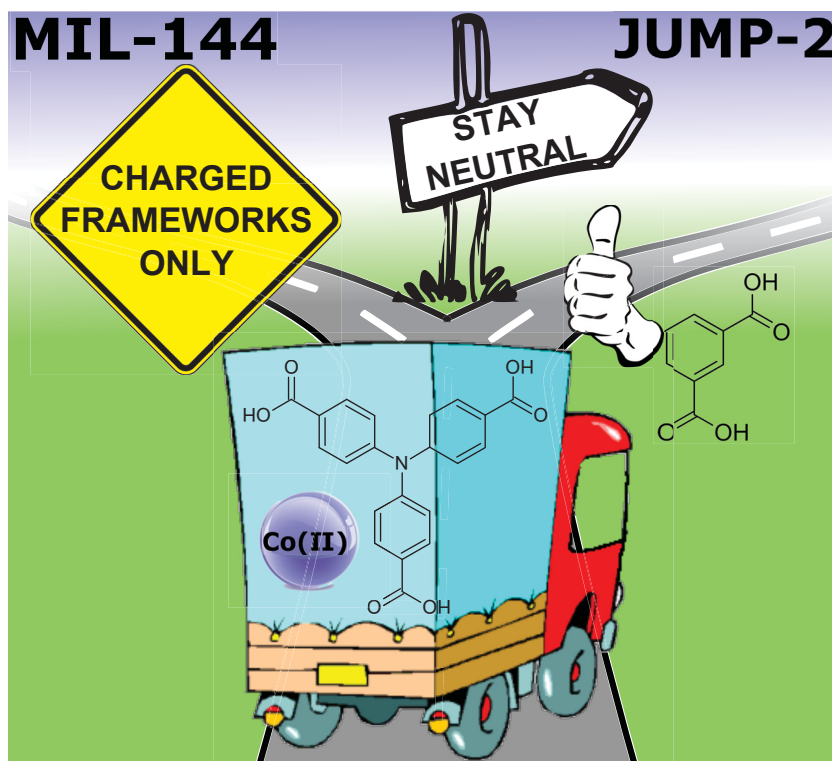
FULL PAPER

Isophthalic acid modulated synthesis of a neutral Co(II) nitrilotribenzoic acid MOF: Magnetic and sorption properties

Oluseun Akintola, Axel Buchholz, Helmar Görls, and Winfried Plass*

Abstract. A new Co(II) MOF (JUMP-3) has been obtained by solvothermal reaction using 4,4',4''-nitrilotribenzoic acid as linker with isophthalic acid employed as template and pH modulator. Its X-ray crystal structure revealed it to be a three-dimensional network composed of trinuclear Co(II) units while the topological analysis showed it to have adopted a 3,6-coordinated net with 3,6T80 topology. Magnetic measurements performed in the temperature range of 2–300 K revealed antiferromagnetic interactions between the Co(II) ions within its linear trinuclear clusters. Investigation of its sorption properties was likewise carried out and it was found to demonstrate modest surface area, slightly less than 400 $m^2 \cdot g^{-1}$.

Introduction

The past few years have seen MOFs emerge as a much sought after class of hybrid materials with potential applications in many diverse areas, including gas storage and separation,[1-4] chemical sensing,[5-7] catalysis,[8-10] resonance imaging, and drug delivery.[11-13] One of their major points of attraction has been the relative ease with, which they can be tuned and tailored to fit certain goals or enhancement of certain properties such as pore size or luminescence.[14-16] Such predictability and tunability can be regarded as being an outcome of the reticular approach whereby the use rigid ligands and combining them with metals can lead to predetermined structures.[17] Combining this strategy with advances in topological research has thus helped to attain a good measure of consistency in MOF synthesis. The implication of this is that, by carefully selecting the ligands it becomes possible to rationally design a framework with desired architecture.[18-19]

Generally, aromatic poly-carboxylates have been the most commonly used type of ligands in constructing MOFs as they impose the required rigidity, which in turn aids in stabilizing the resulting structures.[20-21] They also offer varying types of

[a]   Prof. Dr. W. Plass
      Institut für Anorganische und Analytische Chemie
      Friedrich-Schiller-Universität Jena
      Humboldtstr 8
      07743 Jena
      Sekr.Plass@uni-jena.de

coordination modes such as the *syn-syn*, *syn-anti*, and *anti-anti* modes and these play an important role of modulating magnetic interactions.[22-23]

In addition to the organic linker and metal ion, an equally important factor to be considered is the reaction medium and over time solvents like ethanol, water, and DMF have been utilized in MOF preparation. The latter has gained widespread use and a frequent side-effect is the resultant formation of the dimethylammonium cation under reaction conditions, which then in turn templates the formation of anionic MOFs.[24] Even when there is no generation of a secondary component arising from in-situ solvent hydrolysis as in the case of DMF, solvents can still play a powerful role as templates in MOF synthesis.[25-26] In such instances, the varying sizes of the different solvent molecules will naturally lead to divergent outcomes.

Besides the solvent, other classes of compounds have also been employed as templating agents.[27] Some of these include surfactants,[28] Keggin ions,[29] metalloporphyrins,[30] and inorganic acids[31]. In the same token, organic acids such as phthalic acid or acetic acid have been reported as well.[32-33] In a few cases, these have been found to induce defects in the frameworks, which have been accompanied by interesting consequences.[34-37] Furthermore, they have shown the propensity to influence the morphology and aggregability of the crystals.[38]

In this report, we discuss a new Co(II) MOF from nitrilotribenzoic acid but obtained by using isophthalic acid as structure directing agent. An anionic Co(II) MOF (MIL-144) based on this same ligand has been previously published.[39-40] However, the new MOF was found to be neutral and had a similar topology to MIL-144. The mechanism of formation is proposed to be based on the double-headed action of isophthalic acid as both template and pH modulator. Its porosity will be studied using two different activation methods. Its magnetic properties will also be investigated and reported here as well.

Results and discussion

Synthesis: A common feature in several MOF syntheses that often utilize DMF as solvent is the decarbonylation of the latter, which results in the formation of the dimethylammonium cation. This cation has been known to play a templating role in the syntheses of various anionic frameworks.[41-42] This was likewise

found to be true in the case of the previously reported anionic counterpart to JUMP-3.[39] For its synthesis, isophthalic acid was utilized for the initial purpose of obtaining a mixed ligand MOF with H_3ntb. However, the surprising outcome was a single ligand framework consisting of only the H_3ntb ligand and Co(II) ion without the isophthalic acid playing any visible role in the structure. It is believed that the isophthalic acid rather than acting as a co-ligand, may have suppressed the formation of the dimethylammonium cation, which would have templated the anionic MOF. This is possibly *via* lowering the pH to prevent basic conditions, which would be suitable for decarbonylation of the DMF. In addition to this, it is thought to have simultaneously templated the formation of the neutral MOF instead. Repeating the synthesis at the same temperature (130 °C) but in the absence of the isophthalic acid resulted in no product. Increasing the temperature to 150 °C (operating temperature for MIL-144[39-40]) with the inclusion of isophthalic acid also did not lead to formation of a product. It is therefore likely that the outcome was a combined effect of both temperature and presence of the modulator. We attempted to use phthalic acid instead to see if it would show similar behavior, but it did not yield any crystalline product.
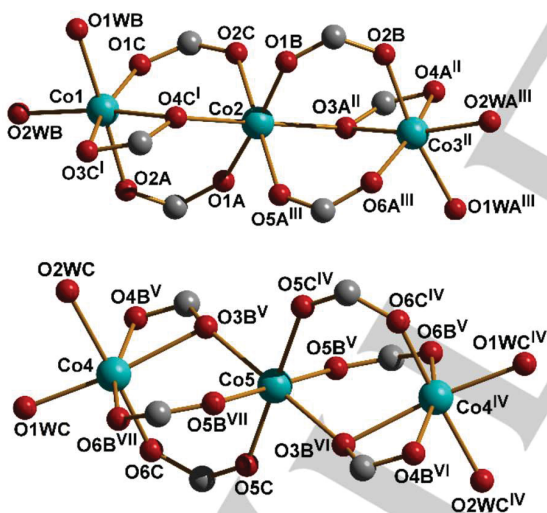
Figure 1 Cut-out view of the trinuclear SBUs displaying the coordination environments around the cobalt(II) ions. Bulky groups have been removed to allow easier view. Symmetry code: I = + x, x − y, −1/2 + z; II = + y, x, −3/2 − z; III = + y, − x + y, 1 − z; IV = 1− x, 1− y, 2 − z; V = 1+ y − x,1 − x, + z; VI = + x, x − y, 1/2 + z; VII = −y + x, + x, 2 − z.

X-ray crystal structure of JUMP-3: X-ray diffraction measurement was performed on the crystalline product obtained directly from the solvothermal synthesis. Unfortunately, the quality

of the crystals was poor and thus only a motif could be obtained. As such, a more detailed description of the crystal structure will not be given.

The data reveals JUMP-3 crystallizes in the hexagonal space group $P\bar{3}c1$ and possesses a 3D network. Its crystallographic asymmetric unit contains four and a half independent Co atoms and three ntb[3−] including two DMF solvent molecules, one of which is on a special position.

In overview, the 3D network can be described as composed of an array of linear trinuclear clusters throughout the structure (see Fig. 1). Each cobalt(II) ion exists within an octahedral coordination environment. The consistence of the octahedral geometries is quite typical for such carboxylate systems.[43-45] The clusters are then connected through the ntb[3−] ligands resulting in the formation of the 3D framework structure as displayed in Fig. 2.
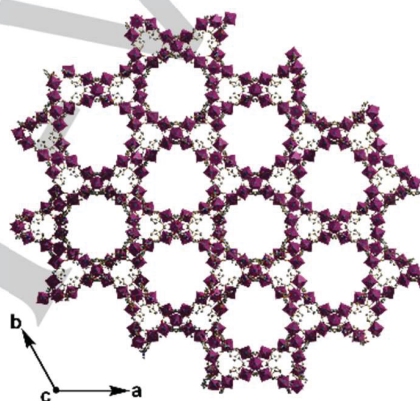

Figure 2. Representation of the crystal structure of JUMP-3 viewed along the [001] direction showing the arrangement of triangular and hexagonal channels. Polyhedra represent cobalt(II) centers.

On closer inspection of the clusters, two slightly distinct types can be found within the structure. The first cluster containing Co1, Co2, and Co3 is slightly irregular with each cobalt ion situated on a general position. The adjacent atoms are bridged within the trinuclear cluster by the carboxylate groups of the ligand. Three types of carboxylate bridges can be identified, one of which is a monodentate $\mu_{1,1}$ mode (O3 and O4) and the other two in a bidentate *syn-syn* $\mu_{1,3}$ mode (O1/O2 and O5/O6) (see Fig. 3). Additionally, the terminal Co1 and Co3 ions are each coordinated by two water molecules.
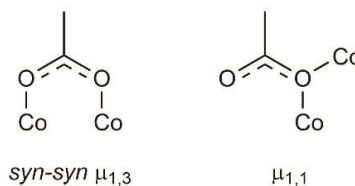

Figure 3. Carboxylate bridging modes found in trinuclear clusters of JUMP-3.

FULL PAPER

The second cluster on the other hand is symmetric stemming from residence of the Co5 on an inversion center. The terminal Co4 ion is also coordinated by water molecules. In terms of its bridging modes, the second cluster is identical to the first. As such, it also has two types of carboxylate bridges, the monodentate $\mu_{1,1}$ mode (O3) and the other two in a bidentate *syn-syn* $\mu_{1,3}$ mode (O3/O4 and O5/O6).

The three-dimensional framework can be described as made up of a combination of pseudo-hexagonal and triangular channels when viewed along the [001] direction resulting in a Kagome lattice (see Fig. 2). The hexagonal channels are large (17-20 Å diameter) and expectedly filled with various types of guests including solvent and isophthalic acid molecules. The existence of the latter could not be confirmed crystallographically, but evidence of its presence is supported by both elemental as well as thermogravimetric analysis. The solvent accessible void of the framework is estimated to be 21525 $Å^3$ per unit cell, which represents 54.5% of its total volume.[46]

Overall, JUMP-3 only shows similarity to its anionic counterpart MIL-144 in terms of network connectivity. In contrast to MIL-144, which had a mixture of dinuclear and trinuclear cobalt SBUs, it is solely composed of trinuclear metal-centered SBUs. [39] To gain further understanding of its network, topological analysis has been carried out using TOPOS.[47] By way of simplification two different nodes are revealed, which are six- and three-connected. The analogous topological net is shown in Fig. 4. The six-connected node is typified by the linear trinuclear clusters with each being connected to six attached carboxylate groups, all of which emanate from the ntb^{3-} ligands (Fig. S1). The amine nitrogen atom in the ligands provides the three-connected node (Fig. S2). Analysis of the topology reveals the network is a 3,6-connected net with the 3,6T80 topology and point symbol $(4^2.6)_2(4^4.6^2.8^8.10)$ (see Fig. 3, Tables S1 and S2). A tile representation of the framework is given in Fig. S3.

Powder Diffraction and Thermal Analysis: To confirm phase purity of the bulk material, powder diffraction of JUMP-3 was performed. Both the experimental and simulated patterns show almost close agreement as shown in Fig. S4. The slight differences can be attributed to the poor quality of the single crystal diffraction data.

The thermal analysis of JUMP-3 shows a steady weight loss up to 370 °C, after which the compound began to thermally decompose (see Fig. S5). The first of the steps is made up of two indistinguishable episodes as illustrated by the differential thermal gravimetric analysis. The earlier mass loss seen at 4.8% would seem to indicate a looser association of the water molecules as compared with the DMF molecules.
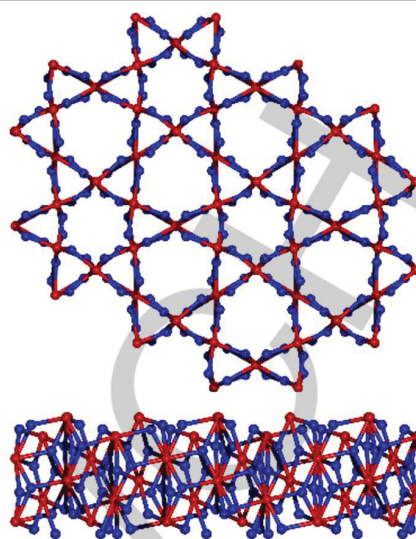

Figure 4. Topological representation of the 3,6-connected net in JUMP-3: View along the [001] direction (above); View along the [010] direction (below). Blue balls represent N atoms at the center of the amine ligand, whereas red balls represent the centers of the trinuclear units, respectively (for details see text).

The total mass loss up to 250 °C is however consistent with the estimated value related to six water and three DMF molecules (observed 9.8%, calculated 9.4%). There is no clear nor distinct mass loss attributable to the guest isophthalic acid molecule, which could be due to the existence of some loose form of association with the framework. The further decomposition of the organic ligand framework was composed of successive weight loss steps resulting in a rest mass of 19.3%, which fits exactly with the calculated value of the 19.3% estimated for CoO (see Fig. S4).

Magnetic Properties of [Co₉(ntb)₆(H₂O)₁₂]n (JUMP-3): The magnetic susceptibility data for JUMP-3 was measured at an applied field of 2 kOe in the temperature range from 2 to 300 K and is shown in Fig. 5 as a temperature-dependent plot of both $\chi_M T$ and χ_M^{-1}.

The room temperature $\chi_M T$ value of JUMP-3 seen at 8.5 $cm^3 \cdot K \cdot mol^{-1}$ is significantly higher than the spin-only value for three magnetically isolated Co(II) ions at room temperature (5.63 $cm^3 \cdot K \cdot mol^{-1}$), indicative of significant orbital contribution.[48-49] It then slowly decreases with lowering temperatures to reach a value of 2.5 $cm^3 \cdot K \cdot mol^{-1}$ at 2 K. It is generally known that spin-orbit coupling in addition to antiferromagnetic coupling of the neighboring cobalt(II) ions is often responsible for the observed behavior.[50] The reciprocal molar magnetic susceptibility χ_M^{-1} plotted versus temperature obeys the Curie-Weiss law

FULL PAPER

between 35−300 K with a Curie constant of 9.4 cm³·K·mol⁻¹ and a Weiss temperature θ = −28.8 K (see Fig. 5).
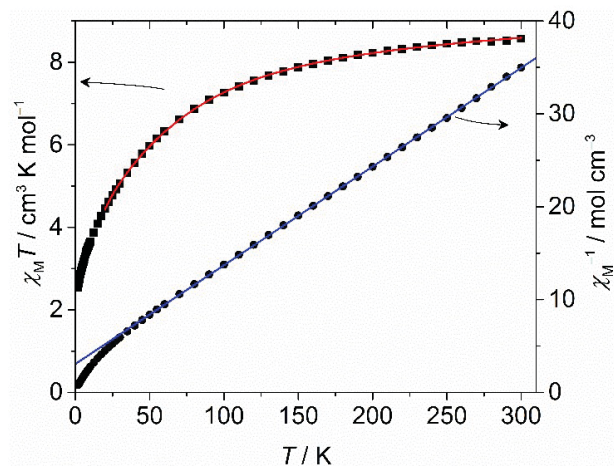

Figure 5: Temperature dependence of the magnetic susceptibility $\chi_M T$ (black squares) and χ_M^{-1} (black circles) per Co₃ unit in JUMP-3 measured at an applied field of 2 kOe. Lines represent best fit (see text for parameters).

The Curie constant falls within the range for three octahedral Co(II) ions with significant orbital contribution.[51] The negative value of the Weiss constant is in agreement with the existence of antiferromagnetic exchange between the Co(II) ions in addition to considerable spin−orbit coupling.[52] As the trinuclear clusters in JUMP-3 are clearly well-isolated from each other within the structure of the framework, this would suggest that the magnetic behavior can be described in terms of these units. Therefore to fit the data, a simple model was constructed, in which a single set of parameters was assumed for all three cobalt(II) centers so as to avoid overparametrization. The Hamiltonian used in fitting the data is stated in Eq. (1).

$$H = J(S_1 S_2 + S_2 S_3) + 3D \left[S(z)^2 - \frac{1}{3} S(S + 1) \right] \quad (1)$$

Fitting of the susceptibility data between 20–300 K was then performed using PHI.[53] The experimental data were best replicated with the following fit parameters g = 2.46, D = 74.4 cm⁻¹, J = −2.4 cm⁻¹, TIP = 1.3 × 10⁻³ cm³·mol⁻¹, and an agreement factor of R = 7.1 × 10⁻³.

The value of the coupling constant J is consistent with reported values for similar trinuclear systems.[43-44] Furthermore, the antiferromagnetic nature of the exchange is in agreement with the coordination modes observed in the clusters, which are the $syn–syn–\mu_{1,3}$ and the $\mu_{1,1}$ (see Fig. 2). This is supported by the observation that the $syn-syn$ and $anti-anti$ conformations often favor antiferromagnetic coupling.[54-55] In addition, the dependence of the exchange coupling on the Co−O−Co bridging

angles has been reported with values larger than 100° favoring antiferromagnetic coupling.[56-57] This would agree with the value of about 109° observed for JUMP-3.

The field dependent magnetization was measured in a temperature range of 2 to 5 K and up to a field strength of 5 T and the data is likewise displayed in Fig. S6. It expectedly shows an increase in the magnetization with increasing field strength attaining a value of 3.6 Nβ at 2 K and 5 T. It clearly does not reach saturation at the conditions described. In addition, the value is far lower than the saturation value of about 3 Nβ (per Co(II) ion) expected for Co(II) ions with a possible S' = ½ state, which supports the existence of antiferromagnetic interactions between the ions.[58-60] However, no fit of the magnetization data could be obtained mainly due to the different nature of the behavior of the trinuclear system at the low temperatures, at which the data were obtained.

To obtain a further understanding of the magnetic behavior of JUMP-3, AC magnetic susceptibility measurements were performed and showed no out-of-phase signal. This indicates the absence of any magnetic ordering and is consistent with magnetically isolated clusters as suggested by the crystal structure.

Gas-sorption properties: The porosity of JUMP-3 was investigated by measurement of the N₂ isotherms. The MOF was activated using both dichloromethane and supercritical CO₂ to obtain JUMP-3[dcm] and JUMP-3[scd], respectively (see Experimental Section for details).
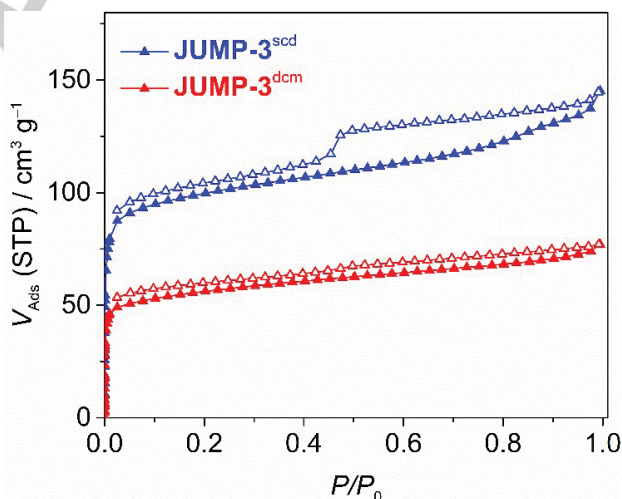

Figure 6: N₂ isotherms of JUMP-3[dcm] and JUMP-3[scd] measured at 77K. Open shapes denote desorption.

The N₂ isotherms of both materials are depicted in Fig. 6 while the relevant results are presented in Table 1. A comparison of both samples shows that drying with supercritical CO₂ was a more

FULL PAPER

efficient method of evacuating the pores when compared to solvent-exchange with dichloromethane.[61] This is seen in the higher sorption displayed in the case of the former. The BET surface area of JUMP-3scd was almost 2-fold higher than that of JUMP-3dcm, which is in line with the increased adsorption. This outcome confirms that activation via supercritical CO_2 is a milder method of evacuating pores of metal organic frameworks. This is due to its tendency to gently evacuate the mesopores without resulting in collapse of the essential micropores.[62] Since the operating conditions (temperature and pressure) are above the critical point, it is thought to prevent the occurrence of surface tension. By extension, capillary forces, which might then otherwise lead to deformation and pore collapse that would consequently occur upon solvent removal are likewise eliminated. This is supported by the *t*-plot analysis, which showed an increase in the micropore area (approximately two-fold, see Figs. S7 and S8 and Table S4). There was also a similar increase in the total pore volumes obtained for both samples. By comparison the observed pore volumes were estimated to be 18% and 33% of the calculated pore volume (0.67 $cm^3 \cdot g^{-1}$ calculated from the crystal structure of JUMP-3). The reduced access could be attributed to the presence of the isophthalic acid guest, which could probably not be easily removed through supercritical CO_2 drying.

The isotherms portrayed in Fig. 7 can be described as irreversible type II isotherms with H3 hysteresis loops suggesting the presence of a small contribution of slit-shaped mesopores in addition to the dominant micropores. There was also a slightly more pronounced loop in JUMP-3scd as compared with JUMP-3dcm.
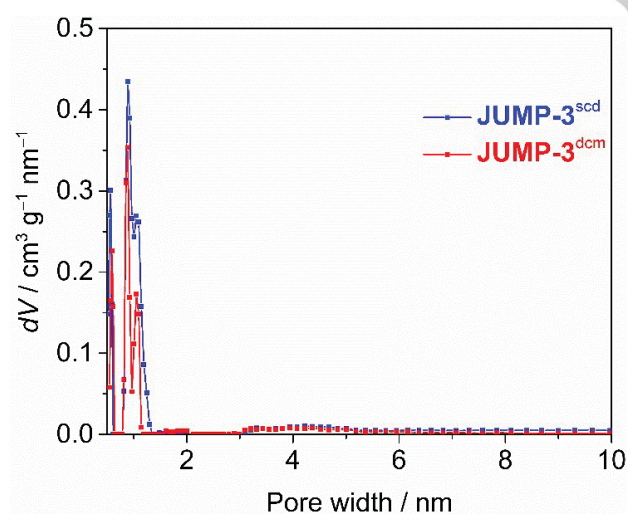

Figure 7: QSDFT calculated pore distribution data for JUMP-3dcm and JUMP-3scd, fitted using N_2 at 77 K on carbon (slit/cylindrical pores, QSDFT adsorption).

From the pore distribution curves obtained from fitting the isotherms using QSDFT kernels provided by Quantachrome Instruments,[63] the majority of the pores were concentrated in the micropore range (< 2 nm), which was in agreement with the results from the *t*-plot analysis. While both samples had the same modal pore sizes, there was apparently a larger population of these pores in JUMP-3scd as compared with its dichloromethane-treated analogue, JUMP-3dcm (see Fig. 7). This clearly confirms that increased access to the pores stemmed from the usage of the supercritical CO_2 treatment in the former as compared with in JUMP-3dcm.

Table 1. Parameters obtained from adsorption isotherms of JUMP-3dcm and JUMP-3scd

Compound	a(BET) $(m^2 \cdot g^{-1})$	Total Pore Vol. $(cm^3 \cdot g^{-1})$	Mean Pore Width (nm)	Modal Pore Width (nm)
JUMP-3dcm	213	0.12	0.9	2.3
JUMP-3scd	383	0.22	0.9	2.2

Conclusions

The new Co(II) MOF based on the nitrilotribenzoic acid ligand here reported was obtained by addition of isophthalic acid into the solvothermal reaction of the former with cobalt(II) chloride. As there was no inclusion of the isophthalic acid within the MOF structure, it was inferred to have suppressed the formation of dimethylammonium cation, which might have otherwise templated the formation of an anionic framework while simultaneously acting as a template for the neutral MOF. The role of isophthalic acid is thus proposed to be two-fold—pH modulation as well as structural templating. Topological analysis determined its underlying net to have a 3,6T80 topology with its trimeric clusters and the central nitrogen being reduced to nodes. It was conclusively shown *via* magnetic susceptibility data to display antiferromagnetic interactions between its Co(II) ions within the trimeric clusters. Additionally, sorption measurements after activation using supercritical CO_2 led to a two-fold increase in its surface area as compared to solvent exchange with dichloromethane. Inclusion of modulators such as in this case has also been shown to offer pathways to obtaining new materials while using already known reactants.

Experimental Section

Materials. Triphenylamine (Alfa Aesar) and cobalt(II) chloride hexahydrate (Aldrich) were obtained commercially and used without further purification. All other chemicals were of AR grade. The tribromotriphenylamine used was prepared from triphenylamine by

modifying an already reported procedure.[64] The final ligand 4,4',4''-nitrilotribenzoic acid (H₃ntb) was obtained in good yield following procedures already described in literature.[39, 65]

Analytical data for H₃ntb. ^{1}H NMR (400 MHz, [D₆]DMSO, 25°C, δ in ppm): 7.13 (d, 3JH,H = 8.7 Hz, 6H), 7.89 (d, 3JH,H = 8.7 Hz, 6H), 12.76 (s, 3H). ^{13}C NMR (100 MHz, [D₆]DMSO, 25°C, δ in ppm): 123.7, 125.9, 131.2, 149.8, 166.7. Selected IR (ATR, cm^{-1}): = 1672 s, 1591 s, 1509 m, 1417 s, 1314 s, 1275 vs, 1173 s, 1129 m, 932 m. EI-MS: m/z (%): 377 (100) [M+].

Physical Measurements. Simultaneous TG/DTA analyses were performed under static air atmosphere using a Netzsch STA Luxx PC analyzer up to 1000 °C. The FT-IR spectra were measured on a VERTEX 70 IR spectrometer by Bruker Optics using the Specac Diamond ATR optional accessory. Mass spectrometry was performed on a MAT SSQ710 mass spectrometer made by Bruker. NMR spectra were recorded with a Bruker AVANCE400 spectrometer. The elemental analyses were done on a VARIO EL III analyzer. The magnetic susceptibilities were measured on the bulk vacuum dried materials in the 2-300 K temperature range with a Quantum Design MPMS-5 superconducting SQUID magnetometer. The data were corrected for diamagnetic contributions. The N₂ physisorption isotherms were measured on an Autosorb-IQ instrument from Quantachrome Instruments Corporation. Solvothermal reactions were carried out in a 23 mL Teflon-lined acid digestion vessel from Parr Instruments, utilizing a programmable oven by Binder. Supercritical CO₂ drying was carried out in a steel autoclave with a 100 mL inner glass chamber by Carl Roth. Powder X-ray diffraction measurements were performed on a Stoe Powder Diffractometer with a Mythen 1K detector at room temperature. Measurements were done using capillary tubes while the Debye Scherrer Scan Mode was applied with a 2θ scan type. The X-ray tube was a Cu-long fine focus tube. The powdered samples were suspended in DMF in a 0.5 mm glass capillary and then measured. The measurement was carried out between 2 and 50° with steps of 2.1° per 20 seconds.

Synthesis

{[Co₉(ntb)₆(H₂O)₁₂]·xH₂O·yDMF·zH₂ip}ₙ: Isophthalic acid (H₂ip, 33 mg, 0.199 mmol) and H₃ntb (50 mg, 0.13 mmol) were dissolved and stirred in DMF (5 mL) for 15 min. Cobalt(II) chloride hexahydrate (0.13 g, 0.52 mmol, Aldrich) was then added and stirred until all solid was dissolved. The solution was placed in a Parr acid digestion vessel and heated at 130 °C for 72 h under autogenous pressure. It was then allowed to cool at a rate of 5 °C·h^{-1}. Violet crystals were later seen upon cooling, which were washed with DMF (5 × 2 mL).
Evacuation of the sample for four hours then followed this.
Yield: 43.2 mg, 56.4% based on ligand with x = 6, y = 3, and z = 1 (after drying under vacuum for four hours.) Drying for even longer periods leads to lower solvent content of the resulting material as corroborated through elemental analysis and TG measurements.
Elemental analysis for {[Co₉(ntb)₆(H₂O)₁₂]·6H₂O·3DMF·H₂ip}ₙ. Calcd (%) for C₁₄₆H₁₃₅Co₉N₉O₆₁ (3486.02 g·mol^{-1}): C 49.27, H 3.90, N 3.62; found: C 49.03, H 3.62, N 3.94. Selected IR (ATR, cm^{-1}): = 3396 br, 1657 s, 1594 s, 1559 s, 1505 w, 1383 vs, 1312 s, 1255 s, 1173 m, 1096 m, 1062 m.

X-ray Structure Determination. The intensity data for the compounds were collected on a Nonius KappaCCD diffractometer using graphite-monochromated Mo–Kα radiation. Data were corrected for Lorentz and polarization effects; absorption was taken into account on a semi-empirical basis using multiple-scans.[66-68]

The structure was solved by direct methods (SHELXS[69]) and refined by full-matrix least squares techniques against F_o^2.(SHELXL-97[69]) All hydrogen atoms were included at calculated positions with fixed thermal parameters. All non-disordered, non-hydrogen atoms were refined anisotropically.[69] Diamond 4.3 and Olex 1.2.7 were used for structure representations.[70-71] The crystal of JUMP-3 contain large voids, filled with disordered solvent molecules. The total size of the voids is 21525 Å^3/unit cell. Their contribution to the structure factors was secured by back-Fourier transformation using the SQUEEZE routine of the program PLATON[46] resulting in 10216 electrons/unit cell.

Nevertheless, the crystals of JUMP-3 were extremely thin and of low quality, resulting in a substandard data set; however, the structure is sufficient to show connectivity and geometry despite the high final R value. We will only publish the conformation of the molecule and the crystallographic data. We will not deposit the data in the Cambridge Crystallographic Data Centre.

Crystallographic and refinement parameters for JUMP-3.
Formula C₁₃₅H₉₃Co₉N₉O₅₁, M = 3187.55, Hexagonal $P\bar{3}c1$, a = 39.7934(6), b = 39.7934(6), c = 28.8035(6) Å, α,β = 90°, γ = 120° V = 39500.1(14) Å^3, T = 133 K, Z = 6, ρ_{calc} = 0.804 g·cm^{-3}, μ = 0.601 mm^{-1}, multi-scan, transmin: 0.6019, transmax: 0.7456, F(000) = 9702[*], 170590 reflections in h(−51/51), k(−51/51), l(−37/37), measured in the range 1.02° ≤ 2Θ ≤ 27.57°, completeness Θ$_{max}$ = 99%, 29872 independent reflections, R_{int} = 0.1195, 16481 reflections with F_o > 4σ(F_o), 863 parameters, 0 restraints, R_{1obs} = 0.1226, wR_{2obs} = 0.3397, $R_{1(all)}$ = 0.1747, $wR_{2(all)}$ = 0.3826, GOOF = 1.313, largest difference peak and hole: 2.584 / −1.218 e Å^{-3}. [*] derived parameters do not contain the contribution of the disordered solvent.

Sample pre-treatment and sorption measurements
Activation with dichloromethane. Activation was performed by solvent exchange with dichloromethane. This was done by immersing the sample (≈50 mg) in dichloromethane (10 mL) for three days. During this period, the solvent was refreshed every 24 h. The supernatant solvent was then removed and the ensuing slurry dried in air. The final resulting air-dried sample was denoted JUMP-3^{dcm} (where the superscript dcm connotes activation by exchange with dichloromethane).

Activation with supercritical CO₂. In an alternative procedure, the sample was pretreated by activating with supercritical CO₂. This was carried out by soaking the as-synthesized JUMP-3 (≈50 mg) in ethanol (10 mL) for three days, during which the ethanol was changed every 24 h by decanting the solvent. Subsequently this was followed by drying with supercritical CO₂. For this procedure, the ethanol-immersed samples were decanted followed by carefully transferring the resultant slurry into an autoclave (100 mL volume) and then sealed. Liquid CO₂ was then introduced into the autoclave (final pressure of 60 bar) and allowed to stand 30 min. The CO₂ was then slowly released from the autoclave over a period of 20 min to remove any likely non-occluded ethanol from the materials. A second batch of liquid CO₂ was introduced into the reactor (again 60 bar) but this time allowed to stand for 24 h. The temperature of the autoclave was then raised to 40 °C to bring the CO₂ to supercritical conditions and maintained for one hour at this temperature. The CO₂ was then slowly released over 30 min with the temperature maintained at 40 °C to prevent any cooling that might result from expansion of the gas during evaporation. The resulting supercritical CO₂ dried sample was denoted JUMP-3^{scd} (where the superscript scd translates to activation by drying with supercritical CO₂).

FULL PAPER

Acknowledgements

References

[1] J.-R. Li, J. Sculley, H.-C. Zhou, *Chem. Rev.* **2012**, *112*, 869-932.

[2] M. P. Suh, H. J. Park, T. K. Prasad, D.-W. Lim, *Chem. Rev.* **2012**, *112*, 782–835.

[3] K. Sumida, D. L. Rogow, J. A. Mason, T. M. McDonald, E. D. Bloch, Z. R. Herm, T.-H. Bae, J. R. Long, *Chem. Rev.* **2012**, *112*, 724–781.

[4] J.-R. Li, Y. Ma, M. C. McCarthy, J. Sculley, J. Yu, H.-K. Jeong, P. B. Balbuena, H.-C. Zhou, *Coord. Chem. Rev.* **2011**, *255*, 1791–1823.

[5] L. E. Kreno, K. Leong, O. K. Farha, M. Allendorf, R. P. van Duyne, J. T. Hupp, *Chem. Rev.* **2012**, *112*, 1105–1125.

[6] Z. Hu, B. J. Deibert, J. Li, *Chem. Soc. Rev.* **2014**, *43*, 5815–5840.

[7] J. Wang, C. He, P. Wu, J. Wang, C. Duan, *J. Am. Chem. Soc.* **2011**, *133*, 12402–12405.

[8] A. Sachse, R. Ameloot, B. Coq, F. Fajula, B. Coasne, D. D. Vos, A. Galarneau, *Chem. Commun.* **2012**, *48*, 4749–4751.

[9] M. Yoon, R. Srirambalaji, K. Kim, *Chem. Rev.* **2012**, *112*, 1196–1231.

[10] J. M. Roberts, B. M. Fini, A. A. Sarjeant, O. K. Farha, J. T. Hupp, K. A. Scheidt, *J. Am. Chem. Soc.* **2012**, *134*, 3334–3337.

[11] C.-Y. Sun, C. Qin, C.-G. Wang, Z.-M. Su, S. Wang, X.-L. Wang, G.-S. Yang, K.-Z. Shao, Y.-Q. Lan, E.-B. Wang, *Adv. Mater.* **2011**, *23*, 5629–5632.

[12] J.-S. Qin, D.-Y. Du, W.-L. Li, J.-P. Zhang, S.-L. Li, Z.-M. Su, X.-L. Wang, Q. Xu, K.-Z. Shao, Y.-Q. Lan, *Chem. Sci.* **2012**, *3*, 2114–2118.

[13] J. D. Rocca, W. Lin, *Eur. J. Inorg. Chem.* **2010**, 3725–3734.

[14] B. Chen, S. Ma, F. Zapata, F. R. Fronczek, E. B. Lobkovsky, H.-C. Zhou, *Inorg. Chem.* **2007**, *46*, 1233–1236.

[15] Y.-Q. Lan, H.-L. Jiang, S.-L. Li, Q. Xu, *Adv. Mater.* **2011**, *23*, 5015–5020.

[16] L. Ma, J. M. Falkowski, C. Abney, W. Lin, *Nat. Chem.* **2010**, *2*, 838–846.

[17] O. M. Yaghi, M. O'Keeffe, N. W. Ockwig, H. K. Chae, M. Eddaoudi, J. Kim, *Nature* **2003**, *423*, 705-714.

[18] M. O'Keeffe, O. M. Yaghi, *Chem. Rev.* **2012**, *112*, 675–702.

[19] E. V. Alexandrov, V. A. Blatov, A. V. Kochetkov, D. M. Proserpio, *CrystEngComm* **2011**, *13*, 3947-3958.

[20] X.-N. Cheng, W. Xue, X.-M. Chen, *Eur. J. Inorg. Chem.* **2010**, 3850–3855.

[21] J. Hong, M. Cheng, Q. Liu, W. Han, Y. Zhang, Y. Ji, X. Jia, Z. Li, *Transition Met. Chem.* **2013**, *38*, 385–392.

[22] H.-P. Jia, W. Li, Z.-F. Ju, J. Zhang, *Eur. J. Inorg. Chem.* **2006**, *2006*, 4264–4270.

[23] O. Fabelo, J. Pasán, L. Canãadillas-Delgado, F. S. Delgado, F. Lloret, M. Julve, C. Ruiz-Pérez, *Inorg. Chem.* **2009**, *48*, 6086–6095.

[24] A. D. Burrows, K. Cassar, R. M. W. Friend, M. F. Mahon, S. P. Rigby, J. E. Warren, *CrystEngComm* **2005**, *7*, 548–550.

[25] X.-R. Hao, X.-L. Wang, K.-Z. Shao, G.-S. Yang, Z.-M. Su, G. Yuan, *CrystEngComm* **2012**, *14*, 5596-5603.

[26] Y.-F. Niu, L.-T. Cui, J. Han, X.-L. Zhao, *J. Solid State Chem.* **2016**, *241*, 18-25.

[27] Z. Zhang, M. J. Zaworotko, *Chem. Soc. Rev.* **2014**, *43*, 5444-5455.

[28] B. Seoane, A. Dikhtiarenko, A. Mayoral, C. Tellez, J. Coronas, F. Kapteijn, J. Gascon, *CrystEngComm* **2015**, *17*, 1693-1700.

[29] S. R. Bajpe, C. E. A. Kirschhock, A. Aerts, E. Breynaert, G. Absillis, T. N. Parac-Vogt, L. Giebeler, J. A. Martens, *Chem. Eur. J.* **2010**, *16*, 3926-3932.

[30] Z. Zhang, L. Zhang, L. Wojtas, P. Nugent, M. Eddaoudi, M. J. Zaworotko, *J. Am. Chem. Soc.* **2012**, *134*, 924-927.

[31] X.-J. Wang, P.-Z. Li, Y. Chen, Q. Zhang, H. Zhang, X. X. Chan, R. Ganguly, Y. Li, J. Jiang, Y. Zhao, *Sci. Rep.* **2013**, *3*, 1–5.

[32] H. Guo, Y. Zhu, S. Wang, S. Su, L. Zhou, H. Zhang, *Chem. Mater.* **2012**, *24*, 444–450.

[33] P.-Z. Li, X.-J. Wang, Y. Li, Q. Zhang, R. H. D. Tan, W. Q. Lim, R. Ganguly, Y. Zhao, *Microporous Mesoporous Mater.* **2013**, *176*, 194–198.

[34] G. C. Shearer, S. Chavan, S. Bordiga, S. Svelle, U. Olsbye, K. P. Lillerud, *Chem. Mater.* **2016**, *28*, 3749--3761.

[35] C. C. Epley, M. D. Love, A. J. Morris, *Inorg. Chem.* **2017**, *56*, 13777--13784.

[36] Vera V. Butova, Andriy P. Budnyk, Alexander A. Guda, Kirill A. Lomachenko, Aram L. Bugaev, Alexander V. Soldatov, Sachin M. Chavan, Sigurd Øien-Ødegaard, Unni Olsbye, Karl Petter Lillerud, Cesare Atzori, Silvia Bordiga, C. Lamberti, *Cryst. Growth Des.* **2017**, *177*, 5422--5431.

[37] A. Schaate, P. Roy, A. Godt, J. Lippke, F. Waltz, M. Wiebcke, P. Behrens, *Chem. Eur. J.* **2011**, *17*, 6643--6651.

[38] Takaaki Tsuruoka, Shuhei Furukawa, Yohei Takashima, Kaname Yoshida, Seiji Isoda, S. Kitagawa, *Angew. Chem. Int. Ed.* **2009**, *48*, 4739--4743.

[39] C. Livage, N. Guillou, A. Castiglione, J. Marrot, M. Frigoli, F. Millange, *Microporous Mesoporous Mater.* **2012**, *157*, 37–41.

[40] O. Akintola, D. Hornig, A. Buchholz, H. Görls, W. Plass, *Dalton Trans.* **2017**, *46*, 8037–8050.

[41] J. Zhang, R. Liu, P. Feng, X. Bu, *Angew. Chem. Int. Ed.* **2007**, *46*, 8388–8391.

[42] X.-R. Hao, X.-L. Wang, Z.-M. Su, K.-Z. Shao, Y.-H. Zhao, Y.-Q. Lana, Y.-M. Fu, *Dalton Trans.* **2009**, 8562–8566.

[43] Z. Chen, X. Liu, C. Zhang, Z. Zhang, F. Liang, *Dalton Trans.* **2011**, *40*, 1911-1918.

[44] T.-F. Liu, J. Lü, C. Tian, M. Cao, Z. Lin, R. Cao, *Inorg. Chem.* **2011**, *50*, 2264-2271.

[45] Z. Su, Z. Song, Z.-S. Bai, J. Fan, G.-X. Liu, W.-Y. Sun, *CrystEngComm* **2010**, *12*, 4339-4346.

[46] A. L. Spek, *Acta Crystallogr* **2009**, *D65*, 148–155.

[47] V. A. Blatov, A. P. Shevchenko, D. M. Proserpio, *Cryst. Growth Des.* **2014**, *14*, 3576–3586.

[48] O. Kahn, *Molecular Magnetism*, Wiley-VCH Inc., Weinheim, **1993**.

[49] F. E. Mabbs, D. J. Machin, *Magnetism and Transition Metal Complexes*, Springer US, **1973**.

[50] L.-F. Ma, Y.-Y. Wang, L.-Y. Wang, D.-H. Lu, S. R. Batten, J.-G. Wang, *Cryst. Growth Des.* **2009**, *9*, 2036–2038.

[51] J. Cao, K.-X. Shang, W.-T. Deng, J.-C. Liu, *Inorg. Chem. Commun.* **2013**, *29*, 183–186.

[52] L. Guan, Y.-H. Zhou, H. Zhang, *Inorg. Chem. Commun.* **2010**, *13*, 737–740.

[53] N. F. Chilton, R. P. Anderson, L. D. Turner, A. Soncini, K. S. Murray, *J. Comput. Chem.* **2013**, *34*, 1164–1175.

[54] S.-J. Liu, L. Xue, T.-L. Hu, X.-H. Bu, *Dalton Trans.* **2012**, *41*, 6813–6819.

[55] T.-F. Liu, H.-L. Sun, S. Gao, S.-W. Zhang, T.-C. Lau, *Inorg. Chem.* **2003**, *42*, 4792–4794.

[56] Y. Liu, H. Li, Y. Han, X. Lv, H. Hou, Y. Fan, *Cryst. Growth Des.* **2012**, *12*, 3505–3513.

[57] M.-H. Zeng, X.-L. Feng, W.-X. Zhang, X.-M. Chen, *Dalton Trans.* **2006**, 5294–5303.

[58] H.-H. Zou, Y.-P. He, L.-C. Gui, F.-P. Liang, *CrystEngComm* **2011**, *13*, 3325-3329.

[59] X.-Y. Wang, L. Gan, S.-W. Zhang, S. Gao, *Inorg. Chem.* **2004**, *43*, 4615–4625.

[60] M.-X. Yao, M.-H. Zeng, H.-H. Zou, Y.-L. Zhou, H. Liang, *Dalton Trans.* **2008**, 2428–2432.

[61] O. Akintola, S. Ziegenbalg, A. Buchholz, H. Görls, W. Plass, *CrystEngComm* **2017**, *19*, 2723–2732.

[62] A. P. Nelson, O. K. Farha, K. L. Mulfort, J. T. Hupp., *J. Am. Chem. Soc.* **2009**, *131*, 458–460.

[63] QUANTACHROME, Odelzhausen.

[64] X. Cao, Y. Wen, Y. Guo, G. Yu, Y. Liu, L.-M. Yang, *Dyes Pigm* **2010**, *84*, 203–207.

[65] S. Dapperheld, E. Steckhan, K.-H. G. Brinkhaus, T. Esch, *Chem. Ber.* **1991**, *124*, 2557–2567.

[66] B. V. Nonius, Delft, The Netherlands, **1998**.

[67] Z. Otwinowski, W. Minor, *Vol. 276* (Eds.: C. W. Carter, R. M. Sweet), Academic Press, **1997**, pp. 307–326.

[68] Bruker-AXS inc., Madison, WI, U.S.A, **2002**.

[69] G. M. Sheldrick, *Acta Crystallogr* **2008**, *A64*, 112–122.

[70] H. Putz, K. Brandenburg, Kreuzherrenstr. 102, 53227 Bonn, Germany, **2016**.

[71] O. B. Dolomanov, L.; Gildea, R.; Howard, J. & Puschmann, H., *J. Appl. Cryst.* **2009**, *42*, 339-341.

[72] J. Rouquerol, P. Llewellyn, F. Rouquerol, *Stud. Surf. Sci. Catal.* **2007**, *160*, 49–56.

Supplementary Information for: Isophthalic acid modulated of a neutral Co(II) nitrilotribenzoic acid MOF: Synthesis, magnetic and sorption properties

Oluseun Akintola, Axel Buchholz, Helmar Görls, Winfried Plass*

1 Additional toplogical information for 1
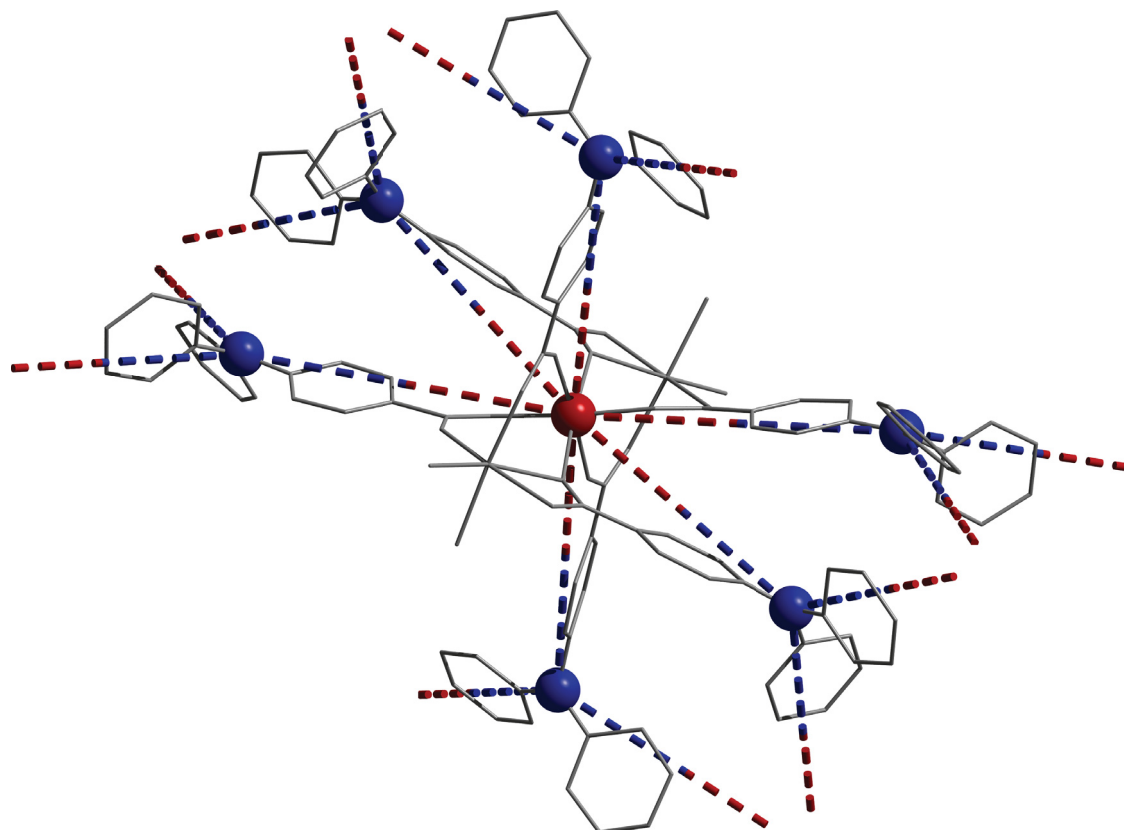

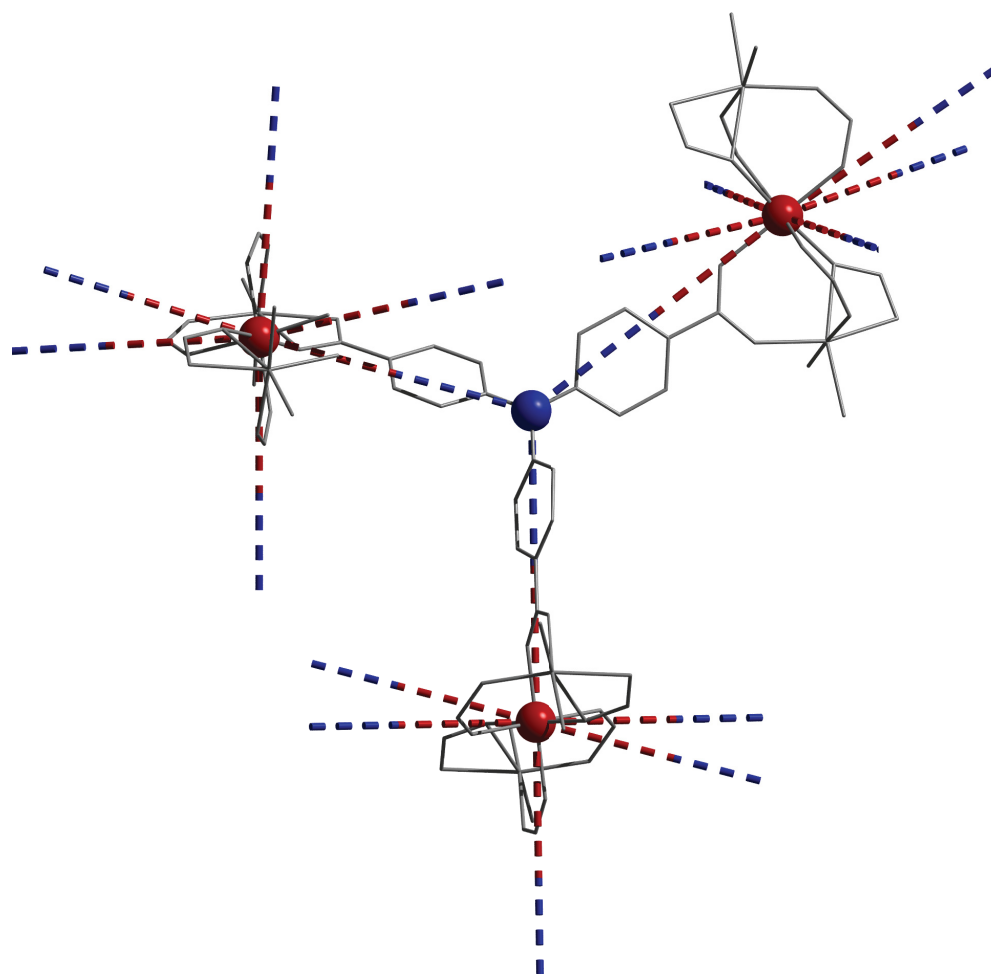**Fig. S1:** Six-connected node found in **1** overlaid over structure. Actual atoms have been grayed out for clarity.

Fig. S2: Three-connected node found in **1** overlaid over structure. Actual atoms have been grayed out for clarity.

Table S1: Coordination sequences for **1** (topological density $TD_{10} = 1192$)

Vertex	CS_1	CS_1	CS_1	CS_1	CS_1	CS_1	CS_1	CS_1	CS_1	CS_1
V1	3	13	16	52	45	134	103	257	171	418
V2	6	8	32	30	90	76	206	140	342	218

Table S2: Vertex symbols obtained from topological analysis of **1**

Vertex	Vertex symbol	Extended Point Symbol
V1	$[4^2.6]$	$[4.4.6]$
V2	$[4^4.6^2.8^8.10]$	$[4.4.4.4.6.6.8_2.8_3.8_3.8_4.8_7.8_7.8_7.8_7.10_{14}]$

2 Tiling of 1

Fig. S3: Tiling of **1** viewed along [001]. Tiles: $3[4^2.8^{2\cdot}]+3[4.8^3]+[4^3.8^{3\cdot}.12^2]$. Transitivity: [2353].

3 Powder diffraction data for 1
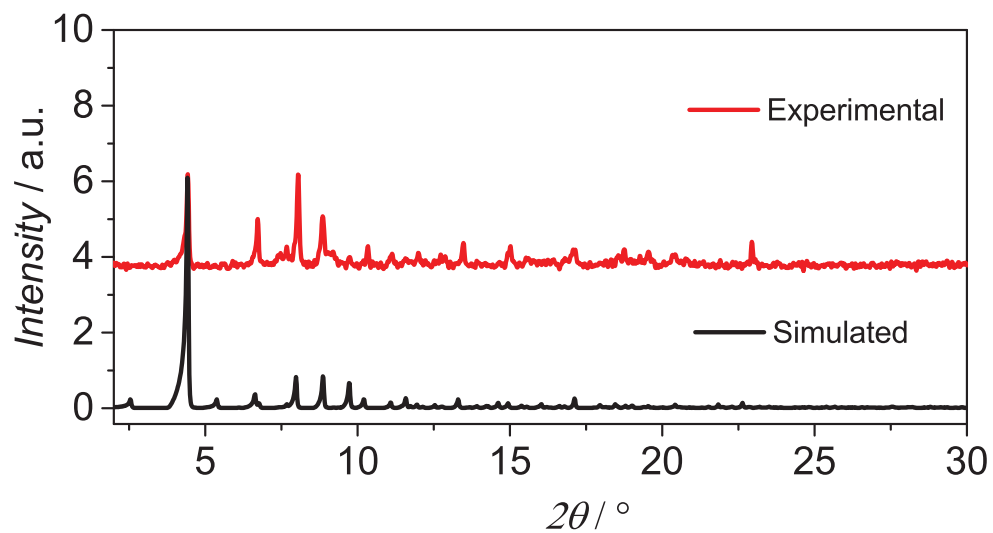
Fig. S4: XRD pattern for **1**; simulated pattern below and experimental pattern above.

4 Thermo-analytical data for 1
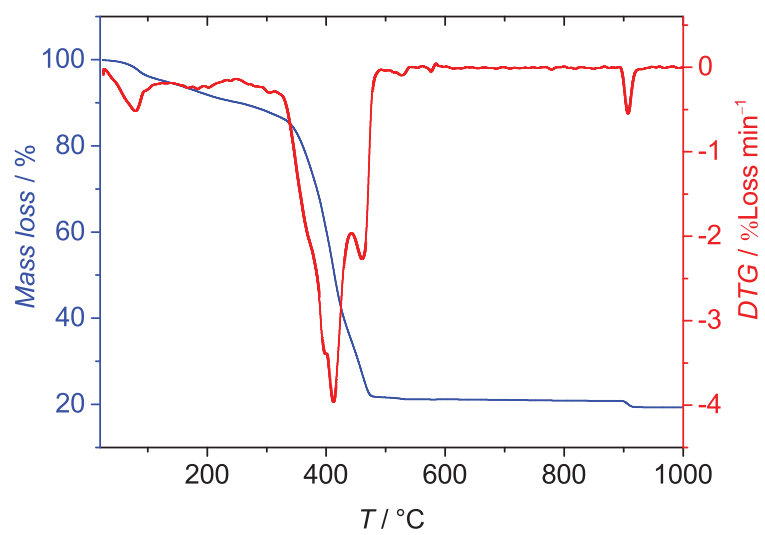
Fig. S5: Thermo-analytical profile for **1** carried out in air.

Magnetic Data for 1
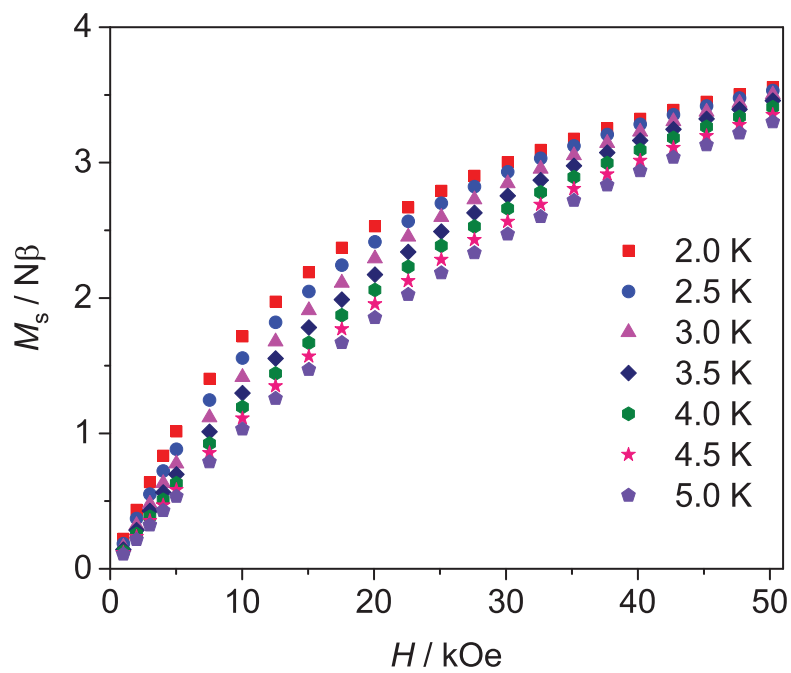
Fig. S6: Field-dependent magnetization for **1**.

5 Additional Sorption data

Table S3: Consistency criteria and other sorption parameters extracted from N_2-isotherms of 1^{dcm} and 1^{scd}

	P/P_o range	C	V_m $(cm^3 g^{-1})$	$1/\sqrt{C}+1$	$P/P_o(V_m)$	BET Area $(m^2 g^{-1})$	R
1^{dcm}	0.003-0.05	1268	48.9	0.027	0.024	213	0.999
1^{scd}	0.001-0.05	913	88.1	0.032	0.032	384	0.999

Table S4: Thickness method summary for sorption data of 1^{dcm} and 1^{scd}

	Intercept	BET Area $(m^2 g^{-1})$	External Area $(m^2 g^{-1})$	Micropore Area $(m^2 g^{-1})$	Micropore Vol $(cm^3 g^{-1})$	Total Vol $(cm^3 g^{-1})$
1^{dcm}	37.699	213	65	148	0.06	0.12
1^{scd}	71.421	383	99	284	0.11	0.22
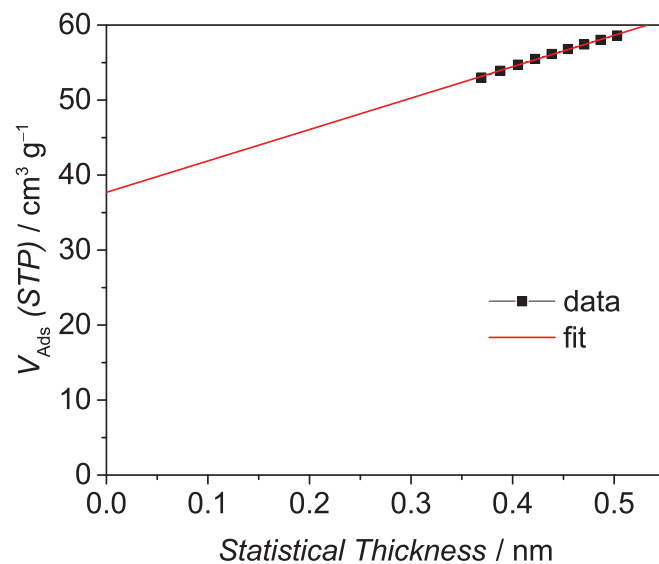
Fig. S7: T-plot for $\mathbf{1}^{dcm}$ calculated by DeBoer method.
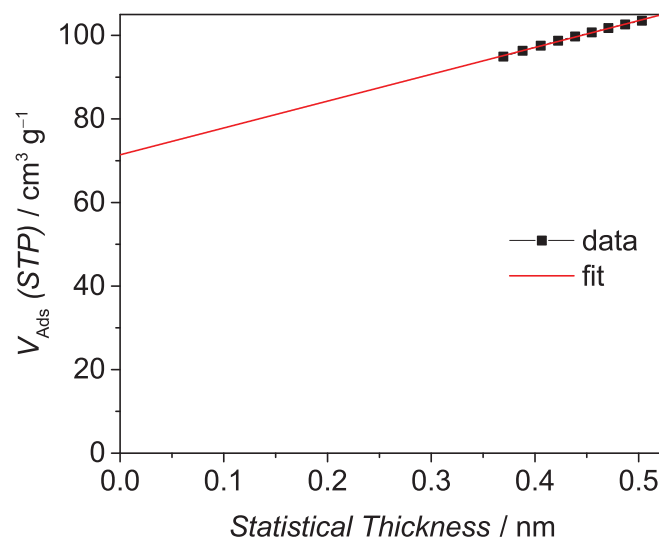
Fig. S8: T-plot for $\mathbf{1}^{scd}$ calculated by DeBoer method.

Publication 5

Facile synthesis of highly thermally stable nanoporous γ-aluminas from aluminum alkoxide precursors

Gholamhossein Mohammadnezhad, Oluseun Akintola, Winfried Plass, Felix H. Schacher, Frank Steiniger, Martin Westermann *RSC Adv.* **2015** *5* 49493–49500
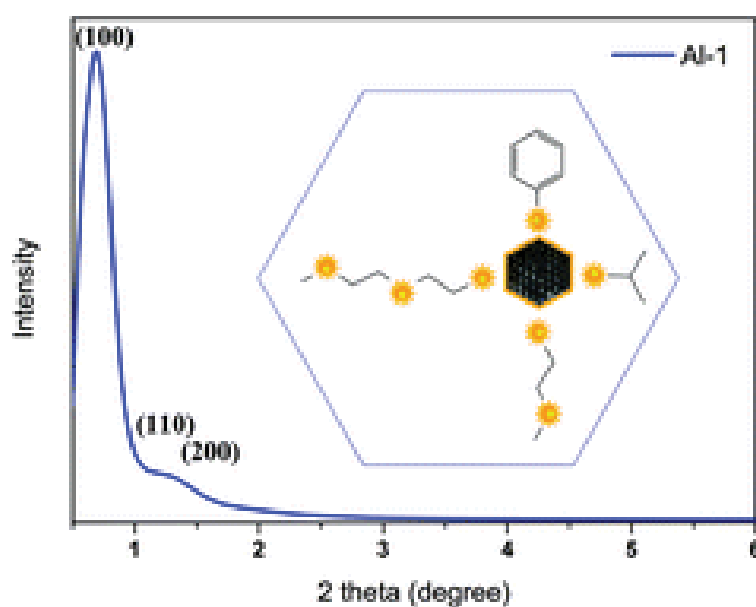
Facile synthesis of highly thermally stable nanoporous γ-aluminas from aluminum alkoxide precursors†

Gholamhossein Mohammadnezhad,*[a] Oluseun Akintola,[b] Winfried Plass,[b] Felix H. Schacher,[cd] Frank Steiniger[e] and Martin Westermann[e]

The effects of aluminum alkoxide single source precursors on the sol–gel synthesis of highly thermally stable nanostructured alumina by nonionic triblock copolymer P123 were investigated. Different crystalline nanoporous alumina materials with large single or bimodal accessible pores were synthesized *via* an efficient single-step process starting from alkoxide precursors utilizing the evaporation-induced self-assembly (EISA) method. The effect of different types of organic groups within the molecular aluminum precursor were explored by variation from iso-propoxide (O^{i}Pr), as an alkoxy group, over phenoxide (OPh), as an aryloxy group, to the presence of ether functions within the alkoxy chains, represented by methoxyethoxide (OCH$_2$CH$_2$OCH$_3$) and methoxyethoxyethoxide (OCH$_2$CH$_2$OCH$_2$CH$_2$OCH$_3$) groups. The prepared samples were characterized by small and wide angle X-ray diffraction, N$_2$ adsorption–desorption, TGA-DTA, and TEM measurements. For the prepared aluminas porosity, surface area, and excellent thermal stability, as well as an adjustable pore size distribution were found which make them suitable for potential application in different processes where single or bimodal accessible pores are necessary.

1. Introduction

Synthesis of functional inorganic materials such as metal oxides with tunable properties has been considered as a challenging issue for both academic and industrial researchers.[1–6] Among these materials aluminum oxides are one of the most important class of compounds which have found a wide range of applications in industrial catalysts, catalyst supports, adsorbents, optics, electronics, or biomedicine.[7–12] Enhancement of the characteristics of these materials such as surface area, particle size, pore size, pore volume, morphology, and dimensionality continues to attract a considerable amount of interest.[13–19] Since the first report of well-ordered periodically organized mesoporous silica in 1992,[20] with outstanding characteristics such as high specific surface area, uniform pore channels, tunable pore size, narrow pore size distribution, and others, the synthesis of different porous materials has become an exciting area of materials chemistry.

Mesoporous aluminas (MAs) have been synthesized by different structural directing agents such as cationic and anionic surfactants,[21,22] and different block copolymers.[23,24] However, thermal stability of these materials and preservation of mesoporous structure upon calcination and processing is of great importance. Since the use of polymeric templates, such as non-ionic triblock copolymers as soft template, large efforts have been devoted to the synthesis of ordered mesoporous aluminas.[25] These types of polymeric templates are striking due to their availability, low price and biodegradability and specifically for their ability to induce the formation of uniform and large pores. Different approaches have been reported for the synthesis of ordered mesoporous aluminas. Early results from the usage of block copolymers resulted in amorphous,[26] disordered,[23] worm-like[27] or disk-shaped mesostructures.[28] However, there have been a few drawbacks such as the complicated hydrolysis behavior, the need to maintain strict control of synthetic conditions, in addition to the time consuming procedures. A remarkable step forward in the synthesis of ordered mesoporous γ-aluminas with high thermal stability has been achieved through the solvent evaporation induced self-assembly (EISA) of P123 triblock copolymer ([(EO)$_{20}$(PO)$_{70}$(EO)$_{20}$]) and aluminum precursors (Al(O^{i}Pr)$_3$, Al(O^{s}Bu)$_3$ or

[a]Department of Chemistry, Isfahan University of Technology, Isfahan 84156-83111, Iran. E-mail: mohammadnezhad@cc.iut.ac.ir; g_m1358@yahoo.com; Tel: +98-31-33913279. Fax: +98-31-33912350

[b]Institute of Inorganic and Analytical Chemistry, Chair of Inorganic Chemistry II, Friedrich Schiller University Jena, Humboldtstr. 8, 07743 Jena, Germany

[c]Institute of Organic Chemistry and Macromolecular Chemistry, Friedrich-Schiller-University Jena, Humboldtstraße 10, 07743 Jena, Germany

[d]Jena Center for Soft Matter (JCSM), Friedrich Schiller University Jena, Philosophenweg 7, 07743 Jena, Germany

[e]Electron Microscopy Center, Jena University Hospital, Ziegelmühlenweg 1, 07743 Jena, Germany

† Electronic supplementary information (ESI) available. See DOI: 10.1039/c5ra05883j

Al(NO$_3$)$_3$) based on a simple and reproducible sol–gel process in ethanol.[29] Thereafter, other metal precursors such as aluminum chloride,[30] aluminum nitrate[30,31] and bohemite[32] with different additives were used based on this procedure for preparation of MAs. The role of acid concentration in the synthesis medium on MAs has also been explored.[33] The physicochemical properties of alumina are highly dependent on the source of aluminum precursors.[34] Aluminum alkoxides are some of the most frequent precursors which have been used for synthesis of aluminas.[35] Moreover, the rate of hydrolysis and condensation of aluminum alkoxides strongly depend on the types of alkoxides groups and consequently the coordination environment of the aluminum centers.[36]

There remains a great interest to explore different parameters in the synthesis of MAs for desired materials. To the best of our knowledge, the effect of utilizing various aluminum alkoxides as precursors in preparation of MAs employing the EISA method in presence of non-ionic polymeric templates has not been explored. Herein, to study the influence of various suitable alkoxides, including O^{i}Pr, OPh, OEtOMe, and OEtOEtOMe, on the structure, morphology, and physicochemical properties of MAs we prepared a series of highly thermally stable nanoporous alumina with tunable pore size and volume as well as crystallinity.

2. Experimental

2.1. Chemicals

Triblock copolymer Pluronic P-123 (average $M_n \sim$ 5800, (EO)$_{20}$(PO)$_{70}$(EO)$_{20}$) was purchased from Aldrich Chemical Inc. Ethanol, iso-propanol, phenol, 2-methoxyethanol, and 2-(2-methoxyethoxy)ethanol were obtained from Merck. HNO$_3$ (65 wt%) was purchased from Carl Roth GmbH. & Co. KG. Aluminum iso-propoxide, and aluminum phenoxide were synthesized from aluminum foil and related alcohol based on the reported procedures.[37,38] Aluminum 2-methoxyehoxide, [Al(OCH$_2$CH$_2$OCH$_3$)$_3$], and aluminum 2-methoxyethoxyethoxide, [Al(OCH$_2$CH$_2$OCH$_2$CH$_2$OCH$_3$)$_3$] were prepared by alcohol exchange method from aluminum iso-propoxide in toluene.[34] Ethanol was dried over sodium and distilled before use under inert atmosphere.

2.2. Synthesis

The Aluminas were synthesized based on the modified procedure reported by Yuan et al.[29] The triblock copolymer Pluronic P-123 (2.00 g) was dissolved in dried ethanol (20.0 mL) at ambient temperature and allowed to stir for 4 h. To this clear solution were added the aluminum alkoxide (0.02 mol) followed by dried ethanol (20.0 mL) and nitric acid (3.4 mL). The resulting solution was stirred for 5 h at room temperature. Subsequently the solvent evaporation process was performed at 60 °C in a convection oven for 72 h. Samples 2 and 4 were further dried at 150 °C for 2 h. Calcination was performed at a heating rate of 1 °C min^{-1} starting from room temperature and kept at 400 or 900 °C for 4 h.

2.3. Characterization

X-ray powder diffraction patterns were collected at room temperature with a Siemens D5000 (Cu-K$_\alpha$, germanium monochromator). Small angle X-ray scattering (SAXS) measurements were performed on a Bruker AXS Nanostar (Bruker, Karlsruhe, Germany), equipped with a microfocus X-ray source (Incoatec ImSCu E025, Incoatec, Geesthacht, Germany), operating at $\lambda = 1.54$ Å. A pinhole setup with 750 mm, 400 mm, and 1000 mm (in the order from source to sample) was used and the sample-to-detector distance was 27 cm. Samples were mounted on a metal rack and fixed using tape. The N$_2$ adsorption and desorption isotherms were measured using a Quantachrome Autosorb-iQ-MP gas sorption analyzer. Thermogravimetric analysis (TGA) and Differential thermal analysis (DTA) were performed with a NETZSCH STA409PC Luxx apparatus under constant flow of air ranging from room temperature up to 1000 °C with a heating rate of 1 K min^{-1}.

For transmission electron microscopy (TEM), for each sample, 20 mg of aluminum oxide were added to 100 μL of absolute ethanol and sonicated at 37 kHz and 240 W for 20 min. After 10 min of sedimentation a drop of 6 μL supernatant was placed on top of a carbon-coated 400 mesh copper grid (Quantifoil Micro Tools, Jena, Germany). Excess liquid was removed by placing a sheet of filter paper below the grid. The samples were then air dried and analyzed using a CM120 electron microscope (Philips, Eindhoven, Netherlands) operated at 120 kV. Images were acquired using a 2k TemCam F216 CMOS camera (camera and software, TVIPS, Munich, Germany). For scanning electron microscopy (SEM) the 400 mesh copper grids previously prepared for the TEM analyses were sputter coated with platinum (2 nm) in a BAL-TEC SCD005 Sputter Coater (BAL-TEC, Liechtenstein) and imaged in a LEO 1530 Gemini field emission scanning electron microscope (Carl Zeiss, Oberkochen, Germany) at 4 kV acceleration voltage and a working distance of 3 mm using an inlense secondary electron detector.

3. Results and discussion

Four different aluminum alkoxide precursors Al(O^{i}Pr)$_3$, Al(OPh)$_3$, [Al(OCH$_2$CH$_2$OCH$_3$)$_3$], and [Al(OCH$_2$CH$_2$OCH$_2$CH$_2$-OCH$_3$)$_3$] have been utilized as molecular precursors for the synthesis of aluminum oxides by evaporation-induced self-assembly in the presence of P123 triblock copolymer. In order to investigate the role of the polymeric template two additional experiments were performed under similar conditions but in absence of template. The effect of four different functional groups in the aluminum precursors have been explored. This includes the iso-propoxide (O^{i}Pr) as an alkoxy group, phenoxide (OPh) as an aryloxy group, and the presence of ether functions on the alkoxy chains, such as methoxyethoxide (OCH$_2$CH$_2$-OCH$_3$) and methoxyethoxyethoxide (OCH$_2$CH$_2$OCH$_2$CH$_2$OCH$_3$), which provide additional donor sites and are therefore expected to lead to decreasing rates of hydrolysis.

The synthetic conditions under which the aluminas were prepared using different molecular precursors are summarized in Table 1. Small angle X-ray scattering (SAXS) measurements

were performed to check for the evidence of the formation of mesopores. The SAXS pattern of sample Al-1 calcined at 400 °C is depicted in Fig. 1. It shows a strong reflex (100) at 0.7° and, in addition, a weak reflex at around 1.2°. The SAXS patterns of the other three samples calcined at 400 °C are depicted in Fig. 2. In these samples the main diffraction reflexes (100) are around 0.6°, which is an indication for meso-structure of these samples, but no long range order was observed. For sample Al-1 the highest intensity for peak (100) is observed while for Al-2 the lowest intensity is observed within the series of template assisted materials (Al-1 to Al-4), which indicates that alkyl or alkylether groups have a better effect on the porosity of the final product. In the presence of alkylether and aryl groups the main diffraction peak (100) is shifted towards lower angles, as can be seen from Fig. 1 and 2. This observation could be related to synergetic effects of released organic molecules, such as ether functionalized alcohols or phenol after hydrolysis of the corresponding alkoxides, with the presence of block copolymer template which results in different pores.

For most of the reported cases considerable drawbacks are observed, as the prepared MAs possess amorphous walls or involve inconvenient multistep synthetic procedures. Consistently the wide-angle XRD measurements of all samples calcined at 400 °C show the occurrence of amorphous structures. The TGA-DTA data of the samples exhibit an exothermic peak at about 860 °C without any weight loss which is due to the crystallization of amorphous alumina. Therefore, all samples have also been calcined at 900 °C. The conservation of the mesoscopic order of Al-1 after calcination at 800–1000 °C has been proved previously,[29] whereas for samples Al-2 to Al-4 the thermal stability of the mesoscopic structure for calcination at 900 °C is indicated by the SAXS measurements depicted in Fig. 3. The wide-angle XRD patterns for the samples Al-1 to Al-4 are depicted in Fig. 4. In all the cases, except for Al-2, calcination at 900 °C results in conversion of amorphous walls to γ-alumina as crystalline phase (JCPDS card no. 10-0425). These results show that in the presence of aliphatic or aliphatic-ether groups, the only observed phase is γ-alumina. However, for Al-2 a different behavior is observed, as in addition to the γ-alumina also sharp and distinct peaks of α-alumina are observed (JCPDS card no. 46-1212). The collective results from SAXS and WAXS (wide angle X-ray scattering) measurements confirm the presence of crystalline mesoporous structures for the samples calcined at 900 °C.

Fig. 5 shows nitrogen adsorption–desorption isotherms of Al-1 to Al-4 treated at 400 °C and 900 °C (for Al-5 and Al-6 see
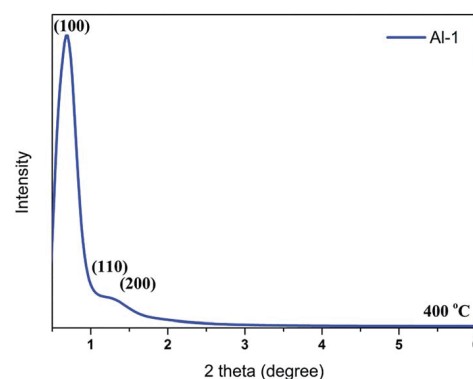

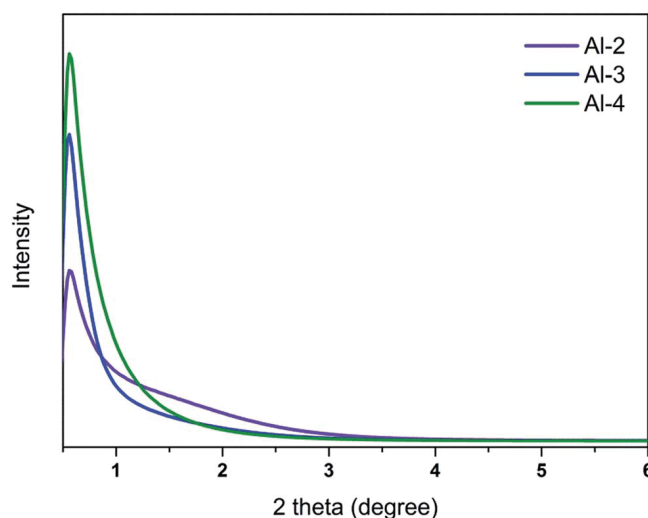Fig. 1 SAXS pattern of Al-1 calcined at 400 °C.

Fig. 2 SAXS patterns of Al-2, Al-3, and Al-4 calcined at 400 °C.

Fig. S1 and S2†). According to IUPAC classification six types of sorption isotherms are possible.[39] All samples, except Al-2 calcined at 400 °C, exhibit type IV isotherms. In fact, the observed isotherm for Al-2 can be regarded as a combination of type I and IV isotherms. The observed type IV isotherms are typical for mesoporous materials. The most characteristic feature of this type of isotherm is the hysteresis loop, which often accompanies the occurrence of pore condensation. The limiting uptake in a range of high $P/P°$ leads to a plateau in the isotherm, which is indicative of complete pore filling. The first part of this type of isotherms can be attributing to monolayer–multilayer adsorption. It has been widely accepted that there is a correlation between the shape of the hysteresis loop and the texture properties of mesoporous materials such as pore size, pore size distribution, and their connections. Hysteresis loops were first classified by de Boer[40] and later by the IUPAC.[39] After calcination at 900 °C all four samples exhibit hysteresis loops of type H1, which is often associated with porous materials containing a distinct tubular pore network or agglomerates of compacts with nearly identical particles.

Also noteworthy are the results of N_2 absorption–desorption for the samples calcined at 400 °C. For sample Al-1 a hysteresis

Table 1 Synthetic conditions for the preparation of aluminas

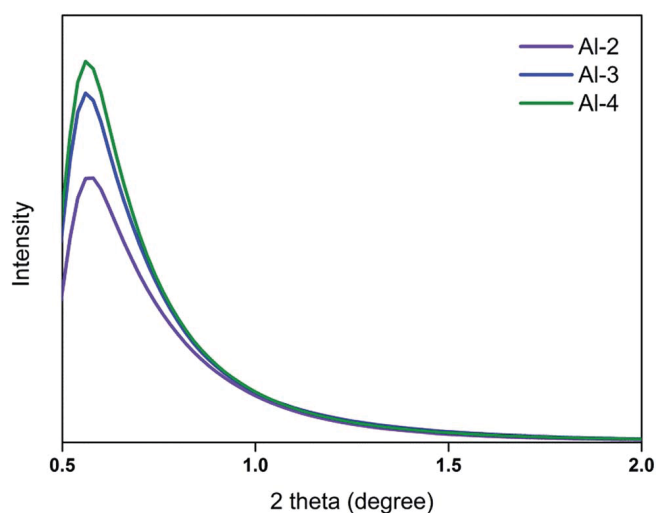| Sample	Alkoxides precursor	Template	Acid
Al-1	Al(O^{i}Pr)$_3$	Plutonic P123	HNO$_3$
Al-2	Al(OPh)$_3$	Plutonic P123	HNO$_3$
Al-3	[Al(OCH$_2$CH$_2$OCH$_3$)$_3$]	Plutonic P123	HNO$_3$
Al-4	[Al(OCH$_2$CH$_2$OCH$_2$CH$_2$OCH$_3$)$_3$]	Plutonic P123	HNO$_3$
Al-5	Al(O^{i}Pr)$_3$	—	HNO$_3$
Al-6	[Al(OCH$_2$CH$_2$OCH$_2$CH$_2$OCH$_3$)$_3$]	—	HNO$_3$

Fig. 3 SAXS patterns of Al-2, Al-3, and Al-4 calcined at 900 °C.

loop of type H2 is observed which is usually taken as an indication of the occurrence of channel-like pores of somewhat uniform size with narrow pore size distribution. For sample Al-3 the hysteresis loop is larger than for Al-1 which is due to continued adsorption up to $P/P° = 1$. This behavior is normally taken as an indication of more complex pore networks involving pores with ill-defined shape and a wide pore size distribution.[39] Overall, the pore size distribution is narrow for Al-1 and bimodal pores are observed for Al-3. As mentioned above, the isotherm observed for sample Al-2 can be regarded as a combination of type I and type IV. This means that in addition to the mesopores or agglomerations of identical nanoparticles, a significant amount of micropores are also present. For microporous materials with type I isotherms a high adsorption potential and narrow pore width leads to micropore filling and therefore high uptake (as shown in Fig. 5 Al-2-400 as well) at relatively low pressures. The limiting adsorption is being controlled by the available micropore volume rather than by the interior surface area. As deduced by WAXS, the calcination of sample Al-2 at 900 °C results in crystallization which is accompanied by the change of its isotherm to type IV and a hysteresis loop of H1 type. This is believed to be an indication of structural change with a significant decrease in the micropore component. There were no significant changes observed in the isotherms of Al-4 after calcination at 900 °C which shows that it retains most of its structural characteristics upon crystallization at higher temperature. These results show that the presence of phenolic groups resulted in bimodal porosity and increased micropore volume while the application of ether groups leads to a wider pore size distribution.

In Table 2 the data for surface area (BET), pore volume, and mean diameter of the pores are presented for the four samples prepared in the presence of polymeric template and the two additional samples, Al-5 and Al-6, which were prepared under the same conditions, but in absence of the template. As expected, the results show that calcination at higher temperature (900 °C) leads to a decrease in the surface area and pore volume.

For the samples calcined at 400 °C the largest surface area is observed in the sample Al-2 but when compared with the others within the same series its pore volume is found to be the lowest. Moreover, for this sample also the smallest average pore diameter within a given calcination temperature is observed, which can be related to its mixed microporous–mesoporous texture. The presence of micropores in this sample reduces the volume and pore size distribution when compared with the other three samples. Besides having the largest observed
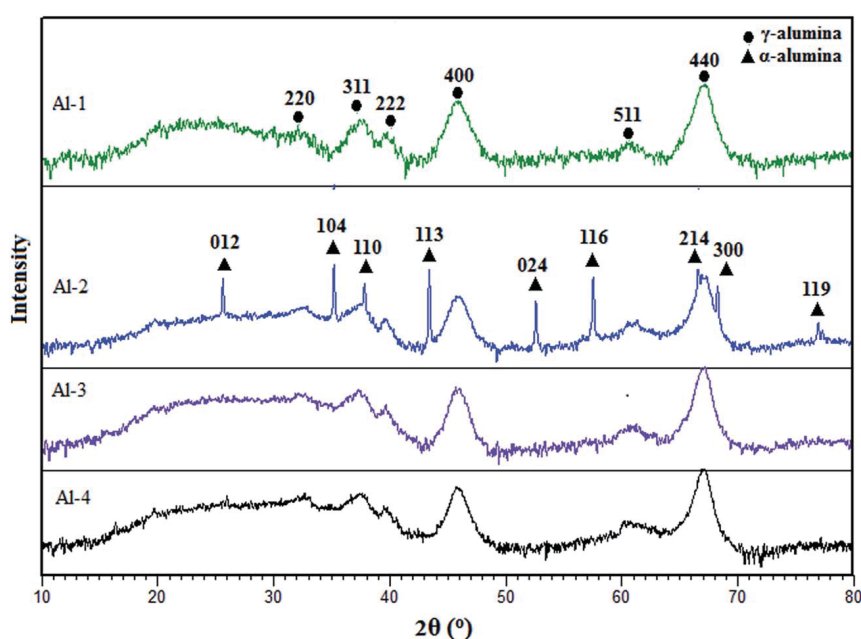

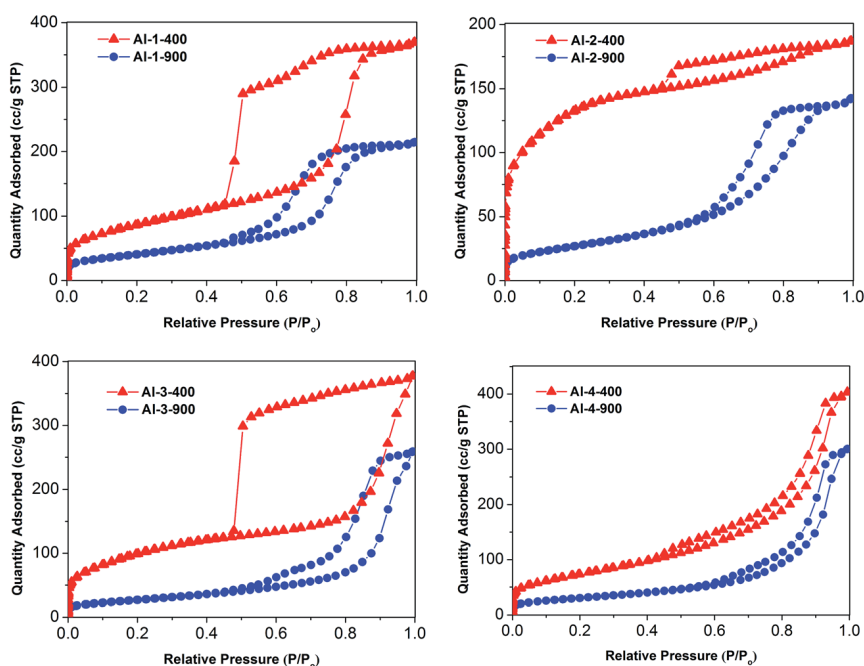Fig. 4 Wide-angle XRD patterns for samples Al-1 to Al-4 calcined at 900 °C.

Fig. 5 Nitrogen adsorption–desorption isotherms of Al-1 to Al-4 calcined at 400 °C and 900 °C represented with red and blue symbols respectively.

Table 2 Pore structure parameters of the samples obtained from different alkoxides precursors

Compounds	Calcination temperature (°C)	BET surface area (m^2 g^{-1})	Total pore volume (cm^3 g^{-1})	Average pore width (nm)
Al-1	400	312	0.57	7.3
	900	147	0.33	9.0
Al-2	400	480	0.29	2.4
	900	99	0.22	8.9
Al-3	400	366	0.58	6.4
	900	97	0.40	16.5
Al-4	400	269	0.63	9.3
	900	109	0.47	17.0
Al-5	400	232	0.19	3.2
Al-6	400	168	0.68	16.2

surface area (480 m^2 g^{-1}), also the presence of two types of pores (micro- and mesopores) is a significant feature for the sample Al-2, which clearly demonstrates the substantial impact of the aluminum alkoxide precursor.

For calcination at 900 °C two groups can be identified, as the average pore size distribution is concerned, with distinct ranges for Al-1 and Al-2 as well as Al-3 and Al-4 at around 9 and 17 nm, respectively. Within the first group the sample Al-1 possesses mesopores with a narrow pore size distribution, a high surface area, and a corresponding pore volume. A closer inspection of the data for samples Al-3 and Al-4 reveals that the utilization of ether-alkoxides in the aluminum precursor not only affects the surface area, but results in a considerable increase of the average pore diameter and volume. The extension of the alkoxide chain with additional potential donor groups, as for

the samples Al-3 and Al-4, leads to a considerably larger pore volume and a slight increase in its average pore size, which is particularly evident for sample Al-4.

To probe the influence of the polymeric template the sample Al-5 was prepared in a manner similar to Al-1 but in absence of template. The results show that the surface area, volume and average pore diameter are significantly decreased and a broader pore size distribution is obtained. For sample Al-6, which was likewise prepared in a manner similar to Al-4 but in the absence of polymeric template, the results show that while the volume and average pore diameter increase, the surface area decreases. The XRD patterns for the samples Al-5 and Al-6 are presented in Fig. 6 and show that their crystallization pattern is similar to the same samples which have been prepared in the presence of template. In Conclusion, these two additional experiments reveal the importance of the presence of polymeric template for the preparation of porous aluminas.

TEM and SEM images of sample Al-1 are depicted in Fig. 7. The images for samples obtained after calcination at 400 °C show the alignment of tubular structures (Fig. 7a and b) and the corresponding presence of a hexagonal arrangement of these tubular structures for both calcination at 400 °C (Fig. 7c) and 900 °C (Fig. 7d). Selected TEM images of the prepared samples are shown in Fig. 8 and 9 which confirm the retention of the porous structure of the samples after heat treatment at 900 °C.

4. Conclusions

The influence of different aluminum alkoxide precursors as one of the most important parameters in the synthesis of nanoporous aluminas has been explored. These results show that all the prepared samples were thermally stable and preserved their
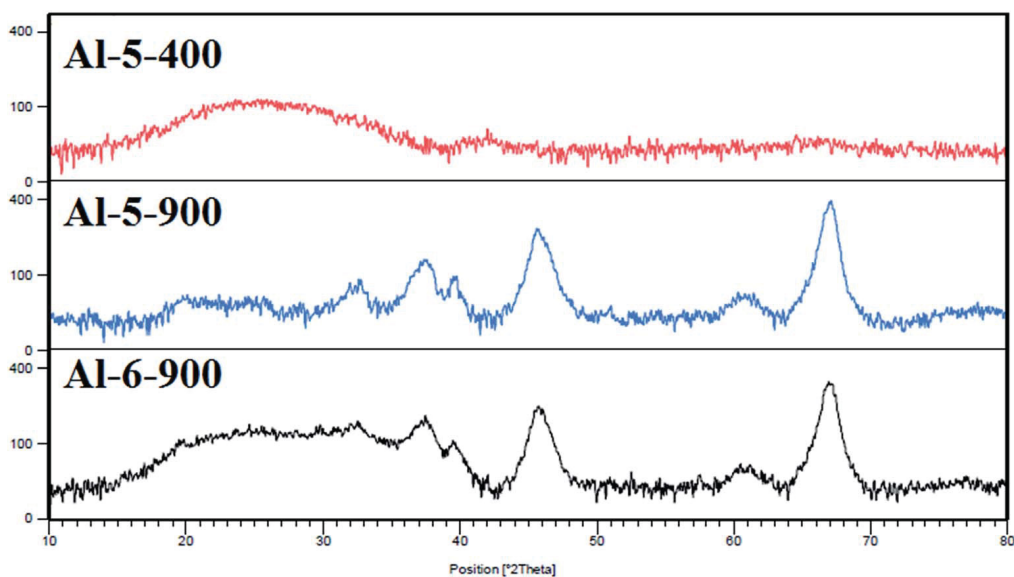
Fig. 6   Wide-angle XRD patterns of samples prepared in absence of any template.
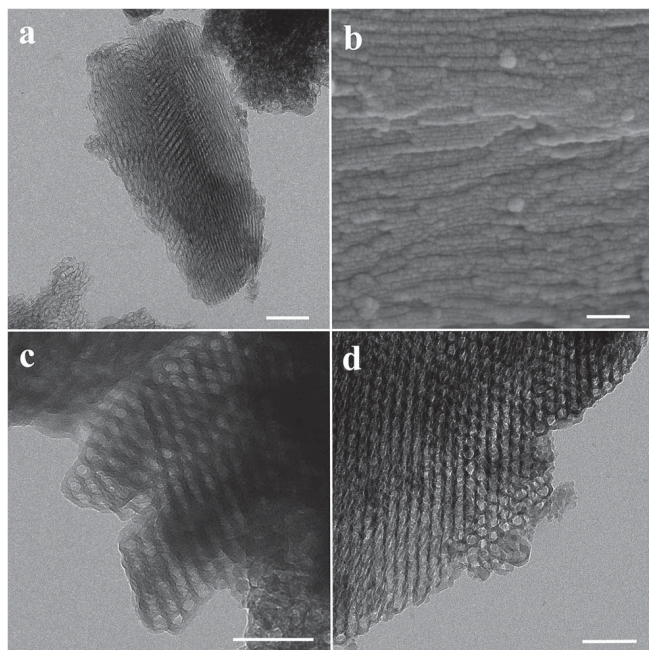

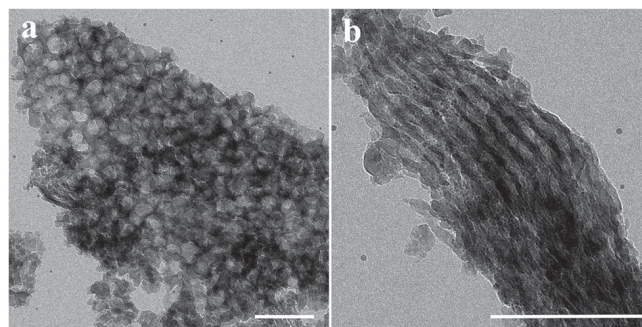Fig. 7   (a) and (b) TEM and SEM images of Al-1 calcined at 400 °C, view along the 110 direction; (c) TEM image of Al-1 calcined at 400 °C, view along the 001 direction; (d) TEM image of Al-1 calcined at 900 °C, view along the 001 direction. Scale bars 100 nm (a and b) and 50 nm (c and d).

Fig. 8   (a) TEM image of Al-3 calcined at 900 °C, view along the 001 direction; (b) TEM image of Al-3 calcined at 900 °C, view along the 110 direction. Scale bars 100 nm.
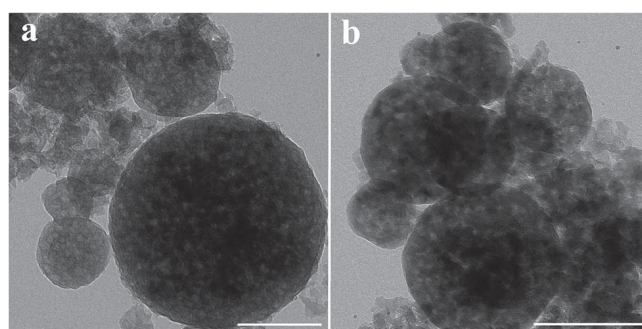

Fig. 9   TEM images of Al-4 calcined at 400 °C (a), and calcined at 900 °C. (b). Scale bars 100 nm.

porous structure upon elevated heat treatment. SAXS also showed that the alkyl or alkylether groups lead to increased porosity of the final product if compared to the aryl group. All the samples were found to be amorphous after calcination at 400 °C with relatively high surface areas. Additionally, the utilization of the aluminum phenoxide precursor leads to formation of a bimodal microporous–mesoporous structure after calcination at 400 °C and a mixed crystalline phase (γ- and α-alumina) with mesoporous-macroporous structure when

calcined at 900 °C, while for the other three samples solely the formation of γ-alumina is observed. The usage of the ether-alkoxides not only affects the surface area, but also results in an increase of the average diameter of the pores and their volumes. The extension of ether-alkoxide chain with additional

ether groups leads to a larger pore volume and a slight increase in its average pore size. Thus, depending on the desired catalytic reaction or catalysis support, each of the molecular precursors could be utilized to obtain tailor-made materials for the intended application.

Acknowledgements

References

1 R. E. Cohen, *Curr. Opin. Solid State Mater. Sci.*, 1999, **4**, 587–590.

2 G. Mohammadnezhad, M. M. Amini and H. R. Khavasi, *Dalton Trans.*, 2010, 10830–10832.

3 J. Hwang, C. Jo, K. Hur, J. Lim, S. Kim and J. Lee, *J. Am. Chem. Soc.*, 2014, **136**, 16066–16072.

4 R. Boppella, P. Manjula, S. Arunkumar and S. V. Manorama, *Chem. Sens.*, 2014, **4**, 19.

5 E. Sattarzadeh, G. Mohammadnezhad and M. M. Amini, *Mater. Lett.*, 2011, **65**, 527–529.

6 M. M. Amini, G. Mohammadnezhad, M. Mirzaee and H. R. Khavasi, *Appl. Organomet. Chem.*, 2010, **24**, 431–438.

7 J. A. Pihl, T. J. Toops, G. B. Fisher and B. H. West, *Catal. Today*, 2014, **231**, 46–55.

8 S. Fogel, D. E. Doronkin, P. Gabrielsson and S. Dahl, *Appl. Catal., B*, 2012, **125**, 457–464.

9 S. Jagtap, M. K. N. Yenkie, N. Labhsetwar and S. Rayalu, *Microporous Mesoporous Mater.*, 2011, **142**, 454–463.

10 G. Macias, J. Ferré-Borrull, J. Pallarès and L. F. Marsal, *Analyst*, 2015, DOI: 10.1039/C4AN01408A.

11 L. R. Hubbard, J. B. Kana-Kana and B. G. Potter, 2014, *Ceramics for Environmental and Energy Applications II: Ceramic Transactions*, vol. 246, pp. 65–75.

12 K. G. Stamplecoskie and J. S. Manser, *ACS Appl. Mater. Interfaces*, 2014, **6**, 17489–17495.

13 S. Faramawy, M. S. El-Shall, M. A. El Wahed, T. Zaki and H. A. El Salam, *J. Am. Sci.*, 2014, **10**, 139–145.

14 B. Huang, C. H. Bartholomew and B. F. Woodfield, *Microporous Mesoporous Mater.*, 2014, **183**, 37–47.

15 D. N. Kelly, R. H. Wakabayashi and A. M. Stacy, *ACS Appl. Mater. Interfaces*, 2014, **6**, 20122–20129.

16 Q. Wu, F. Zhang, J. Yang, Q. Li, B. Tu and D. Zhao, *Microporous Mesoporous Mater.*, 2011, **143**, 406–412.

17 S. M. Grant and M. Jaroniec, *J. Mater. Chem.*, 2012, **22**, 86–92.

18 W. Q. Jiao, M. B. Yue, Y. M. Wang and M. Y. He, *Microporous Mesoporous Mater.*, 2012, **147**, 167–177.

19 S. Shen, W. K. Ng, L. S. O. Chia, Y. Dong and R. B. H. Tan, *Cryst. Growth Des.*, 2012, **12**, 4987–4994.

20 C. T. Kresge, M. E. Leonowicz, W. J. Roth, J. C. Vartuli and J. S. Beck, *Nature*, 1992, **359**, 710–712.

21 J. Aguado, J. M. Escola and M. C. Castro, *Microporous Mesoporous Mater.*, 2010, **128**, 48–55.

22 F. Vaudry, S. Khodabandeh and M. E. Davis, *Chem. Mater.*, 1996, **8**, 1451–1464.

23 K. Niesz, P. Yang and G. A. Somorjai, *Chem. Commun.*, 2005, 1986–1987.

24 Z. Zhang, R. W. Hicks, T. R. Pauly and T. J. Pinnavaia, *J. Am. Chem. Soc.*, 2002, **124**, 1592–1593.

25 C. Marquez-Alvarez, N. Zilkova, J. Perez-Pariente, J. Cejka and C. R. S. Eng, *Catal. Rev.: Sci. Eng.*, 2008, **50**, 222–286.

26 P. Yang, D. Zhao, D. I. Margolese, B. F. Chmelka and G. D. Stucky, *Nature*, 1998, **396**, 152–155.

27 Z. Zhang and T. J. Pinnavaia, *J. Am. Chem. Soc.*, 2002, **124**, 12294–12301.

28 M. Kuemmel, D. Grosso, C. Boissière, B. Smarsly, T. Brezesinski, P. A. Albouy, H. Amenitsch and C. Sanchez, *Angew. Chem., Int. Ed.*, 2005, **44**, 4589–4592.

29 Q. Yuan, A. X. Yin, C. Luo, L. D. Sun, Y. W. Zhang, W. T. Duan, H. C. Liu and C. H. Yan, *J. Am. Chem. Soc.*, 2008, **130**, 3465–3472.

30 W. Cai, J. Yu, C. Anand, A. Vinu and M. Jaroniec, *Chem. Mater.*, 2011, **23**, 1147–1157.

31 M. Z. Liu and H. M. Yang, *Colloids Surf., A*, 2011, **371**, 126–130.

32 P. F. Fulvio, R. I. Brosey and M. Jaroniec, *ACS Appl. Mater. Interfaces*, 2010, **2**, 588–593.

33 S. M. Grant and M. Jaroniec, *J. Mater. Chem.*, 2012, **22**, 86–92.

34 M. Sharbatdaran, M. M. Amini and A. Majdabadi, *Mater. Lett.*, 2010, **64**, 503–505.

35 M. May, J. Navarrete, M. Asomoza and R. Gomez, *J. Porous Mater.*, 2007, **14**, 159–164.

36 K. Tadanaga, S. Ito, T. Minami and N. Tohgi, *J. Non-Cryst. Solids*, 1996, **201**, 231–236.

37 H. Adkins and F. W. Cox, *J. Am. Chem. Soc.*, 1938, **60**, 1151–1159.

38 J. A. Meese-Marktscheffel, R. E. Cramer and J. W. Gilje, *Polyhedron*, 1994, **13**, 1045–1050.

39 K. S. W. Sing, D. H. Everett, R. A. W. Haul, L. Moscou, R. A. Pierotti, J. Roquerol and T. Siemieniewska, *Pure Appl. Chem.*, 1985, **57**, 603–619.

40 J. H. de Boer, *The Structure and Properties of Porous Materials*, Butterworths, London, 1958, p. 68.

Supplementary materials

Facile synthesis of highly thermally stable nanoporous γ-aluminas from aluminum alkoxides precursors

Gholamhossein Mohammadnezhad*, Oluseun Akintola, Winfried Plass, Felix H. Schacher, Frank Steiniger[d],
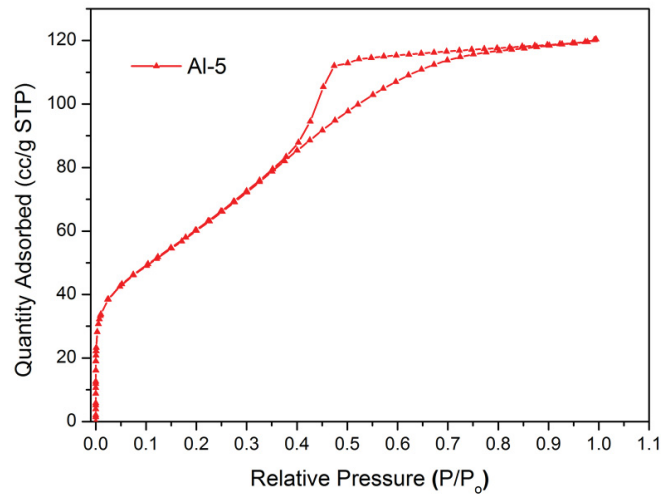
Martin Westermann

Figure S1. Nitrogen adsorption-desorption isotherm of Al-5 calcined at 400 °C.
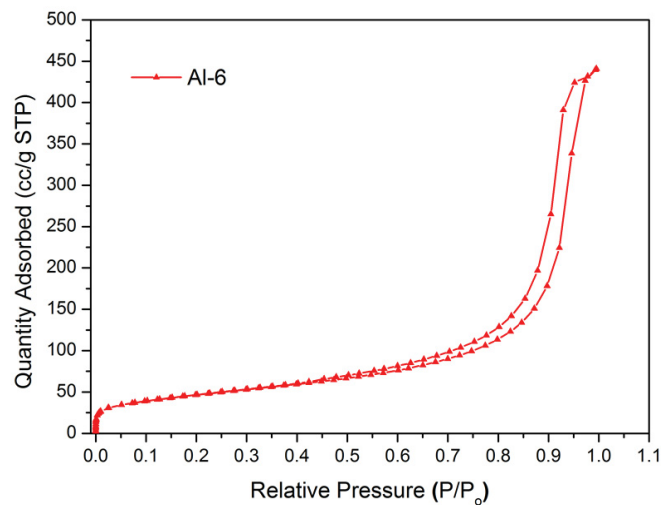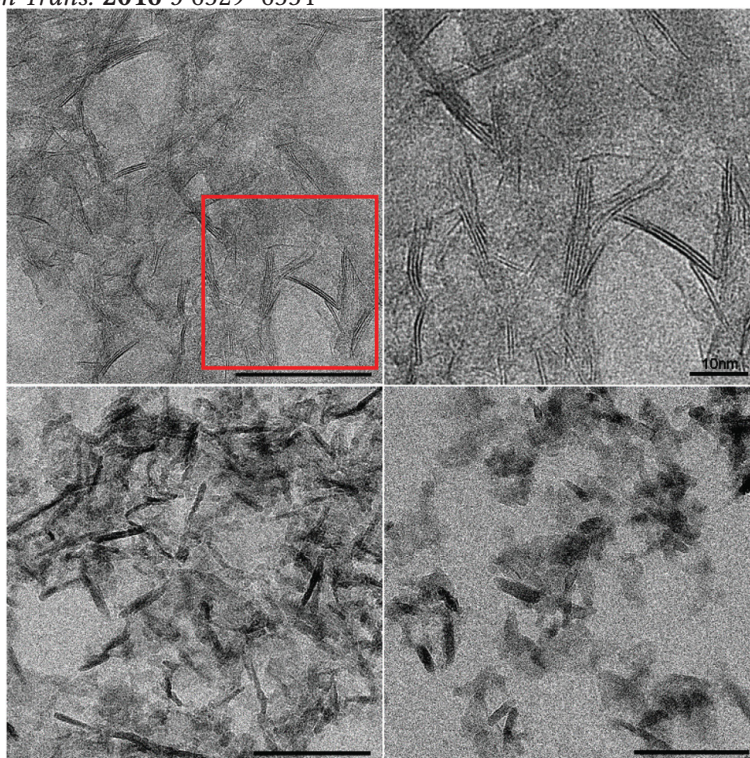

Figure S2. Nitrogen adsorption-desorption isotherm of Al-6 calcined at 400 °C.

Publication 6

A facile, green and efficient surfactant-free method for synthesis of aluminum nanooxides with an extraordinary high surface area

Gholamhossein Mohammadnezhad, <u>Oluseun Akintola</u>, Winfried Plass, Frank Steiniger, Martin Westermann *Dalton Trans.* **2016** *5* 6329–6334

COMMUNICATION

A facile, green and efficient surfactant-free method for synthesis of aluminum nanooxides with an extraordinary high surface area†

Gholamhossein Mohammadnezhad,*[a] Oluseun Akintola,[b] Winfried Plass,*[b] Frank Steiniger[c] and Martin Westermann[c]

Nano boehmite with unprecedented high surface area and pore volume (802 m² g⁻¹, 2.35 cm³ g⁻¹) was prepared using a facile, green and efficient surfactant-free synthesis method. The structure of the material is characterized by the presence of plates with varying thicknesses and morphologies. The calcined samples show curved and rolled plates with a nanotube-like appearance.

Nanoscience and nanotechnology, in which the objects or features studied are typically in the range of 1–100 nm, have been among the most important developing areas in the last few years. Synthesis, characterization, and application of nanoparticles are of fundamental importance to this field. In this regard, a large number of methods such as co-precipitation, sol–gel processes including hydrolytic and non-hydrolytic, hydrothermal, solvothermal, microwave-assisted, and sonochemical methods, template utilization, and biomimetic methods, or a combination of two or more of the above mentioned methods, have been developed for the controlled synthesis of the desired nanoparticles.[1,2]

Utilization of surfactants in nanomaterial synthesis is of particular importance due to their tendency to affect the chemical, physical, and structural properties of the latter, such as size, shape, porosity, and dispersibility.[3–6] However, usage of surfactants is not without its own drawbacks, such as their uncertain biocompatibility in addition to their irreversible adsorption on the surface of nanoparticles. Often the latter case leads to an unpredictable and undesirable impact on their properties, resulting in the reduction of the accessible surface which is a crucial point to be considered especially when catalytic applications are the goal.[5–8]

The commonly used media for surfactant-free synthesis of inorganic nanoparticles over time have been aqueous or non-aqueous and these could be under hydrolytic or nonhydrolytic conditions. Some important features of the surfactant-free methods such as higher yields, lower impurities, utilization of green solvents, simplicity, and greater accessible surface area make them both scientifically and economically interesting.[7,9–13] However, the aqueous approach led to certain limitations being observed, such as low or lack of crystallinity, need for strict control of synthetic conditions, and complicated hydrolytic behavior arising from the dual character of water as a solvent and ligand.[14–16] An obvious alternative to the aqueous approach is to exclude water and this has drawn a considerable amount of interest. In this method, organic species play a large role in the synthesis of the nanoparticles but detailed information regarding the mechanism is not yet clearly understood.[17–19]

Among the wide variety of different nanomaterials, which have been prepared from different routes as mentioned above, nanocrystalline aluminum oxides occupy a particularly interesting niche. They have been used in many industrial processes as adsorbents, in catalysis, as catalyst components, in optics, electronics, high performance ceramics, and in many other applications.[20–24] Syntheses of these materials with enhanced properties, in particular, their surface area, pore volume, morphology, and dimensionality continue to receive extraordinary attention.[25–33]

Alumina (Al_2O_3) and boehmite (AlOOH) have already been prepared by a wide variety of methods, among which is the Bayer process, a famous industrial method for the large scale production of aluminum oxides.[34–39] However, this method still has a few shortcomings such as the large amount of impurities accompanying the products which hampers the utilization of these aluminum oxides as the substrate material for LEDs (light emitting diodes) and other applications[40] An alternative method is the utilization of aluminum alkoxides as pure molecular precursors.[3] In 1986 Fanelli reported the reaction of aluminum *sec*-butoxide in 2-butanol, the parent

[a]Department of Chemistry, Isfahan University of Technology, Isfahan 84156-83111, Iran. E-mail: mohammadnezhad@cc.iut.ac.ir
[b]Institute of Inorganic and Analytical Chemistry, Chair of Inorganic Chemistry II, Friedrich Schiller University Jena, Humboldtstr. 8, 07743 Jena, Germany. E-mail: sekrplass@uni-jena.de
[c]Electron Microscopy Center, Jena University Hospital, Ziegelmühlenweg 1, 07743 Jena, Germany
†Electronic supplementary information (ESI) available. See DOI: 10.1039/c6dt00611f

alcohol, with *in situ* generated water from alcohol dehydration at 250 °C in an autoclave reactor and obtained high surface area amorphous aluminum oxide.[41] A similar reaction in the presence of acid led to the formation of boehmite along with aluminum sulfate with lower surface area (50 m^2 g^{-1}). Jun *et al.* not too long ago presented a method for the preparation of high surface area boehmite and alumina *via* hydrolysis of aluminum alkoxides in their parent alcohols.[42]

Herein, we describe a method for the preparation of high surface area nano boehmite and alumina by using a surfactant-free modified sol–gel route which has been performed in a shorter time with higher surface area and different morphologies to the ones previously reported. A particular feature of this method is avoiding the use of any surfactants as a template and the utilization of pure aluminum alkoxides in their parent alcohol and subsequent hydrolysis of the precursors in the presence of a small portion of aqueous solution of an organic acid with short drying times. The versatility of this method should allow for the synthesis of a wide variety of other single or mixed metal oxide nanomaterials as well as the synthesis of highly pure *in situ* prepared doped semiconductors. Furthermore, modifications of the surface of these nanoparticles make them valuable candidates for targeting applications.

Nano boehmite and γ-alumina were prepared using an accessible and reliable surfactant-free method which does not need any expensive template and stabilizer. It also involves the hydrolysis of clear solutions of either aluminum 2-propoxide or aluminum 2-methoxyethoxide, as single source molecular precursors, in 2-propanol and 2-methoxyethanol (their parent alcohol), respectively. Hydrolysis was performed by addition of a small portion of aqueous solution of acetic acid followed by reflux and aging for 24 h. One of the key factors in this step is the reflux temperature which is determined by the type of the utilized alcohol. Boiling temperatures of 2-propanol and 2-methoxyethanol are about 83 and 125 °C, with the latter being in the suitable range for preparation of nano boehmite. The side-product of the reaction in this stage is liberated alcohol which is also the solvent in addition to a small amount of water and an organic acid. In contrast to the aqueous method, the alcohol was simply recovered by taking advantage of the lower surface tension of the mixture through distillation at lower temperatures using a rotary evaporator thus reducing energy consumption while simultaneously avoiding time consuming filtration. The samples were then dried at 120 mbar, and mild temperature (70 °C) in a short time (3 h) to remove acetic acid. The obtained powders from aluminum 2-propoxide and aluminum 2-methoxyethoxide molecular precursors are named Al-1 and Al-2, respectively and were characterized by wide angle X-ray diffraction (WA-XRD), N$_2$ adsorption–desorption, and TEM measurements.

Fig. 1 shows the WA-XRD data of the dried samples at 70 °C. The data reveals formation of the boehmite phase in both cases (JCPDS card no. 00-005-0190). Since the reflux temperatures of the samples were at the boiling point of their parent alcohols, Al-2 was reacted at a higher temperature and consequently showed better crystallinity. Subsequently, both
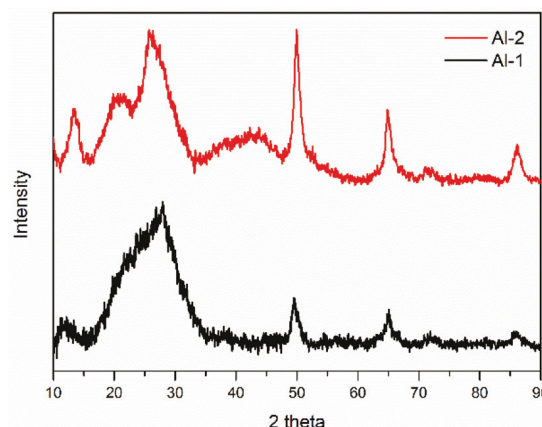

Fig. 1 Wide-angle XRD patterns for samples Al-1 and Al-2 dried at 70 °C.

samples were calcined at 600 and 800 °C. The wide-angle XRD patterns for the samples Al-1 and Al-2 are depicted in Fig. S1 and S2,† respectively. In both cases, calcination at 800 °C results in conversion of boehmite to γ-alumina as the crystalline phase (JCPDS card no. 10-0425). For Al-1 the formation of γ-alumina is already observed at 600 °C, whereas for Al-2 no significant reflections were detected for the sample calcined at 600 °C.

Fig. 2 depicts the N$_2$ adsorption–desorption isotherms and pore size distributions of the as-prepared and calcined samples at 600 and 800 °C. According to the IUPAC classification, these isotherms exhibit classical type IV isotherms.[43] The clearly observed type IV isotherms along with hysteresis loops are typical for mesoporous materials. Moreover, it is evident that the hysteresis loops of Al-1 and Al-2 are not similar. For Al-2 hysteresis loops of type H2 are observed while Al-1 exhibits no limiting uptake in the range of high P/P^0 and reveals hysteresis loops of type H3. It has already been established that there exists a correlation between the shape of the hysteresis loop and the texture properties of mesoporous materials such as pore size, pore size distribution, and their connections. The data of Al-1 indicates the presence of non-rigid aggregates of the plate-like framework giving rise to slit-shaped mesopores. For Al-2 on the other hand, the appearance of its isotherm already suggests the presence of both micropores and mesopores within its pore structure. This was confirmed *via* applying the De-Boer thickness method to obtain the micropore areas (see Fig. S3 and Table S1†). The shape of its hysteresis loop is indicative of the presence of pore blocking effects as seen from the sudden step-down upon closing up, a major characteristic of the H2. Despite the utilization of the same procedure in preparation of the samples, different structural data were obtained, which demonstrates the importance of the selected precursors on their characteristics.

Table 1 summarizes the physicochemical properties of Al-1 and Al-2 including BET surface areas, pore volumes and mean pore diameters.

Remarkably, Al-1, the nano boehmite prepared from the aluminum 2-propoxide precursor shows an extraordinary high specific surface area of 802 m^2 g^{-1} paired with a high pore
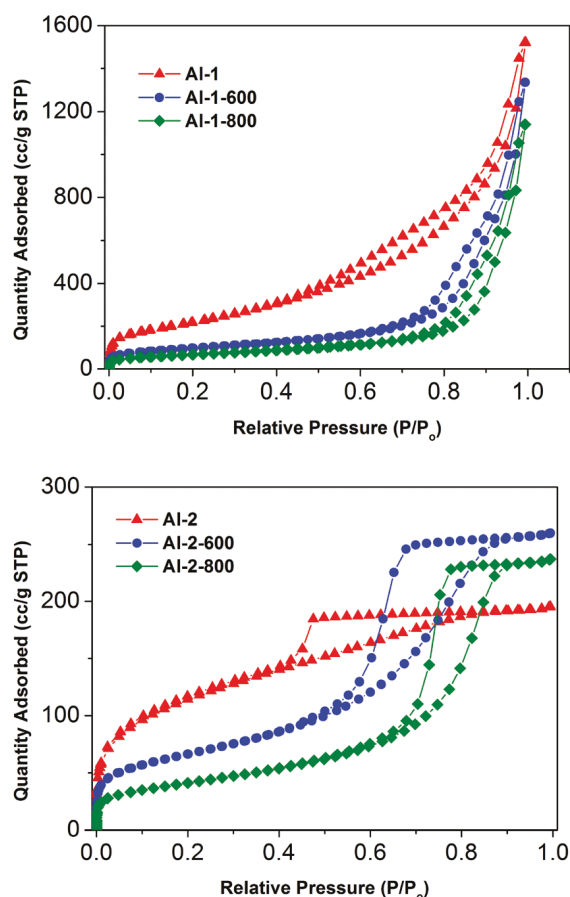
Fig. 2 Nitrogen adsorption–desorption isotherms of Al-1 (top) and Al-2 (bottom) dried at 70 °C, and calcined at 600 °C and 800 °C represented with red, blue, and green symbols, respectively.

The TEM images of samples Al-1 and Al-2 obtained after vacuum drying and calcination (600 and 800 °C) are depicted in Fig. 3 and 4, respectively. The samples dried at 70 °C show the presence of plates with varying thicknesses which are
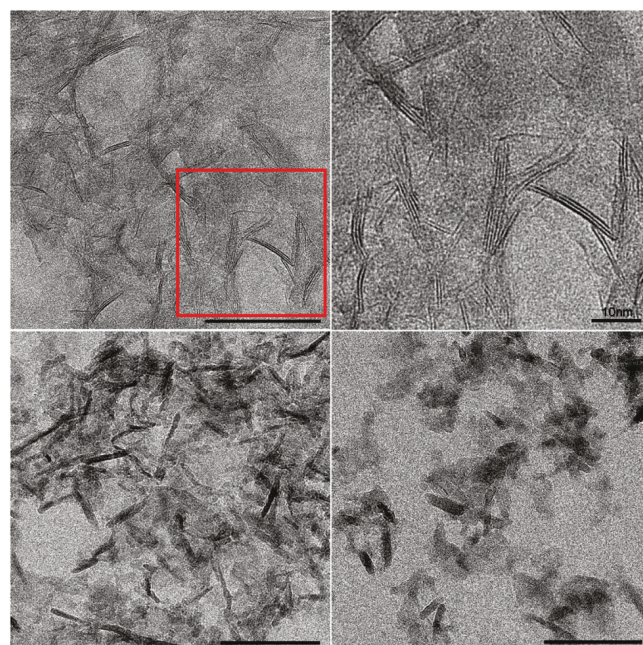

Fig. 3 (Top, left) TEM image of Al-1 dried at 70 °C and expanded part from the area in the red rectangle (top, right); (bottom, left) TEM image of Al-1 calcined at 600 °C; (bottom, right) TEM image of Al-1 calcined at 800 °C. Not labeled scale bars: 50 nm.

Table 1 Pore structure parameters of the samples obtained from alkoxide precursors

Compound	Calcination temperature (°C)	BET surface area (m^2 g^{-1})	Total pore volume (cm^3 g^{-1})	Average pore width (nm)
Al-1	—	802	2.35	11.7
	600	343	2.07	24.1
	800	242	1.77	29.2
Al-2	—	420	0.30	2.9
	600	239	0.40	6.7
	800	149	0.37	9.9

volume of 2.35 cm^3 g^{-1}. This is in contrast to the common observation in the case of aluminas derived from aqueous based synthesis, which show an inverse relationship between the total pore volume and the surface areas. In fact, for Al-1 the pore volume shows a direct relationship to the surface area, with both parameters decreasing at higher calcination temperatures. Similar trends are observed for Al-2, however, with the exception of a comparatively low total pore volume for the as-prepared sample. Interestingly, the average pore size distribution of both samples shows related trends (see Fig. S4 and Table S2†).
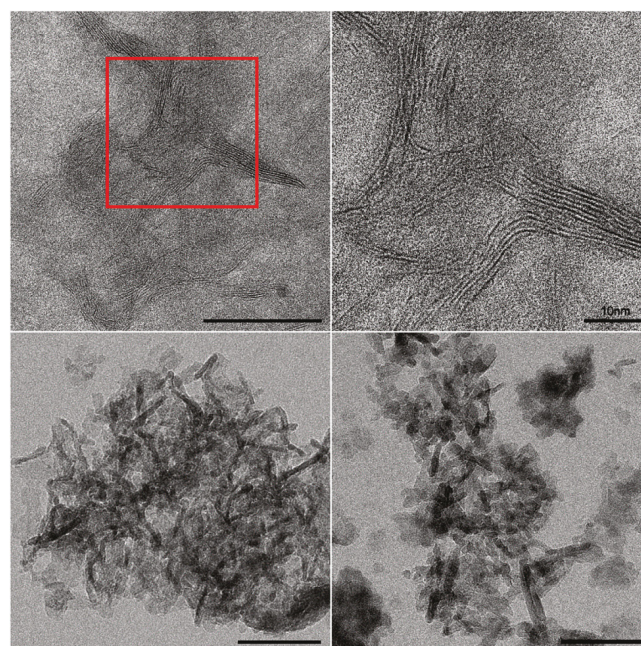

Fig. 4 (Top, left) TEM image of Al-2 dried at 70 °C and the expanded part from the area in the red rectangle (top, right); (bottom, left) TEM image of Al-2 calcined at 600 °C; (bottom, right) TEM image of Al-2 calcined at 800 °C. Not labeled scale bars: 50 nm.

folded and show aggregation (Fig. 3 and 4, top). High temperature treatment at 600 and 800 °C not only leads to formation of γ-alumina but also results in a change of morphology leading to more curved and partially rolled plates with a nanotube-like appearance (Fig. 3 and 4, bottom).

A remarkable advantage of the presented method is the avoidance of any non-green, environmental polluting organic solvents in addition to the ease of recovery of the employed alcohol. The use of small amounts of water and an organic acid facilitates elimination of the alcohol and distillation processes at lower temperatures leading to conservation of the structure and enabling the preparation of high purity materials.

To conclude, the presented procedure represents a surfactant-free method for the synthesis of boehmite (AlOOH) and γ-alumina (Al_2O_3) with substantially high surface area and pore volume from easily prepared non-commercial aluminum alkoxides. The ability to recover and reuse the solvent in a short time is economically favorable, and hydrolysis using a small portion of aqueous organic acid facilitates both the distillation and drying processes.

Acknowledgements

Notes and references

1 C. N. R. Rao, H. R. Matte, R. Voggu and A. Govindaraj, *Dalton Trans.*, 2012, **41**, 5089–5120.
2 B. L. Cushing, V. L. Kolesnichenko and C. J. O'Connor, *Chem. Rev.*, 2004, **104**, 3893–3946.
3 G. Mohammadnezhad, O. Akintola, W. Plass, F. Schacher, F. Steiniger and M. Westermann, *RSC Adv.*, 2015, **5**, 49493–49499 and references therein.
4 Y. W. Jun, J. S. Choi and J. Cheon, *Angew. Chem., Int. Ed.*, 2006, **45**, 3414.
5 J. Park, J. Joo, S. G. Kwon, Y. Jang and T. Hyeon, *Angew. Chem., Int. Ed.*, 2007, **46**, 4630.
6 G. R. Patzke, Y. Zhou, R. Kontic and F. Conrad, *Angew. Chem., Int. Ed.*, 2011, **50**, 826.
7 N. Pinna and M. Niederberger, *Angew. Chem., Int. Ed.*, 2008, **47**, 5292.
8 S. K. Sahoo, J. Panyam, S. Prabha and V. Labhasetwar, *J. Controlled Release*, 2002, **82**, 105.
9 G. Garnweitner and M. Niederberger, *J. Am. Ceram. Soc.*, 2006, **89**, 1801.
10 E. Sattarzadeh, G. Mohammadnezhad and M. M. Amini, *Mater. Lett.*, 2011, **65**, 527.
11 G. Mohammadnezhad, M. M. Amini and H. R. Khavasi, *Dalton Trans.*, 2010, **39**, 10830.
12 G. Mohammadnezhad and M. M. Amini, *J. Sol-Gel Sci. Technol.*, 2016, **77**, 378.
13 Z. Li, J. Han, L. Fan and R. Guo, *CrystEngComm*, 2015, **17**, 1952.
14 A. Dessombz, D. Chiche, P. Davidson, P. Panine, C. Chanéac and J. P. Jolivet, *J. Am. Chem. Soc.*, 2007, **129**, 5904.
15 J. P. Jolivet, C. Froidefond, A. Pottier, C. Chanéac, S. Cassaignon, E. Tronc and P. Euzen, *J. Mater. Chem.*, 2004, **14**, 3281.
16 X. Xia, Y. Zhang, D. Chao, C. Guan, Y. Zhang, L. Li and H. J. Fan, *Nanoscale*, 2014, **6**, 5008.
17 Y. Yin and A. P. Alivisatos, *Nature*, 2005, **437**, 664.
18 S. H. Yu, A. Pucci, T. Herntrich, M. G. Willinger, S. H. Baek, Y. E. Sung and N. Pinna, *J. Mater. Chem.*, 2011, **21**, 806.
19 M. Stefik, F. J. Heiligtag, M. Niederberger and M. Grätzel, *ACS Nano*, 2013, **7**, 8981.
20 M. Trueba and S. P. Trasatti, *Eur. J. Inorg. Chem.*, 2005, **17**, 3393.
21 S. Gunduz and T. Dogu, *Appl. Catal., B*, 2015, **168**, 497.
22 Y. Inoue, T. Matsumura, M. Hazumi, A. T. Lee, T. Okamura, A. Suzuki and H. Yamaguchi, *Appl. Opt.*, 2014, **53**, 1727.
23 G. Zhang, H. Wu, C. Chen, T. Wang, W. Wu, J. Yue and C. Liu, *ACS Appl. Mater. Interfaces*, 2015, **7**, 5522.
24 T. Zhang, Y. Zhou, M. He, X. Bu, Y. Wang and C. Zhang, *J. Eur. Ceram. Soc.*, 2015, **35**, 1337.
25 S. Faramawy, M. S. El-Shall, M. A. El Wahed, T. Zaki and H. A. El Salam, *J. Am. Sci.*, 2014, **10**, 139.
26 B. Huang, C. H. Bartholomew and B. F. Woodfield, *Microporous Mesoporous Mater.*, 2014, **183**, 37.
27 D. N. Kelly, R. H. Wakabayashi and A. M. Stacy, *ACS Appl. Mater. Interfaces*, 2014, **6**, 20122.
28 Q. Wu, F. Zhang, J. Yang, Q. Li, B. Tu and D. Zhao, *Microporous Mesoporous Mater.*, 2011, **143**, 406.
29 S. M. Grant and M. Jaroniec, *J. Mater. Chem.*, 2012, **22**, 86.
30 W. Q. Jiao, M. B. Yue, Y. M. Wang and M. Y. He, *Microporous Mesoporous Mater.*, 2012, **147**, 167.
31 S. Shen, W. K. Ng, L. S. O. Chia, Y. Dong and R. B. H. Tan, *Cryst. Growth Des.*, 2012, **12**, 4987.
32 W. Cai, J. Yu, C. Anand, A. Vinu and M. Jaroniec, *Chem. Mater.*, 2011, **23**, 1147.
33 P. F. Fulvio, R. I. Brosey and M. Jaroniec, *ACS Appl. Mater. Interfaces*, 2010, **2**, 588.
34 G. Zhao, L. Xia, B. Zhong, L. Song and G. Wen, *Ceram. Int.*, 2015, **41**, 2590.
35 H. A. Dabbagh and M. Shahraki, *Microporous Mesoporous Mater.*, 2013, **175**, 8.
36 P. Pardo, N. Montoya and J. Alarcón, *CrystEngComm*, 2015, **17**, 2091.
37 N. M. Vitorino, A. V. Kovalevsky, J. C. Abrantes and J. R. Frade, *J. Eur. Ceram. Soc.*, 2015, **35**, 3119.
38 B. Tang, J. Ge, L. Zhuo, G. Wang, J. Niu, Z. Shi and Y. Dong, *Eur. J. Inorg. Chem.*, 2005, **21**, 4366.

39 A. R. Hind, S. K. Bhargava and S. C. Grocott, *Colloids Surf.,
A*, 1999, **146**, 359.

40 H. Ozaki and T. Fukuda, *U.S. Patent Application*, 14/404114,
2013.

41 A. J. Fanelli and J. V. Burlew, *J. Am. Ceram. Soc.*, 1986, **69**,
C-174.

42 K. W. Jun, Y. J. Lee, S. M. Kim and J. Y. Kim, *U.S. Patent*,
20090104108, Washington, DC, U.S. Patent and Trademark
Office, 2009.

43 K. S. W. Sing, D. H. Everett, R. A. W. Haul, L. Moscou,
R. A. Pierotti, J. Rouquerol and T. Siemieniewska, *Pure
Appl. Chem.*, 1985, **57**, 603.

Supplementary

Experimental Section

Aluminum oxides were synthesized as follows: (a) $Al(O^iPr)_3$ precursor: Freshly prepared $Al(O^iPr)_3$ (0.05 mol) was dissolved in 2-propanol (58 mL) and heated under stirring to 83 °C. Subsequently, an aqueous solution of acetic acid (1.7 mmol in 2.7 mL H_2O) was added to the resulting clear pale yellow solution. The temperature was then increased and the slurry was aged statically at reflux temperature for 24 h. The solvent was recovered by distillation with a rotary evaporator and the obtained sol was dried at 120 mbar and 70 °C for 3 h. (b) $[Al(OCH_2CH_2OCH_3)_3]$ precursor: $[Al(OCH_2CH_2OCH_3)_3]$ (0.06 mol) was dissolved in 2-methoxyethanol (117 mL) and heated under stirring to 125 °C. Subsequently, an aqueous solution of acetic acid (2.1 mmol in 3.2 mL H_2O) was added to the resulting clear solution. The temperature of the mixture was then increased and the slurry was aged under static conditions at reflux temperature for 24 h. The solvent was recovered by distillation with a rotary evaporator and the obtained sol was dried at 2 mbar and 70 °C for 3 h. Calcination of the samples were carried out in static air by heating the samples to 600 and 800 °C at a rate of 1 °C/min and maintaining the final temperature for 4 h. The structures of the samples were characterized by N_2 adsorption-desorption, XRD, and TEM. The N_2 adsorption and desorption isotherms were measured using a Quantachrome Autosorb-iQ-MP gas sorption analyzer; the samples were previously outgassed at 250 °C for 6 h. The Brunauer–Emmett–Teller (BET) surface areas were determined from the adsorption data over different relative pressure ranges all between 0.03– 0.28 while ensuring compliance with the consistency criteria.[41] The total pore volume was calculated from the amount adsorbed at a relative pressure of about 0.99. The pore diameter was obtained by NLDFT method.[42] X-ray powder diffraction patterns were recorded at room temperature with a Siemens D5000 (Cu-Kα, germanium monochromator). For transmission electron microscopy (TEM), for each sample, aluminum oxide (20 mg) was added to absolute ethanol (100 µL) and sonicated at 37 kHz and 240 W for 20 min. After 10 min of sedimentation a drop of 6 µL supernatant was placed on top of a carbon-coated 400 mesh copper grid (Quantifoil Micro Tools, Jena, Germany). Excess liquid was removed by placing a sheet of filter paper below the grid. The samples were then air dried and analyzed using a CM120 electron microscope (Philips, Eindhoven, Netherlands) operated at 120 kV. Images were acquired using a 2k TemCam F216 CMOS camera (camera and software, TVIPS, Munich, Germany).
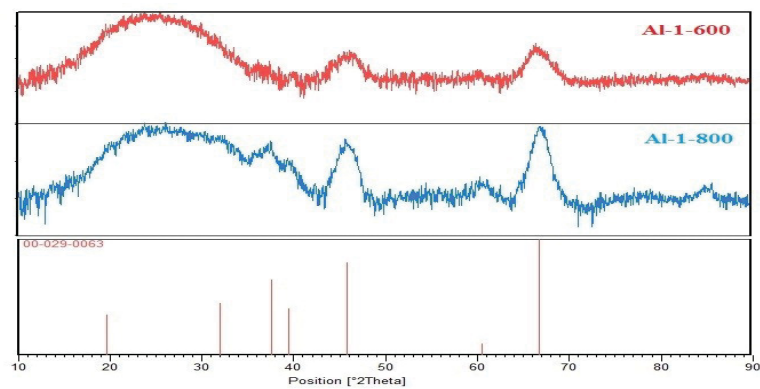
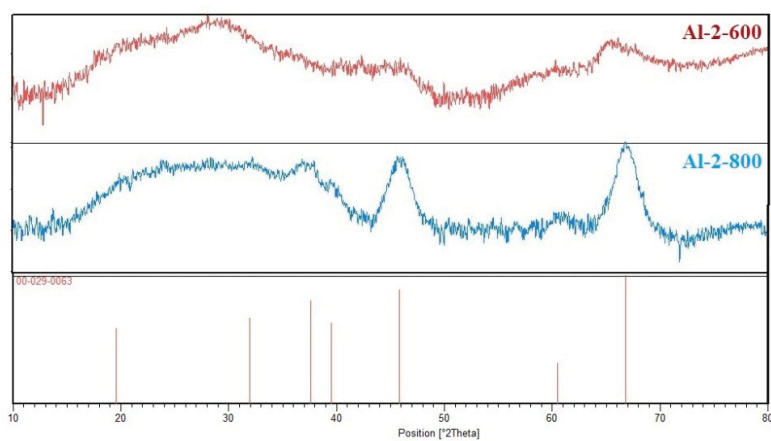**Figure S-1** Wide-angle XRD patterns for **Al-1** calcined at 600 and 800 °C.

Figure S-2 Wide-angle XRD patterns for **Al-2** calcined at 600 and 800 °C.

Table. S-1

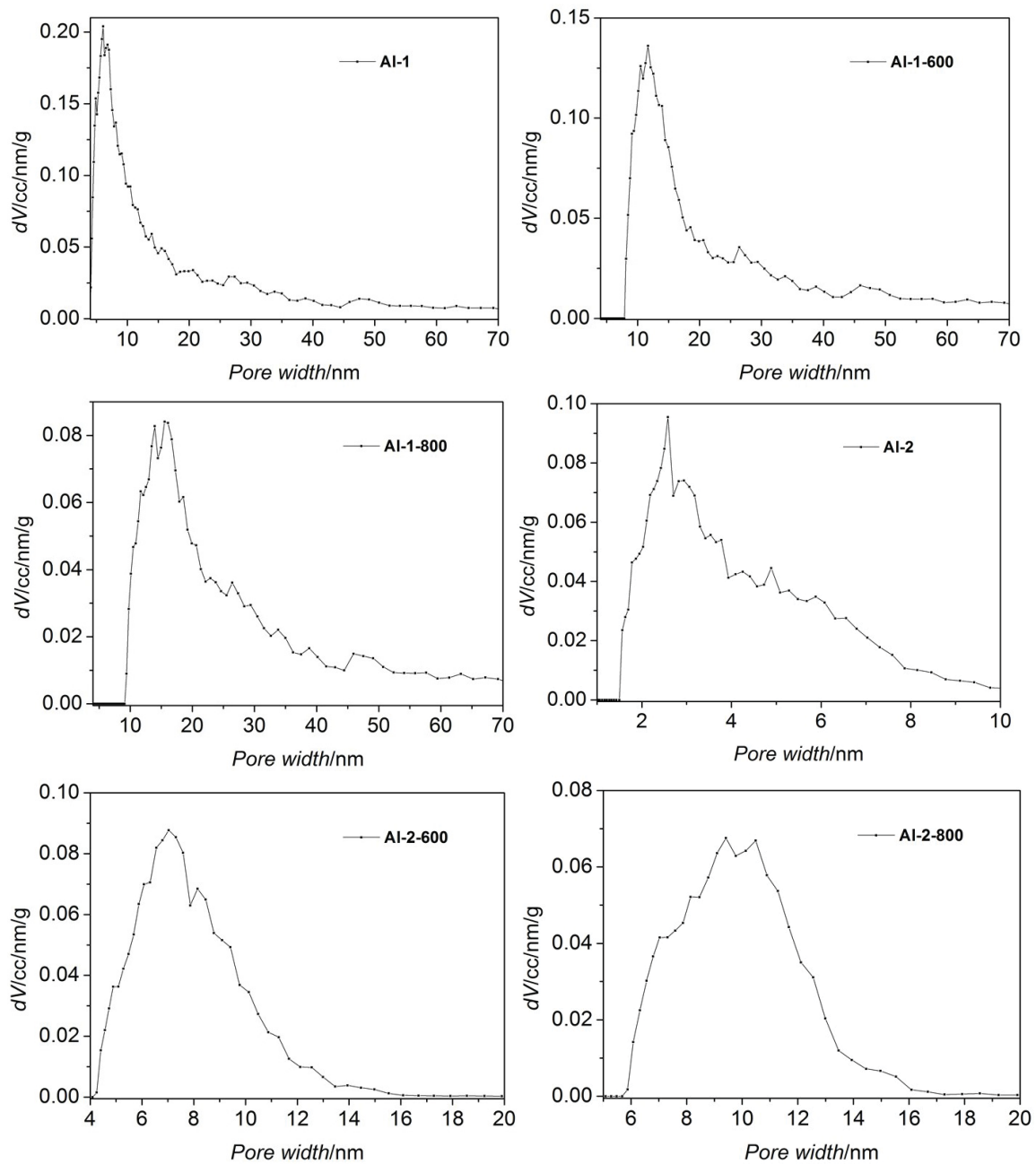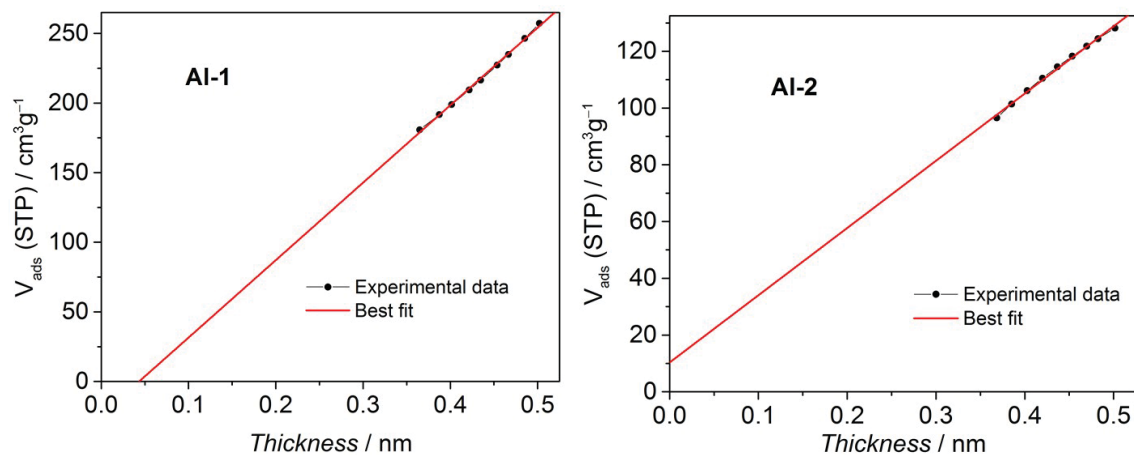|	*P/Po range*	*C*	*Vm*	*P/Po(Vm)*	*θ(P/Po)*
Al-1	0.08-0.28	71.33	184.3	0.10	0.10
Al-1-600	0.03-0.12	147.57	78.8	0.08	0.08
Al-1-800	0.07-0.15	99.6	55.5	0.09	0.09
Al-2	0.05-0.2	79.96	96.6	0.10	0.10
Al-2-600	0.05-0.15	129.42	55.0	0.08	0.08
Al-2-800	0.07-0.18	105.75	34.2	0.10	0.10

Figure S-3

Figure S-4. T-plots for Al-1 and Al-2 calculated by De Boer method.

Table. S-2: Thickness Method Summary

Sample	Intercept	BET Area (m²/g)	External Area (m²/g)	Micropore Area (m²/g)
Al-1	-24.2	802	802	-
Al-2	10.3	420	366	54